Progress in Energy and Combustion Science 96 (2023) 101074

Contents lists available at ScienceDirect

Progress in Energy and Combustion Science

journal homepage: www.elsevier.com/locate/pecs

Elucidation of single atom catalysts for energy and sustainable chemical production: Synthesis, characterization and frontier science

Adrian Chun Minh Loy [a,1], Sin Yong Teng [b,1], Bing Shen How [c], Xixia Zhang [d], Kin Wai Cheah [e], Valeria Butera [d], Wei Dong Leong [f], Bridgid Lai Fui Chin [g], Chung Loong Yiin [h,i], Martin J. Taylor [j,*], Georgios Kyriakou [k,**]

[a] Department of Chemical and Biological Engineering, Monash University, Clayton, Victoria, 3800, Australia
[b] Radboud University, Institute for Molecules and Materials, P.O. Box 9010, 6500 GL, Nijmegen, the Netherlands
[c] Research Centre for Sustainable Technologies, Faculty of Engineering, Computing and Science, Swinburne University of Technology, Jalan Simpang Tiga, 93350, Kuching, Sarawak, Malaysia
[d] Central European Institute of Technology, Brno University of Technology, Purkynova 656/123, Brno, 61200, Czech Republic
[e] School of Computing, Engineering and Digital Technologies, Teesside University, Borough Road, Middlesbrough, TS1 3BA, United Kingdom
[f] School of Engineering, Chemical Engineering Discipline, Monash University Malaysia, Jalan Lagoon Selatan, Bandar Sunway, Selangor Darul Ehsan, 47500, Malaysia
[g] Department of Chemical Engineering, Faculty of Engineering and Science, Curtin University Malaysia, CDT 250, 98009, Miri, Sarawak, Malaysia
[h] Department of Chemical Engineering and Energy Sustainability, Faculty of Engineering, Universiti Malaysia Sarawak (UNIMAS), 94300, Kota Samarahan, Sarawak, Malaysia
[i] Institute of Sustainable and Renewable Energy (ISuRE), Universiti Malaysia Sarawak (UNIMAS), 94300, Kota Samarahan, Sarawak, Malaysia
[j] School of Engineering, Department of Chemical Engineering, University of Hull, Cottingham Road, Hull, HU6 7RX, United Kingdom
[k] Department of Chemical Engineering, University of Patras, Caratheodory 1, Patras, GR 265 04, Greece

ARTICLE INFO

Keywords:
Single atom catalyst
Single atom alloy
Value-added chemicals
Non-noble metals
Sustainable energy production

ABSTRACT

The emergence of single atom sites as a frontier research area in catalysis has sparked extensive academic and industrial interest, especially for energy, environmental and chemicals production processes. Single atom catalysts (SACs) have shown remarkable performance in a variety of catalytic reactions, demonstrating high selectivity to the products of interest, long lifespan, high stability and more importantly high atomic metal utilization efficiency. In this review, we unveil in depth insights on development and achievements of SACs, including (a) Chronological progress on SACs development, (b) Recent advances in SACs synthesis, (c) Spatial and temporal SACs characterization techniques, (d) Application of SACs in different energy and chemical production, (e) Environmental and economic aspects of SACs, and (f) Current challenges, promising ideas and future prospects for SACs. On a whole, this review serves to enlighten scientists and engineers in developing fundamental catalytic understanding that can be applied into the future, both for academia or valorizing chemical processes.

1. Introduction

The first appearance of the term "catalysis" can be backdated to the early 19th Century. Jöns Jacob Berzelius, who was one of the founders of modern chemistry, had successfully discovered the existence of catalytic energy [1], whereas the first-ever documented catalyst application can be traced even earlier to the alchemical era (4th century BC) [2]. Initially, industrial catalysts were mainly used in the Deacon process (the transformation of HCl gas in oxygen to H_2O and Cl), sulphuric acid production, Ostwald process (production of nitric acid from ammonia), and the Haber-Bosch process (production of ammonia *via* nitrogen fixation). To-date, its usage has been extended further into the majority of current industrial chemical productions [3]. Evidence has shown that the development of catalysts was one of the key factors that influence the sustainability and performance of catalytic processes, in terms of

* Corresponding author.
** Corresponding author.
E-mail addresses: adrian.loy@monash.edu (A.C.M. Loy), sinyong.teng@ru.nl (S.Y. Teng), bshow@swinburne.edu.my (B.S. How), ZhangXixia621@126.com (X. Zhang), K.Cheah@tees.ac.uk (K.W. Cheah), valeria.butera@ceitec.vutbr.cz (V. Butera), leong.weidong@monash.edu (W.D. Leong), bridgidchin@curtin.edu.my (B.L.F. Chin), clyiin@unimas.my (C.L. Yiin), Martin.Taylor@hull.ac.uk (M.J. Taylor), kyriakg@upatras.gr (G. Kyriakou).
[1] These authors contributed equally to the work.

https://doi.org/10.1016/j.pecs.2023.101074
Received 28 July 2022; Received in revised form 5 January 2023; Accepted 8 January 2023
Available online 15 February 2023

Abbreviations

AC	Activated Carbon
AC-STEM	Aberration Corrected Scanning Transmission Electron Microscopy
acac	Acetylacetonate
ALD	Atomic Layer Deposition
BTB	Borane Tert–Butylamine Complex (BTB)
BP	Black Pearls® 2000
C–C	Carbon–carbon bond
CMK	Ordered Mesoporous Carbon
CO_2RR	CO_2 Reduction Reactions
CP	Carbon Nanoparticles
CP-MAS NMR	Cross Polarized-Magic-Angle Spinning-Nuclear Magnetic Resonance
CTF	Covalent Triazine Frameworks
CVD	Chemical Vapor Deposition
DFT	Density Functional Theory
DRM	Dry Reforming of Methane
DG	Defective Graphene
DHC	Dinuclear Heterogeneous Catalyst
DRIFTS	Diffuse Reflectance Infrared Fourier Transform Spectroscopy
E_a	Activation Energy
ECN	Exfoliated Graphitic Carbon Nitride
EDX	Energy Dispersive X-ray Spectroscopy
EELS	Electron Energy Loss Spectroscopy
EG	Ethylene Glycolate
EPO	European Patent Office
ER	Eley-Rideal
ESR	Electromagnetic Spin Resonance
EXAFS	Extended X-ray Absorption Fine Structure
FePc	Iron Phthalocyanine
GC–MS	Gas Chromatography-Mass Spectrometry
GN	Graphene Nanosheet
HAADF	High Angle Annular Dark Field
HAP	Hydroxyapatite
HER	Hydrogen Evolution Reactions
HNCS	Hollow N-doped Carbon Sphere
HRTEM	High-Resolution Transmission Electron Microscopy
IR	Infrared
ISAS	Isolated Single Atomic Sites
IWI	Incipient Wetness Impregnation
MAS-NMR	Solid-State Magic-Angle Spinning-Nuclear Magnetic Resonance
MoC	Molybdenum Carbide
MOF	Metal–Organic Framework
MWNT	Multi-Walled Nanotubes
NAP-XPS	Near Ambient Pressure X-ray Photoelectron Spectroscopy
N–C	Nitrogen-doped Carbon
NM	Noble Metal
NMR	Nuclear Magnetic Resonance
NP	Nanoparticle
NT-NF	Nanotube Arrays Supported by a Ni Foam
OER	Oxygen Evolution Reactions
ORR	Oxygen Reduction Reactions
ORS	Operando Raman Spectroscopy
p-CN	Porous Nitrogen-doped Carbon
PMA	Phosphomolybdic Acid
PPy	Polypyrrole
PROX	Preferential Oxidation Reaction
PtTBPP	Tetra(4-tert-butyl-phenyl)porphyrinato Platinum
PVP	Polyvinylpyrrolidone
SA	Single atom
SAA	Single Atom Alloy
SAC	SACs Single Atom Catalyst Single Atom Catalysts
SMSI	Strong Metal–Support Interaction
STEM	Scanning Transmission Microscopy
STM	Scanning Tunneling Microscopy
TER	Termolecular Eley-Ridel
TOF	Turnover Frequency
TPR	Temperature Programmed Reduction
TPD	Temperature Programmed Desorption
UHV	Ultra-High Vacuum
UPD	Underpotential Deposition
UV	Ultra Violet
UVO	Ultra Violet Ozone
WGS	Water Gas Shift
WHSV	Weight Hourly Space Velocity
WIPO	World Intellectual Property Organization
XANES	X-ray Absorption Near Edge Structure
XAS	X-ray Absorption Spectroscopy
XPS	X-ray Photoelectron Spectroscopy
1,3 PD	1,3-Propanediols
2D	2-Dimensional

economic viability, technology feasibility, and environmental impacts [4,5]. Ever since the commercial usage of catalysts has been widespread around the globe. The subsequent innovation and revolution of catalyst development have ceaselessly progressed (Fig. 1). This review focuses on the emerging catalyst technologies from the last decade to state-of-the-art, atom efficiency and sustainable single atom catalysts (SACs) as well as highlighting the frontiers for future research into clean energy and growth.

The term SAC refers to a catalyst where individual metal atoms are isolated and dispersed across/throughout a supporting material [13]. To retain such high atomic dispersion efficiency, strong interactions between the isolated metal atoms and the coordination sites are exerted, creating a unique tunable electronic structure. The single atom-level dispersion of metal atoms on a support is not only able to maximize the atomic efficiency by offering a greater number of active sites but at the same time generate uniform and well-engineered active sites [14]. These sites can be altered to finely tune the reactivity and selectivity of chemical reactions by manipulating coordination sites (e.g., ligand tuning) and defect designs [15]. In addition, undesirable deleterious side reactions can be mitigated if requiring more than one atomic active site, due to the high dispersion and isolation [16]. These compounded features lead to a remarkable catalytic performance which has been found to outperform conventional mono/bimetallic catalysts with bulk nanoparticles. Therefore, SACs (plural of a single atom catalyst) are currently noted as "rising stars" for the future of sustainably producing fine chemicals [17] and are often envisioned as the natural bridge between heterogeneous and homogeneous catalysis [18]. Fig. 2 presents some of the major research contributions related to the use of single atoms as catalysts in chronological order.

Although single atom sites have a long history in heterogeneous catalysis spanning over five decades, the term SAC was first introduced in 2011 by Qiao et al. [19]. This work serves as an attempt to examine whether a single atom (denoted as M_1 where M is the active metal used) can provide better catalytic activity, selectivity, and stability as compared to other nanometer-sized and sub-nanometer-sized particles (i.e. clusters or atom ensembles). In general, the synthesized Pt_1/FeO_x SAC catalysts show greater reactivity for both CO oxidation and the Preferential Oxidation Reaction (PROX) reaction (by 2–3 times) than

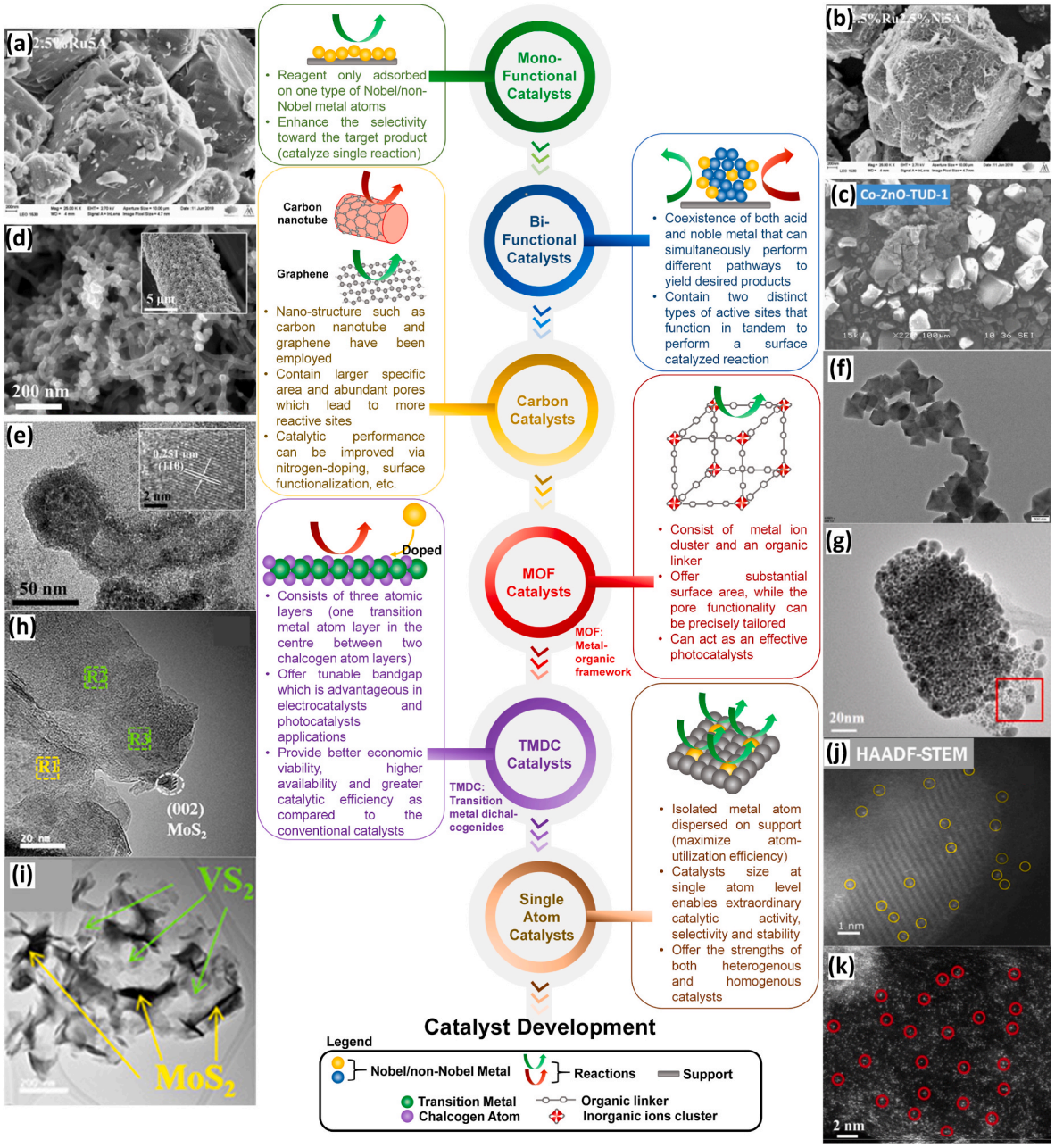

Fig. 1. The progression of catalyst development from bulk nanoparticles to advanced support materials and single atom catalysts. Micrograph of (a) mono-functional 2.5%Ru5A catalysts [6] (adapted with permission from Elsevier b.v.), (b) bi-functional 2.5%Ru2.5%Ni5A catalysts [6] (adapted with permission from Elsevier b.v.), (c) bi-functional Co–ZnO-TUD-1 catalysts [7](adapted with permission from Springer Nature), (d) Ti–FeO–CNT catalyst via SEM [8](adapted with permission from Elsevier b.v.), (e) FeO–CNT via TEM [8](adapted with permission from Elsevier b.v.), (f) UiO-66-NH_2 MOF catalysts [9] (adapted with permission from Elsevier b.v.), (g) Ag@MOF-5 catalysts [10] (adapted with permission from Elsevier b.v.), (h) VS_2/MoS_2 catalysts, where R1 represents the (002) and (100) crystal planes of MoS_2, while R2 and R3 represent the (101) and (100) crystal planes of VS_2 [11] (adapted with permission from American Chemical Society), (i) VS_2/MoS_2 catalysts showing position of VS_2 and MoS_2 [11] (adapted with permission from American Chemical Society), (j) Pt_1/TiO_2 catalysts [11] (adapted with permission from Elsevier b.v.), (k) Zn_1–N–C catalyst [12] (adapted with permission from Royal Society of Chemistry).

that of bulk nanoparticle-based Au/Fe_2O_3 catalysts, capable of providing high reactivity for CO oxidation [20,21]. In addition, the Pt_1/FeO_x SAC was found to be fully regenerated even after 2 cycles of thermal treatments. These findings were no doubt a bombshell to the research community, given that the commercial Pt/Al_2O_3 catalysts are often less favorable than Au/Fe_2O_3 catalysts for both CO oxidation and PROX reaction due to their higher cost. This research proved that a high atomic efficiency level catalyst is one of the feasible directions for the future of sustainable catalysis research, especially chemical reactions that require high noble metal loadings. A year later, a study conducted by Kyriakou et al. [22] found that lower activation energy (E_a) for hydrogen dissociation can be achieved by using isolated Pd atoms across a Cu(111) surface under ultra-high vacuum conditions for hydrogenation reactions. The authors used the term Single Atom Alloy (SAA) to describe this class of material. In the same year, Knurr and Weber [23] explored the theoretical design of SACs for the solvent-driven CO_2 reduction process *via* a first-principle calculation. Lin et al. [24], on the other hand, extended the utility of SACs to the water gas shift (WGS) reaction in 2013. Both Pt_1/FeOx and Ir_1/FeO_x catalysts showed extraordinary catalytic performance for WGS, presenting a specific rate

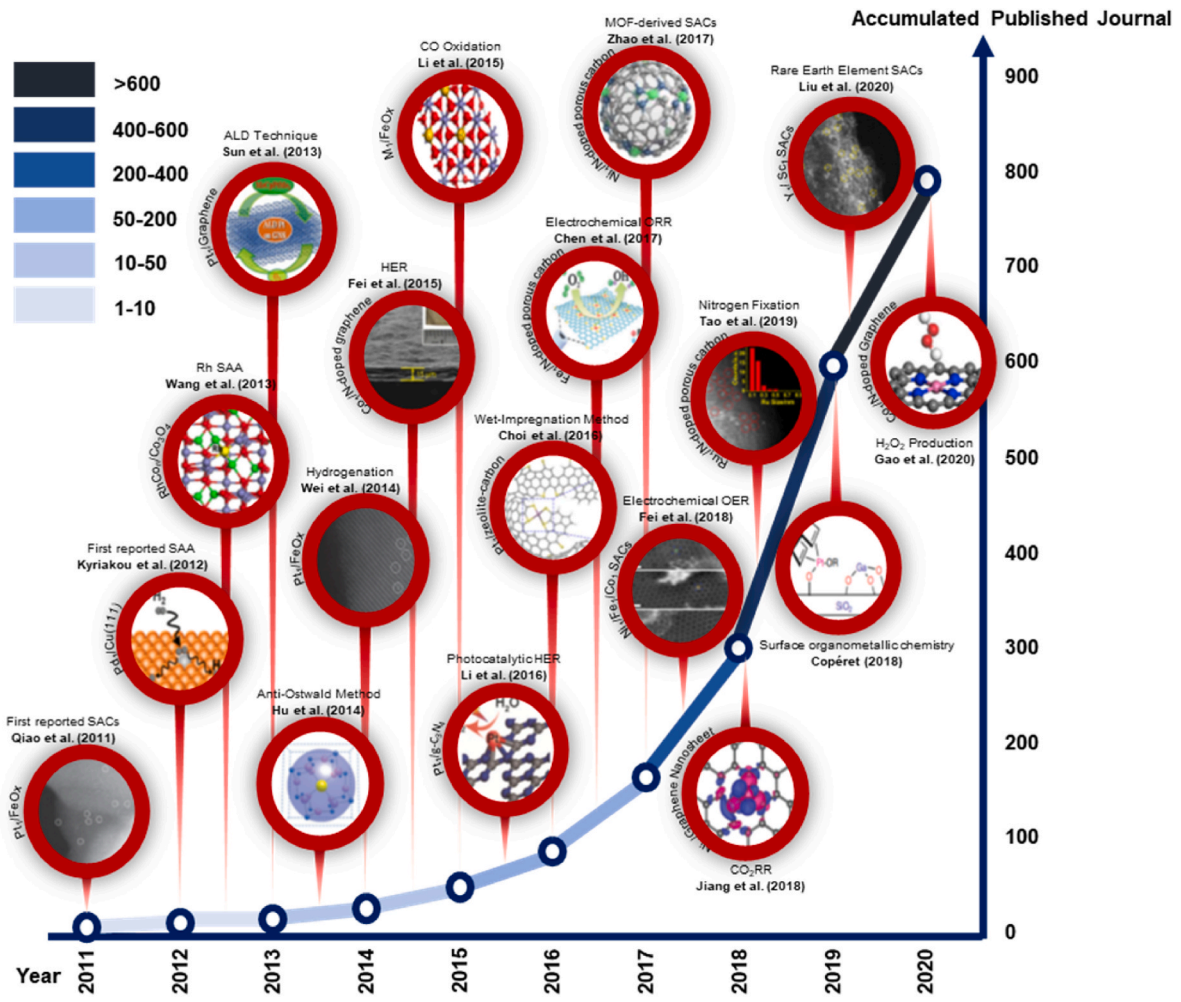

Fig. 2. Chronological view on the use of single atoms as catalysts-related publications (note: Data obtained from Scopus database *via* keywords of "single-atom catalyst" and "single atom catalysts").

of around 2–3 times higher than previous Pt/MoC and Au/CeO_x catalysts. Another interesting finding was reported in the work conducted by Wang et al. [25], which investigated the selective catalytic reduction of NO in the presence of H_2 with an Rh_1/Co_3O_4 catalyst. The surface of Rh_1/Co_3O_4 had reconstructed into $RhCo_n/Co_3O_4$, an SAA at 220 °C. More interestingly, this re-constructed catalyst offered superior catalytic performance, when compared with its original form. In addition to the Rh–Co alloy, the catalytic activity enhancement on CO oxidation attributed to the single transition metal-atom substitution in V_4O_{10} has also been studied based on Density Functional Theory (DFT) calculations [26]. Aside from this, an advanced fabrication technique "atomic layer deposition (ALD)" has been discovered to design and synthesize a SAC with atomic-level control on its composition and thickness [27].

Thereafter, numerous works have discovered the potential of noble metal-based SACs for various reactions, which include, but are not limited to glucose oxidation using Au_1/Pd nano clusters [28], the reduction of I_3^- to I^- using Pt_1/FeO_x [29], HCHO oxidation with Ag_1/hollandite manganese oxide [30], syngas-to-C_2 oxygenates conversion with Rh-based SACs [31], N-alkylation and α-alkylation using Ir_1-doped polypyrrole [32] and Zn_1/N-co-doped porous carbon [33], CH_4 oxidation using Pt_1/La_2O_3 (NM indicates noble metal) [34]. A major use of SACs and SAAs has been found for hydrogenation reactions, specifically, nitroarenes using Pt_1/FeO_x [35], 1,3-butadiene using both Pd_1/graphene [36] and Pt_1/m-Al_2O_3 [37]. Other reactions have been NO reduction with Pt_1/FeO_x [38], hydroformylation of olefins using Rh_1/ZnO [39], oxygen evolution reaction (OER) using Rh_1, Ru_1, Ir_1 and Pd_1 supported on Co_3O_4 [40], and extensively for CO oxidation using various atomic catalysts such as Au_1, Rh_1, Pd_1, Cu_1, Ru_1, Ti_1/FeO_x [41]. In addition, the study on the use of a SAA has also been extended for other reactions such as the Ullmann reaction of aryl halides using Au–Pd SAA [42], the dehydrogenation of propane using Cu–Pd SAA [43], the hydrogenation of C_2H_2 using Ag–Pd SAA [44], the oxidation of formic acid using Ag–Pt SAA [45], the selective hydrogenation of furfural using Pd atoms alloyed into a Cu nanoparticle supported on alumina [46] and the dehydrogenation of 4-hydroxypentanoic acid [47]. In addition to the reactions shown above, the use of single atoms has been effective for electrochemical applications, work can be found starting from 2015 and has been extensively explored from 2016 onwards. These applications encompass Oxygen Reduction Reactions (ORR) using Pt_1/TiN [48], Pt_1/zeolite-templated carbon [49] and have recently extended to a SAA which contains Pt_1 and Co nanoparticles that co-encapsulated on N-doped graphitized carbon nanotubes [50]. Hydrogen Evolution Reactions (HER) have been studied using Pt_1 over 2D g-C_3N_4 [51], CoP-based nanotubes [52], curved carbon supports [53], and TiO_2 nanosheets modified with graphene [54]. Additionally, the electrochemical NO reduction was explored using Pt-CTF/CP [55], N_2 reduction using Mo_1/N-doped carbon [56] and Ru_1/N-doped porous carbon [57]. The electrochemical CO_2 reduction reaction (CO_2RR) was investigated using various atom systems utilizing metals such as Pt_1, Pd_1, Cu_1 and Ag_1/graphene [58].

Despite the astounding performance of noble metal-based SACs, the high unit price and the low abundance of noble metals are undoubtedly

the key compromising factors that hamper the wide employment of SACs [59,60]. With the motivation for enhancing the sustainability of SACs deployment, a notable number of research works have been conducted to examine the potential of noble metal-free SACs. In 2013, Wang et al. [26] performed a systematic DFT calculation to examine the potential of four single-atom transition metals for CO oxidation, where three of them were non-noble metals (i.e. Sc_1, Ti_1, and Co_1). To the best of the authors' knowledge, this is the earliest reported application of non-noble metal-based SACs. The attention on non-noble metal-based SACs has grown rapidly since 2018. Their applications have been extended to non-oxidative CH_4 conversion using Fe_1/SiO_2 [61]; HER with Co_1 on N-doped graphene [59], graphitic carbon nitride [62], N-doped graphyne [63], and Ni_1 on α-SiX (X = N, P, As, Sb, Bi) [64]; ethylene benzene oxidation using Co_1/CN [65]; electrocatalytic ethanol oxidation using a hybrid material of Pd nanoparticles and Ni_1 single atom [66]; oxidative desulphurization with Cr_1/multiwalled carbon nanotubes [67]; CO oxidation using Ni_1 over FeO_x [68], phosphorene nanosheet [69], Sc_1 and Fe_1 on honeycomb borophene/Al(111) heterostructure [70], and Ti_1 on MXene [71]; acetylene hydration using Zn_1 with S/N co-doped defective graphene supports [72]; the electrochemical CO_2RR with Ni_1 on N-doped porous carbon [73], graphene nanosheets [74], carbon black [75] and other ZnN_4-based SACs [76]; CO_2 hydrogenation with various non-noble metal-based SAC (Mn_1, Fe_1, Co_1, Mo_1) supported on graphitic carbon nitride [77]; ORR has been carried out with Co_1 on defective N-doped carbon graphene [78], Fe_1 supported on N-doped porous carbon [79], hierarchically structured porous carbon [80], cellulose-derived nanocarbon [81] and phosphomolybdic acid cluster [82]; and the Oxygen Evolution Reaction (OER) has been carried out on Fe, Co and Ni-based SACs on N-doped graphene [83], N-doped biomass-derived porous carbon [84] as well as γ-graphyne monolayer [85]. Lastly, the production of H_2O_2 was found to be effective *via* hydrogenation routes Ni-based SACs [86]. In fact, based on the comparative studies conducted in some of these works, the non-noble metal-based SACs were found to be more attractive and preferable. For instance, Liang et al. [68] found that the molecular interaction between a Ni atom and an adsorbed CO gas molecule is weaker than CO binding irreversibly with Pt_1 and Ir_1 atoms. This further leads to a lower barrier in CO_2 formation (i.e., enhances the CO oxidation process) under the use of Ni. A recent computational study also suggested that the Fe-, Co- and Ni-based SACs were capable of providing a comparable catalytic activity for CO oxidation as compared with the noble metal-based SACs (e.g., Pd-, Pt-, Ru- and Rh-based SACs) [87]. However, on the flip side, some studies focused on exploring strategies to combat the economic drawbacks of noble metal-based catalysts (e.g., Wang et al. [88] found that the use of monolayer WO_3 has great potential to reduce the Pt noble metal usage on the catalyst fabrication).

In addition to the aforementioned non-noble metals, in the 2020s, the use of rare earth elements (e.g. La, Y, Ce, and Sc) as SACs were proposed. It is anticipated that the multi-shell electrons of the rare earth metals will lead to strong adhesive bonding between the rare earth element and a support material [89]. Strong metal-support interactions are favorable as they have been found to reduce the chance of atoms aggregation, a common problem during the synthesis of SACs. In other words, it can promote scalable mass production of SACs. To-date, yttrium, scandium, and praseodymium-based SACs (Y_1, Pr_1 and Sc_1) have been tested for N_2 and CO_2 reduction reactions [89,90]; while erbium SACs (Er_1) have been tested for the effective photocatalytic CO_2 reduction [91]. On the other hand, the impact of integrating a second metal species into a SAC has also started to get more attention from researchers. It is believed that such bimetallic catalysts can offer better catalytic performance than that of monometallic catalysts given the synergetic effect between the two metal species [90,92]. Evidently, the bimetallic Ir_1Mo_1/TiO_2 SAC synthesized in a recent work [92], is capable of offering a greater selectivity (>96%) for a hydrogenation process, as opposed to the low selectivity of their monometallic forms (i.e., less than 40% for Ir_1/TiO_2 catalysts and negligible activity for Mo_1/TiO_2 catalysts). A similar strength of bimetallic SAC has also been discovered by Kaiser and co-workers [93]. The addition of Pt single atoms into the Au SAC can inhibit the sintering effect up to 800 K, which eventually leads to a 2-fold increment in catalysts' shelf life. The potential of such bimetallic SAC has been investigated for hydrogenation (e.g. Ir_1Mo_1/TiO_2 catalysts [92]; Pt_1Sn_1/N-doped carbon [94]), HER (e.g. Ru_1Pt_1/N-doped carbon catalysts [95]; Ni_1Co_1/N-doped carbon catalysts [96]), Fenton reaction (e.g. hyaluronic acid-coated Fe_1Co_1/N--doped carbon catalysts [97]), acetylene hydrochlorination (e.g. Pt–Au-based bimetallic SAC [93]) and dichlorination (e.g. Fe_1Cu_1/N--doped porous carbon catalysts [98]). Meanwhile, some studies have focused on the versatile and scalable techniques for the mass production of SACs, e.g. dry ball milling [99,100], pyrolysis [60], one-pot pyrolysis [101], incipient wetness impregnation [49], anti-Ostwald method [30], photochemical strategy [102], thermal emitting strategy [103], cascade anchoring strategy [104], surface organometallic chemistry [105], and electrochemical deposition [106]. Some of those even focus on exploring ways to realize ultrahigh metal loading for SAC (e.g. 10–20 wt% Ru catalysts [107], >20 wt% Cu_1-based SACs [108,109], >20 wt% Co_1-based SACs [110]), where most synthesis methods are through thermal processing (e.g., pyrolysis [65,111] and annealing [108]).

Fig. 3(a) and (b) present the accumulative journal publications between 2011 and 2020, which directly relate to SAC research. Interestingly, China and the United States, the top publication hubs for SAC research, collectively account for 67.1% of the total scholarly outputs. It is then followed by Australia, Singapore, South Korea, Japan, Canada, the United Kingdom, Germany, and Spain, with a relatively gentle annual growth in publication numbers. In terms of patent applications, China has the largest patent filing numbers (>90% of the total patent filed) thus far, based on the European Patent Office (EPO), and World Intellectual Property Organization (WIPO) databases, as shown in Fig. 3 (c) and (d). All the afore-presented trends have evidently shown the growing interest and potential in SAC research and development. This review paper, therefore, attempts to provide useful insights related to the development of SACs, to pave the way for potential future SAC research, especially for applications in the field of clean energy. The review is organized as follows: Section 2 outlines the synthesis and fabrication methods, specially designed for SACs. Whereas the characterization methods used in SAC research are discussed in Section 3. This is followed by current SAC state-of-the-art applications as well as the respective up-scaling challenges highlighted in Sections 4 and 5, respectively. It is then rounded up by a concluding remark in Section 6.

2. Synthetic routes towards single atom catalysts

A single atom catalyst comprises highly dispersed single atoms of a metallic species onto a support material. However, innovative synthesis methods are needed given the thermodynamically instable nature of single atoms, so that the agglomeration phenomena during the synthesis and reaction processes (as surface free energy is lower in metal cluster form as compared to single atoms form [117]) can be avoided, if not, be reduced [118]. The description of these methods is presented in the following sub-sections, where some of the respective key remarks are summarized in Table 1.

2.1. Conventional synthesis methods

2.1.1. The co-precipitation method

Co-precipitation is a classical method used for the synthesis of nanoparticle (NP) based catalysts by precipitating the metal in the form of hydroxide from a salt precursor with the aid of a base[119] (see Fig. 4 (a)). In 2011, Qiao et al. successfully produced the Pt SAC by dispersing the Pt atoms onto defects in FeO_x [19]. This was carried out *via* the co-precipitation of aqueous ferric nitrate (1 mol/L) and hexachloroplatinic acid (0.076 mol/L) with sodium carbonate (1 mol/L). The co-precipitation was conducted at 50 °C and at pH 8. To mitigate the

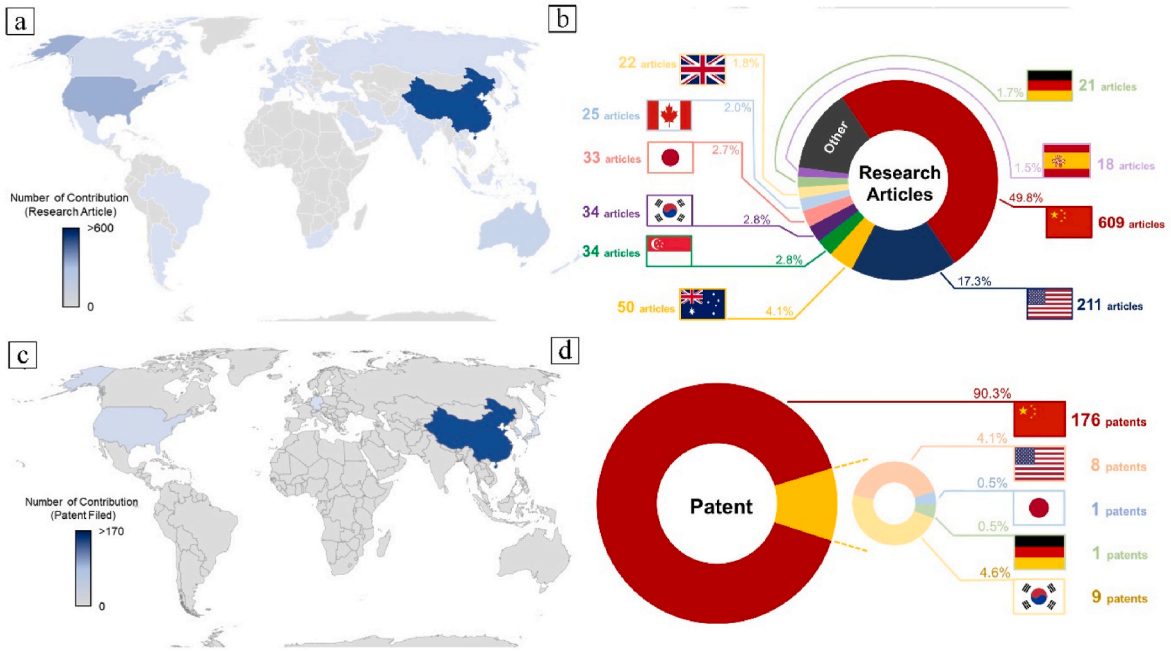

Fig. 3. (a) A map showing the total number of journal articles published for each country between 2011 and May 2020 [112], (b) the respective publications share (Data: Scopus database [113] *via* keywords of "single-atom catalyst" and "single atom catalysts"), (c) A map showing the total number of filed patents for each country between 2011 to May 2020 [112], and (d) the respective patent share (Data: Google Patent [114], WIPO [115], EPO [116] *via* keywords of "single-atom catalyst" and "single atom catalysts").

tendency of forming metal clusters, the Pt loadings were kept low (around 0.17 wt%). This, in fact, is the major limitation of this method, some practical applications physically need higher metal loadings [118]. The obtained slurry was dried and calcined at 333 °C and 473 °C respectively for 5 h each. Finally, the catalysts were reduced using H_2/He at 473 °C for 0.5 h. The resultant SACs were proven to demonstrate remarkable stability and reactivity for CO oxidation. In addition to CO oxidation, the co-precipitation strategy has been applied to synthesize effective SACs for the WGS reaction [24], NO reduction [38], electrooxidation catalysis [148], CO_2 activation [149] and carbon–carbon (C–C) coupling reactions [150]. However, due to the requirement of using low metal loadings (<1%) the capabilities of supported SACs are limited as metal oxide supports are not suitable for electrochemical testing [151]. There are other common pitfalls associated with the co-precipitation method, such as it being (a) time consuming, (b) not suitable for reactants that have a significant difference in precipitation rates, (c) trace impurities may be precipitated together with the desired product [152], and (d) some metal atoms are anchored in the carrier interface which makes it unable to serve as an active site for the catalytic reaction [118,122].

2.1.2. *Impregnation method*

Impregnation is a widely used and standard method of producing supported nanoparticles due to its simple execution, low waste generation, and cost effectiveness [155]. In general, this method starts with the dispersion of an aqueous solution, containing metal precursors, onto a support material. The mixture is then dried and calcined to anchor the metal atoms onto the support, be that in defect sites, onto the surface, or into the porous network of a mesoporous material, this process is depicted in Fig. 4(d). There are two iterations of the impregnation method, including wet impregnation (excess amount of solution is used; recycling is needed to mitigate waste [121]) and dry impregnation (also name as incipient wetness impregnation (IWI); which requires a lower solution volume but it is difficult to ensure uniform dispersion of metal atoms on the support [122]). For instance, Choi et al. [49], the pioneered work which synthesized Pt_1/zeolite-templated carbon *via* a wetness impregnation protocol. In their work, the mixture of carbon and $H_2PtCl_6{\cdot}5.5H_2O$ was dried at 353 °C under reduced pressure (0.3 bar); the products were further dried and reduced using H_2 flow at 523 °C for 3 h. As a result, SACs with a relatively high Pt loading (5 wt%) were synthesized. In another attempt from Yang and co-workers [48], Pt atoms have been found to atomically disperse on TiN under a low metal loading of 0.35 wt% using the dry impregnation approach. Note that higher metal loadings could lead to the formation of NPs or clusters due to atom agglomeration. It is postulated that this could be due to a weak precursor–support interaction [49]. To-date, SACs derived from impregnation methods have been applied to oxygen reduction [48,49], formic acid and methanol oxidation [48], formaldehyde oxidation [156], and CO oxidation [157].

2.1.3. *Strong Electrostatic Adsorption*

Strong electrostatic adsorption (SEA) is a special type of wet impregnation in which the pH of the solution is adjusted to maximize the electrostatic interaction between metal precursors and the oxide surface [123] (Fig. 4(b)). It is anticipated that the oxide surface will be protonated (i.e., positively charged) under a pH condition lower than the point of zero charge (PZC; pH condition that led to zero interactions between metal precursor and support); while it is deprotonated (i.e., negatively charged) under a pH condition higher than the point of zero charge [121,158]. Taking advantage of this feature, monolayers of O^-, OH, and OH^{2+} can be formed by controlling the pH values of the solution, which further results in the capability of anchoring varied metal precursors onto the support [159]. Note that the ligand that connects the metal precursor with the surface will be removed during calcination [160]. Using the study performed by DeRita and co-workers [153] for example, SEA is used to enhance the adsorption of Pt atoms onto the TiO_2 surface. By controlling the pH at 12.2 (greater than PZC), the surface will be deprotonated and thus, attract the metal ion complexes of the precursor (i.e., $[(NH_3)_4Pt]^{2+}$). The ligand can then be removed through calcination to form a SAC [159]. In 2019, a US research group has attempted to synthesize a $Pt_1/SiO_2@Al_2O_3$ *via* SEA with the use of H_2PtCl_6 as the Pt-precursor [158]. Interestingly, given that the metal ion complexes ($PtCl_6^-$) are carrying negative charges, the Pt atom are adsorbed at a pH lower than PZC instead. Some other successful SEA

Table 1
A summary of reported SACs, synthesis, structure, and applications.

Synthesis Approach	Experimental Purpose	Other Remarks
Co-precipitation method	• Can be applied to prepare metal-based catalysts with uniform dispersions of multiple active elements simultaneously • Metal is precipitated from a salt precursor with the existence of base solutions [119]	• The two key drawbacks that restrict its scalability are the requirement of low metal loading (to avoid agglomeration) and the lower metal usage efficiency as some metals are anchored in the interface of the bulk carrier (reaction spectators)
Impregnation method	• Metal from the precursor is anchored on the substrate through either adsorption (for wet impregnation) or capillary action (for dry impregnation) depending on the precursor amount used [120]	• Recycling of the excess precursor solution in wet impregnation is needed to minimize waste [121] • Dry impregnation does not create excessive waste that needs to be recycled, however, uniform dispersion of metal atoms is not guaranteed [122] • Additional post-treatment is needed to remove the counter-ions (from the metal precursor salts) which are retained on the support [121]
Strong electrostatic adsorption	• The pH of the solution is tuned to maximize the electrostatic interaction between metal precursors and the oxide surface [123] • The metal precursor will be adsorbed onto the surface under the desired pH environment [124]	• Best suited for low metal loadings [125] • Adsorption behavior is heavily dependent on the unique topology of the support (defects, functional groups, etc.) [124]
Ball-milling	• Initiate physical and chemical transformation between catalysts precursors *via* mechanical energy (known as "mechanochemistry" [126]) • Does not involve any uses of additives and solvent [100]	• Traditional high-energy ball milling approach requires the use of specific metal precursors (which are expensive and not commercially available) and specific operational conditions [127] • Scalability can be improved by coupling the ball milling approach with subsequent thermal treatments (e.g. calcination [127]) • Not suitable to synthesize co-catalysts which involves liquid-phase synthetic steps [128] Not suitable for metals that are prone to agglomeration such as Fe and Cu.
Atomic layer deposition	• A vapour phase deposition approach where metal atoms are atomically deposited in a layer-by-layer manner by exposing the substrate to the reactive precursor vapours [14,27] • The self-limiting gas surface reaction enabled precise control on the catalyst design and development [118,129] • Metal aggregation can be mitigated by lowering the ALD growth temperature [130]	• Restricted by expensive operational and capital costs [127] • Weak interaction between the synthesized catalysts and substrates jeopardized the stability of the SACs [131]
Surface organometallic chemistry and coordination site strategy	• Coordination site strategy assigns support sites with chemical linkers [132]. • Commonly uses N-binding to implant single atoms into a larger matrix	• Yields a great catalytic activity, selectivity and stability. • High thermal stability, however requires chemical linkers.
Defect design strategy	• A by-design introduction of defects onto the surface of the substrate. The engineering of defects might improve performances [133].	• Possibly provides a large number of individual active sites and improves the selectivity of the desired process
High temperature-induced strategy	• Precursor-support interaction can be enhanced via temperature [134]. • Includes pyrolysis-assisted, thermal emitting, cascade anchoring, and ultra-high temperature strategies.	• Temperature-induced strategy allows for a shorter synthesis time. • Higher temperature requirements will lead to elevated operational costs for large-scale synthesis.
Freeze-drying assisted strategy	• Mixture of metal and support precursor is freeze-dried instead of oven-dried • Obtained catalysts would contain higher microporosity which allowed greater catalytic reactivity and stability [135]	• Higher operational cost [136,137] (attributed to energy consumption) and maintenance cost [138] are the main concern
Photochemical method	• Uses a powerful light source to deposit single atoms on a support via ion reduction [139].	• Requires capital and operating costs for the light source during synthesis.
Electrochemical method	• Metal ions can be deposited onto cathodes in an electrolyte solution [140].	• Scalable and relatively cost-effective. • Deposition parameters and control must be well-considered [141].
Chemical Etching	• A strategy to re-disperse nanoparticles on support as single atoms via chemical interactions [142].	• Low quality nanoparticle aggregates can be upgraded to SACs in a versatile approach. • Etching chemicals may be hazardous [143].
Deposition–precipitation	• Metal species are reacted with support molecules, forming a uniform suspension [144]. • Oxygen defects help reduce the metal species to single atom entities.	• Time of synthesis may be ~6 h [145]. • Precise control of concentration, pH and temperature is often required.
Mass-selected soft-landing	• Metal atoms are vaporized by laser and selectively deposited on the support with the aid of metal filter [118,146]	• Operated under ultrahigh vacuum conditions which lead to higher cost [147] • Low yield fabrication limits its industrial application [13,118]

applications for SAC synthesis include Pt_1/CeO_2 [160,161] and Rh_1/phosphotungstic acid [162] catalysts for CO oxidation; Pd_1 (and Pt_1)/hydroxyapatite [163]; and Ni_1/hydroxyapatite for dry methane reforming [164]. Nevertheless, the metal loadings of the SAC synthesized from SEA method are usually kept low (<5wt%) [125]. Besides, the adsorption behavior is highly sensitive to the types of functional groups and the presence of defects on the support surface [124]. This is problematic since this method is heavily dependent on the electrostatic interaction to achieve atomic dispersion on the support surface.

2.1.4. Ball-milling

The ball-milling method, or the so-called mechanochemistry strategy, has gained interest in the synthesis of heterogeneous catalysts due to its (a) efficiency to homogeneously mix multiple precursors together [165]; and (b) is simple to scale-up [126]. In the early discovery of SACs, the ball-milling method, Fig. 4(c) was been proposed by Deng et al. [99] to synthesize FeN_4/graphene nanosheets. During the ball-milling process, kinetic energy is used to break the chemical bonds of the substrates as well as the macrocyclic structure of the added metal–ligand complex, slowly at 450 rpm for 20 h [99,166], while the shearing action of the

milling process is known to generate a large amount of heat which can thermally decompose organic molecules [167]. The resultant compounds such as FeN_4 or CoN_4 then interact with the defect sites of graphene that were formed during the ball-milling process, to form the desired SACs. Similar to other methods mentioned, the metal loadings must be kept low (~2.7 wt%) to avoid agglomeration of the high-surface-energy metal atoms [168]. Nevertheless, such an approach possesses limited scalability that is required, this is due to (a) unique precursors which are usually expensive and not commercially available (e.g., metallophthalocyanine); and (b) specific operational conditions (e.g., under argon atmosphere) [127]. Therefore, the ball milling-assisted approach which is coupled with calcination (or other thermal treatments) approach has recently attracted more attention from research groups [100,169]. Recently, kg-scale fabrication of noble atom-based SACs has been successfully demonstrated in the work developed by He et al. [169]. In this work, the noble metal precursor $Pd(acac)_2$ and support precursors $Zn(acac)_2$ were mixed at a weight ratio of 1:400 and subsequently distributed into four agate grinding jars. Each jar contains 50 grinding balls of 6 mm diameter and 20 with a 10 mm diameter. The mixtures were ground for 10 h at a speed of 400 rpm. To note, the use of the acac ligand generally aids the anchoring process of the metal precursors into the bulk support during the ball-milling process [169]. The resulting milled mixtures were calcined at 400 °C for 2 h. He and co-workers [169] have successfully produced Pd_1/ZnO, Ru_1/ZnO, Rh_1/ZnO, and Pd_1/CuO *via* the afore-proposed procedure. Interestingly, no significant scaling-up effect was observed as the kg-scale, Pd_1/ZnO exhibits almost the same catalytic performance (about 92% styrene yield *via* hydrogenation of phenylacetylene) as compared to the small-scale fabrication (10 g-scale) under the same conditions (10 mg of catalyst and 0.5 mmol of phenylacetylene were used, the reaction was conducted for 20 min at a temperature of 50 °C) The ball-milling method has been successfully applied to the fabrication of SACs for oxidation of benzene [99], hydrogenation of acetylene [170], phenylacetylene [169], 2-methyl-3-butyn-2-ol [171], glycerol hydrogenolysis [172], organic pollutant degradation [173], Fenton-like reaction [174], HER [175], ORR [176,177], CO oxidation [169], and photoreaction [128]. Nevertheless, (a) restricted scalability especially for co-catalyst synthesis which inevitably involves liquid-phase processes [128]; and (b) the occurrence of metallic impurities from the machinery on the catalysts are the other common weaknesses of this approach [178].

2.1.5. Atomic layer deposition

Atomic Layer Deposition (ALD) is another prominent synthetic technique for the fabrication of SACs given its capability to precisely control the atomic deposition, dispersion of metal species and coating thickness [27,129]. This strength makes it a prominent approach particularly for studying the insights on SAC synthesis [122] and the influences of various parameters involved in the synthetic processes [14,122]. Generally, a complete cycle of ALD encompasses two main steps, shown in Fig. 4(e). In the first step, metal precursors such as methylcyclopentadienyl-trimethylplatinum ($MeCpPtMe_3$) will react with oxygen atoms which were adsorbed onto the substrate's surface. The subsequent O_2 exposure was oxidized into the metal precursors and thus, form a new adsorbed O_2 layer on top of the metal surface (metal–oxygen (M−O) species). In a complete cycle, the surface of the support is exposed to a 1 s pulse of metal precursor, followed by 20 s pulse of N_2 to purge the system and then a 5 s pulse of O_2, continually. To note, the metal loading can be finely tuned by altering the number of ALD cycles, e.g., Pt loading of 2.1 wt% or 7.6 wt% on N-doped graphene nanosheets can be achieved *via* 50 and 100 ALD cycles, respectively [179]; 150 ALD cycles can increase the Pt loading on graphene to 10.5 wt% [27]. Thus far, ALD has been applied to generate Pt-graphene SACs for the methanol oxidation reaction [27], an N-doped graphene support for HER [179], and a CeO_2 support for CO oxidation [180]. This synthetic procedure has now been extended to synthesize Pd and Fe-based SACs [36,181]. In a recent work conducted by Zhang et al. [182], a Pt–Ru bimetallic catalyst fabricated using the ALD method has proven to provide 50 times higher reactivity for HER as compared to a commercial Pt catalyst (Pt mass loadings for bimetallic catalysts and commercial catalysts are 61.2 μg cm^{-2} and 1.24 μg cm^{-2}, respectively). On the other hand, the Pd_1/graphene catalysts produced *via* the ALD method are capable of achieving 100% butene selectivity, up to 95% conversion in the selective hydrogenation of 1,3-butadiene conversion, where the attained selectivity to 1-butene (the desired product which can be used as co-monomer in polyethylene production) was more than 70% [36]. This is superior as compared with conventional Pd/C catalysts which routinely achieve ~60% selectivity, at the same conversion. Other to-date applications of ALD include, but are not limited to Co_1-modified Pt nanoparticles catalysts for ORR [183], Ru_1/PtNi catalysts for methanol oxidation [184]. However, the ALD process is slow and demands greater energy consumption, as well as requiring an ultraclean surface [185]. All these compounded issues lead to a higher fabrication cost [127]. Together with the low stability of the synthesized SAC [122,131], both serve as the key factors that need to be considered under large-scale production [186].

2.1.6. Chemical etching

Chemical etching is a convenient and straightforward method to redisperse nanoparticles on substrates as single atoms. Contrary to other synthesis approaches where monoatomic particles are embedded onto the substrate as a "bottom-up" approach, the chemical etching strategy is a "top-down" approach where larger clusters are first embedded on the substrate and then redistributed as single atoms [142]. As an example, Feng et al. [187] prepared nanoparticles of Ru, Rh, Pd, Ag, Ir, and Pt on an activated carbon support, respectively. Chemical etching was performed using a mixture of CO and CH_3I at 240 °C for 6 h. The dispersion of Rh nanoparticles to single atom was studied, and the work found that $I^{\bullet}$ radicals and CO promote the breakage of Rh–Rh bonds. Chemical etching using H_2O_2 on MoS_2 catalyst [188] has also successfully synthesized single-atom vacancy catalysts to improve the HER performance, showing that S-vacancies provided an effective surface electronic structure for boosted electrical transport properties. Few-layer $Ti_{3-x}C_2T_y$ nanosheets [189] are first prepared by etching Ti_3AlC_2 in a solution of lithium fluoride and hydrochloric acid. From this process, some Ti atoms will be ripped off, and when $[PtCl_6]^{2-}$ complex ions are stirred with the nanosheets, Pt^{4+} ions will be adsorbed onto the surface, forming a SAC. Collective researchers from both Chen and Tang's laboratory [143] also demonstrated that nanoparticle graphene with doped Ni can be chemically etched by HCl solution, causing the structure of Ni nanoparticles to be inherited by the graphene. With an etching time of less than 6 h, Ni SACs have been identified *via* Selected Area Electron Diffraction (SAED) and High-Resolution Transmission Electron Microscopy (HRTEM).

2.1.7. Deposition–precipitation strategy

Using the deposition–precipitation strategy, a metal solution is mixed and reacted with support molecules to form a uniform suspension. The reaction temperature and pH are precisely controlled to deposit the metal species on the support [144], forming SACs. This technique was popular for oxide support, for example, Fu et al. [190] synthesized Au-ceria SAC *via* the dropwise addition of $HAuCl_4$ into the suspension of ceria particles in an aqueous solution of $(NH_4)_2CO_3$ at a pH of 8. The deposition–precipitation strategy was gradually extended for different SACs, such as Wang et al. [145], who studied Au/Sn–TiO_2, concluding that the creation of oxygen vacancies on the TiO_2 surface by single-site Sn had led to better selective activation. For this, Zhang et al. [145] also mentioned that when oxygen defects are generated *via* the deposition–precipitation method, the metal species precursor can be reduced to form single metal atoms. Mochizuki et al. [191] demonstrated the preparation of Au_1/NiO SACs by the deposition–precipitation strategy by mixing and calcination of $HAuCl_4$ and NiO support. Atomic-resolution HAADF-STEM was used to directly observe Au single

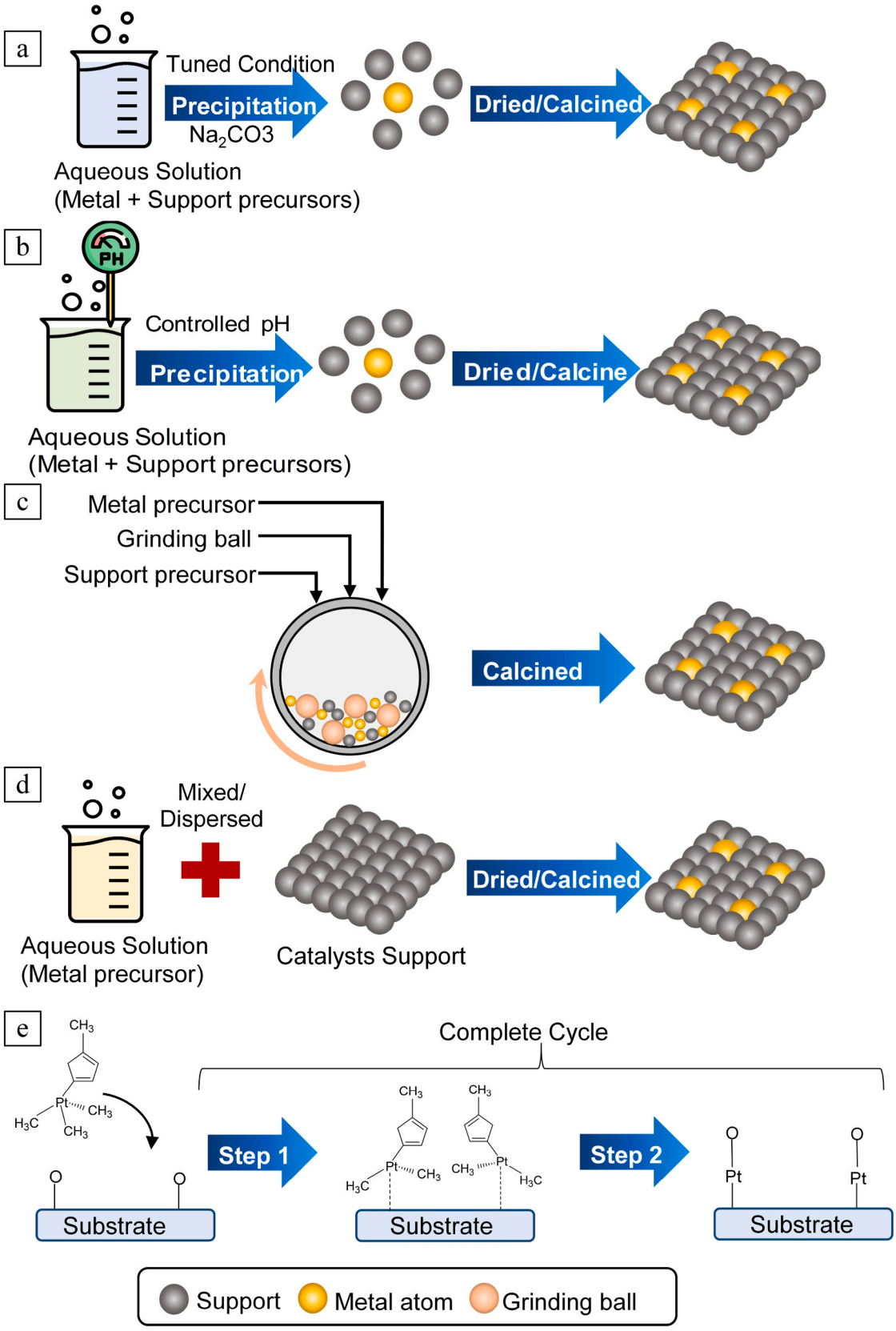

Fig. 4. Schematic illustration of conventional synthetic methods for SACs where (a) is the co-precipitation method [27] (adapted with permission from Springer Nature), (b) is the Strong electrostatic adsorption method [123] (adapted with permission from Elsevier b.v.), (c) is the ball-milling [151] (adapted with permission from Royal Society of Chemistry), (d) is impregnation method [153] (adapted with permission from American Chemical Society), and (e) is the ALD method [154] (adapted with permission from Royal Society of Chemistry).

atoms on NiO where the loading was 0.93 wt%. Yang et al. [192] reported a ~1 wt% loading of Au atoms on titania, showing applications for SACs in WGS reactions. The work uses an Au deposition–precipitation strategy with UV irradiation of the titania support in ethanol. Excess Au loadings were also removed using sodium cyanide, leaving atomically dispersed Au on titania. This shows that the deposition–precipitation strategy is a versatile method for even when an excess of metal loading was introduced, removal is possible.

2.2. Novel synthesis methods

2.2.1. Surface organometallic chemistry and coordination site strategy

The interaction between single metal atoms and the surface atoms of support materials decides the nature of the catalyst stability. The coordination site strategy assigns support sites with chemical linkers to adsorb or bind metal atoms, preventing migration and agglomeration [132]. One of the most common synthesis methods for a SAC is to use specialized N-based linkers, exploiting coordinate bonds or N-binding to implant single atoms into a larger matrix such as in a metal–organic framework. Recently, Gong et al. [193] used polypyrrole (PPy) molecules as N_2-based linkers, which can fill into the 1D channel of a (non-nitrogenous) MOF (constructed by divalent Mg^{2+}/Ni^{2+} ions and 2, 5-dioxido-1,4-benzenedicarboxylate ligand) to form a PPy@MgNi-MOF-74 composite, illustrated in Fig. 5(a). The composite is then annealed at 900 °C to anchor the N atoms from PPy onto a porous carbon composite, followed by the thermal decomposition of PPy (removing the carbon from MOF linkage). This ultimately forms a high-performance Ni_{SA}-N_2-C electrocatalyst that has been used for the reduction of CO_2 to CO [193]. For the application of an H_2 evolution photocatalyst, Li et al. [51] used a liquid-phase reaction with g-C_3N_4 and H_2PtCl_6, followed by low-temperature annealing. This procedure synthesized a Pt/g-C_3N_4 SAC. Here, FT-EXAFS was used to deduce a coordination number of 5, which suggests that Pt single atoms were bonded on the top of the five-membered rings of the C_3N_4 network. The photocatalyst was able to give a high H_2 generation rate of 162.8–318 μmol h^{-1} with a Pt loading content from 0.075 to 0.16 wt%. In general, most works [132,194] implement this strategy by ushering the single atom onto coordinated sites with a chemical linker, followed by a thermal method and other post-treatment to remove and carbonize unrequired synthetic reagents. The most critical variable for controlling the synthesis of SACs using this strategy is the concentration of the metal producing the single atoms and the annealing temperature [51]. A well-established coordination strategy known as surface organometallic coordination (SOMCs) from coordination compounds has been developed to produce single-site atom catalysts [105]. During the grafting of SOMCs, several fragments of reaction intermediates are linked to a surface-supported metal (e.g., Metal-M; M−H, M–R, M = CR_2, M = O, M = NR, M–O–OR), enabling direct access of the metal atom to the surface. Copéret [195] has reported that the selective formation of isolated sites of metal *via* SOMF on a heterogeneous catalyst is more favorable than *via* wetness impregnation methods, which favor the formation of larger nanoparticles or clusters. He also demonstrated that a single-site heterogeneous catalyst can be prepared using SOMC combined with thermolytic molecular precursors (TMP). These TMP can be removed readily upon thermal treatment, giving a high flexibility SOMC/TMP procedure to engineered heterogeneous catalysts. For instance, few well-defined isolated site based SACs (e.g. Cr(III) supported on Al_2O_3) have been developed by the combination of SOMC and thermolytic molecular precursors (TMPs), yielding a greater catalytic activity, selectivity and stability of Al_2O_3 than the Cr(III)/Al_2O_3 bulk catalyst [196]. In 2017, a combination of SOMC and ALD approach was being developed by Liu to produce a SAC with uniform nuclearity Pt/Al_2O_3 [197]. By pairing the ALD strategy for mitigating agglomeration, the Pt organometallic complexes can remain monatomic even upon high-temperature thermal treatments and post ligand removal (Fig. 5 (b). Notably, the Pt/Al_2O_3 SAC does not exhibit any thermal sintering, even at 400 °C, whereas samples without ALD overcoats exhibited significant particle agglomeration under similar conditions. Alternatively, there were also efforts to synthesize SACs for hydrogenation *via* less energy intensive SOMC (without subsequent thermal treatment). An ultra-low Pt single loading (~1 wt%) was coordinated on phosphomolybdic acid (PMA)-modified active carbon [198]. The Pt SAC was synthesized by anchoring Pt on the four-fold planar geometry on PMA. The hydrogenation of N–O, C═O, C═C, and C≡C groups were studied, and the Pt-PMA/AC SAC exhibited comparable or better turnover frequencies (TOF) compared to a conventional Pt/AC catalyst. This demonstrates that single atoms have the potential to be anchored into organometallic compounds, which stabilizes the SAC structure while providing high catalytic activity.

2.2.2. Defect design strategy

Poorly defined vacancy defects on ordered support may lead to difficulties in identifying and controlling the precise structure of the attained SAC. Therefore, a defect design strategy aims to engineer the defects on a support to stabilize the SAC surface, allowing a higher possible metal loading, providing a large number of individual active sites, as well as improve the selectivity of the desired process [133]. One of the directions followed has led to a number of works being carried out to study the effect of O_2 vacancies in mixed metal oxides to stabilize active sites [200,201]. Additionally, vacancy defects on graphene or layered materials have been probed in a similar way [202,203], as well as, heteroatom defects in crystals, cation and anion vacancies [204,205]. Shen and co-authors [206] demonstrated that defects in graphene can alter the charge distribution on a carbon plane, giving evidence that graphite with more exposed edges can provide superior electrocatalytic performance. Apart from the carbon-based materials, other defect-rich oxide materials also were used as supports in the synthesis of SACs (e.g., CoO [207], TiO_2 [199], and CeO_2 [208]). Wang et al. [207] have employed an adsorption method to prepare an Rh-based SAC (Rh/CoO), which was stabilized in the defect sites on the surface of CoO nanosheets through the electrostatic interaction. The developed Rh/CoO SAC displayed higher selectivity toward propene hydroformylation to butyraldehyde compared to Rh/bulk-CoO. TiO_2 is also another suitable support for SAC preparation that has abundant defective sites. From Fig. 5 (c), a wrap-bake-peel synthetic strategy to fabricate an enzyme-like Cu-based SAC supported on the TiO_2 was proposed by Lee et al. [199]. The amorphous TiO_2 was first coated on SiO_2 core before the Cu atoms were adsorbed on the amorphous surface. Then, a second layer SiO_2 coating was introduced to form the SiO_2–TiO_2–Cu_1–SiO_2 core−shell materials with a sandwich-like structure. Subsequent steps such as calcination, baking, and NaOH leaching were performed to ensure the single Cu atoms were located at the Ti sites of anatase TiO_2. This synthetic strategy gas facilitated a valence control of co-catalyst Cu atoms and generated a reversible valence change in photoactivation that enhance photocatalytic hydrogen generation activity.

2.2.3. High temperature-induced strategy

It was widely known that higher thermal stability of SACs can be granted by fabricating the catalysts under higher temperatures since the precursor–support interaction will be enhanced under high temperatures [134]. Some of the state-of-art techniques reported are strong metal-support interaction (SMSI) promoted production [125], the non-defect stabilized approach [133], and the high thermal redispersion approach [209].

For instance, based on a work published in 2015, the single atom active sites on a support can be formed SMSI approach during pyrolysis [60]. It is attractive due to its capability in yielding SACs with good metal dispersion although in higher metal loadings (5–20 wt%) [101, 210]. Cheng et al. [210] reported the performance of the pyrolysis-assisted method in fabricating a series of atomically dispersed transition metals (M refers Ni, Co, NiCo, CoFe, and NiPt) on N-doped carbon nanotubes with metal loading of 20±4 wt%. Findings showed

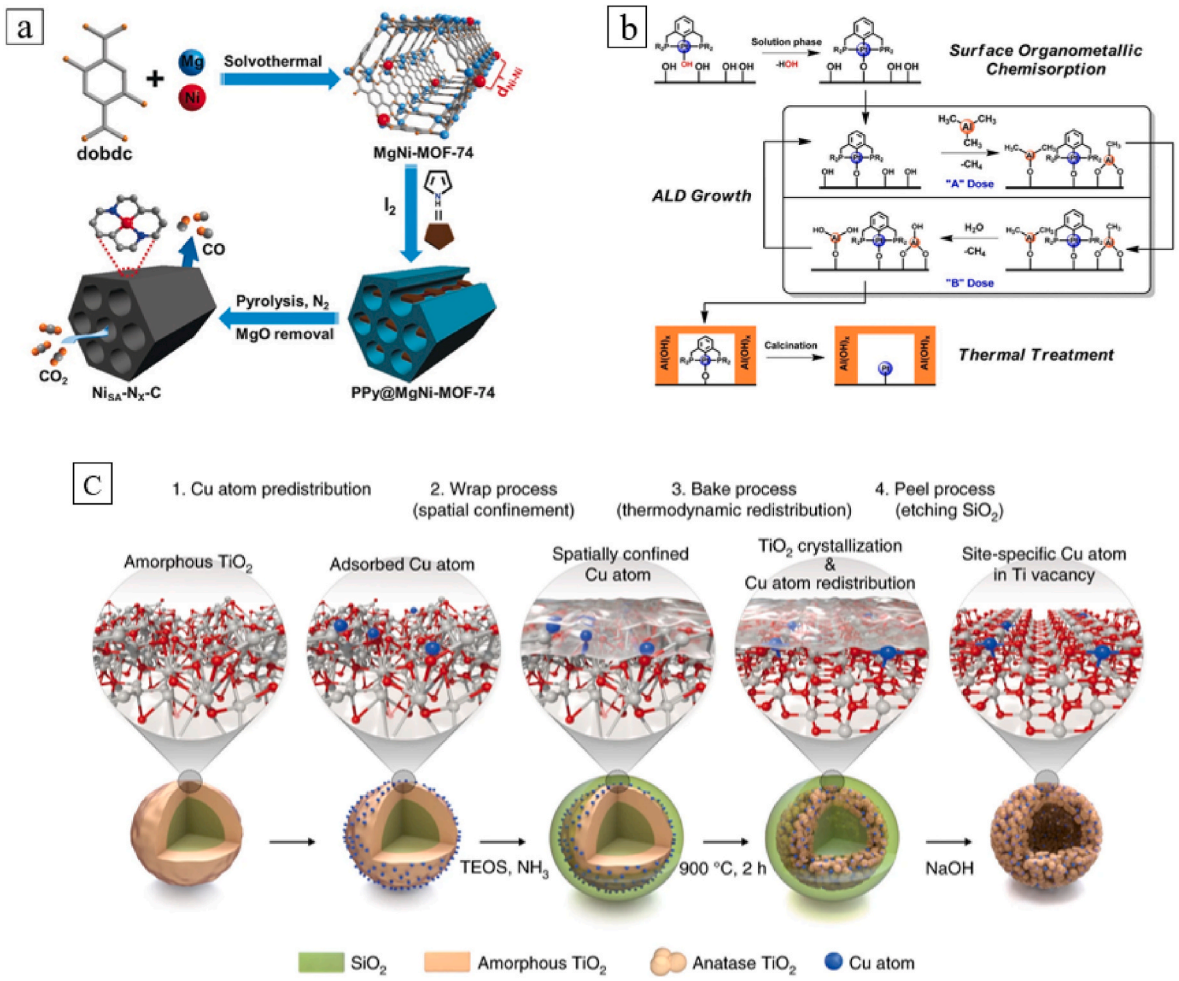

Fig. 5. Schematic diagram for (a) the fabrication of Ni_{SA}-N_x-C catalysts using coordination site strategy, remark: dobdc = 2,5-dioxido-1,4-benzenedicarboxylate [193] (adapted with permission from John Wiley & Sons, Inc.), (b) Synthesis of Pt/Al_2O_3 SAC using the ALD strategy [197] (adapted with permission from American Chemical Society), (c) Synthesis of Cu/TiO_2 photocatalyst using a modified wrap–bake–peel process [199] (adapted with permission from Springer Nature).

that the M single-atom/N-doped carbon nanotube fabricated *via* a pyrolysis-assisted method exhibited outstanding catalytic performance not only on ORR and HER but also in electrochemical CO_2 reduction [101,211]. In general, the pyrolysis-assisted method consists of three general steps, (a) mixing of metal and support precursors, (b) pyrolysis, and (c) post-treatment, e.g., washing, drying, acid treatment (for removal of residual unencapsulated metal or unwanted ligands). Taking the deposition of Co_1 on the N-doped carbon as an example (Fig. 6(a)), the first step was to prepare the catalysts precursors by mixing urea, glucose, $CoCl_2{\cdot}6H_2O$, NaSCN, and ethanol at room temperature. Then, the mixture was treated with ultrasonic treatment to form a homogeneous mixture. It was subsequently, dried at 60 °C for 8 h to remove trace ethanol residues. The resultant solids were then ball-milled to form the desired catalyst precursor. Next, the obtained materials were pyrolyzed (>600 °C), and subsequently cooled to room temperature under an inert (N_2) atmosphere. This resulted in the formation of Co_1/N-doped carbon SAC with a uniform distribution of Co atoms. Before the SACs can be used, it was cooled and treated in acid (0.5 M, H_2SO_4 at 80 °C for 8 h) to remove any non-coordinated Co atoms and precursor impurities. To note, the yielded Co_1/N-doped carbon catalyst possesses the greatest catalytic activities for ORR and HER as compared to the other two conventional catalysts (Pt/C catalysts and Co/N-doped carbon catalysts), as well as excellent reusability where there was no degradation after 11,000 continuous catalytic cycles [211]. Recently, pyrolysis was also used as an efficient tool to downsize metal from the range of 100–1 nm. Based on the findings discovered by Wei et al. [134], the sintering and atomization occurred during the pyrolysis of metal-NP (i.e., Pd, Pt, Au), where atomization (i.e., the transformation of metal-NP to SA) took place at high temperature (900–1000 °C); whereas sintering was observed between 300 and 1000 °C. This represents an attractive top-down synthesis path to derive SACs from a metal NP. In fact, the pyrolysis-assisted approach appeared to be promising for the synthesis of SACs with ultra-high metal loading (>20 wt%) [65,111].

Aside from this, a recent method to synthesize single-atom metals from bulk metals on the catalyst surface using high temperatures were also being developed [214]. This thermal emitting strategy provided an economically attractive advantage for producing single atom nano-catalyst from their bulk materials. Qu and co-authors [214] have used pyrolysis at 900 °C to create Zn nodes and defect sites on a pyrolyzed zeolitic imidazolate framework-8 (ZIF-8). Then, a Cu foam was reacted with NH_3 gas to form $Cu(NH_3)_x$. These $Cu(NH_3)_x$ species were then trapped by the defects in the pyrolyzed N-rich carbon support, which forms the Cu-single atom N-rich carbon support (Cu–SAs/N–C) catalyst. The work also showed that Co or Ni could be used to replace the Cu bulk metal, confirming its application towards a wide range of SAC syntheses. Later, Qu and co-authors [103] used this thermal emitting strategy to synthesize a high-performance Pt-SAC on defective graphene (Pt–SAs/DG) (Fig. 6(b)). For this synthesis dicyandiamide (DCD) and Pt dispersed on graphene oxide (GO) were placed under Ar flow and heated to 1100 °C. At this temperature the DCD underwent pyrolysis, generating NH_3 gas. Due to the strong coordination interaction between NH_3 and Pt atoms, the volatile $Pt(NH_3)_x$ species was formed. The Pt entities

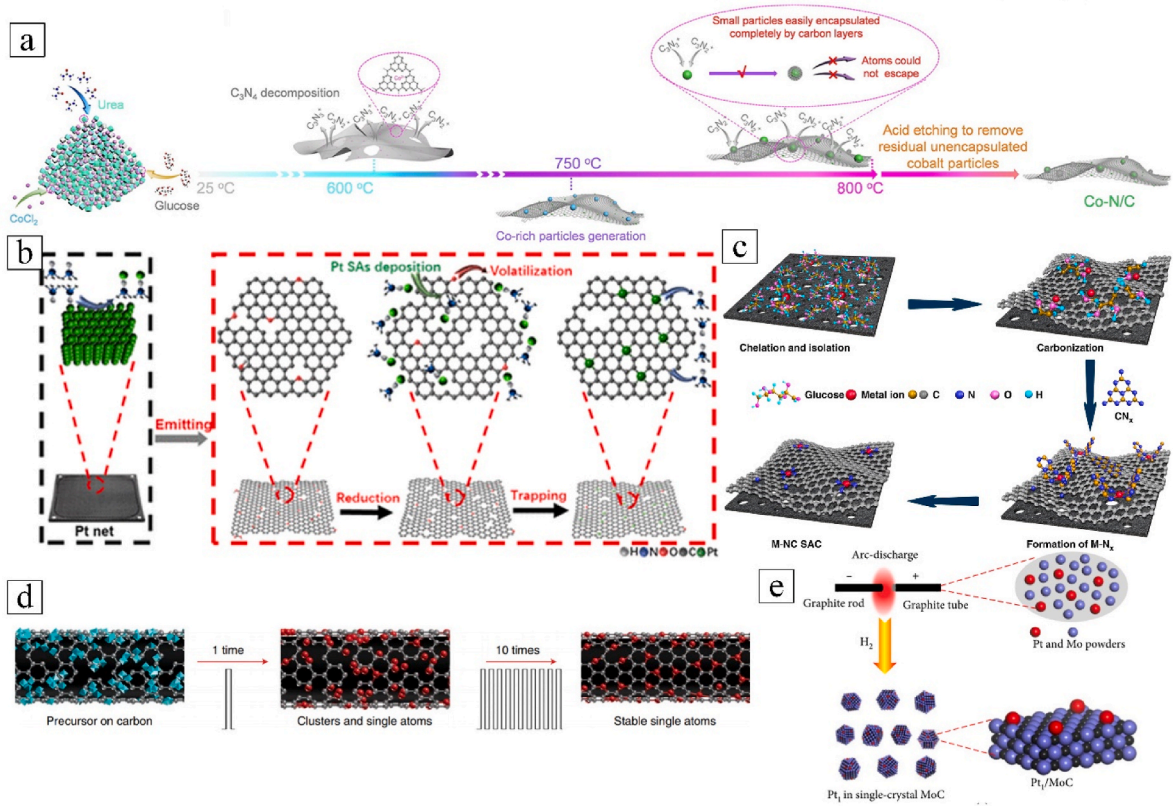

Fig. 6. Schematic diagram for thermal-assisted strategies: (a) production of Co_1/N-doped carbon using pyrolysis-assisted method [211] (adapted with permission from Elsevier), (b) formation of Pt–SAs/DG using thermal emitting strategy [103] (adapted with permission from ACS), (c) Mass production of high-loading single-atomic metal-nitrogen catalysts using a cascade anchoring strategy [104] (adapted with permission from Springer Nature), (d) High temperature shockwave strategy [212] (adapted with permission from Springer Nature), and (e) Fabrication of Pt_1/MoC *via* high temperature arc-discharge strategy [213] (adapted with permission from American Association for the Advancement of Science).

were oxidized by O atoms based in the GO, forming $Pt^{\delta+}$ ($0 < \delta < 4$) species. After that, O content from the GO was removed through thermal processing to produce graphene with defects (DG). Lastly, the isolated Pt SAs/DG catalysts were formed by trapping the $Pt^{\delta+}$ ($0 < \delta < 4$) species on the DG. Notably, the prepared Pt–SAs/DG catalyst demonstrated high activity for HER and selective oxidation of various organosilanes. This demonstrates that even the surface of the catalyst can be freely changed by using the thermal emitting strategy, giving a high potential for future SAC synthesis on a large-scale production.

Zhao and co-authors [104] recently proposed a cascade anchoring strategy to synthesize a SAC with a high-loading with the possibility for large-scale production. The work demonstrates that the cascade anchoring strategy could synthesize metal-N_x moieties, anchored on carbon support (M−NC) with flexibility for the metal atom. Moreover, the metal loading for the synthesized catalyst was reported up to 12.1 wt %. First, metal ions (e.g. Mn, Fe, Co, Ni, Cu, Mo, and Pt) were fixated using a chelating agent (such as glucose). The isolated metal ions are then anchored onto the O_2-rich porous carbon support where the glucose can bind to the carbon support due to interaction with O-containing groups (Fig. 6(c)). Next, the compound was mixed with a nitrogen source melamine, and pyrolyzed over 600 °C to react the carbon-N species with melamine to form a SAC with M-N_x moieties. A similar anchoring strategy using immobilization and pyrolysis was also performed for the synthesis of Pt-single atoms on a commercial carbon black, Black Pearls® 2000 (PtSA@BP) [215] for the HER reaction. This work used a tetra(4-*tert*-butyl-phenyl)porphyrinato platinum (PtTBPP) complex as the N and Pt precursor while simultaneously providing a monodisperse purpose. The molecules achieved porphyrin adsorption equilibrium after being stirred for 12 h. After washing (by ethanol and deionized water) and drying under reduced pressure, the PtTBPP/BP hybrid underwent two-stage pyrolysis, giving a final Pt loading of 2.5 wt %.

Nevertheless, SACs synthesis at temperatures >1000 °C is still challenging to be achieved *via* conventional strategies. To overcome this technical barrier, two ultra-high temperature-assisted strategies, namely the high-temperature shockwave strategy [212] and the high-temperature arc-discharge strategy [213] were developed. The former method utilized periodic on-off shock heating (on-state temperature can achieve up to 2727 °C; while the off-state period operates for 10x longer, leading to a lower average temperature of 127 °C) to stabilize the single metal atom on the support. This makes the strategy compatible with various materials. Yao and co-workers [212], for the first time, synthesize Pt single atoms that are deposited on the CO_2-activated carbon nanofiber *via* a high-temperature shockwave strategy. The metal precursor, H_2PtCl_6 was dispersed on the carbon nanofiber and subsequently subjected to the heating shockwave. Their studies revealed that the dispersion of Pt clusters can be eliminated by increasing the heating cycles (Fig. 6(d)). Interestingly, all the weak Pt–Pt bonds and types 1–3 Pt–C bonds were transformed into stronger types 4–10 Pt–C bonds after multiple cycles of shock heating, thus, resulting in higher thermal stability.

The latter strategy utilized high-temperature arc discharges to in-situ form and stabilize Pt single atoms on molybdenum carbide (MoC) support at a temperature up to 4000 °C (higher than the limit of the former strategy). To synthesize Pt_1/MoC *via* this method, a mixture of Pt and Mo powders was first prepared and filled into the anode-side graphite tube (Fig. 6(e)). Whereas the cathode is made of a pure graphite rod. The synthesis process begins when the arc starts to be generated from the arc chamber. The entire process took tens of minutes (other methods take hours to complete the synthesis) which makes it an efficient and

attractive fabrication tool. The resultant SACs exhibit excellent performance and thermal stability for the hydrogenation of quinoline. However, both the aforementioned methods are still in their infancy, and follow-up works are needed to upscale the overall synthesis process to cope with the demands for mass production of SACs.

2.2.4. Other ingenious strategies

2.2.4.1. Freeze-drying assisted strategy. A freeze-drying method has also gained interest from the catalysis community as it enables a large specific surface area of the support, while more importantly, the mobility of the metal precursors can be mitigated simultaneously [135]. A few researchers have therefore incorporated the freeze-drying process into SACs fabrication to better design and control metal precursor deposition. Taking a Co-based SAC as an example (Fig. 7(a)), Fei et al. [59] mixed the metal precursor ($CoCl_2{\cdot}6H_2O$) and support precursor (graphene oxide) at a ratio of 1:135. The mixture was then sonicated in deionized water, and subsequently freeze-dried for 24 h to produce brownish powders. Next, the powder was annealed at 750 °C for several hours to activate the Co_1/N-doped graphene. The work has proven that the obtained catalysts can work as effective HER catalysts under both acidic and alkaline environments. Thus far, the freeze-drying method has been extended to create Fe-based SACs for ORR [216] and Fenton-like reaction [217], Pd-based SACs for selective hydrogenation [218] and Zn-air batteries application [219], Ni-based SACs for CO_2 methanation [220], Pt-based SACs for HER [221], Co-based SAC for lithium-sulfur batteries application [222], and bimetallic SACs (e.g., Co_1–Fe_1-based SACs for HER [223]). Despite the potential of having greater reactivity and stability of catalysts as compared to the conventional oven-drying approach [224], the high operational cost still appears as one of the main conundrums for the freeze-drying assisted strategy [136].

2.2.4.2. Photochemical method. Photochemical methods rely on a powerful light source (e.g. UV lights) to deposit single atoms on support *via* ion reduction. In years gone by the photochemical method was used for solar O_2 production in metal deposition onto a semiconductor photoanode [139]. For instance, the deposition of Co on a ZnO electrode in a K_3PO_4–$CoCl_2$ precursor solution under UV light emission to oxide the Co^{2+} ions, adhering it to the ZnO surface[142]. This method was recently adopted into Pt SAC preparation by Liu et al. [102]. They have successfully developed an "ultra-low" Pt loading and highly stable atomically dispersed Pd_1/TiO_2 SACs for catalytic hydrogenation of aldehydes (Fig. 7(b)). The single atom Pt-loaded (up to 1.5 wt% loadings) TiO_2 nanosheets on ethylene glycolate (EG) were synthesized by stepwise UV-induced radical formation which causes Cl^- removal by EG radicals [102]. The adsorption of photons and electronically excited states were reported to be the two key steps in the photochemical reduction process. Later, this photochemical method was used to synthesize Pd-loaded (001)-exposed anatase nanocrystals and Pd-loaded TiO_2 SACs for the purpose of styrene hydrogenation and CO oxidation [226]. For solar water oxidation, an Ir dinuclear heterogeneous catalyst (DHC) on a Fe_2O_3 surface was prepared by ultraviolet ozone (UVO) cleaner system, providing a paradigm for SACs with multiple active sites [227]. A photochemical solid-phase synthesis method was used to adsorb $PtCl_6^{2-}$ onto an N-doped porous carbon and directly reduced by UV light to Pt atoms achieving 3.6 wt% loadings [228]. Another novel method to prevent atom nucleation is by using iced photochemical reduction [225]. This strategy (Fig. 7(c)) coupled with the freeze-drying technique, freezes the atom-carrying aqueous solution before UV treatment and successfully synthesizes a stable SAC with Pt atoms on various support (e.g., amorphous carbons, mesoporous carbon, graphene, multi-walled carbon nanotubes, TiO_2 NP, and ZnO nanowires) for HER.

2.2.4.3. Electrochemical method. The electrochemical Method is a

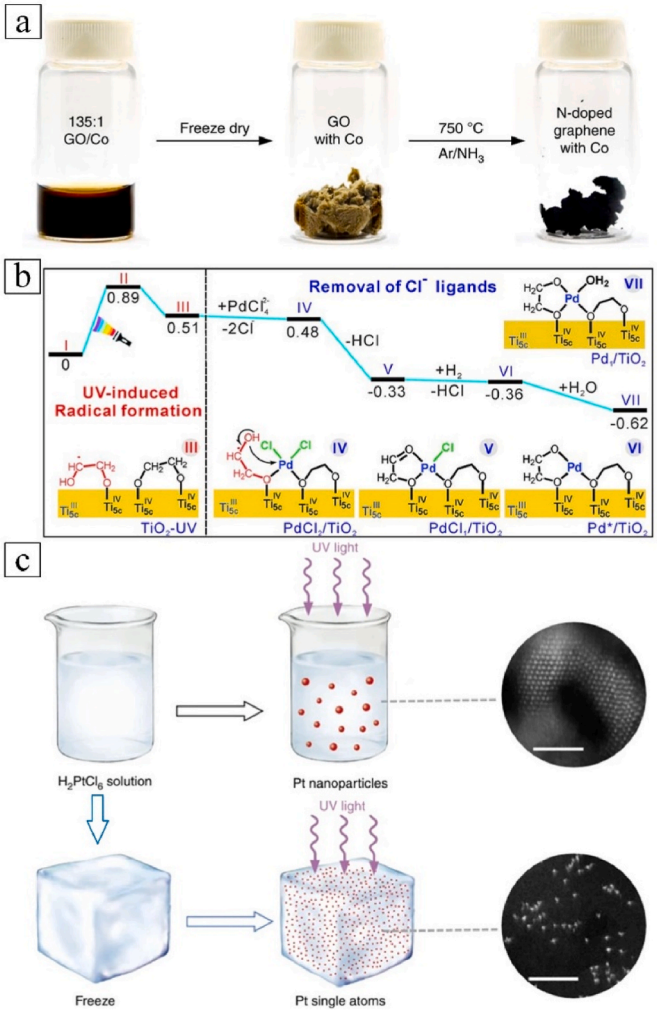

Fig. 7. Schematic diagram for (a) freeze-drying method to synthesize Co_1/N-doped graphene [59] (adapted with permission from Springer Nature), (b) Energies and models of intermediates and transition states in the Stepwise preparation mechanism of Pd_1/TiO_2 using EG radical [102] (adapted with permission from American Association for the Advancement of Science), (c) Fabrication of Pt single atoms using iced-photochemical process [225] (adapted with permission from Springer Nature).

widely accepted electrocatalyst preparation method by most researchers; this is because the metal ions can be easily deposited onto cathodes in an electrolyte solution without any complicated procedure [229]. Therefore, it is one of the attractive, scalable, facile, and cost-effective methods which is capable of synthesizing and activating single atom electrocatalysts with the aid of electrochemical potential. To-note, the size, and the respective metal loadings can be fine-tuned by altering the deposition parameters such as metal ion concentration and deposition time [140]. More importantly, the SACs derived from this method are binder-free that can be used directly in electrocatalysis [140]. Some works have proved its capability in SAC fabrication. Notably, in the work conducted by Fan et al. [230], the formulated Ni–C-based catalysts were successfully activated *via* the series of treatment processes, i.e., HCl leaching treatment (for removal of redundant Ni metal) and electrochemical cyclic-potential treatment (for activation). Unexpectedly, throughout the entire activation process, Ni atoms were atomically dispersed and anchored onto the carbon support, which therefore formed Ni-based SACs (Fig. 8(a)). On the other hand, some works have attempted to in-situ grow the Pt single atoms onto Ni foam [52], single-walled carbon nanotubes [231], and a bismuth ultramicroelectrode [140]. Aside from that, Zhang et al. [232], for the first

time, proposed the use of the electrochemical method to synthesize an atomic Pt and Co co-trapped carbon catalyst. Thus far, the SACs fabricated using this method have shown superior HER activity and electrocatalytic stability as compared to the conventional Pt/C (20 wt% Pt) catalysts (e.g., the catalytic activity of the PtSA-NT-NF catalysts synthesized by Zhang et al. [52] were 4 times greater than that of Pt/C catalysts). More recently, a self-terminating electrodeposition technique for SACs fabrication was proposed [141]. Generally, by controlling the electrical potential at the underpotential deposition (UPD) state, the metal-support bonding can become dominant as compared to the metal–metal bonding, which favors the formation of SACs. The continuous atom growth will be terminated once the surface-limited reaction has reached saturation. This further ensures the formation of SACs instead of metal clusters (Fig. 8(b)). More interestingly, it can be operated under ambient temperature which makes it an energy-efficient SAC fabrication method. Moreover, the two ultra-high temperature-assisted strategies (i.e. high temperature shockwave strategy and the high temperature arc-discharge strategy) presented in Section 2.2.3 can also be, arguably, categorized as electrochemical methods as the use of electric fields was involved.

2.2.4.4. Mass-selected soft-landing. The mass-selected soft-landing approach is an emerging technique for SAC synthesis. It starts with the vaporization of metal atoms using a high-frequency laser, where the vaporized metal atoms are selected by a mass filter to control the deposition of the metal on the support surface [118,146] (Fig. 9). To-date, since this method is capable of providing exact tuning and control of the size of metal deposited on the support surface, it has been employed in a couple of SAC works for generating fundamental insights [13,233]. For example, to study the impact of Pt atom number on electrochemical catalysis, Weber and co-workers [234] have synthesized Pt_n/Indium Tin Oxide (ITO) catalysts ($1 = n \leq 14$) using the mass-selected soft-landing method. In their work, the Pt_n^+ clusters (and atoms) produced from the laser vaporization were channeled through a quadrupole mass filter to generate a beam containing the desired cluster (or single atom) size which was then deposited on the ITO surface. Earlier in 2000, one of the pioneering works [235] had also attempted to verify the catalytic kinetics of Pd_n/MgO(100) catalysts ($1 = n \leq 30$) for the trimerization reaction using a mass-selected soft-landing method where they found the SAC (Pd_1/MgO(100)) can significantly reduce the activation energy requirement. Aside from that, this approach has been applied to synthesize bimetallic SACs for OER and ORR [236]; Pt_1/glassy carbon substrate catalysts for ORR [237]; Pd_1/TiO_2 catalysts for CO oxidation [238]; and Au_1/TiO_2 catalysts for CO oxidation [239]. Nonetheless, the need for ultrahigh vacuum conditions and low production yields has inevitably lowered the scalability of this method [13,118].

3. Characterization methods

The existence and spatial distribution of isolated single atoms are crucial for understanding the relationships between structures and the properties in SACs. However, it is quite challenging to identify the single atoms at an atomic-scale due to the requirement of high spatial resolution tools. In recent decades, techniques have been developed towards an atom-scale resolution that can be employed to the SACs at different ensemble level signals, of all responsive species, which can minimize the deceptive information and accurately reflect the real active atomic species. Hereby, in this section, we provide an overview of various advanced characterization techniques for SACs, which can be classified into several categories: (a) High-resolution electron microscopy, (b) X-ray irradiation spectroscopy, (c) *in situ* spectroscopy, and (d) magnetic resonance spectroscopy.

3.1. High-resolution electron microscopies

3.1.1. High angle annular dark field microscopy

With the development of advanced microscopes, the direct observation of NPs or atoms in/on catalyst supports has been realized. With the aid of different electron microcopies such as Aberration-Corrected High Angle Annular Dark Field/Scanning Transmission Electron Microscopy (AC-HAADF/STEM), the fine distributions and precise location of single atoms in the catalyst can be evaluated, differentiated using bright and dark field imaging.

Transmission electron microscopy is one of the most widely used characterization methods to determine the structure and particle size of

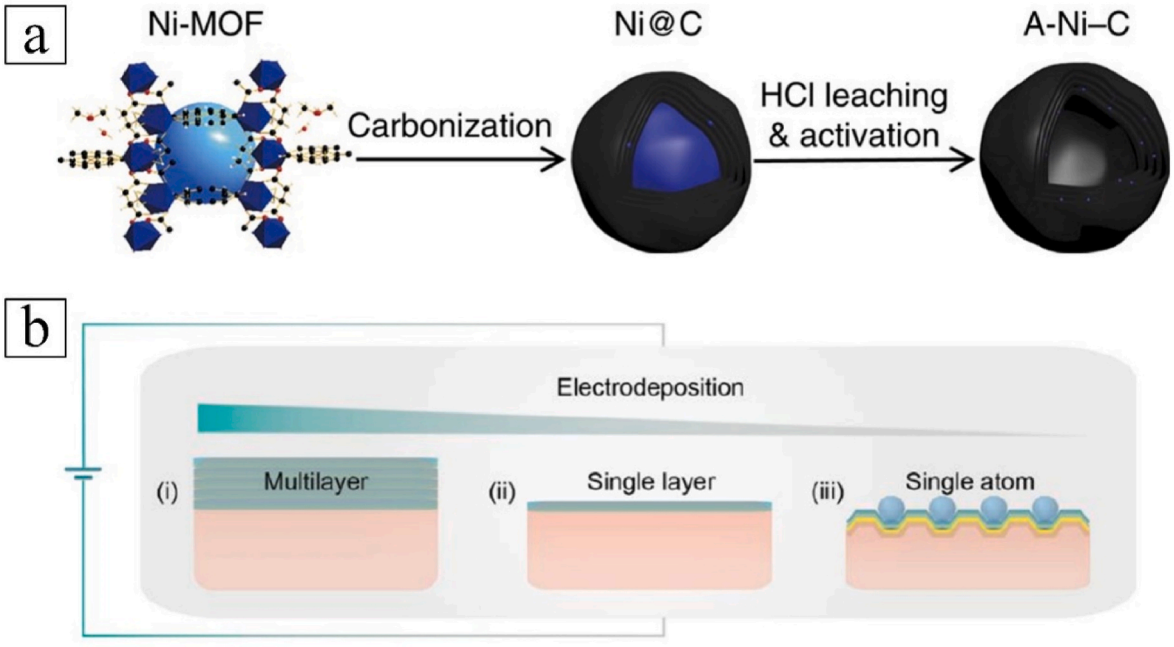

Fig. 8. (a) Schematic illustration of electrochemical method to activate and synthesize Ni–C catalysts [230] (adapted with permission from Springer Nature), and (b) Schematic diagram for self-terminating electrodeposition method [141] (adapted with permission from Springer Nature).

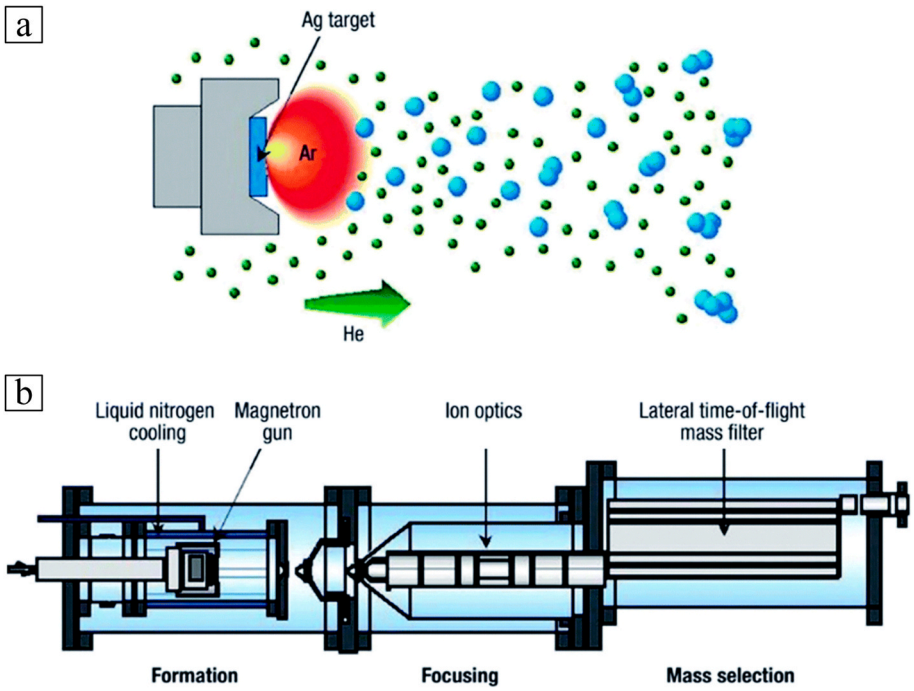

Fig. 9. (a) Formation of a metal atom via high-frequency laser source; (b) Structure of equipment used for mass-selected soft-landing method [146] (adapted with permission from Royal Society of Chemistry).

active sites in heterogeneous catalysts. It provides a clear observation of the catalyst morphology and structural change before and after interactions between metal atoms and supports [240,241]. Lately, the improvement of spatial resolution in electron microscopes has granted the possibility of identifying the active sites of SACs at a single atom level. Specifically, HAADF-STEM is one of the high-end techniques in which the high angle annular dark field imagery is coupled with a standard scanning transmission electron microscope to provide the bright/dark contrast of different elements at a sub-angstrom level resolution [242]. For HAADF-STEM, the intensity of images obtained follows the thickness of samples and the atomic number up to an exponential value of 1.4–2, but still, it is not powerful enough to identify the isolated single atoms in a SAC [243]. To improve the precision, the aberration-corrected HAADF-STEM is often used to distinguish the atoms from the support materials based on their different values and, further provide direct evidence of the existence of SACs [244,245]. For example, Qiao et al. [19] reported about Pt/FeO_x catalysts and demonstrated how individual Pt atoms uniformly dispersed on a FeO_x surface using HAADF-STEM (Fig. 10(a)). Both individual Fe (Fig. 10(b)) and Ir (Fig. 10(c)) atoms can be clearly distinguished from other lighter metal atoms (highlighted by red circles) such as Si, Al, Na, C and O [246,247]. However, there is also a shortcoming where the isolated atoms in the images are not clearly shown due to the phase contrast caused by the multiple metal loadings, impurities, and the inhomogeneity of substrates (e.g. lighter elements are usually invisible when imaged together with heavier, differences in contrast). Thus, Electron Energy Loss Spectroscopy (EELS) or Energy Dispersive X-ray Spectroscopy (EDX) are often combined with HAADF-STEM to provide an in-depth insight into the catalyst [246]. Based on this method, metal atoms (e.g. Fe, Co, Ni) can be clearly distinguished from the carbon-supported SACs *via* STEM/EDX, where metal atoms are reported to be stabilized by the carbon surface [59,246,248] (Fig. 10(d)). However, when the atomic number of single metal atoms and supports are close, it will be challenging to obtain obvious contrast in HAADF-STEM [249]. In recent work, Guo et al. [250] prepared the Cu/Al_2O_3 SAC with a high loading of 8.7 wt%, but there were only a few Cu single atoms observed by HAADF-STEM owing to the weak image contrast of Cu and Al_2O_3. Hence, coupling of HAADF-STEM with other in-situ spatial resolution synchrotron characterization techniques is value-added to probe the structural information of the SAC (i.e, HAADF-STEM-Syn Infrared and HAADF-STEM-Syn X-ray Diffraction).

3.1.2. *Scanning Tunneling Microscopy*

Another persuasive technique for directly observing the SAC structure is by using Scanning Tunneling Microscopy (STM), in which the surface images of the conducting or semiconducting materials at the atomic level can be attained [251,252]. The typical advantage of STM is to in-situ track the reaction process on a well-defined surface and provides the opportunity to explore catalytic mechanisms in real time [253,254]. STM operates under ultra-high vacuum at the broadband temperature range from near −273 °C to around 1027 °C [255,256]. Over the decades, STM has been widely used in industries to track heterogeneous catalyst performance, as such, STM is applied to study the soft-landing deposition and atomic-layer deposition synthesized methods of SACs for the application in 1,3-butadiene hydrogenation [257], CO oxidation [258], and NO reduction [259]. For SAAs, STM can directly capture the images of metallic single atom entities (e.g., Pt [257], Ni [260], Au [261], etc.) deposited on singe crystal surfaces together with reactive hydrogen [22,257]. Fig. 11(a and b) shows Pt atoms existing as isolated protrusions substituted onto the Cu(111) surface and H atoms spillover onto the Cu surface [257]. More recently, ultrahigh vacuum high-speed STM has been adopted to observe the real-time growth process of single Ni atoms on graphene. The catalytic effect of individual Ni atoms at the edges of a growing graphene flake was captured at the millisecond time scale by STM (Fig. 11(c and d)), providing an overall picture of the diffusion of mobile nickel atoms that catalyzes the graphene growth on the edges of SAC islands [260].

3.2. *X-ray irradiation spectroscopies*

3.2.1. *X-ray Absorption Spectroscopy*

X-ray Absorption Spectroscopy (XAS) is a state-of-the-art synchrotron technique to characterize the local environment of atoms in materials by measuring the variation in the absorption coefficient under the

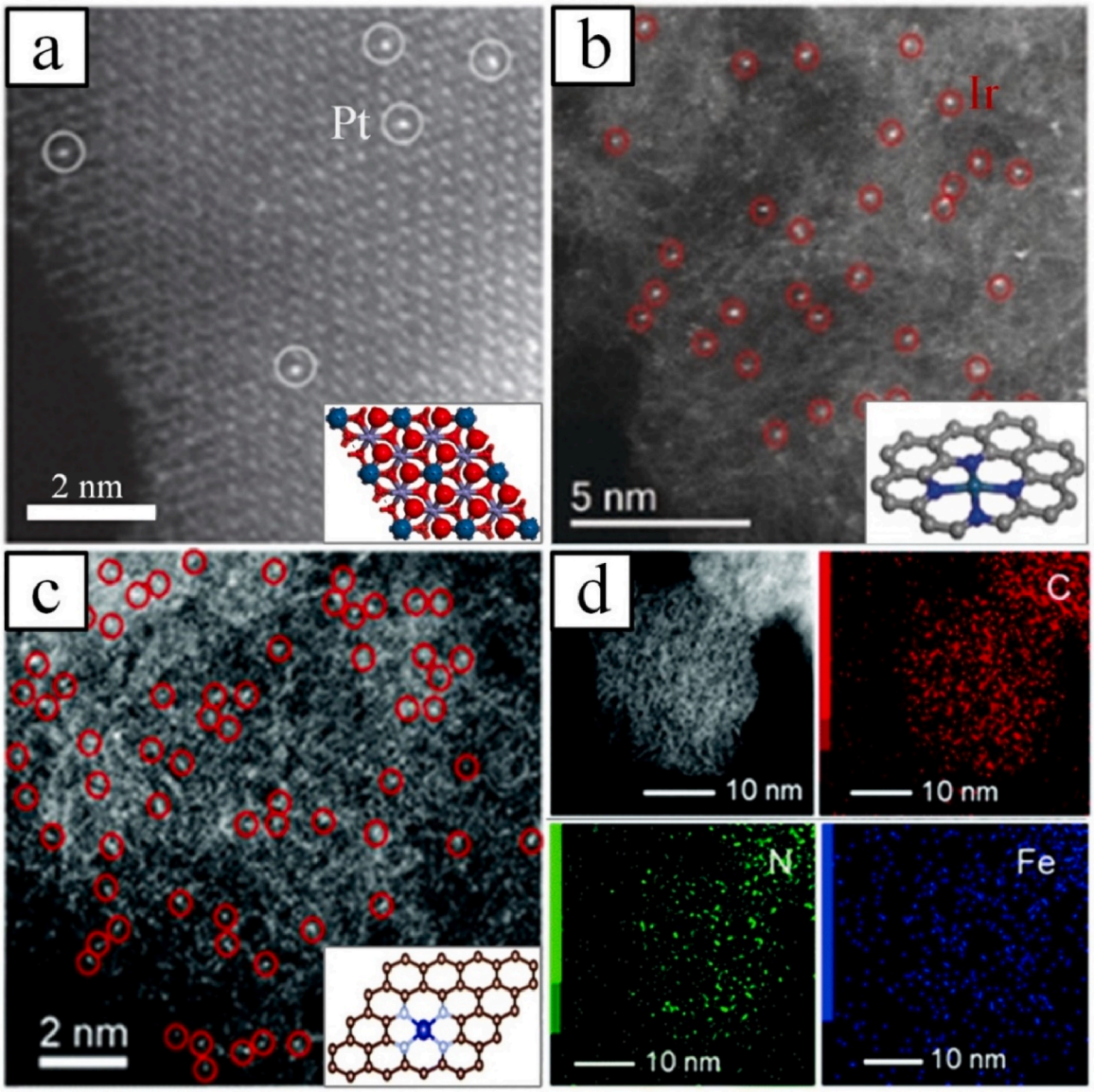

Fig. 10. (a) HAADF-STEM image of Pt/FeO_x where Pt atoms are circled in white [19] (adapted with permission from Springer Nature), (b) AC-HAADF-STEM image of Fe–SAs/NC where Fe single atoms are circled with red circles [246] (adapted with permission from John Wiley & Sons, Inc.), (c) High-resolution HAADF-STEM image of Ir-SAC where Ir atoms are circled in red [247] (adapted with permission from Royal Society of Chemistry), (d) AC-HAADF-STEM and corresponding EDX elemental mappings of an individual Fe–SAs/NC; C (red), N (green) and Fe (blue) [246] (adapted with permission from John Wiley & Sons, Inc.).

scanning of X-ray radiation in an energy range around the absorption edge [198,262]. XAS can be divided into three regions, pre-edge, near edge, and extended range (Fig. 12(a)). When the measurement range is near the absorption edge, it stands for X-ray absorption near edge structure (XANES); while the extended X-ray absorption fine structure (EXAFS) is usually measured beyond the absorption edge in the range of 50 to >1000 eV. From both forms of characterization (which are often obtained in the same scan), detailed structural information can be provided by these techniques, including the bond lengths, the angle between chemical bonds, oxidation states, and the number of coordinating species. EXAFS is usually used to show the coordination and absence of metal–metal interactions, indicating that the supported metal atoms are individual and that particles or clusters are absent. However, if the elements of the materials are sensitive to electronic and oxidation environments, XANES will be a more suitable characterization technique. For instance, Qu et al. [214] reported the preparation of Cu single atoms on N-doped carbon (Cu SAs/N–C). EXAFS results revealed that Cu–SAs/N–C exhibits a dominant Cu–N coordination at 1.48 Å, and there was no Cu–Cu coordination since no Cu–Cu characteristic peaks were observed. As for comparison, the main peak of Cu–Cu coordination was observed at 2.24 Å on a Cu reference foil. XANES was then performed for further analysis, and it showed the intensity of the line for Cu–SAs/N–C located between those for the Cu foil and CuO, revealing its typical electronic structure ($Cu^{\delta+}$, $0 < \delta < 2$) (Fig. 12 (b)).

3.2.2. *Near ambient pressure X-ray photoelectron spectroscopy*

X-ray Photoelectron Spectroscopy (XPS) is another widely used technique to characterize the chemical states and electronic structures of surfaces [39,75,265]. It has been used in many SACs to determine the chemical state and analyze their electronic environment, such as Pt/Fe–N–C [266], Pt/CeO_2 [267], ZnN_x/C [268]. Taking Chen and co-workers' work as an example [269], two peaks in the Pt 4f spectrum at binding energies of 75.8 and 72.4 eV, ascribing to $4f_{5/2}$ and $4f_{7/2}$ level were attained. From the XPS analysis, we can clearly distinguish that those peaks are between the Pt^{2+} and Pt^0 states. The peak positions were between those of Pt(II) and Pt(0), suggesting that Pt atoms carry

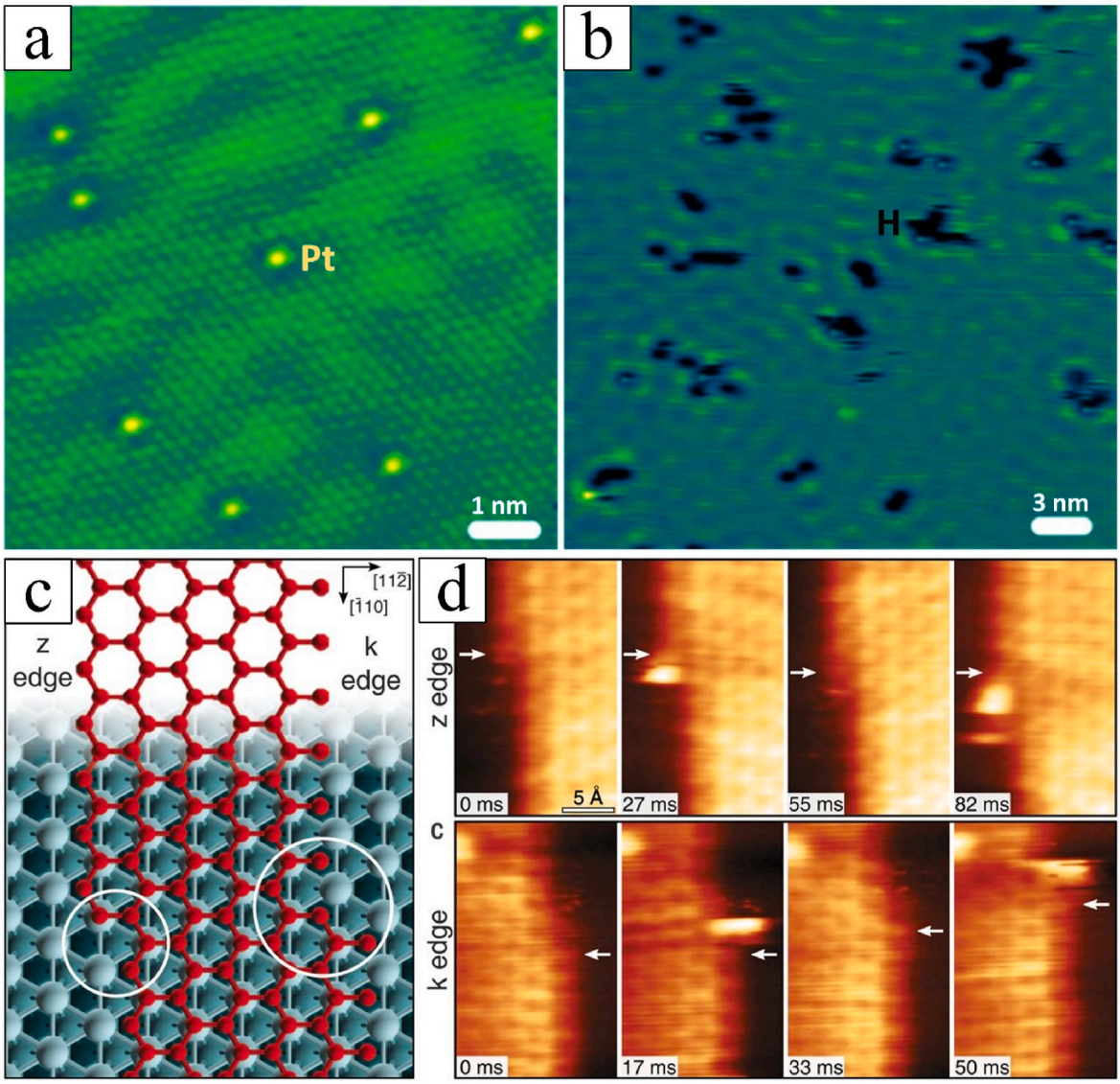

Fig. 11. STM image of monolayer Pt/Cu(111) SAC where Pt atoms (yellow) were exposed [257] (adapted with permission from Springer Nature), (b) STM image of hydrogen atom and spillover onto the Cu in the Pt/Cu(111) SAC, which appears as depression [257] (adapted with permission from Springer Nature), (c) Graphene growth along z and k edges. Zigzag (z) and Klein (k) edges of a top-fcc EG layer on Ni(111) [260] (adapted with permission from American Association for the Advancement of Science); where the kink structures at the edges are highlighted by white circles, (d) High-speed STM sequence acquired at 437 °C in quasi-constant height mode at the z edge; where white arrows indicate the position of C atoms in fcc-hollow sites near the kink [260] (adapted with permission from American Association for the Advancement of Science).

partially positive charge through electron transfer between metal and supports owing to enhanced metal−support interactions. More recently, with the rapid development of the in-situ technique, near ambient pressure X-ray photoelectron spectroscopy (NAP-XPS) was discovered to track the surface of a catalyst particle at a relatively high temperature in the gas phase (mbar pressure range). With the aid of this technique, the study of dynamic modifications at single atom-support surfaces in the vapor phase environment can be investigated, providing a sophisticated defect design of next-generation SAC catalysts [270]. Most importantly, not only the surface but also bulk-dissolved elements can be detected. The element species that may influence the chemisorption or charge delocalization of SAC atom can be analyzed, which provides a precise reaction mechanism of the catalyst in the gaseous phase [162].

3.3. Other in-situ spectroscopy

3.3.1. Infrared spectroscopy

By comparing with X-ray spectroscopy, the transmission infrared spectroscopy or Diffuse Reflectance Infrared Fourier Transform Spectroscopy (DRIFTS) uses a lower wavelength of infrared light reflection and transmission to evaluate the spatial resolution of the SACs (e.g. Acidic sites-Pyridine/NH_3 as probe and Basic sites-CO_2/CO as probe) or the change of organic phases of catalysts at time-resolved mode [271, 272]. In addition, DRIFTS is commonly used in conjunction with EXAFS, where EXAFS provides information about the electronic and geometric structure of the SACs, while DRIFTS follows the evolutionary formation of the surface bonding between single atoms and specific acidic and basic sites, aiding the understanding of the catalyst-absorbance mechanism in operando environment [273,274]. For instance, the infrared frequency of CO adsorbed on isolated metal atoms is different from that on clusters/NPs, this is because single metal atoms generally have

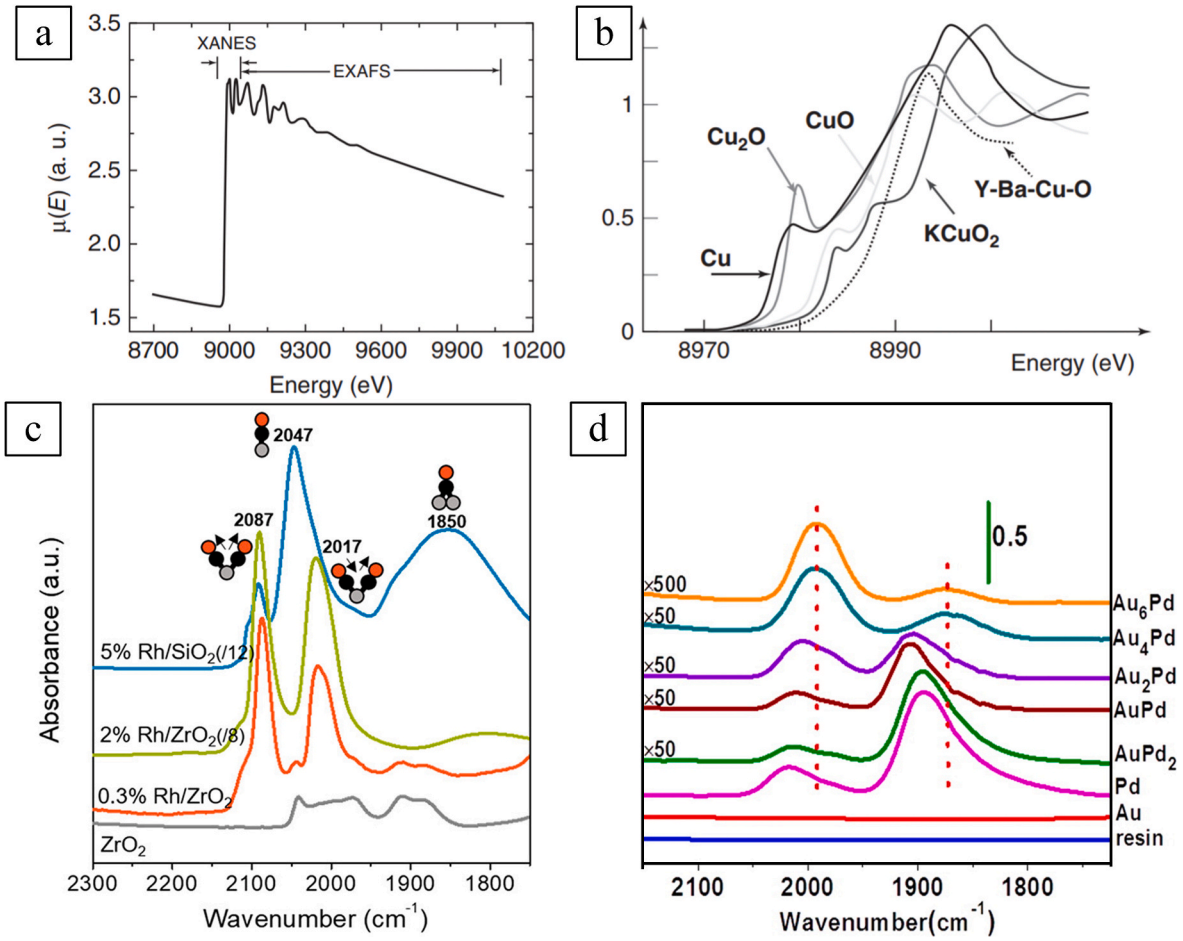

Fig. 12. (a) XANES and EXAFS regions are indicated for the K-edge signal of crystalline Cu [263] (adapted with permission from John Wiley & Sons, Inc.), (b) Identification of Cu oxidation state from the Cu K-edge XANES spectrum [214], Chemical state and coordination information for a Cu SAC [214] (adapted with permission from Springer Nature), DRIFT spectra of (c) 5 wt.% Rh/SiO_2, 2 wt.%, 0.3 wt.% Rh/ZrO_2 and ZrO_2 support as control [264] (adapted with permission from Springer Nature), (d) Au–Pd/resin SAC with different Au/Pd atomic ratios [42] (adapted with permission from American Chemical Society).

different chemical states due to their different coordination structures with the support [275]. Referring to Fig. 12(c), on increasing the loading of Rh on ZrO_2, the surface structure and mechanism for CO molecule adsorbed can be studied *via* absorbance peaks (e.g., atop, bridging, and a terrace site). In short, Infrared spectroscopy can be used to provide insights into the surface adsorption mechanism with respect to the single atom loading in SACs. Taking Au–Pd SAA supported on ion exchange resins (Au–Pd/resin) for the Ullman reaction as an example [42]. DRIFTS recorded the bonding profile of CO (probe molecule) on the Au–Pd/resin SAC with different Au/Pd ratios, in which two absorption bands were observed at 1895 and 2020 cm^{-1} which signifies the CO bridged and on-top adsorption onto the Au–Pd (Fig. 12 (d)).

3.3.2. *Operando Raman Spectroscopy*

Operando Raman Spectroscopy (ORS) is an in-situ technique to analyze the structures of materials at various scales from bulk to nanoscale layers through different photon energies. The application of ORS can provide unique means for a deeper fundamental understanding of layered nanomaterials and atomic-scale catalysts [276,277]. In 2019, the first attempt of investigating the atomically dispersed Rh metal on phosphotungstic acid (Rh/PMA SAC) during CO oxidation *via* ORS was proposed by Yan's group [278]. Based on the spectra shown in Fig. 13 (a), it shows that even after CO oxidation reaction at temperatures 573 K, the heteropoly acid structure of the Rh/PMA remains intact, suggesting that no formation of metal oxides after CO adsorption of Rh single atom. Apart from investigating the dispersion of single atoms, ORS has been used to investigate the molecular fingerprints of the MoS_x species present during the electrochemical HER in an $HClO_4$ electrolyte [279]. Based on the Raman profile (Fig. 13(b and c)), the structural evolution of MoS_x films during HER can be attained. As such, the peak at 2530 cm^{-1} was captured at potentials relevant to H_2 evolution, which corresponded to the S–H stretching vibration of MoS_x–H moieties. MoS_x-AE showed additional two peaks at 520 and 550 cm^{-1} which are not seen for MoS_x-CE. These were ascribed to the ν(S–S) terminal, and ν(S–S) bridging vibrations, respectively. Hereby, ORS can be acknowledged as one of the spectroscopic techniques that are typically used to determine vibrational and rotational modes of active species bonds on the atomic metal–metal coordination.

3.4. *Magnetic resonance spectroscopy*

3.4.1. *Nuclear magnetic resonance*

Nuclear Magnetic Resonance (NMR) for single atom detection is a solid-state spectroscopic technique used to identify the electron structures or chemical bonding of the core structure of a catalyst. The application of solid-state magic-angle spinning-nuclear magnetic resonance (MAS-NMR) has been widely reported to investigate the co-relationship of the precursor ligand bonding during the synthesis of SACs [280,281]. In 2017, Zhang and co-authors [37] have synthesized a highly active Pt-based SAC (Pt/m-Al_2O_3) by impregnating the Pt atom on the mesoporous Al_2O_3 support for selective hydrogenations and CO oxidation reaction. Based on the MAS-NMR analysis shown in Fig. 14

(a), they found that most of the Al^{3+} species were in tetrahedral, pentahedral, and octahedral shapes, differing from nanoparticles Pt/Al_2O_3 where the Al^{3+} pentahedral peak was not seen. This further confirmed that the significant pentahedral-coordinated Al^{3+} species have resulted from the calcination and reduction process, in which the Pt-atom was bound onto the Al surface *via* bridging O atoms. In addition, Zhang and co-authors [198] also synthesized a SAC with Pt on a phosphomolybdic acid-modified active carbon (Pt-PMA/AC) for hydrogenation reactions. A ^{31}P MAS-NMR was used to study the electron structure of the support with and without the Pt atom loading. Through the MAS-NMR study, it revealed changes in the environment for P bonding in the Pt-loaded PMA/AC. Lately, Shao et al. [245] adopted the ^{13}C cross-polarized-MAS NMR (CP-MAS NMR) technique to analyze carbon bonding on an Ir-based porous organic polymer with aminopyridine functionality (Ir/AP-POP). Various carbon bonding (such as C═O, Py-C, Ar–C, and Py-C) were identified in the Ir/AP-POP catalyst which assisted in understanding the catalytic mechanism for converting CO_2 to formate by quasi-homogeneous hydrogenation (Fig. 14(b)).

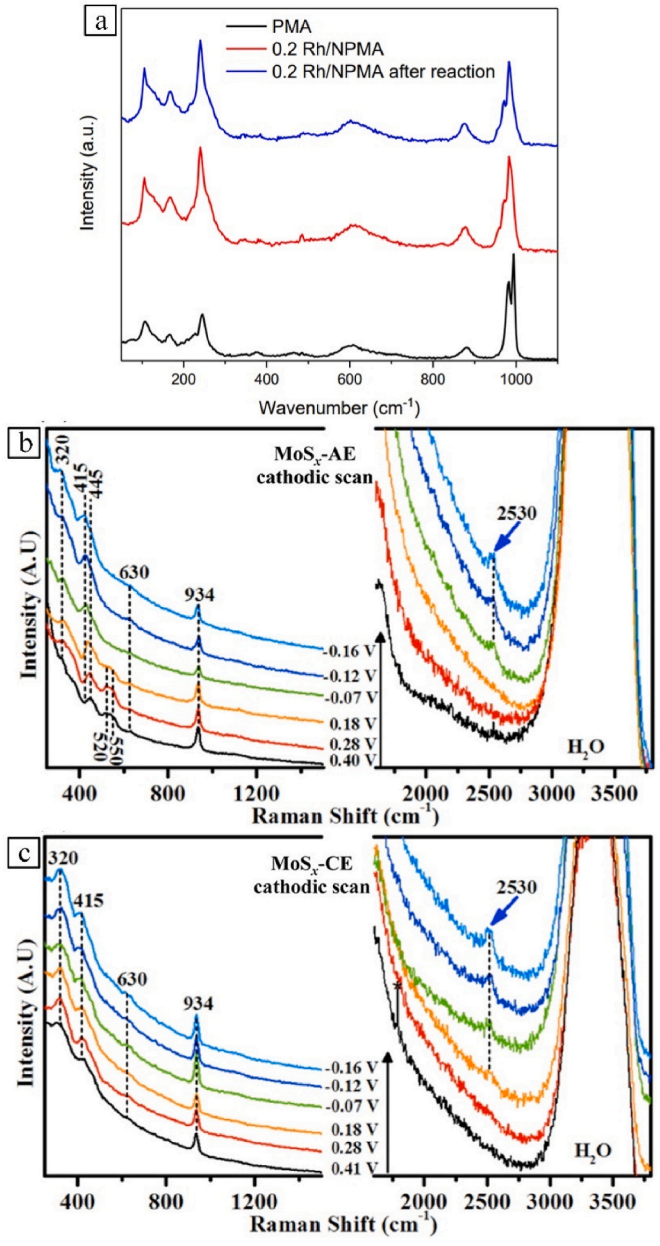

Fig. 13. (a) Raman Spectra of PMA and 0.2 Rh/NPMA before and after CO oxidation reaction at up to 300 °C [278] (adapted with permission from American Chemical Society), (b) MoS_x-AE [279] (adapted with permission from American Chemical Society), and (c) MoS_x-CE films were electrodeposited from a plating solution at 0.7 and −0.4 V, respectively [279] (adapted with permission from American Chemical Society).

3.4.2. Electromagnetic Spin Resonance

Electromagnetic Spin Resonance (ESR) is another characterization technique to investigate materials with unpaired electrons. This can be used to analyze the atomic state and coordination environment of SACs. For instance, the partial reduction of Cu(II) to Cu(I) due to graphene-induced charge transfer in a mixed-valence Cu/functionalized graphene SAC (G(CN)–Cu) can be confirmed through ESR measurement [282] (Fig. 15(a)). Based on the fresh catalyst ESR spectra, only the unpaired electron signal from isolated paramagnetic Cu(II) cations (d^9) was observed, whereas the Cu(I) cations (d^{10}) were not detected. The authors make a comparison of the ESR spectra of the G(CN)–Cu catalyst dispersed in hexane before and after adding H_2O_2. Notably, there was an increase in the intensity of Cu(II)-induced signal after adding the peroxide, this suggests that the Cu(I) was oxidized to Cu(II). Adding to that, ESR also can analyze the Curie behavior of the catalyst (inset in Fig. 16(a)), such as the non-presence of magnetically interacting Cu(II) centers in the catalyst. This observation indicated that there are no antiferromagnetic interactions or any formation of bulk CuO clusters. Recently, Jin et al. [283] also reported the superior performance of the partially oxidized Ni single-atom sites in polymeric carbon nitride for elevating photocatalytic H_2 evolution. Based on these findings, the change of oxidation state in Ni has modulated the catalyst's electronic structure, leading to an optimized photocatalytic activity, where fewer unpaired electrons were observed in deeply oxidized Ni single atoms (Fig. 15(b)). ESR can be concluded as a powerful technique to identify the electronic configurations of metal atoms in SACs, specifically for unpair electron detection.

3.4.3. Other characterization techniques

Along with the state-of-art characterization techniques, there are also some supplementary techniques that also provide information on the thermal stability of SACs (Thermogravimetric analysis, TGA), Brunauer–Emmett–Teller specific surface area of SACs (N_2 adsorption), single atom metal loading on the SACs (Inductively Coupled Plasma Mass Spectrometry, ICP-MS), and dispersion of the single atoms on the SACs (H_2/N_2O chemisorption [94,285,286]). With the aid of the supplementary characterization (Table 2), a more in-depth understanding of the intrinsic physicochemical properties of the catalyst can be elucidated. For instance, Zhang et al. reported that the fabricated PtCu SAA can yield a high turnover frequency that reaches up to 2.6×10^3 $mol_{glycerol} \cdot mol^{-1}_{PtCu-SAA}$ h^{-1} in glycerol hydrogenation, which is to our knowledge the largest value among reported heterogeneous metal catalysts [172]. Under this context, the dispersion of the Pt atoms on the SAA is highly important, and such an important piece of information only can be extracted from ICP-MS and N_2O chemisorption. Another example can be derived from a study reported by Li et al., with the aid of N_2 physisorption, they managed to observe that the Zn SACs are having multiple types of pores (i.e, micro, meso, and macro), which induces a large surface area of 1002 m^2 g^{-1}, that is ~10 folds higher than the commercial zinc catalyst [287,288].

4. Application of SACs in clean energy and chemicals production

As shown in Table 3, SACs have been applied to various heterogeneous reactions (e.g. C–C coupling, oxidation, reforming reactions, and hydrogenation) for chemical and fuel production. Herein, we aim to provide a comprehensive summary of SAC usage by discussing: (a) How does the heterogeneous structure of SACs affect the catalytic activity; (b) How does the structure evolution process response to a wide variety of intrinsic and extrinsic factors and (c) What are the underlying catalytic

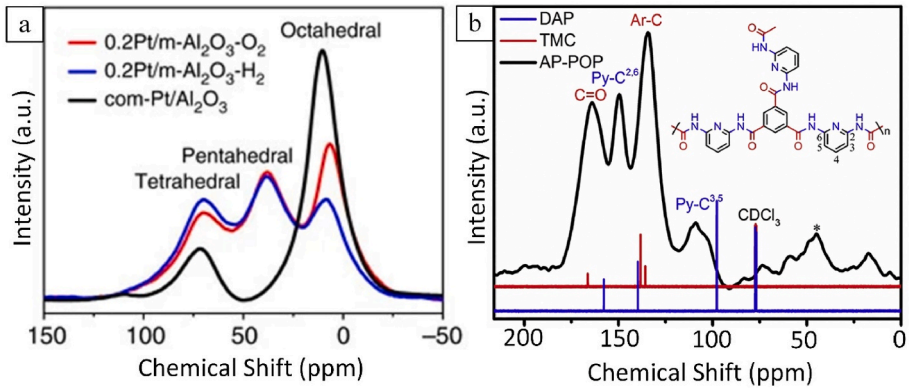

Fig. 14. (a) ^{27}Al MAS-NMR spectra of 0.2Pt/m-Al_2O_3–O_2, 0.2Pt/m-Al_2O_3–H_2, and commercial Pt/Al_2O_3 (observed tetrahedral, pentahedral, and octahedral coordinated Al_2O_3) [37] (adapted with permission from Springer Nature), (b) ^{13}C/CP-MAS NMR spectrum of aminopyridine-porous organic polymer(AP-POP) (observed presence of C═O, C–N, and C–Ar bonds) [245] (adapted with permission from Elsevier b.v.).

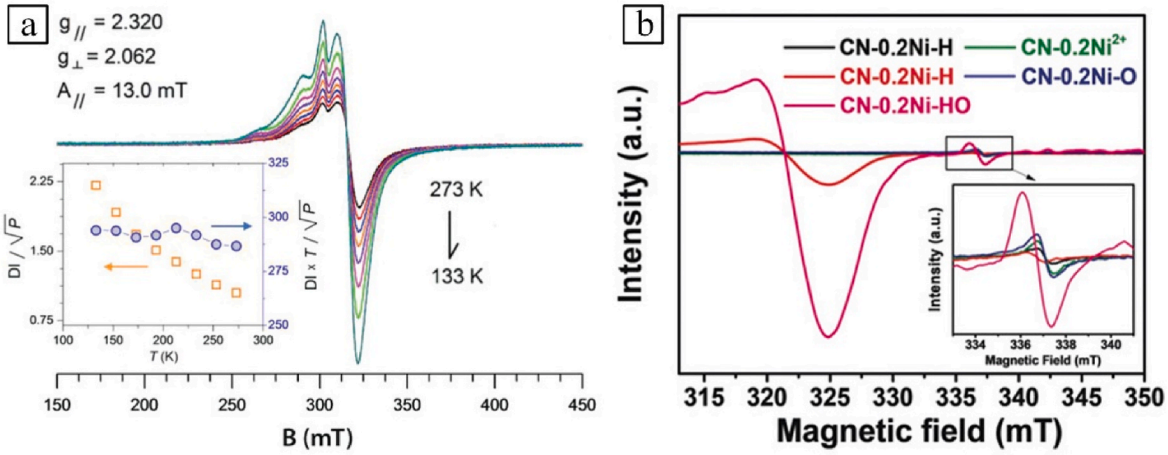

Fig. 15. (a) X-band of powder spectra of G(CN)–Cu catalyst in the temperature range of 0–140 °C [282] (adapted with permission from John Wiley & Sons, Inc.) and (b) ESP spectra of CN, CN-0.2Ni^{2+}, CN-0.2Ni–H, CN-0.2Ni–O and CN-0.2Ni–HO at 25 °C [283] (adapted with permission from John Wiley & Sons, Inc.).

mechanisms in different possible reactions. This section summarizes all the recent experimental activities of SACs including the operating conditions, type of reactors as well as catalyst loading that affect the yield and selectivity of the desired products. Besides that, the Computational DFT calculation which includes the binding energy, the electronic structure, and possible catalytic reaction routes of the SACs is also discussed. As known, the first-principles DFT calculations allow the investigations of the energetics of processes at the atomic-level with high precision and provide quantum mechanical-based insights into the related electronic structure of these processes and their influence on catalyst reactivity [289,290]. It is worth mentioning that not only well-understood catalyst mechanisms but also controversial hypotheses are cautiously discussed.

4.1. Selective coupling

The mechanistic fundamental questions of C–C coupling reactions on heterogeneous catalysts are still not fully understood and the metal active phases are debated [432,433]. This is because the atoms on the surface of NPs usually have different coordination numbers along with variable chemical environments (electronic effects) than those of their neighboring atoms which influences the catalytic activities [434,435]. Another relevant issue related to the use of NPs is the infeasibility of using high loadings of expensive noble metals, this reduces their attractiveness for bulk production. Thus, the synthesis of highly dispersed noble metal SACs as a catalyst is highly desirable as it could overcome this issue by maximizing the metal atomic efficiency, as well as reducing the catalyst cost [13,19]. However, single atoms are known for aggregation, leading to clusters and finally nanoparticles. In order to avoid their aggregation and induce stabilization of the single atoms, several methods have been proposed: a) the cascade anchoring strategy of the atom onto a metal oxide support [24,35]; b) a reductionist approach by alloying with other alloys to form an SAA [436,437]; or c) depositing single atoms into different oxide supports or organic frameworks for superior metal-support interactions [27,36,438]. As a whole, SACs are an attempt to bridge homogeneous and heterogeneous catalysis closer to understanding and revolutionizing the C–C coupling field.

4.1.1. Research advances of SACs in selective coupling reactions

The catalytic activity of a SAC depends closely on the nature of the active isolated metal atom and the presence of functional groups, if attached by linkers, the support used can also induce a significant electronic perturbation to the atomic active site for electron charge transfer. As a result, the single dispersed atoms of metal anchored on to a support surface are expected to have a reduced number of coordination sites for reactants or intermediates in comparison with metal NPs supported on a surface due to the absence of different active sites. More importantly, once the metal is anchored on a solid support, it can be easily regenerated for the next cycle of reaction without any complex treatment [17]. Table 4 outlines the applications of SACs in the C–C coupling process.

As proclaimed by Tao's group [284], the developed Pd-based SAC

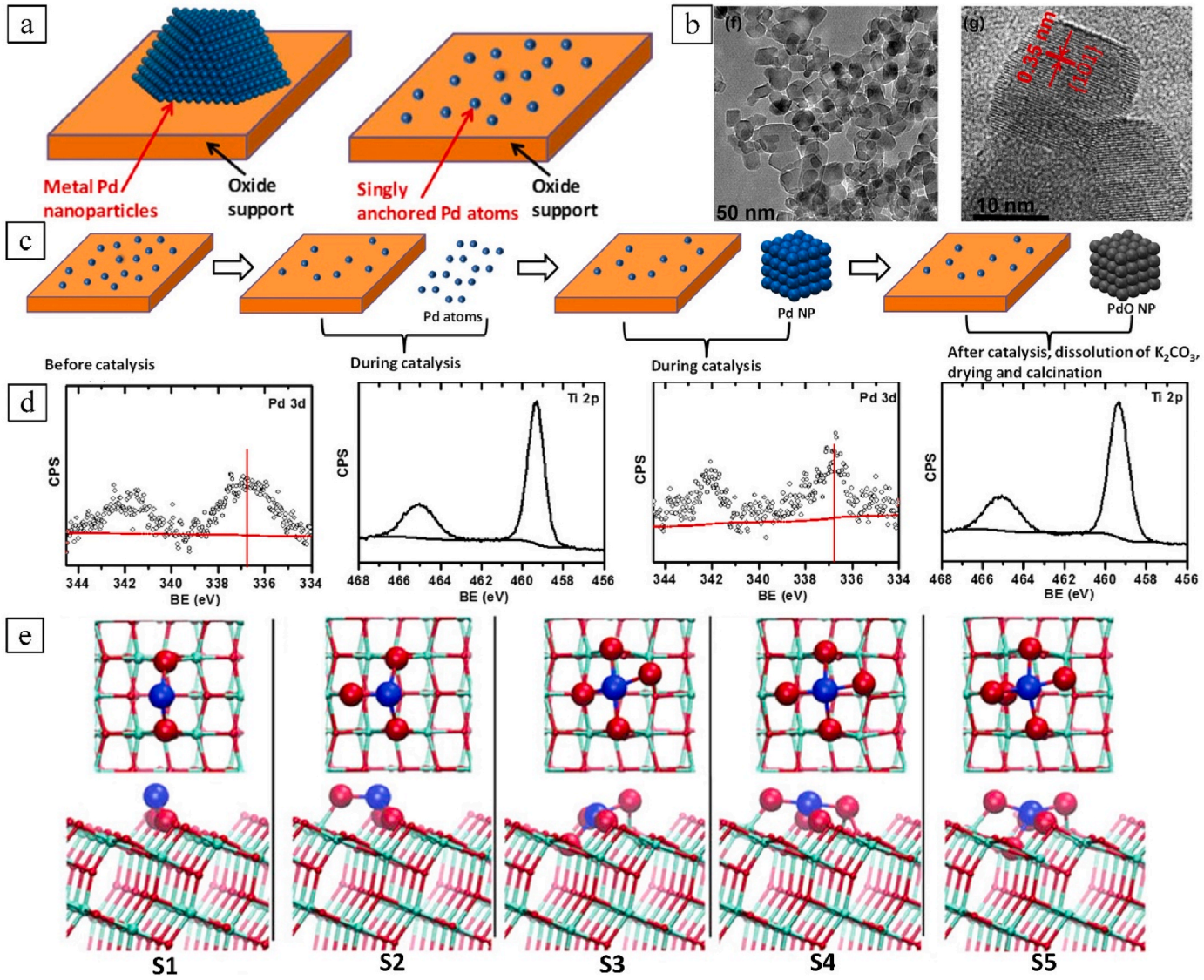

Fig. 16. Schematic representation showing the structural models of (a) Pd NP catalyst and Pd single-atom catalyst (Pd_1/TiO_2) [284], (b) TEM image of Pd_1/TiO_2 SAC (10 and 50 nm) [284], (c) Schematics showing (from left to right) Pd_1/TiO_2 SAC, detachment of Pd atoms during catalysis, forming Pd nanoclusters [284], (d) XPS spectra the Pd/TiO_2 before reaction and after reaction (left to right) [284] (all figures are adapted with permission from the American Chemistry Society).

anchored on TiO_2, Pd_1/TiO_2 *via* a deposition−precipitation method was highly selective and active for more than 10 C–C reaction cycles of phenylacetylene and iodobenzene (Fig. 16(a)). Based on XANES and EXAFS, the coordination of Pd atoms attached to TiO_2 was confirmed where each Pd atom is bound to four oxygen atoms of the TiO_2 surface support, forming PdO_4 units, and the exposed surface of the lattice fringe of the TiO_2 is (101) with an average TEM particle size of 20–25 nm (Fig. 16 (b)). To further explore the deactivation and detachment of Pd atoms from Pd_1/TiO_2 catalyst after the reaction (Fig. 16(c)), the authors have also performed the durability test of the spent Pd single atoms on a TiO_2 support by measuring the concentrations of Ti and Pd in a solution (after centrifugation), followed by characterization using XPS (Fig. 16 (d)). Surprisingly, the peak positions of Pd $3d_{5/2}$ were the same, indicating that the Pd atoms on TiO_2 supports have the same chemical oxidation state before and after the reaction. Regarding the deactivation study, the authors have performed a hot filtration-leaching analysis; notably, no metals were detected in the filtered solution, indicating the strong bonding between the Pd atoms (active sites) and TiO_2 (support). Moreover, computational investigations based on DFT calculation have also been carried out to identify the most thermodynamically favorable structure, which corresponds to Pd single atoms anchored to four oxygen atoms of TiO_2 through Pd–O–Ti bonds.

Lately, Chem and co-workers [441] reported a heterogeneous catalyst consisting of Pd single atoms anchored on exfoliated graphitic carbon nitride (Pd-ECN) for the C–C reaction of bromobenzene with phenylboronic acid pinacol ester while benchmarking with homogeneous and other bulk heterogeneous catalysts (Fig. 17 (a)). Microwave-assisted deposition was used in this study to deposit palladium on ECN, a pristine high-surface area form of graphitic carbon nitride. STEM coupled with EXAFS was used to investigate the presence of Pd single atoms, while XPS was adopted to study the electronic properties of the Pd atoms incorporated in the ECN. In addition, the DFT calculations were also carried out to understand the promising C–C coupling performance of Pd-ECN. Molecular dynamics simulations performed at different temperatures show that Pd atoms were confined within a given cavity, even though they still have some degree of freedom. This simulation evidence agreed with the experimental XPS observations, suggesting that the Pd atoms occupy two preferred positions: in the first one, Pd was located close to the surface plane, while in the second one, the metal was in between the two-top planes.

Table 2
Characterization techniques for bulk to nanoscale catalysts.

Catalysts	Primary techniques	Secondary techniques	Remarks
Single-atom catalyst (50-1 Å)	AC-STEM, XAS, IR, ICP-MS, STM, NAP-XPS,XANES, EXAFS	NMR, ORS, ESR, N_2 physisorption, TGA, chemisorption	a) Advantages • XAS is seen as a critical technique for proving if a SAC is present. This method can clearly show M–M bonding, if it is present in the EXAFS, there clusters or further. • Atomically resolved electron microscopy can elucidate the presence of a single atom, often due to differences in contrast between support and atom via dark field HAADF imaging. • Scanning Tunneling Microscopy has the ability to direct atoms across a surface by using the tip, this can allow for detailed observations of the adsorption/desorption of chemisorbed molecules. b) Limitation • Sustained time under an electron beam can cause atoms to agglomerate of cluster. • Low metal loadings and high dispersions can result in very long imaging times for electron microscopy. Not to mention contrast difficulties between support and single atom, especially if they are impregnated between lattices (d-spacing). • Due to low metal loadings, often the axial detection method is required for ICP, this can lead to a greater noise:signal ratio.
Nanoparticles (1–100 nm)	HR-TEM, IR, NAP-XPS,TPR/TPD/TPO	ICP-MS, ESR, XAS, N_2 physisorption, TGA, NMR	a) Advantages • Standard transmission electron microscopy can easily image down to 2/3 nm for an unsupported nanoparticle. • Bulk nanoparticles often have metal loadings >1 wt.% which means that standard radial detection can be used. • For XAS data you expect to see M–M bonding so it is easier to assign with reference materials than single atom equivalents. b) Limitation • Unless there is a clear difference in contrast between the nanoparticle and support, often an aberration-corrected transmission electron microscope is still required for nanoparticles <3 nm. • For nanoparticles of sufficient size, differentiating them from individual particles can be difficult as they will appear agglomerated or of similar size as the support itself. • Nanoparticles of size larger than pores in a support material will either block the pore or ultimately lower the surface area and measurable porosity of the material.
Bulk catalyst (1–100 μm)	TEM, FEG-SEM, TGA, N_2 physisorption, N_2O chemisorption, TPR/D	IR, ICP-MS, NAP-XPS, TGA,	a) Advantages • Bulk materials are very easy to process using scanning electron microscopy as you can images from the mm → μm scale. • Bulk generated materials are often made at scale so obtaining representative samples for ICP and TGA are possible for statistical analysis. b) Limitation • Active site analysis can be problematic if particles are large (>20 nm), this can often lead to particle agglomeration.

In the reaction mechanism, the first step corresponds to the molecular adsorption of bromobenzene to the metal center and the consequent change of the Pd coordination number. The authors reported that the ability of Pd to change its coordination is crucial to the observed catalytic performance. In the second step, bi-hydrated potassium phenylboronic acid pinacol ester was adsorbed, and the cation from the salt occupied the nearest neighbor empty cavity. Thanks to the displacement of Br^-, phenylboronic acid pinacol ester coordinates, the subsequent trans-metalation was found to be the rate-determining step of the overall reaction (Fig. 17(b and c)). After the elimination of the boronic pinacol ester, the new C–C bond was formed. The elimination of the product restores the initial coordination of the Pd atom. Even though the overall reaction mechanism catalyzed by Pd-ECN reflects that reported for Pd $(PPh_3)_4$ molecular catalyst, in the latter case the role of the ligands is crucial: the elimination of two ligands occurs prior to the reaction, and it opens the coordination sphere of Pd, allowing the coordination of the substrate. A third ligand was then released during the trans-metalation step.

As mentioned above, heterogeneous alloyed SACs or known as SAA can be prepared using two metals, *via* isolation of the single metal atom by another metal atom. The synergistic effect between the two metals will alter the geometric and electronic structures of alloyed SACs, potentially inducing exceptional catalytic performance for various reactions [22,443]. Zhang and co-workers [42] have reported a durable and efficient Au -Pd SAA for the Ullmann reaction of aryl halides in water. The investigated Pd-based SAC exhibited an excellent Ullman coupling activity, not only of aryl bromides and iodides but also of the less reactive aryl chlorides. As known, aryl chlorides are less expensive, readily available, and more sustainable than their analogous aryl bromides and iodides. For this reason, their utilization as substrates is highly desirable. However, in the literature, only a few examples of Pd NP catalysts were reported to be worked well with aryl, but the bi-metallic SAA presented by Zhang and collaborators furnishes a valid alternative. The Au–Pd SAA was prepared with an ion exchange-$NaBH_4$ reduction method, and the presents of Pd single atoms were isolated by the Au atoms as confirmed by the EXAFS and DRIFTS analysis. The DRIFTS result was in good agreement with the EXAFS result, indicating that the Au alloyed Pd single atom configuration was formed at Au/Pd $\geq$ 4. Remarkably, the Au–Pd SAA managed to convert ~90% of aryl without deactivation over the course of eight cycles.

Another class of C–C coupling reaction includes the hydroformylation of olefins to produce aldehydes, which are important intermediates to produce other chemicals. Wang et al. [207], have recently developed CoO-supported Rh single-atom catalysts (Rh/CoO) with remarkable selectivity towards propene hydroformylation. The authors investigated the yield and selectivity of butyraldehyde by increasing the Rh weight loading (e.g., 0.2, 1.0, and 4.8 wt.%). The highest turnover frequency (TOF) number of 2065 h^{-1} and selectivity of

94.4% for butyraldehyde were obtained when the catalyst with the lowest Rh weight loading. Furthermore, the stability of 0.2% Rh/CoO was also studied by recycling the catalyst five times. Over the cycles, the catalyst remained highly active, similar to the initial reaction, the selectivity slightly decreased to 94.0% by the final cycle. To further understand the facilitation and adsorption of propene on Rh single sites in an atmosphere containing both H_2 and CO (syngas), a DFT investigation was performed. The DFT calculations showed indeed that after the adsorption of H_2 and CO, Rh atoms moved from the original lattice position, leading to a reconstruction of Rh active atoms that facilitate the adsorption of propene. Furthermore, DFT calculations also showed dissociative adsorption of the H_2 molecule, leading to the formation of an OH group on the CoO surface, while CO preferentially binds to the Rh active site, due to the strong interaction with Rh single atoms. DFT was also used to investigate the reaction mechanism that proceeds through three consecutive steps: a) one of the adsorbed H atoms will attack the C═C bond in the adsorbed propene molecule; b) CO will insert into the opened C═C bond; and c) the second adsorbed hydrogen atom will then combine with the C atom in the reactively formed terminal C═O to form the final product. The remarkable activity and selectivity, and high stability of 0.2% Rh/CoO are of high importance for potential applications in industrial processes by reducing the cost and pollution efficiently. Another remarkable example from Zhang's group, thermally stable Rh-based SACs which favor the hydroformylation of olefins has been synthesized [39]. Notably, the Rh_1/ZnO SAC has demonstrated a very high TON of 40,000 with 99% selectivity towards aldehyde products, which is to our knowledge the largest value among reported heterogeneous metal catalysts. This level of selectivity has not been previously reported for Rh, without the use of specific support materials such as polymers (ligand steric effects), or zeolites (confinement effects), adding great impact and benefit to the SACs. Also, the fabricated SAC has shown a high stability profile in terms of recycling, where no obvious leaching or aggregation of Rh active metals were observed after a 4^{th} run of experiments.

As shown in Table 2, all the examples mentioned imply that SACs can be a valid alternative to bridge both homogenous and heterogeneous catalysts for C–C coupling reactions. However, the development of SACs with notably improved performances relies on the contribution of both theoretical and experimental investigations. DFT methods can be applied to investigate crucial aspects that are not directly accessible by experiments, such as the nature of the active sites of different SACs and the ways substrate molecules interact with single atoms [444]. Overall, the electronic metal-support strong interactions are a critical concern to increase the catalytic performance of coupling, and thus, modulation of the charge density of anchored single metal atoms should be emphasized in future research.

4.2. Selective hydrogenation

Selective hydrogenation represents essential processes in the organometallic chemistry process, particularly in the petrochemical and fine chemical industries. For petrochemicals, selective hydrogenation is the most common route to eliminate the impurities such as alkynes and dienes in the ethylene industry for downstream polymerization [445]. Meanwhile, in the pharmaceutical industry, alkenyl, carbonyl, and carboxyl functional groups of the feedstock are required to be selectively reduced through H_2 to their corresponding alkenes, alcohols, and amine products which are key intermediates for fine chemicals production [446]. Notably, a quarter of the chemical industrial processes include at least one hydrogenation step, and therefore it is not surprising that the selective hydrogenation reaction is one of the hot topics investigated in the catalysis field [447]. However, it is a challenging task when two or multiple functional groups coexist in the substrate and also, the hydrogenation of C═C bonds is much easier than that of the C═O bonds, thermodynamically favored by 35 kJ/mol [448].

A new generation of catalysts for selective hydrogenation reactions has been developed to tackle the challenges by introducing the "active site isolation" strategy. Atom assemblies and isolation techniques can exhibit different physicochemical properties in altering different hydrogenation mechanisms and show a better catalytic hydrogenation activity compared to NP counterparts [449,450]. Lately, SACs have also been widely applied in the selective hydrogenation of styrene, acetylene, glycerol, crotonaldehyde, and nitriles; mainly attributed to lowering the activation barriers, governing catalytic reactivity, enhancing the adsorption model, and also possessing uniform single active sites [213,451]. For example, isolated Pd atoms on a Cu surface lower the reaction barriers of both hydrogen uptake and subsequent desorption from the Cu metal surface, enhancing the selectivity of styrene hydrogenation [22]. Meanwhile, anchoring single Rh (Rh_1) atoms to Mo edge vacancy sites of 2-dimensional MoS_2 could also facilitate the H_2 dissociation in hydrogenation [401]. There are also studies reporting that encapsulating Ni atoms with transition metals can improve covalent chemical bonding, owing to the inherent vulnerability of nickel-based SACs under acidic hydrogenation conditions [452].

4.2.1. Research advances of SACs used for selective hydrogenation

A comprehensive summary of the catalytic performances of different SACs for selective hydrogenation reactions is listed in Table 5. Although the operational conditions, reactor configuration, catalyst loading, temperature, and pressure may vary greatly, it has been shown that a low Pt loading can be incorporated into graphite shells, generating 'carbon onions' (Pt/C) via an arc-discharge method. This was found to provide remarkable conversion and reaction selectivity, comparable with other hydrogenation SACs [453]. Notably, the Pt@C exhibits a high catalytic reactivity and stability towards the chemo-selective hydrogenation of functionalized nitroarenes under mild reaction conditions. High selectivity of p-chloroaniline at >99% was obtained using EtOH under optimized reaction conditions, 40 °C, 1.0 bar of H_2 pressure, 40 mg of catalyst loading, and 1 h reaction time. On top of that, the synthesized Pt/C catalyst displays a superior reusability performance over at least 10 cycles and without any loss in hydrogenation activity and selectivity, suggesting that the graphitic shells of carbon 'onions' prohibited a chemical coarsening of the Pt single atoms, which alters the effective penetration channels for the transport of ions and electrons during the catalytic reaction [453]. The proposed encapsulated graphite shells of the SAC were also processed using HRTEM images (Fig. 18 (a–c)), with a well-distributed Pt(111) interplanar size of 0.255 nm. This clearly shows the effect of arc medium concentration, where Fig. 18 (a) utilizes a 0.975 mM salt which generates Pt nanoparticles, whereas an arc medium concentration of 0.0195 mM created a dispersed catalyst that was atomically resolved (Fig. 18 (b)). The x-ray diffractograms in Fig. 18 (d), clearly show that the Pt SAC does not have a (111) feature, contrary to the Pt NP catalyst.

Lately, Zhang and colleagues [198] have studied the anchoring effect of mesoporous γ-Al_2O_3 on Pt atoms, likely on the catalyst's stability through unsaturated pentahedral Al^{3+} coordination for the hydrogenation of a ketone. The superior catalytic activity highlights the applicability of the catalyst for hydrogenation reactions in a small amount of Pt species loadings on Al_2O_3. As reported in a previous study, aromatic rings normally coordinate with multiple metal atoms before undergoing hydrogenation and remain to interact with the metal surface during stepwise hydrogenation [457]. However, the proposed mechanism is not possible for SACs as found in this study [456] where the hydrogenation ring on Pt/Al_2O_3 is almost fully suppressed. Alternatively, the Pt species favors C═O bond adsorption and activation forming an η1(O) configuration [458,459]. In the η1(O) configuration, the acetophenone will be adsorbed on to a Pt single-atom site for reacting with H_2 to form 1-phenylethanol. Then, the intermediate product transfers to the Al_2O_3 support where it is strongly bound before desorbing into the solution phase, suppressing the deactivation of a Pt site, and enhancing the reusability of the catalyst for the next cycle. A similar result has been obtained by Lucci et al. [257] in which the synthesized Pt/Cu(111) SAA can be

Table 3
Summary of reported SACs, synthesis, structure, and applications.

Metal	Support	Synthesis method	Reaction
Pt	• Al_2O_3 [37,158,291–294] • Carbon/Graphene [27,49,51,53,58,103,134,179,225,295,296] • CeO_2 [297] • FeO_x [19,24,29,35,38,87] • Molybdenum carbide [213] • SnO_2 [234] • SiO_2 [158,298] • TiN [48] • TiO_2 [220,293] • ZrO_2 [299] • ZnO [220]	• ALD [27,53,179,300] • Co-precipitation [19,24,29,35,38,68] • Deposition–precipitation [301] • Ice-photochemical process [225] • IWI [48,51,298,302–305] • Mass-selected soft-landing [234,237] • Mechanical milling [294] • Micro-gas blasting [306] • Pyrolysis-assisted [293,297] • SEA [153,158–161,163] • Sol–gel [37,291] • Thermal emitting strategy [103] • Ultra-high temperature-assisted strategy [134,213] • Wet impregnation [49,291,299,307]	• CO oxidation [19,27,37,68,87,158–160,291,294,297,303] • CO_2RR [299] • Dehydrogenation [307] • Ethanol oxidation [234] • Formaldehyde oxidation [301] • HER [51,53,103,179,225,300] • Hydrochlorination [296] • Hydrogenation [35,52,134,213,298] • Methanol decomposition [302] • NO reduction [38] • ORR [48,49] • Reduction of triiodide [29] • WGS reaction [24,306]
Pd	• Al_2O_3 [308,309] • Carbon/Graphene [36,58,103,218] • CeO_2 [306,310,311] • FeO_x [312,313] • Hydroxyapatite [163] • Ion exchange resin [42] • MgO [235,314] • MnO_2 [315] • $Ni(OH)_2$ • SiO_2 [44,316] • TiO_2 [102,181,238,317] • ZnO [169] • ZrO_2 [311,318]	• ALD [36,181] • Ball-milling [319] • Co-precipitation [312,313] • Ion-exchange reduction method [42] • IWI [42,44,295,309,310] • Low temperature-induced Strategy [218,219] • Mass-selected soft-landing [235,238] • Micro-gas blasting [306] • One-pot hydrothermal process [315] • Photochemical method [102] • Pyrolysis-assisted method [318,320] • SEA [163] • Thermal emitting strategy [103] • Ultra-high temperature-assisted strategy [134] • Wet impregnation [308,309,311,316,321]	• Alcohol oxidation [320] • Benzene oxidation [321] • C_6H_6 formation [219,235,295,314] • CO oxidation [41,87,169,238,308,310,312] • CO_2RR [314] • HER [103,316] • Hydrochlorination [295] • Hydrodechlorination [311] • Hydrogenation [22,36,44,102,163,169,317,318,322] • Methanol decomposition [181] • NO reduction [309] • OER [219,315] • ORR [219,315,322,323] • Ullmann reaction [42]
Ir	• Carbon [295] • CMK [324] • $Co(OH)_2$ [106] • CoO_x [306] • FeO_x [24,324] • Fe_2O_3 [227] • Fe_3O_4 [325] • $MgAl_2O_4$ [326] • NiFeP [327] • NiMnO [328] • NiO [306] • Porous organic polymer [245] • WO_3 [329] • ZIF [245,247,330]	• Atom trapping [326] • Co-precipitation [24,324] • Electrochemical method [106] • Facile method [327] • IWI [245,295] • Micro-gas blasting [306] • Photochemical method [227,329] • Pyrolysis-assisted method [247,330] • Mass-selected soft-land [325] • Wet impregnation [328,331]	• CO Oxidation [24] • HER [106] • Hydrochlorination [295] • Hydrogenation [245,331] • N_2O decomposition [326] • ORR [330] • OER [106,247,323,327] • Solar water oxidation [227,329] • WGS reaction [24,306,324]
Au	• Carbon/Graphene [103,295] • Carbon nitride [332,333] • CeO_2 [100,334–336] • Co_3O_4 [337] • FeO_x [41,87,335,338] • CuO [339] • NiO [191] • Ni_2P [340] • TiO_2 [192,239,341,342] • WO_3 [343]	• Ball milling [100] • Co-precipitation [338] • Deposition–precipitation [191,337,339] • Facile method [333,335] • High temperature-induced method [340] • IWI [295,342] • Mass-selected soft-landing [239] • Photochemical method [343] • Pyrolysis-assisted method [334] • Solution plasma process [336] • Thermal emitting Strategy [103]	• CO oxidation [191,239,338,339] • CO_2RR [332,344] • HER [103] • Hydrochlorination [295] • Methane oxidation [343] • Methanol self-coupling reaction [342] • PROX [100,335] • OER [333,340] • ORR [333] • WGS reaction [192,334]
Fe	• Ag_2O [345] • Al_2O_3 [345] • Carbon/Graphene [79,236,346–353] • Carbon nitride [318,354–356] • CeO_2 [345] • SiO_2 [61,357] • TiO_2 [86,357,358] • Triazine-based framework [359] • WO_3 [360] • ZnO [345,361] • ZrO_2 [86]	• ALD [357,358] • Ball milling [353] • Co-precipitation [347] • Facile method [362] • Ion-exchange method [86] • Mass-selected soft-landing [236] • Molten salt-assisted method [354] • Pyrolysis-assisted method [79,345,346,348–350,356,363] • Sol–gel method [361] • Wet impregnation [352,355,360]	• Advanced oxidation processes [356] • CO oxidation [87,357] • CO_2RR [351,354] • CS_2 conversion [345] • Fenton-like reaction [362,363] • Fischer-Tropsch [355] • HER [350] • Hydrogenation [86,346,347,353,364] • Methane-to-ethylene conversion [61] • N_2 photofixation [349] • Nitrogen reduction [347] • NO reduction [347,360] • OER [236] • ORR [79,236,323,332,348,361] • Peroxidase-like activity [358] • Tetramethylbenzidine oxidation [352]
Ni	• Carbon/Graphene [74,101,143,214,230,236,353] • Carbon nitride [101,365–367] • CeO_2 [368] • Hydroxyapatite [369,370]	• Ball milling [353] • Coordination site strategy [370] • Co-precipitation [368] • Electrochemical method [230]	• CO_2 methanation [220] • CO_2RR [74,101] • Cross-coupling [367] • Dry reforming [164,368,369,371]

(*continued on next page*)

Table 3 (*continued*)

Metal	Support	Synthesis method	Reaction
	• MgO [149] • TiO_2 [370] • Y_2O_3 [220] • ZnO [361] • ZrO_2 [86]	• Facile method [371] • Ion-exchange method [86] • Low temperature-induced strategy [220] • Mass-selected soft-landing [236] • Microwave-assisted method [367] • Pyrolysis-assisted method [101] • SEA [164,369] • Sol–gel method [361] • Solvothermal method [365] • Thermal emitting strategy [214] • Wet impregnation [74,143,366]	• HER [143,230,370,372] • Hydrogenation [86,149,220,353,373] • OER [101,236] • ORR [101,214,236,323,361,374] • Photoredox process [366] • Water splitting [365]
Ru	• Al_2O_3 [375,376] • Carbon [57,295,377,378] • Carbon nitride [86,379,380] • CeO_2 [182,368,381,382] • CoV layered double hydroxide [383] • FeO_x [384] • Fe_3O_4 [385,386] • NiFe [148] • PtNi [184] • TiO_2 [182,387,388] • ZnO [389] • ZrO_2 [390]	• ALD [184] • Ball-milling method [319] • Coprecipitation [148,384] • Coordination Site Strategy [381] • Electrochemical method [383] • Facile method [375] • Hydrothermal treatment [376,379,386] • Ion-exchange method [182,387] • IWI [295,377,388] • Low temperature-induced strategy [389] • Photochemical method [391] • Pyrolysis-assisted method [377] • Sol–gel method [385] • Wet impregnation [378,380,382,390]	• CO oxidation [319] • CO_2RR [378] • Dichloroethane degradation [375] • Dry reforming [368] • Haber-Bosch process [382] • HER [182,379,386,387] • Hydrazine electrooxidation [148] • Hydrochlorination [295] • Hydrogenation [376,385] • Hydrosilylation [381,390] • Methanol oxidation [184] • N_2 fixation [380,388] • N_2 reduction [57] • OER [377,383] • ORR [391] • Reductive catalytic fractionation [389] • WGS reaction [384]
Rh	• Al_2O_3 [392–395] • Carbon [295] • CeO_2 [381,396–398] • Co_3O_4 [25,40] • Heteropoly acid [162] • Hydroxyapatite [399] • MnO_2 [400] • MoS_2 [401] • Phosphotungstic acid [162] • SiO_2 [402] • TiO_2 [394,403] • ZMS-5 zeolite [404] • $ZnO^{91,}$ [405]	• Ball-milling method [319] • Coordination site strategy [381] • Co-precipitation [399] • Deposition–precipitation [402,403] • Facile method [405] • Ion-exchange method [40] • IWI [295,392,393,400,403,404] • SEA [162,394] • Wet impregnation [25,395,397,398]	• CO oxidation [41,87,162,405] • Hydrochlorination [295] • Hydroformylation [399] • Hydrogenation [364,393,394,397,398,401,404] • Hydrosilylation [381] • Methane oxidation • Nitrogen reduction [400] • NO reduction [25,392,396] • OER [40] • WGS [402,403]
Cu	• Al_2O_3 [250,395,406,407] • Carbon/Graphene [214,408–412] • Carbon Nitride [374,413–417] • Cr_2O_3 [406] • MnO_2 [418] • TiO_2 [86,419] • ZrO_2 [86,420] • ZnO [361]	• Ball milling [353] • Co-precipitation [420] • Evaporation-induced self-assembly method [250] • Hydrothermal method [418,421] • Ion-exchange method [86,416] • Photochemical method [411] • Pyrolysis-assisted method [414,419,422] • Sol–gel method [361] • SEA [406] • Thermal emitting strategy [214,408] • Wet impregnation [374,395,407,413,415,417]	• CO oxidation [418] • CO_2RR [406] • Glaser-Hay Coupling [409] • HER [413] • Homoallyborane synthesis [250] • Hydrogenation [86,353,407,420] • Hydrogen peroxide reduction [417] • Methane oxidation [415] • Nitrile-azide cycloaddition [416] • OER [421] • ORR [214,361,374,408,421,422] • Tetracycline degradation [414]
Co	• Al_2O_3 [321] • Carbon/Graphene [59,177,236,353,423] • Carbon nitride [424,425] • MnO_2 [424] • MoS_2 [426] • N_3P_1 site [427] • SiO_2 [426,428] • TiO_2 [426] • ZnO [361]	• ALD [423] • Ball milling [353] • Electrochemical method [425] • Freeze-drying method [59] • Mass-selected soft-landing [236] • Pyrolysis-assisted method [211,426,427,429,430] • Redox-driven hydrolysis [431] • Sol–gel method [361] • Thermal emitting strategy [214] • Thermal polymerization [424] • Wet impregnation [321,426,428]'	• Benzene oxidation [321] • CO_2RR [351,429] • Fenton-like reaction [424] • HER [425] • Hydrogenation [347,353,423,427] • Methane oxidation [428] • Nitrogen reduction [347] • OER [236,426] • ORR [214,236,361] • Toluene oxidation [431]

reused more than six times TPD cycles with constant selectivity of butadiene to butene (~25%) as shown in Fig. 19(a) [257]. Further quantification of Pt atoms through CO titration after each run has highlighted the durability of Pt/Cu(111) SAC where the concentration of Pt atoms on the surface layer of the catalyst remained consistent with the number of Pt atoms present prior to each hydrogenation reaction, suggesting that the single isolated Pt atoms in Cu are capable of H_2 spillover without breaking C–C bonds as well as reduce the possibility of Pt poisoning. As seen in Fig. 19(b), the addition of Pt onto Cu NPs enhanced the rate of hydrogenation, where a higher hydrogenation activity was observed in $Pt_{0.2}Cu_{14}/Al_2O_3$ than $Pt_{0.1}Cu_{14}/Al_2O_3$. Additionally, the addition of Pt single atoms to the catalyst could lower the hydrogenation reaction temperature (onset at 40 °C), which is 35 °C, i.e., lower than that of the monometallic Cu_{15}/Al_2O_3 catalyst under the same conditions. In order to demonstrate the hydrogenation capability of the Pt–Cu SAC in different stressful conditions (with impurities), the authors tested the SAC in the presence of excess propylene and found that the propylene has no significant effect on the activity and selectivity of hydrogenation

Table 4
Application of SACs in C–C coupling process.

Types of Reaction Mechanism	Reaction conditions	Synthesizing method	Key Takeaways	Ref.
Coupling between iodobenzene and Phenylacetylene to biphenyl.	**Type of catalyst**: 0.10, 0.20, 2.0 wt.% Pd/TiO_2 **Type of reactor**: Batch **Catalyst loading**:50 mg **Reaction temperature**: 40 °C **Reaction pressure**: -	Deposition precipitation	The highly dispersed Pd atoms (Pd_1/TiO_2) were 10 times more active than the conventional Sonogashira cross-coupling reaction. Pd_1 atoms anchored to four O atoms of TiO_2 through Pd– O–Ti bonds are thermodynamically favorable due to a minimal number of choices of binding sites for reactants. The 2.0 wt.% Pd/TiO_2 exhibits nearly 100% conversion with a >75% selectivity.	[284]
Suzuki coupling reaction of -iodoanisole (5 mmol), 4-methylbenzene boronic acid to 4-Methoxy-4′-methylbiphenyl	**Type of catalyst**: 0.35 mol.% of Pt or Pd in Pt–S-MWNT and Pd–S-MWNT **Type of reactor**: Batch **Catalyst loading**: - **Reaction temperature**: 70 °C **Reaction pressure**: -	Conventional chemical vapor deposition (CVD)	Higher catalytic activity was obtained in Pt–S-MWNT (~2–30 times) compared with the commercial Pt/C, and Pd/C metallic catalysts. A high reaction yield of 99.5% was attained in Pt–S-MWNT about 6 times higher value than the Pd–S-MWNT. High stability of Pt–S-MWNT can be observed where the yield of products maintained >80% after 12 cycles.	[439]
Hydroformylation coupling of propene to butyraldehyde	**Type of catalyst**: 0.2, 1.0, and 4.8 wt.% Rh/CoO **Type of reactor**: Fixed Bed Reactor **Catalyst loading**: 50, 10, and 2.1 mg **Reaction temperature**: 100 °C **Reaction pressure**: -	Galvanic replacement reaction	The structural reconstruction of Rh single atoms in Rh/CoO was the main driving force facilitating the adsorption and activation of reactants. A high TOF number of 2065 h^{-1} with 94.4% selectivity for butyraldehyde were attained using 0.2% Rh/CoO. The increase in Rh loading caused aggregation of the isolated Rh atoms to form nanoclusters of different atomicity.	[207]
Non-oxidative methane coupling to acetylene and ethylene	**Type of catalyst**: SiO_2-confined Fe catalyst (0.4 wt.% Fe@CRS) **Type of reactor**: Fixed bed reactor **Catalyst loading**: 0–1.2 g **Reaction temperature**: 1027 °C **Reaction pressure**: 1 bar	Ball milling	The CH_4 consumption rate monotonically was directly proportional to the reaction temperature at a fixed $\cdot CH_3$ partial pressure. Fe@CRS mediated the C–C coupling reaction at a low temperature, thereby producing mainly acetylene rather than ethylene. At 1027 °C onwards, the CH_4 conversion and acetylene selectivity increased significantly withFe@CRS catalyst residence time.	[440]
Suzuki coupling reaction of -bromobenzene with phenylboronic acid pinacol ester to biphenyl	**Type of catalyst**: 0.66 wt.% Pd-ECN **Type of reactor**: Fixed bed reactor **Catalyst loading**: 30 mg **Reaction temperature**: 50–140 °C **Reaction pressure**: 2–10 bar	Microwave irradiation assisted deposition	No variation of conversion or selectivity was observed over 13 h on stream, indicating that Pd-ECN lies in a stable structure with leaching resistance. The pivotal role of the CN was to enable adaptive coordination of the Pd. The isolated Pd atoms showed superior yields to the desired products (24–73%), and outperformed other homogeneous Pd $(PPh_3)_4$ counterparts.	[441]
C–C coupling of primary and secondary alcohols to α,β-unsaturated ketones	**Type of catalyst**: Co_{1mmol}−N–C/CMK **Type of reactor**: Batch **Catalyst loading**: - **Reaction temperature**: 70 °C **Reaction pressure**: 1bar	Pyrolysis + ball milling	A high TOF (3.8 s^{-1}) was achieved on the Co atom, outperforming other counterparts (e.g. Pd/C, Ag/Al_2O_3, and Au–Pd/hydrotalcite). Co single atoms in the Co–N–C structure were highly stable against sintering and acid leaching even at high temperature of 800 °C. 71% yield of unsaturated ketones was attained using Co–N–C/CMK after 6 h of reaction.	[60]
Selective C–C Coupling in CO_2 Electroreduction for CO production	**Type of catalyst**: Ni_{1mmol}/CNT **Type of reactor**: Batch **Catalyst loading**: - **Reaction temperature**: 25 °C **Reaction pressure**: 1bar	Pyrolysis	A high TOF number of 100,179 h^{-1} with high stability (>100 h) were attained. The CO_2 reactant did not chemically interact with Ni-CNT and the, Ni center in Ni-CNT maintained its +2-valence state during the process, suggesting the oxidation of Ni^{+} to Ni^{2+} during interaction with CO_2 molecules. A uniform morphology and well-defined $Ni–N_4$ moiety on a carbon nanotube was successfully developed.	[442]

to butadiene as displayed in Fig. 19(c). At below 120 °C, ~100% of butadiene was converted accompanied by a minor propylene concentration (<1%) converting to propane, implying that the Pt–Cu SAC maintains active and is stable. The use of Pt in Cu NPs (Pt_1Cu_{20}/Al_2O_3) has also been shown recently for the liquid phase hydrogenation of furfural, here a promoted Cu nanoparticle was found to be far more active and selective than bulk bimetallic alloys and monometallic equivalents [249]. Additionally, for the same reaction, an array PdCu SAA was created by Islam and co-workers, with decreasing Pd content to determine the atomic limit required for efficient hydrogenation [46], critically finding that 0.0067 wt% of Pd could be used to radically improve the reactivity of a Cu host nanoparticle on γ-Al_2O_3. Another work using a Pd–Cu SAA is by Jiang and co-workers [454]. This work exploited the change in the structure coordination during the impregnation of ultra-low Pd loading (50 ppm) in a host Cu nanoparticle. They found that the Pd_1/Cu SAC is highly effective for both hydrogen spillover and selective hydrogenation. Notably, The Pd_1/Cu catalysts displayed excellent catalytic performances in the semi-hydrogenation of phenylacetylene to styrene at 303 K under 0.1 MPa H_2. The selectivity of ~96% towards styrene was achieved at a conversion of 100%. This work was supported by DFT calculations which highlights the benefit of atom arrangement on the activity of the catalyst itself, globally finding the rate of reaction for Pd–Cu (111) was substantially lower than a Pd–Cu(100).

There is another interesting well-dispersed single/pseudo Pt SAC catalyst impregnated on mesoporous WO_x developed by Zhang's group [460]. Under the reaction conditions of 160 °C, 1 MPa H_2 pressure, and a high glycerol concentration (50%), the Pt/WO_x SAC processed a very

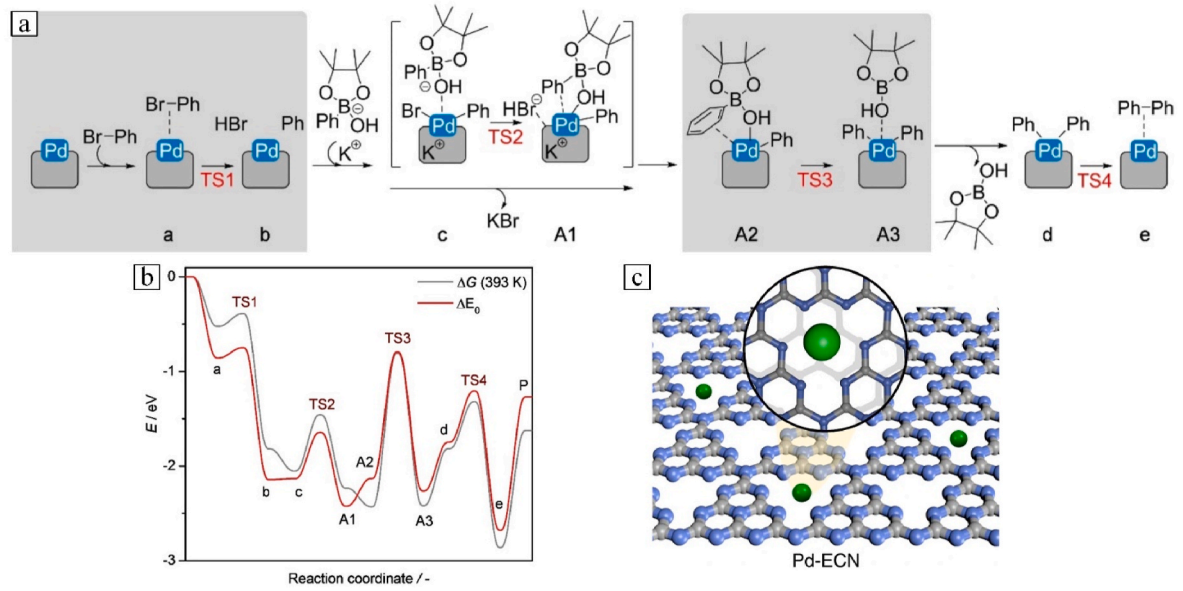

Fig. 17. (a) Reaction pathways of the Suzuki coupling of bromobenzene with phenylboronic acid pinacol ester on Pd-ECN [441], (b) Corresponding energy level and reaction coordinate of reaction pathway [441], (c) Schematic illustration of the palladium atom anchored on exfoliated graphitic carbon nitride (Pd-ECN) SAC [441]. (all figures are adapted with permission from Springer Nature).

high space-time yield (3.78 g_{Pt}^{-1} h^{-1}) towards 1,3-propanediol (1,3 PD) as shown in Fig. 20(a). Based on the transition of the catalyst in preparation (Fig. 20(b–d)), a well homogenously dispersed Pt atom of 2.59 wt % was impregnated on WO_3 support without any formation of nanoclusters, suggesting that the isolation of Pt over WO_x was successfully achieved. To further understand the physiochemical property of SACs a mechanism for how the Pt/WO_x SAC behaves for the selective glycerol hydrogenation was proposed in Fig. 20(e), [460]. Firstly, the unshared-pair of electrons in the glycerol's O atoms was trapped by the unoccupied W^{6+} d orbital, forming an ether-like bond with a W atom (Step 1). The strong interaction with the W atom will weaken the bond between the O and H atoms and facilitate the oxidation of an H atom (Step 2). Then, extraction of protons from the terminal O atom of W═O occurred and formed W–OH, while the W^{6+} species was partially reduced (Step 3). This finding was proven by Raman spectroscopy, where the terminal W═O band intensity decreased significantly after contacting with glycerol. In step 4, the WO_x Brønsted acid sites were consumed, catalyzing the dehydration pathway and stabilizing the formation of the secondary carbocation from glycerol. Owing to the oxophilic characteristic of W species, the H_2 is assumed to be heterolytically dissociated on the interface between Pt and WO_x, exhibiting both acid sites ($H^{\delta+}$) and hydrogenation sites ($H^{\delta-}$). Thus, rapid hydrogenation of 3-hydroxypicolinic acid can occur and gives rise to a high yield of 1,3-PD (Step 5). This study provided an in-depth synergistic mechanism between Pt and WO_x species for the production of 1,3-PD. The design of the WO_x supported pseudo-single atom Pt catalyst yielded a high selectivity of 1,3-PD (45.7%) under a low H_2 pressure environment.

Despite many experimental works reported on the robust nature of the SACs for selective hydrogenation reactions, there is still a lack of molecular calculations and microkinetic simulations to back up the hydrogenation activity and mechanisms [463–465]. In 2018, Thirumalai and co-authors [461] reported the reactivity of a series SAAs consisting of Au, Ag, and Cu nanoparticles doped with single atoms of Pt, Pd, Ir, Rh, and Ni in the hydrogenation of acetylene to ethylene *via* DFT calculations. They reported that from the d-band model generated by Hammer and Nørskov, AuPd and AgPd were chosen as the potential candidate for hydrogenation. The findings indicate that the acetylene most likely adsorbs at the FCC sites of AuPd and AgPd. By comparing the binding energies of acetylene at the FCC site and atop sites, it reveals that acetylene was less stable on the atop sites by 0.111 eV for AuPd and 0.008 eV for AgPd, meanwhile the ethylene adsorption at the FCC sites and atop sites differ by 0.23 eV for AuPd and 0.019 eV for AgPd. Notably, the acetylene and ethylene prefer bonding as α-bonded complexes on pure metal surfaces. However, in the presence of a reactive Pd atom in a relatively inert host, they bind strongly with the surface through α-complexes in an atop conformation. Furthermore, the energetics of hydrogenation is more favorable for single atom alloys rather than their respective pure host metals (Fig. 20(f)), deducing that the single atom alloys are favorable for the formation of the vinyl intermediate, attributing to the strong adsorption on the Pd atom which resulted in excellent selectivity towards the formation of ethylene. The co-adsorption energy of intermediate on AuPd and AgPd are very close, suggesting that the Pd atom in the alloys is mainly responsible for driving the reaction forward. As noted, the energy barrier for ethylene desorption is almost negligible on single atom alloys, resulting in immediate desorption which prevents further hydrogenation of ethane.

Moreover, a DFT study in conjunction with Scaling Relations Kinetic Monte Carlo (SRMC) simulations reported by Jørgensen and Gronbeck [462], found that the main reaction mechanisms for hydrogenation of acetylene−ethylene will be C_2H_2 adsorption. However, the C_2H_2 adsorption is exothermically stronger on Pd(111) as compared to Cu (111) and Pd/Cu(111). Meanwhile, the H_2 dissociative adsorption is barrier less on the Pd-containing surfaces, but it is high for the Cu(111). The observation for the absence of an H_2 dissociation barrier on Pd and a considerable barrier on Cu is consistent with the previous studies [22, 466]. Based on these simulations, it can be concluded that the Pd/Cu (111) SAA has a selectivity higher than that of Pd(111), mainly due to the weak binding of ethylene on Cu as compared to Pd while a strong binding of C_2H_4 at the edges and corners sites hinders the ethylene desorption before further hydrogenation. In short, acetylene−ethylene hydrogenation should contain minority sites that readily dissociate hydrogen and the majority sites where ethylene is weakly adsorbed. Nonetheless, all the above findings have opened a promising avenue to the rational design of SACs for selective hydrogenation. Despite much-perceived subjectivity on the stability of SACs under high-temperature conditions for selective hydrogenation reactions, many experimental works have demonstrated that SACs can provide stable activity under many reaction cycles or reaction times for this application.

Table 5
The application of SACs in selective hydrogenation.

Types of reaction	Reaction conditions	SACs preparation method	Key findings	Ref.
Hydrogenation of Acetylene to Ethylene	**Type of catalyst**: $AgPd_{0.025}/SiO_2$, $AgPd_{0.01}/SiO_2$ and $AgPd_{0.005}/SiO_2$ **Type of reactor**: Fixed bed reactor **Total flow rate**: - **Catalyst loading**: 30 mg **Reaction temperature**: 250–500 °C **Reaction pressure**: 6.8 atm	Incipient wetness impregnation	A low Pd loading of 168 ppm ($AgPd_{0.005}/SiO_2$ catalyst) was sufficient to yield 92.6% conversion of acetylene with 92.3% selectivity of ethylene. The high conversion was obtained *via* analogous Au -Pd SAA systems over a wide temperature window. An optimal Pd/Ag surface composition and isolated electron rich Pd atoms structure can be obtained through high temperature pre-reduction.	[44]
Hydrogenation of Crotonaldehyde to Crotyl alcohol	**Type of catalyst**: Rh_1/MoS_2 **Type of reactor**: Batch **Total flow rate**: - **Catalyst loading**: 20, 50, 100, and 150 mg **Reaction temperature**: 80 °C **Reaction pressure**: 5 atm	Incipient wetness impregnation	The single Rh atoms anchored to the edges of 2D MoS_2 sheets maintained a 100% conversion of crotonaldehyde to crotyl alcohol even under sustained reaction times. The electron transfer from the Rh_1 atoms to the surrounding S atoms of the MoS_2 sheets was the origin of the positive oxidation state of the anchored single Rh_1 atoms.	[399]
Hydrogenation of Nitrobenzene to Aniline	**Type of catalyst**: 0.25%Pt/γ-Al_2O_3 **Type of reactor**: Fixed bed **Total flow rate**: - **Catalyst loading**: 65 mg **Reaction temperature**: 80–155 °C **Reaction pressure**: 4.4 atm	Incipient wetness impregnation	The maximum TOF of nitrobenzene attained was 2.67×10^5 mol_{NB} h^{-1} mol_{Pt}^{-1}; the Pt/γ-Al_2O_3 catalyst also shows excellent reusability of more than 20 times without losing its catalytic activity.	[453]
Hydrogenation of Nitriles to Secondary amines	**Type of catalyst**: Quasi Pd_1Ni SAA **Type of reactor**: Batch **Total flow rate**: 200 mL/min **Catalyst loading**: 0.98, 2.0 and 3.5 wt.% of Pd loadings on Ni/SiO_2 **Reaction temperature**: 80 °C **Reaction pressure**: 6 atm	Atomic layer deposition	The TOF of Pd–Ni/SiO_2 SAC (515 hr^{-1}) was 8x and 4x higher than Pd/SiO_2 (64 h^{-1}) and Pt/SiO_2 (127 h^{-1}), respectively. The conversion of nitrile (~83%) and selectivity towards dibenzylamine (~97%) remained almost the same after 8 runs of experiments. The isolation of Pd with Ni shows a high catalytic activity in hydrogenation of nitriles, yielding a high selectivity of secondary amines >94%.	[451]
Semi-hydrogenation of phenylacetylene to styrene	**Type of catalyst**: 1 μmol% Pd_1/Cu **Type of reactor**: fixed bed reactor **Total flow rate**: - **Catalyst loading**: 60,000 mL h^{-1} g^{-1} **Reaction temperature**: 30 °C **Reaction pressure**: 1 atm	Galvanic replacement	100% phenylacetylene conversion with ~96% towards styrene was achieved using 1 μmol% Pd_1/Cu. The catalyst activity of $Pd_1/Cu(100)$ was about three times higher than that of $Pd_1/Cu(111)$	[454]
Semi-hydrogenation of phenylacetylene to styrene	**Type of catalyst**: $Pd_{0.5}/Ni_{0.5}$@γ-Al_2O_3 **Type of reactor**: Batch reactor **Total flow rate**: - **Catalyst loading**:10 mg **Reaction temperature**: 25 °C **Reaction pressure**: 1 atm	Incipient wetness impregnation	98% phenylacetylene conversion with 94% towards styrene was achieved using $Pd_{0.5}/Ni_{0.5}$@γ-Al_2O_3 SACs. The $Pd_{0.5}/Ni_{0.5}$@γ-Al_2O_3 SAC remains stable, no change to catalytic activity was observed after 10 runs.	[455]
Hydrogenation of phenylacetylene to styrene	**Type of catalyst**: $Pd_{0.18}Cu_{15}/Al_2O_3$ **Type of reactor**: Fixed bed **Total flow rate**: - **Catalyst loading**: - **Reaction temperature**: 250 °C **Reaction pressure**: 6.9 atm	Galvanic replacement	The high selectivity towards styrene *via* $Pd_{0.18}Cu_{15}/Al_2O_3$ was due to hydrogen spillover on the Cu surface. High selectivity towards styrene (94%) associated with high phenylacetylene conversion (90%) was attained using $Pd_{0.18}Cu_{15}/Al_2O_3$ after 8 h. The styrene selectivity attained from $Pd_{0.18}Cu_{15}/Al_2O_3$ was ~6–7 folds higher than that of $Pd_{0.18}/Al_2O_3$ at 3 h of reaction.	[443]
Hydrogenation of nitroarenes to 3-aminostyrene	**Type of catalyst**: 0.08 wt.% Pt/FeO_x **Type of reactor**: Batch **Total flow rate**: - **Catalyst loading**: - **Reaction temperature**: 40 °C **Reaction pressure**: 3.0 atm	Co-precipitation	High conversion (88.4%) and selectivity (98.2%) of 3-aminostyrene were obtained using 0.08% Pt/FeO_x. A high TOF of 1500 h^{-1} was attained in both the SACs and pseudo-SACs, which is 20x higher than that of other Pt/TiO_2 catalysts reported. The presence of Pt^+ centers, with the absence of Pt–Pt metallic bonding favored the adsorption of nitro groups, leading to a high catalytic performance	[35]
Hydrogenation of Levulinic acid to γ-valerolactone	**Type of catalyst**: 0.6 wt.% Ir@ZrO_2@C **Type of reactor**: Batch **Total flow rate**: 0.5 mL/min **Catalyst loading**: 100 mg **Reaction temperature**: 180 °C **Reaction pressure**: 40 atm	Facile synthesis	High selectivity (~100%) towards γ-valerolactone was attained and the catalyst was found to be highly recyclable, seven consecutive runs without any major deactivation. The high stability of the Ir@ZrO_2@C under acidic conditions is due to the strong interactions between the isolated $Ir^{\delta+}$ species and nano tetragonal ZrO_2 support.	[456]

4.3. Selective reforming

SACs have emerged as a new frontier in catalysis for hydrogen production from methane reforming and water-gas shift reactions. Dry Reforming of Methane (DRM) has received much attention in the hydrogen production sector, as this sustainable process exploits two major greenhouse gases (GHG), carbon dioxide and methane to produce industrially important syngas. Table 4 shows the application of SACs for hydrogen production, specifically in DRM and the WGSR over the last five years. Numerous supported precious metal SACs (e.g., Pd, Pt, Ru, and Rh) and a few transition metals SACs (Ni and Co) have been used for DRM. Despite the high coking resistance of precious metal-based catalysts, the use of precious metals in the synthesis of catalysts is often regarded as a non-sustainable approach due to the high cost and low availability of noble metals, which are typically limited for large-scale applications [467]. On the other hand, Ni-based catalysts are

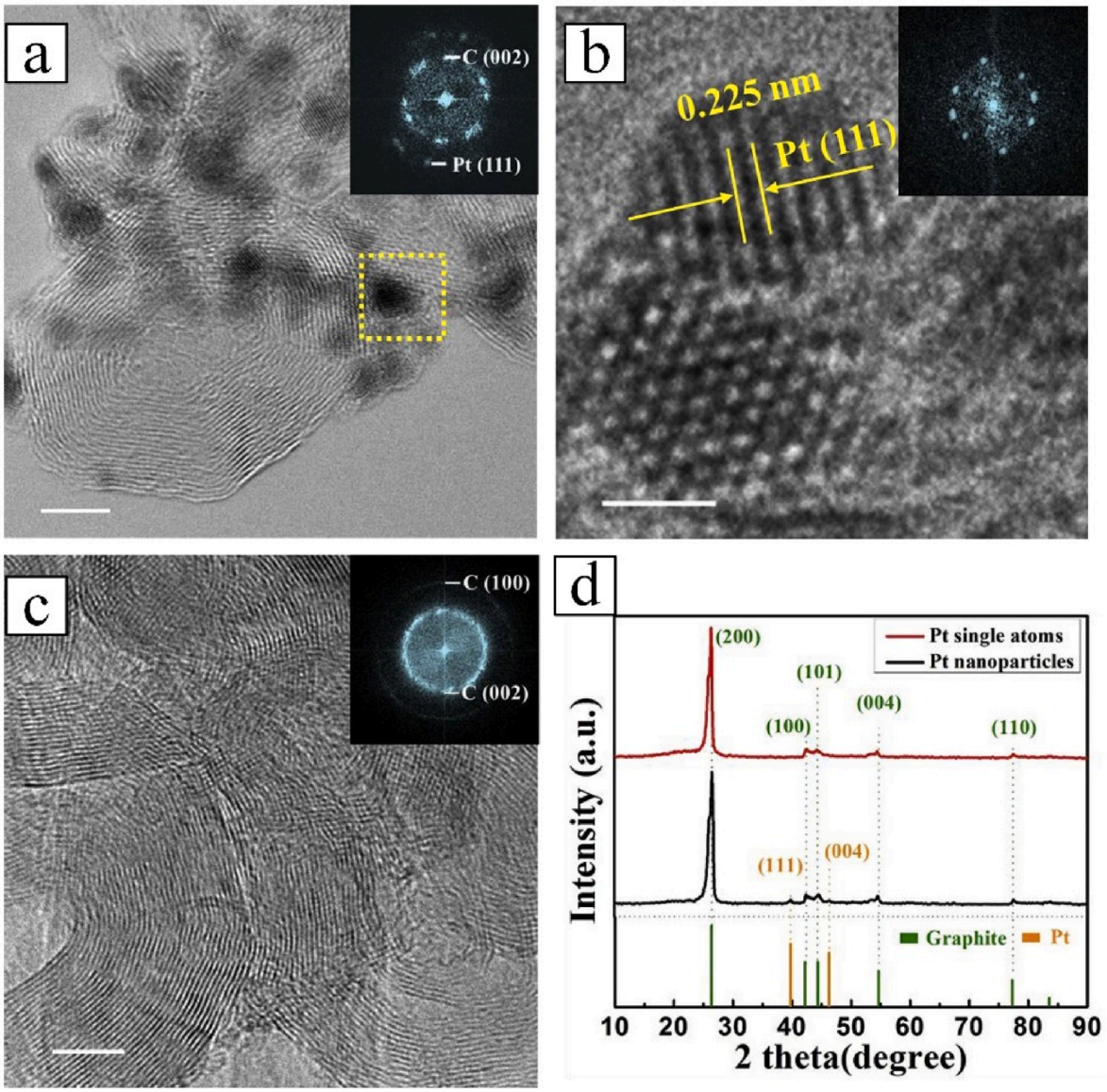

Fig. 18. Morphology of Pt/C catalysts: TEM images of Pt@C catalysts produced under different conditions, the concentrations of arc medium solution were (a) 0.975 mM and (b) 0.0195 mM [453]; (c) high magnification of the selected rectangular area of (a), (d) XRD profile of Pt/C catalysts produced [453] (all figures are adapted with permission from Elsevier).

generally more economical and are more abundant. Despite the low cost and high availability, Ni exhibits a high sintering tendency, poor deactivation resistance, and high affinity toward coke deposition on the active sites under a reaction temperature over 800 °C [468,469]. Ni-based catalysts are well-known for their high sintering tendency *via* particle migration and Ostwald ripening under a high reaction temperature and steam environment. The sintering and agglomeration of the active phase increase the particle size and reduces the dispersion of the metal atoms [469,470]. The number of atomically dispersed active species also decreases significantly and eventually leads to poor activity performance. Furthermore, severe carbon deposition on the Ni active site was also reported extensively in the literature. With such bulky NPs formed from the sintering phenomenon, a side reaction of methane pyrolysis readily takes place on the metallic NP sites due to the very high adsorption energy. The methane pyrolysis reaction could produce a layer of carbonaceous material on the metallic surface which in turn leads to catalyst deactivation after a long period of reaction time [471].

4.3.1. *Research advances of SACs in selective reforming processes*

As previously mentioned, the coking resistance and stabilization of an atomically dispersed active phase on a support material during a long time on stream are still regarded as one of the few major challenges encountered in the DRM and are yet to be resolved by academic and industrial practitioners. In line with the efforts in addressing the coking resistance and stabilization issue, numerous previous works have reported the considerable effect of CeO_2 on the size, dispersion, stability, and deactivation resistance of active sites [203]. For the synthesis of SACs, it is summarized that the support material should possess a high affinity with the active phase leading to a high dispersion and strong metal-support interaction (SMSI) [164]. A list of SACs used for methane reforming, steam reforming, and water gas shift reactions is tabulated in Table 6. In a recent work by Tang et al. [368], a novel bimetallic Ni/Ru SAC supported on CeO_2 was synthesized and proposed for the DRM application. As shown in AP-XPS spectra (Fig. 21(a)), the catalytic surface of $Ce_{0.95}Ni_{0.025}Ru_{0.025}O_2$ SACs consists of two sets of atomically dispersed Ni and Ru species. Also, the fraction of Ce^{3+} during the reaction at 550 °C was much higher than before the reaction, as evidenced

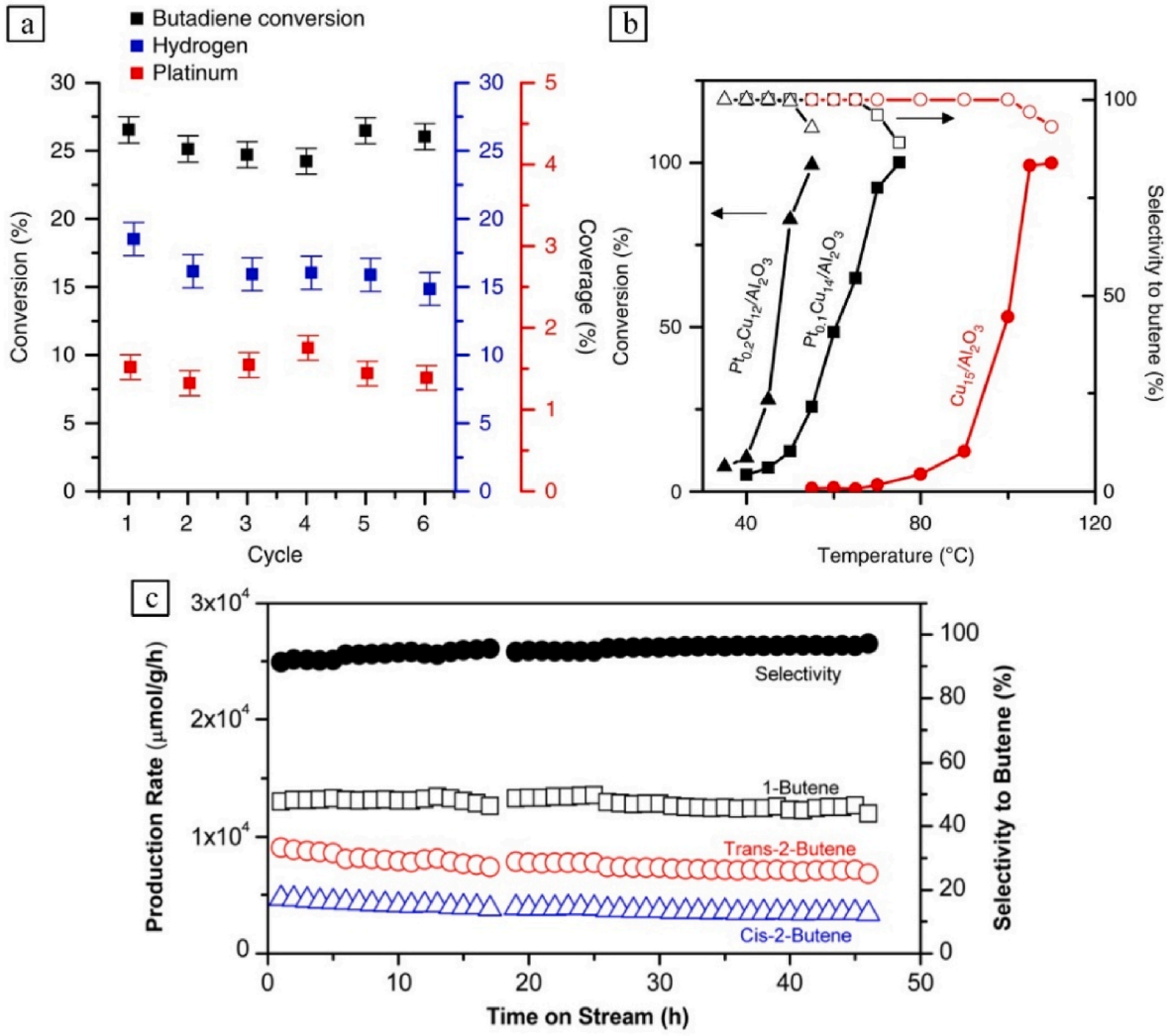

Fig. 19. (a) Catalytic reaction cycles after the co-adsorption of butadiene, followed by chemisorption of H_2 and CO on 0.02 ML Pt–Cu(111) [257], (b) The relation of conversion, selectivity to butene and temperature of $Pt_{0.2}Cu_{12}/Al_2O_3$, $Pt_{0.1}Cu_{14}/Al_2O_3$, and Cu_{15}/Al_2O_3 catalysts [257], (c) TOS hydrogenation activity test for $Pt_{0.1}Cu_{14}/Al_2O_3$ at 160 °C [257]. (all figures adapted with permission from Springer Nature).

by the formation of a plateau in the region of 885.2±1.5 eV, implying that no overlapping of photoemission features of Ce^{3+} and Ce^{4+} of CeO species in the catalyst. Based on the experimental findings, both active species were found to be highly active for methane reforming with a high turnover rate of 73.6H_2 per site per second at 833 °C (Fig. 21(b)). The conversion of CH_4 on $Ce_{0.95}Ni_{0.025}Ru_{0.025}O_2$, 91% was much higher than that of $Ce_{0.95}Ru_{0.05}O_2$ and $Ce_{0.95}Ni_{0.05}O_2$ at 700 °C, implying that there is a positive synergistic effect between Ni and Ru cations which enhance the DRM activity. Furthermore, computation studies also uncovered the synergetic effects and complement functions of the atomically dispersed Ni and Ru under a low concentration of 2.5 metal atomic %. Ni atoms are highly active in the adsorption of CH_4, and Ru atoms have a high affinity toward CO_2. From the operando studies of chemical and coordination environments, both Ni and Ru single atoms anchored on the CeO_2 surface remained in a cationic form instead of a metallic state. This was found to promote the catalytic performance of the SAC significantly up to 600 °C, outperforming NP counterparts, as depicted in Fig. 21 (c).

Akri et al. [164] synthesized a highly active and carbon-resistant Ni SAC supported on hydroxyapatite (HAP) using a Strong Electrostatic Adsorption (SEA) method. The 0.5 wt.% Ni SAC exhibited the highest CO_2 and CH_4 reaction rates of 816.5 mol/(g_{cat} h) and 1186 mol/(g_{cat} h), respectively, which was four and five times higher than the reaction rate of nickel NP catalysts. The 0.5 wt.% Ni SACs displayed excellent carbon deposition resistance as evidenced by the negligible weight loss of spent Ni SACs when characterized under thermal gravimetric analysis (TGA). Despite its high activity performance and carbon deposition resistance, the Ni SACs suffered from poor stabilization of the atomically dispersed Ni phase. Severe sintering and aggregation of Ni atoms were observed in the 0.5 wt.% Ni SACs, which led to its high deactivation rate after a few hours of reaction. The same research team also attempted to reinforce the stability of the previous Ni SACs by using a polyvinylpyrrolidone (PVP) assisted preparation method. A small amount of PVP was added during the co-precipitation process of the Ni SAC. It was found that the catalytic stability of Ni SACs improved significantly with very little carbon deposition on the catalyst surface. Such improvement in the catalytic behavior could be attributed to the highly dispersed Ni single atoms on the surface, hindering the inner active site from sintering phenomena during the reaction.

In another study by Akri et al. [369], the stabilization effect of ceria-doped hydroxyapatite (Ce-HAP) for atomically dispersed Ni species was investigated. From the in-situ XPS and Temperature Programmed Reduction (TPR), both characterization techniques unambiguously revealed that the ceria-doped HAP stabilized the atomically dispersed Ni from sintering and aggregation under a high temperature-reducing H_2 environment. Despite the high reduction

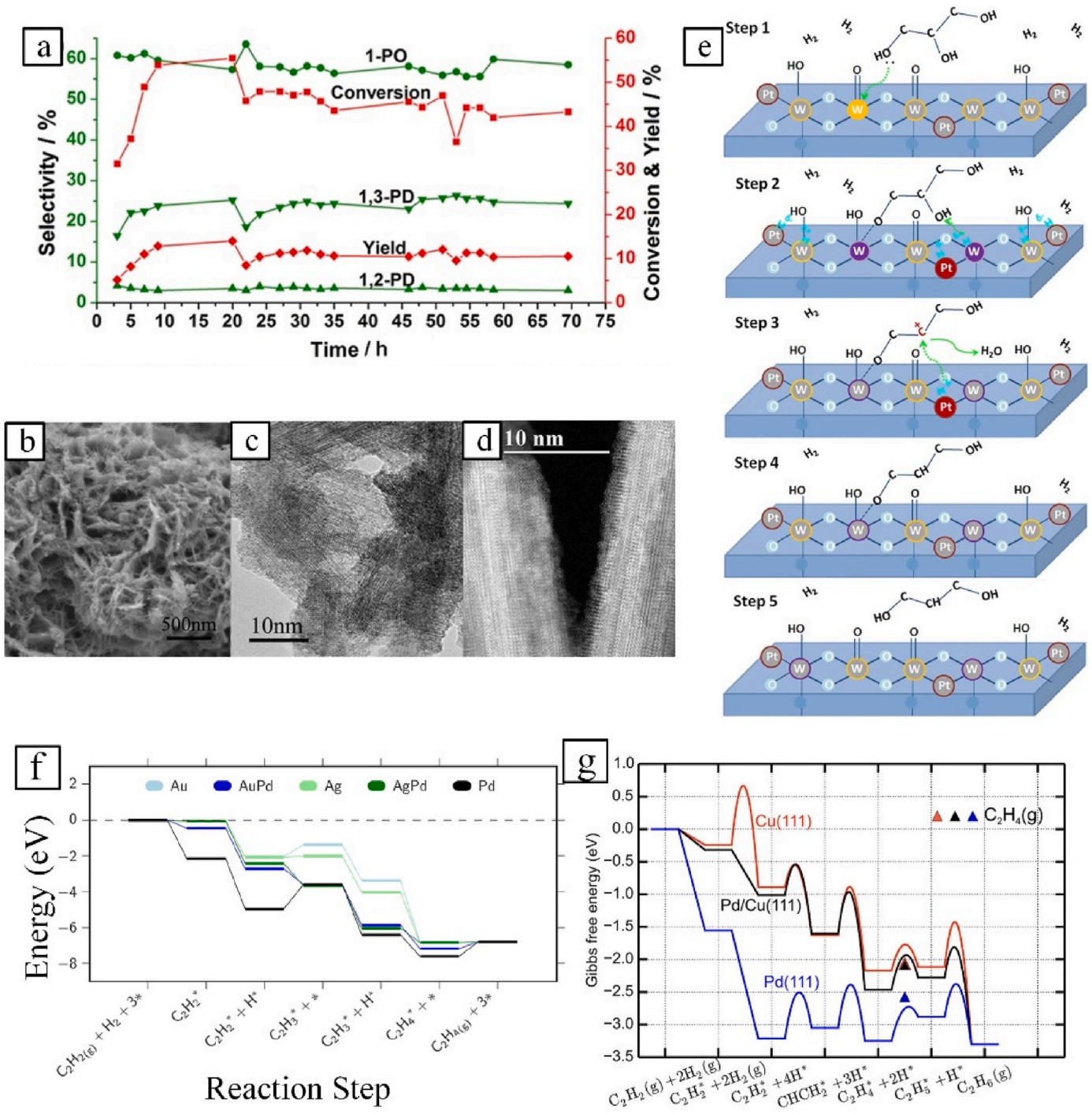

Fig. 20. (a) Stability test of Pt/WOx was conducted in fixed-bed reactor [460]; (b) SEM image for WO_x [460] (adapted with permission from John Wiley and Sons inc.), (b–c) SEM and TEM images for Pt/WO_x at 10 and 50 nm [460] (adapted with permission from John Wiley & Sons inc.), (d) AC-STEM image for Pt/WO_x (adapted with permission from John Wiley and Sons inc.), (e) Proposed reaction scheme for the hydrogenolysis of glycerol to 1,3-PD over Pt/WO_x [460] (adapted with permission from John Wiley and Sons inc.), (f) Potential energy diagram for the hydrogenation of acetylene to ethylene (darker shades represent single atom alloys, while the corresponding lighter shades represent the pure metal surfaces) [461] (adapted with permission from Springer Nature), (g) Gibbs free energy for the reaction of Pd sites in Pd(111), Cu sites in Cu(111), and Pd sites in Pd/Cu(111) [462] (adapted with permission from American Chemical Society).

temperature, the $Ni(OH)_x$ and NiO species on the Ce doped support remained unreduced and displayed high resistance behavior as compared to the undoped counterparts. In the end, the Ce species was reported to act as a stabilizing anchor for the atomically dispersed Ni rather than to suppress carbon deposition. As compared to the SAC work by Tang et al. [368], the 2 wt.% Ni SAC supported on Ce-doped HAP in Akri et al. [369] delivered similar catalytic performance and superior stability under identical reaction conditions, without using a precious metal. A low 0.5% Ni/HAP SAC (20 times less Ni loading) exhibited a comparable CH_4 reforming activity to that of the 10% commercial Ni/HAP under similar reaction conditions.

Despite several experimental studies reporting that Pt SAC is highly active for low temperature (120–400 °C) selective reforming and WGS, the arguments on: a) The characteristic behavior of Pt atoms in the WGS reaction at low temperature, b) The stability of Pt atoms under a reducing atmosphere and an elevated temperature, and c) The isolated

Pt atoms behave only as spectators in the process [475,476]. The fundamental questions have finally been resolved by Ammal and Heyden [477] through a DFT calculation, in which positively charged single Pt atoms stabilized on a TiO_2 (110) surface can be as active as Pt clusters for the WGS reaction at low and high temperatures. The calculation revealed that the interface edge Pt and single Pt^{2+} sites exhibited a high WGS activity at low temperatures whereas the corner Pt interface sites become active at higher temperatures. As such, the single Pt^{2+} sites acted as a stabilizer on an active reducible surface such as TiO_2 while the oxygen vacancies in the support play a significant role in enhancing the WGS activity. A possible reaction pathway for the WGS was also proposed, containing the redox, carboxyl, and formate pathways, shown in Fig. 22(a). As reported, the redox reaction was the dominant pathway between the temperature range of 200–400 °C, while high TOFs are possible for this active site. Meanwhile, the carboxyl pathway with redox regeneration was less favorable than the formate pathway with redox regeneration. Its rate was very close to that of the classical redox pathway at temperatures below 300 °C. In addition, the single Pt^{2+} sites tend to stabilize on the CeO_2(110) sites with H as ligands, owing to the similar characteristics and advantages of both homogeneous and heterogeneous catalysts [478,479]. Based on the free energy profiles as displayed in Fig. 22(b), we can also clearly see that the presence of additional surface H atoms could reduce the energy barrier for the interfacial H-transfer process (TS23) by about 0.2 eV, compared to the CO-assisted redox pathway (TS18), suggesting that the associative carboxyl with redox regeneration pathway is likely the most favorable pathway.

The excellent catalytic activity and stability of Pt nanoclusters reported by Ammal and Heyden [477] are in good agreement with Guo et al. [468]. In 2014, Li's group [473] synthesized stable and highly active Pt-based SACs for methanol steam reforming using the desorption-absorption method, by embedding the isolated precious metal atoms of Pt and Au onto a ZnO surface. A spin-polarized DFT calculation coupled with STEM characterization was performed to investigate the intrinsic nature of the active sites of the catalyst. The DFT calculation revealed that the corresponding formation energies of single Pt and Au atoms were 0.22 and 0.86 eV, respectively, which were much lower than the reservoirs in equilibrium with large metal counterparts. This observation indicates that the embedded Pt and Au are thermodynamically stable and resistant to segregation during the catalytic reactions and thus, providing a stronger binding toward the intermediates, as well as lowering reaction barriers. The enhancement of the catalytic activity can be seen where the TOF found in the single Pt sites embedded onto ZnO(1010) surfaces are over 1000 times higher than that of the pristine ZnO. The hypothesis was further confirmed by electron beam irradiation, where the isolated Pt single atoms were found to be relatively stable after anchoring onto ZnO(1010). All the HAADF images show no Pt or Au clusters/particles in the synthesized Pt_1/Au_1/ZnO SAC.

In short, to cater to higher reforming rates, multi-functional SACs should be developed with a significant number of interfacial sites, resulting from the presence of individually dispersed metal atoms on the support. This could avoid the coking resistance and stabilize the atomically dispersed active phase on a support material under a long time-on-stream. Moreover, due to the involvement of multiple species and commonly complex reaction mechanisms in the catalytic reforming process, the usage of DFT for the study of reaction-free energy to unravel potential reaction pathways provides many useful insights for designing SACs from first-principles. Furthermore, although methane-based reactions are the most applicable for catalytic reforming in the industry, more effort should be carried into branching out toward other chemical species to understand the possibilities of SAC in additional applications.

4.4. Selective oxidation

Extending to the energy matrices, novel SACs have been widely applied in the selective oxidation field. As such, the unique catalytic performance of SACs has demonstrated a huge prospect in various oxidation reactions such as CO oxidation or PROX, aerobic oxidation of alcohols, formaldehyde oxidation, and methane oxidation [13,480]. The sub-nanometer clusters of single metals were reported to have a better enhancement in catalytic activity or selectivity compared to larger bulk nanoparticles [481,482]. Apart from that, the utilization efficiency of the metal catalyst and selectivity, either for the adsorption or desorption activities of the active species can be modified *via* metal atom isolation, which directly influences the reactions kinetics [480,483]. Due to the interesting behavior found in metal SACs, these have attracted numerous researchers to have an in-depth understanding of their behavior and mechanism [102].

However, a common problem faced for selective oxidation reactions is the decrease in size from a nanoparticle to a single atom, in which the surface free energy of metals increases significantly with decreasing particle size, promoting aggregation of small clusters of the catalyst [13]. This can be prevented by implementing a high surface area support material that could interrelate well with the metal atoms, and postulating an isolated metal that can accommodate the metal surfaces, metal oxides, and carbon materials in the system [484,485].

4.4.1. Research advances of SAC in selective oxidation

According to Duprez and Cavani [486], selective oxidation is achievable using the famous Mars and van Krevelen mechanism that involves different transition metal ion oxides that display redox properties such as Cu, V, Mo, Cr, Te, Sb, Bi, and Fe [487]. Among all the metal ion oxides, the atomically dispersed Co and Cu catalysts have been reported to exhibit the highest catalytic activity in the selective oxidation of benzyl alcohol and 5-hydroxymethylfurfural (M = Fe, Cr, Co, Ni, Cu) [488]. In 2017, The first pioneering work of non-noble Co-based SAC for selective oxidation was reported by Guan's group. An atomically dispersed Co on N_2-doped graphene (denoted as Co-NG) in an ammonia medium *via* pyrolysis technique was synthesized [489]. Notably, a high benzyl alcohol conversion (94.8%) and benzaldehyde selectivity (97.5%) were achieved over 6 h and 120 °C using a small amount of Co-NG (5 mg). However, under the absence of N_2 doping, a much lower conversion of 42.5%) than Co-NG in selective oxidation of benzyl alcohol was attained. As reported previously, the single metal atom on a carbon matrix can be stabilized by introducing N atoms as an "anchor" [99]. The N_2 doping does not solely strengthen the interaction between the metal atom and the support but also promotes electron transfer, which resulted in a firmly anchored, atomically dispersed metal atom on supports [490,491]. A possible catalytic reaction mechanism for the aerobic oxidation of benzyl alcohol over Co-NG was also postulated as follows: Firstly, the oxygen molecules were weakly adsorbed on the Co center, followed by electron transfer activation to form a superoxide species (Co 3d orbitals to O_2 2p antibonding orbitals). Lastly, the superoxide species will react with the hydrogen bonding of benzyl alcohol to produce benzaldehyde [492,493].

Furthermore, Harrath et al. [364] also studied the catalytic mechanism of M/ZrO_2 SAC (M = single atom of Rh, Pd, Ir, Pt, Fe) for a one-step conversion of CH_4 to CH_3OH. Their work also found that Rh/ZrO_2 SAC induced the dissociative adsorption of H_2O_2 on its surface with great binding energy (−2.87 eV), favoring the selective oxidation of CH_4 pathway. Subsequent steps in the reaction pathway of Rh/ZrO_2 SAC include the adsorption of methane, and formation of C–H bond (which forms a methyl radical and HOO–Rh site) to further produce CH_3OH or by-product CH_3OOH (Fig. 23(a)). Apart from that, the non-noble Fe/ZrO_2 SAC was also expected to give high selectivity of methanol due to the lower energy barrier for methyl radical formation (0.49 eV lower) and methanol formation (0.13 eV lower) on O–Fe/ZrO_2 compared to O–Rh/ZrO_2 (Fig. 23(b)). Notably, the pathway to produce the CH_3COOH by-product *via* a Fe/ZrO_2 SAC was suppressed due to a kinetically thermodynamic unfavorable energy barrier of 2.77 eV, suggesting a high selectivity for the main product CH_3OH can be obtained.

Inspired by the excellent results of the application of SACs in various

Table 6
Application of SACs in methane reforming, steam reforming, and water gas shift reactions.

Types of reaction	Reaction conditions	SACs preparation method	Key findings	Ref.
Dry methane reforming	**Type of catalyst**: 0.5 wt.% Ni/Hydroxyapatite **Type of reactor**: Fixed bed reactor **CH_4:CO:He ratio**: 1:1:3 **Total flow rate**: 50 mL/min **Catalyst loading**: 50, 6.16, and 3.65 mg **Reaction temperature**: 750 °C **Reaction pressure**: 1 bar	Co-precipitation	A high reaction rate of 1186.2 and 816.5 mol $gNi{-}1.h^{-1}$ for CO_2 and CH_4, respectively were obtained using the 0.5 wt% Ni/HAP catalyst. The stability of Ni-single atoms was improved through the PVP-assisted synthesis method where there was only a minor reduction in conversion and selectivity after 16 h of reaction. At temperatures higher than 450 °C, both concentrations of CH_4 and CO_2 started to decrease progressively, indicating the onset point of the dry methane reforming reaction.	[164]
Methane reforming for production of alkene (C2 products)	**Type of catalyst**: 1 wt.% Pt/CeO_2 **Type of reactor**: Fixed bed reactor **CH_4:He ratio**: 1:99 **Total flow rate**: 20 mL/min **Catalyst loading**: 0.2 g **Reaction temperature**: 900–1000 °C **Reaction pressure**: 1bar	Co-precipitation	Atomically dispersed Pt catalysts have superior methane conversion compared to NP counterparts. Pt/CeO_2 SAC demonstrated the highest methane conversion (14.4%) and selectivity toward C_2 products, where ethylene (33.2%) and acetylene (35.1%) were the major products. Pt/CeO_2 NPs had a low methane conversion (9.7%) with poor ethylene (8.3%) and acetylene (6.3%) selectivity.	[208]
SDry methane reforming	**Type of catalyst**: 0.5 wt.% Ni/HAP-Ce **Type of reactor**: Fixed bed reactor **CH_4:CO:He ratio**: 1:1:3 **Total flow rate**: 50 mL/min **Catalyst loading**: 50 mg **Reaction temperature**: 900–1000 °C **Reaction pressure**: 1 bar	Co-precipitation	0.5% Ni/HAP SACs exhibited comparable initial activity to the 10 Ni/HAP despite the former having 20 times less Ni loading than the latter. 0.5% Ni/HAP SACs have 2–4 times higher specific activity than the 10% Ni/HAP-Ce with the same TOF.	[369]
Dry methane reforming	**Catalysts**: 5 wt.% Ru–$Ce_{0.95}Ru_{0.05}O_2$, 5 wt.% Ni–$Ce_{0.95}Ni_{0.05}O_2$ 2.5 wt.% Ru + 2.5wt.% Ni -$Ce_{0.95}Ru_{0.025}Ni_{0.025}O_2$ **Type of reactor**: Fixed bed reactor **CH_4:CO ratio**: 1:1 **Total flow rate**: 40 mL/min Catalyst loading: 50 mg **Reaction temperature**: 300–600 °C **Reaction pressure**: -	Co-precipitation	$Ce_{0.95}Ru_{0.025}Ni_{0.025}O_2$ SACs achieved the highest H_2 selectivity of 98.5% at 600 °C. The measured TOF at 560 °C was as high as 73.6H_2 per site per second. $Ce_{0.95}Ru_{0.05}O_2$ and $Ce_{0.95}Ni_{0.05}O_2$ had a lower H_2 selectivity of 82.9% and 80.0% as compared to $Ce_{0.95}Ru_{0.025}Ni_{0.025}O_2$.	[368]
Steam reforming of methane	**Catalysts**: $Rh/12CeO_2{-}Al_2O_3$ **Type of reactor:** Plug flow reactor **CH_4:H_2O: He ratio**: 1:3:104 **Total flow rate**: 540 mL/min **Catalyst loading**: 5 mg **Reaction temperature**: 500 °C **Reaction pressure**: 1 bar	Incipient wetness impregnation	Co-existence of Ru in the form of dispersed atoms and NPs in $Rh/12CeO_2{-}Al_2O_3$, exhibited a high catalytic performance with the lowest deactivation percentage of 17% after 48 h under stream at 500 °C. $Rh/12CeO_2{-}Al_2O_3$ SAC shows a 17% lower level of deactivation whereas unpromoted Rh/Al_2O_3 has a high deactivation rate of 40%.	[472]
Water gas shift reaction	**Catalysts**: 0.01, 0.044, 0.22, and 1.1 wt.% Pd/FeO_x **Type of reactor**: Fixed bed reactor **CO:H_2O: He ratio**: 1:5:44 **Total flow rate**: 30 mL/min **Catalyst loading**:100 mg **Reaction temperature**: 500 °C **Reaction pressure**:1 atm WHSV:18,000 mL/(g_{cat} h)	Co-precipitation	The FeO_x support promoted and stabilized a high dispersion of Pd metal atoms, enhancing the activity of Pd catalysts in the WGS reaction. Pd SACs (0.01 wt.% Pd/FeO_x and 0.044 wt.% Pd/FeO_x) exhibited a higher atom efficiency than its cluster/NP counterpart. A high TOF of 0.82 s^{-1} and reaction rate of 27.6 molCO/(g_{cat}.h) was attained using 0.01 wt.% Pd/FeO_x.	[313]
Water gas shift reaction	**Catalysts**: 0.01 wt.% Ir/FeO_x **Type of reactor**: Fixed bed reactor **CO:H_2O: He ratio**: 1:5:44 **Total flow rate**: 30 mL/min **Catalyst loading**: 100 mg **Reaction temperature**: 300 °C **Reaction pressure**: 1 bar	Co-precipitation	Ir/FeO_x SACs were extremely active for WGS reactions with Ir loading as low as 0.01 wt.%. The highest CO reaction rate achieved was 43.4 mol/(g_{cat}.h), which is one order of magnitude higher than its NP and cluster counterparts. Single Ir atoms acted as the key active site and contributed 70% of the overall WGS activity.	[24]
Steam reforming of methanol	**Catalysts**: 0.0125 wt.% Pt/ZnO and Au/ZnO **Type of reactor**: Fixed bed reactor **CH_3OH:H_2O:He ratio**: 1:1.5:10 **Total flow rate**: 46 mL/min **Catalyst loading**: 50 mg **Reaction temperature**: 390 °C **Reaction pressure**: -	Co-precipitation	Presence of atomically dispersed Pt and Au species improved the binding energies of reactant and intermediates (increased by 0.99–1.84 eV) on a ZnO (1010) surface and reduced the formation energy of oxygen vacancies (~1.31 eV). Higher CH_3OH conversion and CO_2 selectivity were obtained using Pt/ZnO (43%, 88%), as compared to Au/ZnO (28%, 100%).	[473]
Dry reforming of methane	**Catalysts**: 5 wt.% Ni/MgO **Type of reactor**: Fixed bed reactor **CH_4: CO_2:N_2 ratio**: 1:1:1 **Total flow rate**: 45 mL/min **Catalyst loading**: 50 mg **Reaction temperature**: 600–800 °C **Reaction pressure**: 1 bar	Co-precipitation	5 wt.% Ni/MgO exhibited the highest activity because it bonded the reactant and intermediate more strongly than the other two candidates. 2.5 wt.% Ni/MgO binds the reactant and reaction intermediates weakly and the number of neighboring Ni site was too little to catalyze the DRM reaction.	[474]

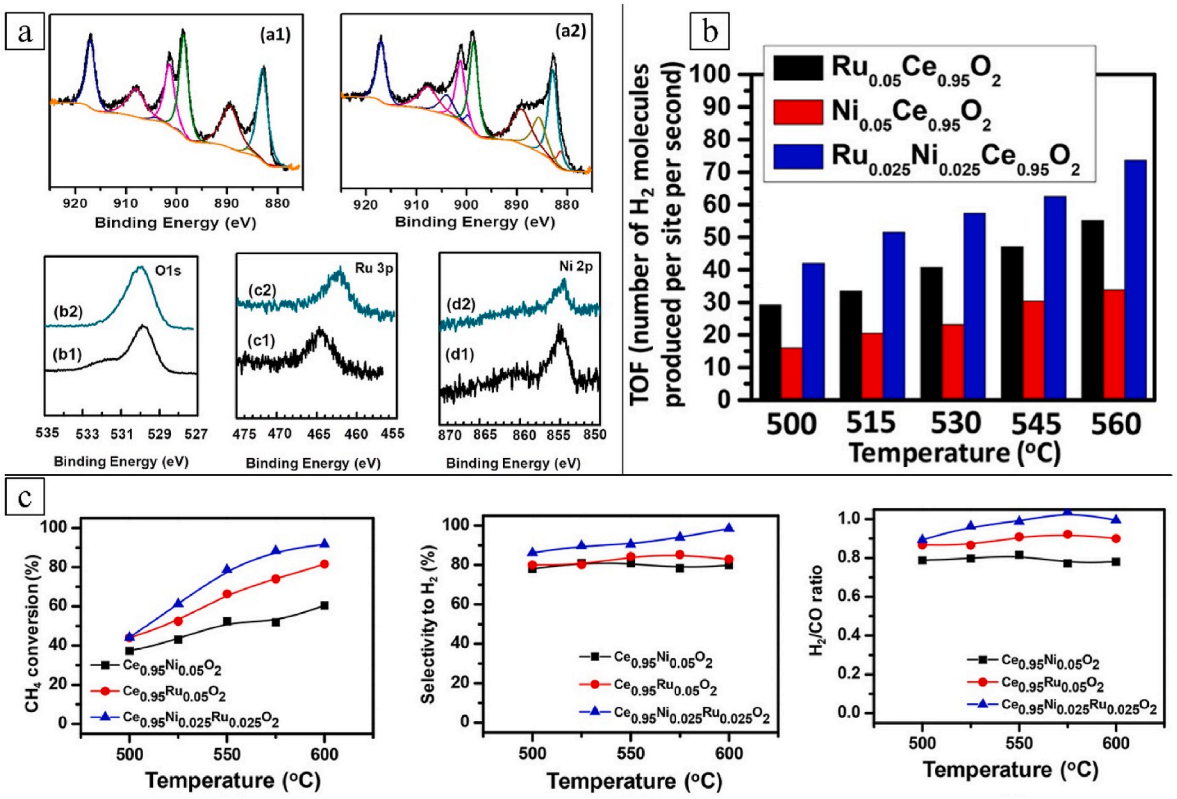

Fig. 21. (a) NAP-XPS photoemission features of $Ce_{0.95}Ni_{0.025}Ru_{0.025}O_2$ before catalysis (a1, b1, c1, and d1); and during catalysis at 550 °C. (a2, b2, c2, and d2) [368]. (b) Turnover frequency (TOF) of methane reforming in terms of hydrogen production per Ru atom of $Ce_{0.95}Ru_{0.05}O_2$, per Ru atom of $Ce_{0.95}Ru_{0.5}O_2$ and per Ni atom of $Ce_{0.95}Ni_{0.025}Ru_{0.025}O_2$ at 500–560 °C [368]; (c) Catalytic performance of $Ce_{0.95}Ni_{0.5}O_2$, $Ce_{0.95}Ru_{0.5}O_2$, and $Ce_{0.95}Ni_{0.025}Ru_{0.025}O_2$ in methane reforming at 500–600 °C [368]. (all figures are adapted with permission from the American Chemical Society).

selective oxidative reactions as shown in Table 7, more studies further challenged the selective benzylic C–H oxidation of hydrocarbon derivatives under mild conditions. This is because most studies have reported that selective oxidation of saturated C–H bonds is difficult and aggressive conditions (>120 °C and 10 bar oxygen pressure) are usually required to obtain a high selectivity of desired products [494]. In 2019, Bakandritsos together with his co-workers disclosed a mixed-valence Cu-based SAC for oxidative homocoupling of benzylamines [282]. Fig. 24(a) shows that the G(CN)–Cu SAC was synthesized using the coordination of Cu(II) ions to CN-functionalized graphene (cyano-graphene, G(CN)) where the graphene-induced charge-transfer reduced the Cu(II) ions anchored to G-CN into the Cu(I). Surprisingly, the G(CN)–Cu SAC was able to yield an excellent conversion (up to 98%) and selectivity (up to 99%) under mild conditions (85 °C, 1bar). In addition, the G(CN)–Cu SAC remained at a very high conversion rate (94%), even after 5 recycling steps with no change in product selectivity (98%) (Fig. 24(g)). This observation was supported by the TEM images, in which a clear detection of Cu atoms can be observed before and after the catalytic reaction (Fig. 24(b–f)), suggesting the active sites of the Cu are not prone to sintering even during a high reaction temperature. In addition to that, the XPS analysis also further confirmed the high catalytic activity of the G(CN)–Cu SAC, in which there was no change of the Cu mixed valance state from 1st to 5th cycles (Fig. 24(h)). The G(CN)Cu also displayed a high turnover frequency (TOF = 13 h^{-1}) at low temperatures (<100 °C), proving that it has a strong electron-withdrawing character (withdraw electron from CF_3-substituted benzylamine) than that of the current best performing NP catalysts in the literature (e.g., CuO nanoflakes and Cs/MnO_x) [495,496]. Through the DFT analysis and EPR measurement, a possible oxidative amine coupling mechanism for the study was proposed as shown in Fig. 24(i). Firstly, the oxidative dehydrogenation of the benzylamines started with O_2 reduction in the active copper enzymes through its preferential coordination with Cu(I) centers (step 1), which leads to the formation of copper-oxyl intermediate between the Cu ions (step 2). In order to yield the formation of an imine, a two-hydrogen abstraction from the neighboring amine by the reactive oxyl species was essential (step 3). In step 4, the hydroxyl radicals produced were trapped and finally, the NH_3 and N-benzylidene-benzylamine were produced through the amine–imine coupling. Lastly, the catalyst was regenerated and can be reused for further oxidative coupling of benzylamines.

With respect to theoretical screening works, there have been few studies investigating the fundamental mechanism of oxidation *via* SACs [498,499]. For instance, the fundamental insights of CO oxidation catalyzed by using single Au atoms supported on Thoria (Au/ThO_2) through DFT with Hubbard-type On-site Coulomb interaction simulation (DFT + U) were reported lately [498]. From the computational study, three main steps mechanism of facilitation of the Au-doped ThO_2 (111) surface for CO oxidation was analyzed: 1) Reaction between the gaseous phase CO between the lattice O_2^- through Mars-van Krevelen (MvK) mechanism, 2) the adsorption process of gaseous phase of O_2^- at the vacancy site to form the activated O_2^-, 3) CO molecule reacts with O_2^- to form the intermediate of OCCCO* which breaks down into CO_2, and O* adatom. Based on the findings, the developed Au-doped ThO_2 (111) showed a positive catalytic activity for CO oxidation with a lower adsorption rate and the rate-limiting step was determined to be the adsorption of O_2 which takes place at the ThO_2 site on the surface.

Han et al. [500] investigated the Pd stripe and Pd single atom-doped Cu(111) surfaces for $COOCH_3$ selective oxidation. Specifically, three structures of Pd monolayer, Pd_4Cu_8 and Pd single atom (Pd_1) on Cu(111) were studied as shown in Fig. 25(a)). For the conversion of $COOCH_3$ to dimethyl oxalate (DMO), the strain effect decreases the activation barrier on Pd_1–Cu(111), while the ligand effects caused a non-dominant

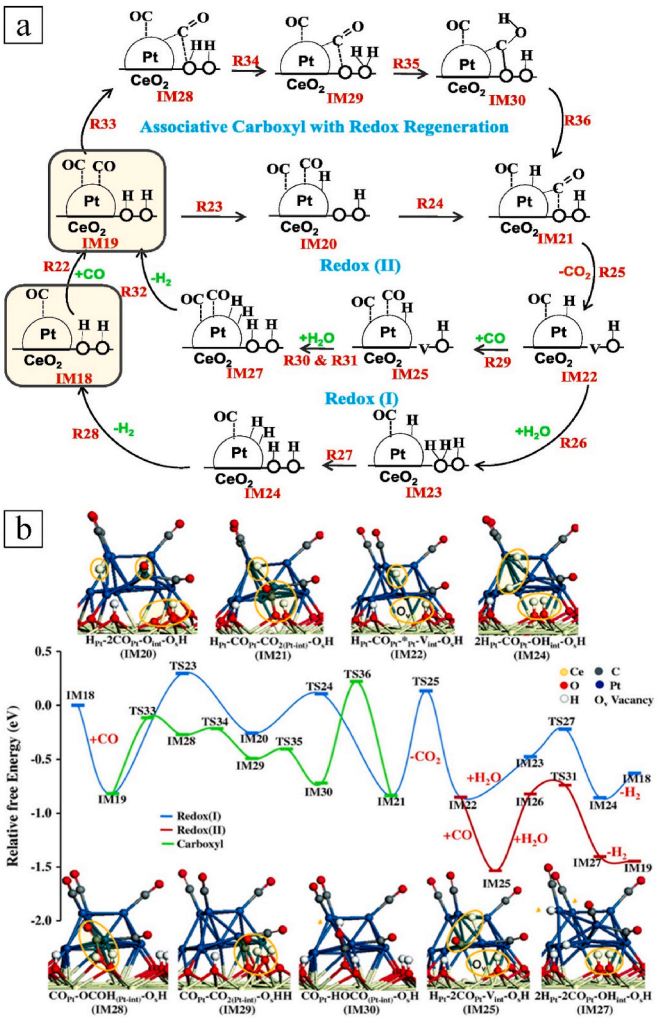

Fig. 22. (a) Possible reaction pathway of CO- and H-assisted WGS reaction steps for Pt/CeO_2(111) [478] and (b) Free energy profile for CO- and H- assisted redox and associative carboxyl with redox regeneration pathway on Pt/CeO_2(111) [478]. (adapted with permission from Elsevier)

increase in the activation energy barrier (Fig. 25(b)). This effect was similar for Pd monolayer but was the contrary for Pd_4Cu_8/Cu(111). From Fig. 25(c), it can be clearly seen that the Pd_1–Cu(111) was showing an exothermic reaction energy associated with low activation energy, indicating that the oxidation reaction occurs much easier on the Pd_1–Cu (111) as compared to its counterparts. In addition, two possible reaction pathways related to $COOCH_3$ oxidation were studied through micro-kinetic analysis. In both pathways (Fig. 25(d and e)), the results were in good agreement that the DMC (108.8 kJ/mol) was more favorable to be produced compared to the DMO (192.6; 107.5 kJ/mol) due to a lower energy barrier of the rate-determining (Fig. 25(d)). A similar observation was also depicted in Fig. 25(e) in which the activation barrier of the Pd_4Cu_8/Cu(111) and Pd_1–Cu(111) surfaces was 107.5 and 91.6 kJ/mol, respectively [500].

Lately, another remarkable investigation of the synergistic effect of tri-metals in a Crown Jewel-Structured (IrPd)/Au SAC for selective oxidation has been revealed by Zhang and co-authors [493]. The presence of negatively charged Au and Ir atoms has elucidated two kinds of charge transfer modes, creating a synergistic effect that enhanced the catalytic activity of the (IrPd)/Au SACs to a maximum level. In order to further understand the synergistic effect, a DFT analysis was performed. The study revealed that electron transfer between O_2 and anionic Au and Ir atoms possessed a hydroperoxo–like species *via* donating an excess electronic charge to the antibonding orbital. The adsorbed O_2 molecule on the (111) face of Au of (IrPd)Au model clusters possessed the highest negative charge numbers, suggesting that this is the key factor that leads to an enhancement of synergistic catalytic activity for selective aerobic oxidation.

4.5. Selective photochemistry and electrochemistry

Over the decades, photocatalysts and electrocatalysts have attracted huge attention as a method of addressing the global environmental issue and energy crisis [501,502]. Along this line, SACs have been engaged as promising candidates in the fields of photocatalysis and electrocatalysis due to their high catalytic activity, stability, and pathway selectivity [19,503]. In recent years, SACs have been utilized for a wide range of applications, such as hydrogen evolution, oxygen evolution, CO_2 reduction, pollutant removal and degradation, and chemical synthesis [504–506].

Photocatalyst is a unique class of materials that can accelerate chemical reactions on exposure to a specific type of light (UV, UV–Vis, or Visible). Photocatalysts offer sustainable and environment-friendly catalytic solutions by utilizing green and inexhaustible solar light to facilitate chemistry reactions compared to traditional thermal activation processes. In general, photocatalysts work using the same principle as semiconductors, when the photocatalyst is exposed to light, an electron in the valence band can absorb the energy of photons and is excited to the conduction band, leaving a hole (positive charge) in the valence band. Therefore, the electron–hole pair is produced in this process, which can provide both oxidation and reduction environments to accelerate chemical reactions [507]. Various bulk materials have shown photocatalytic capabilities, including metal oxides (TiO_2, V_2O_5, ZnO, Al_2O_3, Fe_2O_3) [508], carbon dots [509], metal–organic-frameworks (MOFs) [510], 2D materials [511], and plasmonic metals [512]. However, current photocatalysts are facing great challenges because of fast photogenerated electron–hole recombination, limited visible-light response, and slow electron transport [513]. Along this line, SACs have emerged as capable photocatalysts that could be the answer to overcoming the typical problems that hinder conventional photocatalysts.

On the other hand, electrocatalyst is a type of catalyst used to increase the rate of electrochemical reactions by facilitating the conversion between electrical and chemical energy [514]. The reaction processing in electrolysis is dominated by circuit-induced carriers, which can drive reactions far from their equilibrium potential, enabling access to difficult reaction pathways. Solid metals or oxide electrodes are usually used as heterogeneous electrocatalysts and the electrochemical processes occur at or near the liquid–solid interface. These reactions usually include multistep ion/electron coupled electron transfer with high reaction kinetics, requiring efficient catalysts to accelerate the processes [515]. Homogeneous electrocatalysts are soluble or dispersed in solutions, activating the reactions in the solutions. The processes are indirect electron transfers instead of the direct electron transfer between electrode and an electrolyte. A vast array of materials has been used as electrocatalysts, including noble metals, noble metal oxides, transition-metal-based materials, MOFs, and metal-free-carbons [516–520]. Electrocatalysts have been widely used in energy storage and conversion, metallurgy, and chemical synthesis applications. However, a bottleneck of wide spread electrocatalyst usage is the high cost of noble metals and low natural abundance, limiting the large-scale development of electrocatalysts. Noble metals are usually present in the forms of nanoparticles in conventional catalysts, however, the previous concept of efficient nanoparticles is flawed by the fact that these are in fact to be considered bulk materials due to extended terrace sites. Reducing the size of catalysts is an efficient method to expose more high-energy active sites. SACs offer promising access to address this issue due to natively possessing a maximum atom utilization. In this section, we highlight and introduce recent advances in electrocatalysis

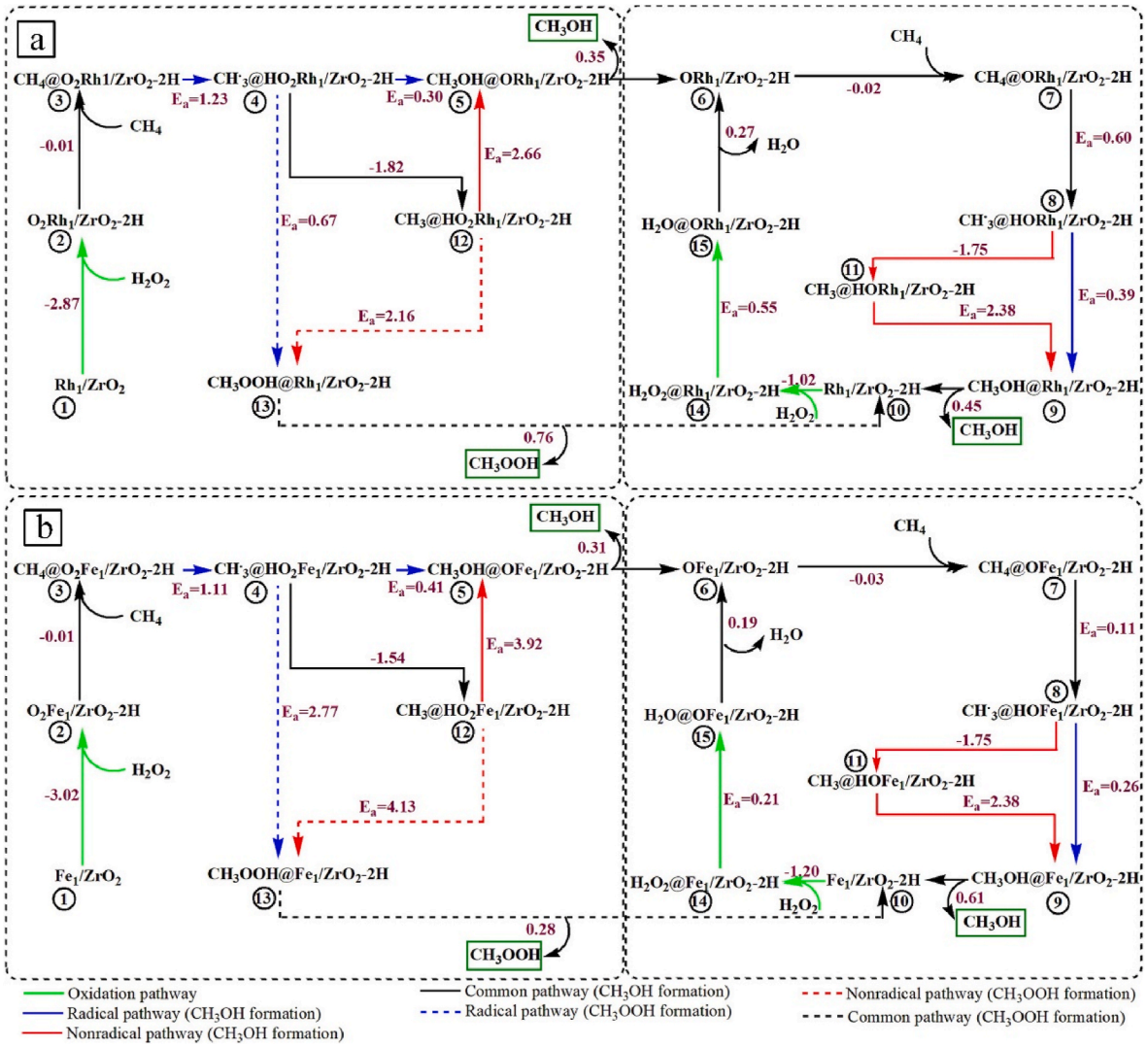

Fig. 23. Reaction network for conversion of methane on (c) Rh/ZrO_2 SAC and (d) Fe/ZrO_2 SAC [364] (adapted with permission from American Chemistry Society).

and photocatalysis using SACs, focusing on applications in CO_2 conversion and hydrogen fuel cells (Table 8).

4.5.1. *Research advances of SAC for electrochemical CO_2RR*

The CO_2 released in the atmosphere from both large, industrial point sources, and small, mobile sources are considered the main culprit for global warming. Its capture and utilization have received growing attention since it is a promising strategy for reducing its concentration in the atmosphere, and simultaneously obtaining valuable chemicals and fuels [528]. However, due to the very stable structure of the CO_2 molecule, its conversion requires the utilization of catalysts. In this regard, electrocatalytic CO_2 reduction reaction (CO_2RR) holds great promise among various chemical approaches [529,530], since it can be carried out under ambient conditions with promising activity [530]. For this process to be environmentally friendly, the energy input should be obtained from a renewable and non-CO_2 emitting electricity source, and combined with the utilization of 'green' electrocatalysts. Noble metal atoms are known for their superior activity, selectivity, and long-term stability in CO_2RR, but their high cost and scarcity hinder their extensive use [531,532]. However, this issue is reduced in SACs, where the metal loading is notably decreased.

The first example of electrochemically driven CO_2RR over SACs was proposed in 1974 by Meshitsuka et al. [533] who showed that cobalt and nickel phthalocyanines attached to graphite electrodes are active catalysts for the electrochemical reduction of carbon dioxide. Since then, SACs have been extensively explored and several other promising SACs for CO_2RR have been proposed [50,534,535]. Unlike gas-phase reactions, electrochemical reactions would have the additional requirement of high-conductivity support materials, such as carbon or doped metal oxide. The introduction of heteroatoms in the support matrix was found to be a useful strategy for modulating the electronic structures and stabilizing the metal atoms, resulting in an overall enhanced catalytic activity [536,537]. Furthermore, the process of "anchoring" the metal atom to the support involves a charge transfer among the central metal sites and the substrate [523]. This type of metal-support interaction has been extensively investigated in SACs to regulate the electronic structure of catalysts, which consequently affects the intrinsic activity of active sites toward various electrocatalytic reactions [538]. Moreover, the local environments of the metal active sites in atomically dispersed metals determined the significantly different behavior between SACs and their bulk and nanoparticle counterparts [539,540]. For instance, while the bulk and nanoparticle electrodes of Mn, Fe, Co, and Ni mainly produce H_2 [540], the M–N–C (M = Mn, Fe, Co, Ni) SACs show great activity for the electrochemical CO_2 conversion to CO, and the suppression of the competing HER [541].

The introduction of SACs into CO_2RR has yielded a high efficiency towards desired fine C_1–C_5 chemicals [542,543]; notably, SACs have shown promising results in boosting the catalytic conversion of CO_2 up

Table 7
The application of SACs in different selective oxidation reactions.

Types of reaction	Reaction conditions	SACs preparation method	Key findings	Ref.
Selective oxidation of benzene to phenol	**Type of catalysts:**1.5, 2.7 and 4.0 wt.% FeN_4/GN **Type of reactor:** 50 mL batch reactor **C_6H_6:H_2O_2:CH_3 ratio:** 1:15:7.5 **Catalyst loading:** 50 mg **Reaction temperature:** 25 °C **Reaction pressure:** -	Ball milling	Improved activity performance in direct oxidation of benzene to phenol under 25 °C, with a catalytic conversion of 23.4% and phenol yield of 18.7%. Phenol yield of 8.3% was achieved under 0 °C for 24 h.	[99]
Selective oxidation of benzyl alcohol to benzaldehyde	**Type of catalysts:** Co on N-doped graphene Co-NG-750, **Type of reactor:** 50 mL two-necked bottle flask **O_2 flow rate:** 20 mL/min **Catalyst loading:** 5 mg **Reaction temperature:** 130 °C **Reaction pressure:** 1 bar	Pyrolysis	Atomically dispersed Co-NG-750 catalysts had much superior atom efficiency and exhibited high selective oxidation activity. Co-NG-750 demonstrated the highest benzyl alcohol conversion of 97.5% and benzaldehyde selectivity of 97.5% with an average TOF of 500 $h^{-1.}$ for a 5 h reaction.	[489]
Selective oxidation of benzyl alcohol to benzaldehyde	**Type of catalysts:** M-N-C, where M is Cr, Fe, Cu, Ni, and Co **Type of reactor:** 50 mL batch reactor **Catalyst loading:** 0.13–0.4 mg **Reaction temperature:** 55 °C **Reaction pressure:** 2.5–10 bar	Modified sacrificial support technique.	The Cu–N–C was the most active catalyst as compared to its counterparts with the highest activity of benzyl alcohol oxidation with the reaction rate of 204 × 10^{-8} mol/s g_{cat} and TOF of 34 × 10^{-3} s^{-1}, mainly attributed to atomic dispersion of Cu resided at N-coordinated site and promotes facile beta hydride elimination step. Among the M-N-C catalysts. Fe–N–C catalyst has the smallest loss of activity after 8 h of benzyl alcohol oxidation.	[488]
Selective Oxidation of Methane to Formaldehyde	**Type of catalysts:** <0.1 wt.% Co/SiO_2 **Type of reactor:** fixed-bed reactor **CH_4:O_2:N_2:H_2O ratio:** 48:2:50:10 **Total flow rate:** 1.1 × 10^2 mL/min **Catalyst loading:** 50 mg **Reaction temperature:** 400–500 °C **Reaction pressure:**1 bar	Incipient wetness impregnation	The selectivity of formaldehyde was up to 75% at 500 °C. despite a low loading of 0.05 wt.%. The TONs increased by ~10 times with the increase in the reaction temperature. The highest TON of 44 was obtained using 0.05 wt.% of Co/SiO_2.	[428]
Selective oxidation of C–H bonds to ketone and alcohol	**Type of catalysts:** Fe–N–C **Type of reactor:** - **Total flow rate:** - **Catalyst loading:** 10 mg **Reaction temperature:** 25 °C **Reaction pressure:** 1 bar	N/A	The coordination sphere of the Fe atom (from Fe^{3+} included only N atoms) formed Fe-N_x (x = 4, 5, and 6) moieties. The Fe–N–C catalyst displayed a high catalytic performance of converting heterocyclic substrates and aliphatic hydrocarbon (cyclohexane) into ketones with >98% selectivity.	[480]
Preferential Oxidation of CO for CO_2 production	**Type of catalysts:** 10 to 50, 100, and 1000 g of Au/CeO_2 **Type of reactor:** Batch **Total flow rate:** - **Catalyst loading:** - **Reaction temperature:** 120 °C **Reaction pressure:** -	Ball milling	The specific rate and TOF of 5.8 mol CO h^{-1} $gmetal^{-1}$ and 0.32 s^{-1} were attained using Au_1/CeO_2 The highly stable Au_1/CeO_2 SACs demonstrated 100% CO conversion for PROX at 120 °C.	[100]
Selective oxidation of methacrolein to methyl methacrylate	**Type of catalysts:** 0.0075 wt. % Ni–Au/SiO_2 **Type of reactor:** Batch reactor **Catalyst loading:** 50 mg **Reaction temperature:** 60 °C **Reaction pressure:** 8.85bar	Sequential reduction technique	Addition of Ni atoms in Au NPs improved the Au activity as Ni–Au SACs demonstrated 100% methyl methacrylate selectivity similar to the catalytic performance of conventional pristine Au catalysts. NiAu SACs were catalytically more active (~2 folds) than pristine NPs in the reaction temperature range at 60 °C.	[497]

to nearly 100% in some cases [544]. Very recently, Li and collaborators [521] reported a single-Fe-atom catalyst tuned with phosphorus (Fe–N/P–C) on commercial carbon black as a robust electrocatalyst for CO_2 reduction (inset in Fig. 26 (a)). The single-Fe-catalyst was synthesized by pyrolyzing a mixture of activated carbon black (ACB) with Fe^{3+} (Fe^{3+}−ACB), urea, and triphenylphosphine in an argon atmosphere. Fourier transform-EXAFS sheds light on the coordination configuration of the single-Fe-atom catalysts. These findings, together with elemental composition and oxidation state analysis from in-situ XPS and AC-STEM-EDX (Fig. 26 (a) and (b)) confirm the presence of atomically dispersed Fe atoms without Fe aggregation (no Fe–Fe bonding from XAS measurements). A high mass-normalized turnover frequency of 508.8 h^{-1} at a low overpotential of 0.34 V, and a high Faradaic efficiency of 98% have been determined for the Fe–N/P–C SAC, that support the outstanding catalytic activity for the CO_2 conversion to CO DFT calculations have been performed to further investigate the catalytic mechanism. The theoretical results have shown that the HER is largely restricted on the P-tuned Fe–N–C catalyst. Moreover, Bader charge analysis underlines a lower oxidation state of Fe which contributes to the CO_2 activation and CO desorption. (Fig. 26 (c) and (d)).

Even though the conversion of CO_2 to CO is appealing since it is a key step in the preparation of Fischer−Tropsch synthetic fuels, extensive efforts need to be devoted to fine-tuning SAC coordination environments, to accurately change catalytic selectivity with multiple electron-

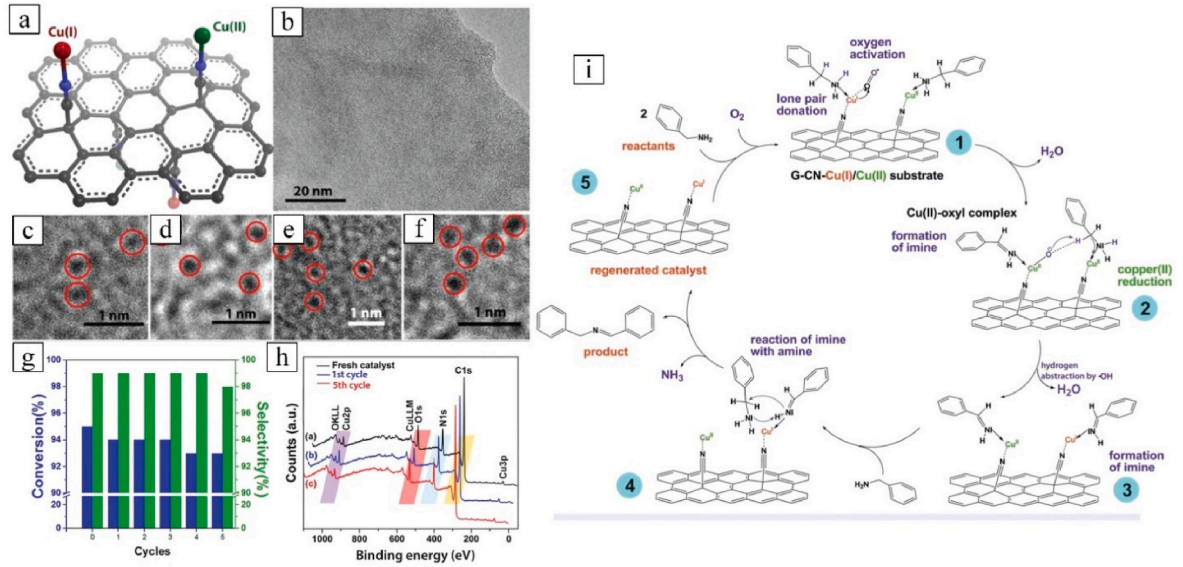

Fig. 24. (a) Schematic model of G(CN)–Cu SAC [282]; (b) TEM image of G(CN)–Cu SAC. HRTEM images (c, d) before and after (e, f) catalytic reaction of G(CN)–Cu SAC (Red circle is the Cu atom) [282]; (g) Effects of reaction cycles on conversion and selectivity using G(CN)–Cu SAC [282]; (h) Effects of the change of binding energy and valence state of Cu atom in the G(CN)–Cu SAC [282]; and (i) Proposed reaction mechanism of the oxidative coupling of benzylamines *via* G(CN)–Cu SAC [282] (all figures have adapted with permission from John Wiley and Son).

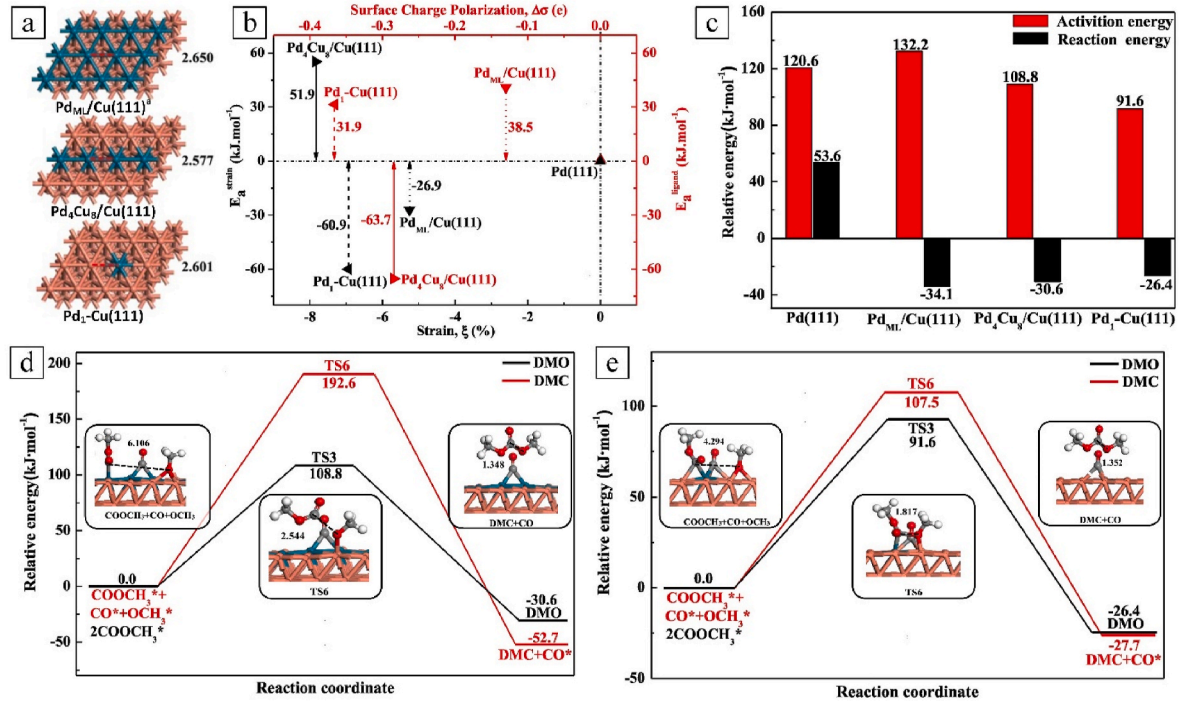

Fig. 25. (a) Configuration illustration of Pd_{ML}-Cu(111) (ML = monolayer), Pd_4Cu_8/Cu(111) and Pd_1–Cu(111) surface [500]; (b) Strain contribution and ligand contribution for conversion of $COOCH_3$ to DMO [500]; (c) Reaction and activation energy for the rate-determining step ($COOCH_3$ to DMO) on Pd_{ML}-Cu(111), Pd_4Cu_8/Cu(111), and Pd_1–Cu(111); The potential energy profile for the rate-determining step in the favorable reaction path toward DMO and DMC synthesis over the (d) Pd_4Cu_8/Cu(111) surface, and (e) Pd_1–Cu(111) surface [500]. (all the figures are adopted with permission from Elsevier).

reducing products which still remains a great challenge and are rarely investigated at present. The electroreduction of carbon dioxide into methanol, which involves a six electron transfer process, has been studied by Yang and collaborators [522] who prepared isolated Cu atoms decorated 'through-hole' carbon nanofibers (CuSAs/TCNFs), with abundant and homogeneously distributed Cu single atoms (CuSAs) for efficient electrochemical CO_2RR, with high stability. CuSAs/TCNFs exhibit 44% Faradaic efficiency and -93 mA cm^{-2} partial current density of methanol. Moreover, the preparation of the CuSAs/TCNFs membrane fulfills the industrial production requirements. DFT calculations underline that the desorption of the adsorbed *CO on CuSAs/TCNFs model is slightly endergonic, suggesting that the CO desorption does not occur, and the *CO intermediate is further hydrogenated to methanol. In recent work, Cai and co-workers [523] proposed a carbon dot (CDs)-supported SAC, which consists of a single-Cu-atom coordinated to two N and two O sites bound to the

edge of graphitic carbons (Cu-CD), as an efficient electrocatalyst for the conversion of CO_2 to CH_4 (eight electron transfer process). The unique structure of the synthesized Cu-CD catalyst allows for high Faradaic efficiency of 78%, superior CH_4 catalytic selectivity at high negative bias, and suppression of the HER. Moreover, the limiting step for CH_4 production was found to be a lower energy value than that reported in other works.

4.5.2. Research advances of SACs for hydrogen fuel cells

Proton exchange membrane fuel cells (PEMFCs) are among the most promising devices to convert chemical energy to electrical energy [545–547]. In these devices, the cathode catalyzes the Oxygen Reduction Reaction (ORR), and the anode catalyzes the oxidation of fuels, such as hydrogen (HOR). The desired ORR is a four-electron process leading to the production of water ($O_2 + 4H+ + 4e^- \rightarrow 4H_2O$), that involves the cleavage of the exceptionally strong O═O bond, whose bond energy is 498 kJ mol^{-1}. Therefore, in order to overcome the slow kinetics of the ORR, efficient electrocatalysts are required. On the other hand, the anode reaction is the hydrogen oxidation reaction ($H_2 \rightarrow 2H+ + 2e^-$), which is a relatively simpler reaction than ORR [514]. Platinum-based materials are the most widely used electrocatalysts for both the ORR and HOR in PEMFCs. However, its extension to large-scale and industrial applications is hindered by high costs and low reserves. Based on that, the development of non-Pt catalysts is of paramount importance. In this regard, the work of Jasinski [548] on the ORR activity of cobalt phthalocyanine paved the way for the development of atomically dispersed M–N–C materials, which exhibit strong ORR performance and great potential for substituting noble metal Pt-based catalysts. DFT was used to investigate the adsorption energy of oxygen intermediates involved in the ORR process on M–N–C, consisting of carbon nanostructures functionalized with pyridinic nitrogen atoms and transition metals [549]. The study revealed differences of up to 0.7 eV among the adsorption energies of the oxygen intermediates on different moieties, which underlined the importance of precisely determining the local site structures in M–N–C materials for understanding their reactivity.

Recently, a Cu SAC was proposed by Cui and collaborators [550].

Table 8
The application of SACs in photocatalytic and electrocatalytic reactions.

Types of reaction	Reaction conditions	SACs preparation method	Key findings	Ref.
CO_2 reduction reaction	**Type of catalysts:** Fe–N–P/C **Type of reactor:** H cell **Catalyst loading:** 0.535 and 0.658 wt.% **Reaction temperature:** 25 °C	Pyrolysis	A high mass-normalized turnover frequency of 508.8 h^{-1} at a low overpotential of 0.34 V, and a high Faradaic efficiency of 98%	[521]
CO_2 reduction reaction	**Type of catalysts:** Cu decorated through-hole carbon nanofibers (CuSAs/TCNF) **Type of reactor:** Undivided cell **Catalyst loading:** 1.3–1.4 wt.% **Reaction temperature:** 25 °C	Chemical Etching	44% Faradaic efficiency and −93 mA cm^{-2} partial current density of methanol, in addition to long-term stability	[522]
CO_2 reduction reaction	**Type of catalysts:** carbon-dots-based SAC margined with unique CuN_2O_2 sites **Type of reactor:** H cell **Catalyst loading:** 0.22–0.35 wt.% **Reaction temperature:** Room temperature	Pyrolysis	High Faradaic efficiency of 78%, superior CH_4 catalytic selectivity at high negative bias, and suppression of the HER	[523]
Oxygen reduction reaction	**Type of catalysts:** CuN_2C_2 **Type of reactor:** A standard three-electrode quartz cell with catalyst-coated glassy carbon (GC) rotating-disk electrode **Catalyst loading:** - **Reaction temperature:** 25 °C	Pyrolysis	Cu SAC showed higher ORR stability and comparable ORR activity with respect to Pt/C in alkaline medium	[524]
Photocatalytic reduction of CO_2	**Type of catalysts:** Co-SA@SP-800 **Catalyst loading:** 30 mg **Reaction temperature:** 5 °C **Reaction pressure:** 0.08 MPa	Incipient wetness impregnation.	With the ultrathin feature of the isolated single-atom cobalt, Co–Bi_3O_4Br demonstrated high photocatalytic performance with high selective yield of CO and formation rate of 107.1 μmol g^{-1} h^{-1}	[525]
Photocatalytic reduction of CO_2	**Type of catalysts:** Co-SA@SP-800 **Catalyst loading:** 2 mg **Reaction temperature:** 25 °C	Incipient wetness impregnation.	CO production yield of 1.64 × 10^4 μmol g^{-1} and a CO selectivity of 84.2% after 2 h of UV illumination. Isolated single atomic Co–N_4 sites reduce the energy barrier for desorption of CO* during CO_2 to CO conversion.	[526]
Photocatalytic reduction of CO_2	**Type of catalysts:** Fe@g-C_3N_4 **Sunlight irradiation range:** 400–550 nm	Pyrolysis	The electronic structures of Fe@g-C_3N_4 SACs were optimized with suitable d-band position and shifted to the Fermi level. This improved the reducibility of the electrons and increased the number of active sites for photocatalytic reactions. The photocatalytic activities enhanced significantly with high photocatalytic H_2 generation rate (3390 μmol h^{-1} g^{-1}) and apparent quantum efficiency value of 6.89% at 420 nm.	[527]
Photocatalytic reduction of CO_2	**Type of catalysts:** $Cu_{0.01}$/3DOM-TiO_2 **Type of reactor:** 170 mL top irradiated reactor **Sunlight irradiation range:** 320–780 nm **Catalyst loading:** 5 mg **Reaction temperature:** 25 °C	Pyrolysis	Cu SACs exhibits higher activity and CH_4 selectivity from CO_2 reduction in the gas–solid system while demonstrated a favorable performance in ethylene formation in liquid–solid system. Good durability of the SACs with well-maintained activity and selectivity after a prolonged irradiation time.	[419]

The catalyst was prepared via a pyrolysis method using Cu phthalocyanine (CuPc) as the precursor and carbon nanotubes as carriers. Aberration-corrected STEM and operando XAS techniques have been used to determine the morphology and electronic properties of the catalyst. The Cu SAC showed higher ORR stability and comparable ORR activity with respect to Pt/C in an alkaline medium, which makes this catalyst a capable non-noble ORR catalyst for fuel cell applications. Moreover, DFT calculations have been performed and suggest that the transformation process from OOH* to O* is the rate-determining step of the ORR on the Cu SAC.

Characterization techniques such as XAS, along with computational methods have been used to gain insights into the dynamic evolution of active sites in operando processes, whose information is crucial for an in-depth understanding of the catalytic behavior of SACs. For instance, Han and co-workers [524] demonstrated the substrate-induced activity improvement of CuN_2C_2 SACs embedded into sp^2-hybridized carbon graphite frameworks. Specifically, the authors state that the increase of the geometry distortion of single-atom CuN_2C_2 active sites, formed when going from a graphene-like material to a small-diameter carbon nanotube (CNT), leads to an improved ORR activity. Indeed, the higher strain in CNT substrates implies a more significant distortion of the CuN_2C_2 moieties during the ORR, which results in strengthening the Cu–O bonds of Cu and the oxygen atoms of the adsorbed species, while weakening the original Cu–N/Cu–C bonds. As a consequence, a higher electron transfer to the adsorbed O_2 molecules is achieved, thus enhancing the ORR activity up to six-fold.

4.5.3. Recent advances of SACs for photocatalytic CO_2 conversion

Photocatalytic reduction of CO_2 to value-added carbon-based fuels and chemicals is one of the most active research fields. In recent years, SACs have been developed and applied extensively as a new class of high-efficient catalysts for photocatalytic CO_2 reduction reaction (CO_2RR), using natural sunlight as an energy source. Apart from their high atom utilization, large specific surface area, and uniformity of active sites, the heterogeneous single atom photocatalysts have many other favorable features including improved energy efficiency with good excitation under visible light, and reducing recombination of photogenerated charges as well as high selectivity towards CO_2 adsorption. Despite efforts being made to develop an efficient photocatalyst with high H_2 generation performance, the poor visible light utilization rate, low quantum yield, severe aggregation of electron pairs caused by photogenerated electrons, and its low stability are some of the barriers and hindrances in bringing these advanced photocatalysts towards practical applications and commercialization.

An example of applying SACs for photocatalytic CO_2RR was by Gao et al. [551], two types of single atoms, palladium, and platinum, were supported on graphitic carbon nitride and investigated as photocatalysts for photocatalytic CO_2RR. From the DFT calculations, the graphitic carbon nitride support itself offers a source of hydrogen atom (H*) from the hydrogen evolution reaction (HER). The deposition of Pd and Pt atoms onto carbon support evidently improves the visible light absorption performance, which renders them an ideal candidate for photocatalytic CO_2RR. For Pd and Pt-based catalysts, the former produces more HCOOH as a product of CO_2 reduction and the latter prefers to form CH_4 from CO_2 with a much higher rate-determining barrier of 1.16 eV, as compared to that of Pd catalysts (0.66 eV). The CO_2 reduction pathways to HCOOH and CH_3OH on Pd/g-C_3N_4 and CO_2 to CH_4 on Pt/g-C_3N_4 catalysts were illustrated in detail, as shown in Fig. 27(a) and (b), respectively.

Noble metals including Pd, Au, and Pd are commonly used as co-catalysts for the photocatalytic reduction of CO_2 due to their inherent low activation energy and effective charge separation. However, such rare elements are still considerably expensive which impedes its large-scale commercial application. Recently, the incorporation of earth–abundant transition metals (e.g. Cu, Ni, Co, and Fe) as an economic alternative for photocatalytic CO_2RR applications has sparked great interest among the scientific community. Chen et al. [419] designed and developed a Cu single-atom catalyst with three-dimensional ordered mesoporous TiO_2 ($Cu_{0.01}$/3DOM-TiO_2) from a template-assisted in-situ pyrolysis method. The proposed synthesis strategy not only caters to a wider light absorption range but offers some specific active sites for the absorption and transformation of CO_2 molecules *via* different pathways (Fig. 27(c)). From the results, the novel single atom photocatalyst exhibits a high methane selectivity of 83.3% with a formation rate of 43.5 μmol g^{-1} h^{-1} under a gas–solid system (Fig. 27(d i-ii)). Whereas under a liquid–solid system, the same single atom catalysts favored the formation of ethylene with a selectivity of 58.4% and formation rate of 6.99 μmol g^{-1} h^{-1} (Fig. 27(d iii-iv)) [551]. From the reaction mechanism study it was revealed that methane is generated from the *CHO intermediates in the gas–solid system while ethylene is produced as the main product from dimerization of *CO and *CHO in the liquid–solid system [551].

Zhang et al. [526] investigated the photocatalytic performance of cobalt-based photocatalysts with Co single atoms isolated and anchored on a commercial 'super conductive' carbon black (Co-SA@SP-800). The as-prepared photocatalyst demonstrates a significant improvement in photoactivity, CO selectivity, and cycling stability, which is mainly due to the highly active isolated Co–N_4 single atomic sites with conductive carbon support. Considering the unique electronic structure of Co SACs toward photocatalytic CO_2 reduction, Di et al. [525] introduced ultra-thin Bi_3O_4Br nanosheets to isolated single atoms Co as an active site and form Co–Bi_3O_4Br catalysts for CO_2 photoreduction reaction. From the results, the designed catalysts exhibited an improved selective CO formation rate of 107.1 μmol g^{-1} h^{-1}, which is ~4 and 32 times higher than that of the atomic layered Bi_3O_4Br and bulk Bi_3O_4Br nanoparticles, respectively [525].

Apart from cobalt-based SACs, both nickel and iron are two low-cost earth–abundant transition metals that can be decorated as SACs for photocatalytic reactions. Zhang et al. [527] designed a highly efficient photocatalytic system by dispersing single-site iron atoms and anchoring on a porous crimped graphitic carbon nitride (g-C_3N_4) polymer. Surprisingly, the synergistic effect of Fe and g-C_3N_4 support promoted the solar-photon-driven activities [527] and led to a higher photocatalytic hydrogen generation rate of 3390 μmol h^{-1} g^{-1}. Similarly, Jin et al. [283] decorated the same support with partially oxidized Ni single atoms with abundant unpaired d-electrons, which improved the absorption performance of visible light and mobility of charge carriers. As a result, the photocatalytic H_2 production rate was improved by 30-fold as compared to that of the bulk g-C_3N_4 and other kinds of polymeric semiconductors.

5. Challenges of SACs bulk production

The unique and promising features of SACs have created a huge application potential in many areas. However, the scalability of this novel material remains a challenging barrier to mass production [14]. Several SAC production challenges need to be addressed to achieve maximum commercial value as shown in Fig. 28.

5.1. Scalability for large-scale application

Various synthesis methods have been considered including physical and chemical methods. Despite many SACs synthesis methods having been developed, the upscaling of laboratory settings into commercial production has not been effective [552]. Physical methods require complex and expensive equipment, while chemical methods cannot be adapted to synthesize SACs containing other transition metals [553]. Besides, a larger-scale synthesis of SACs containing almost any transition metal with high metal loading, with a single synthetic strategy has proven to be elusive. He et al. [169] emphasized that the fabrication cost for SACs remains feasible for commercial production. Additionally, some experiments such as mass-selected soft-landing [554] and atomic

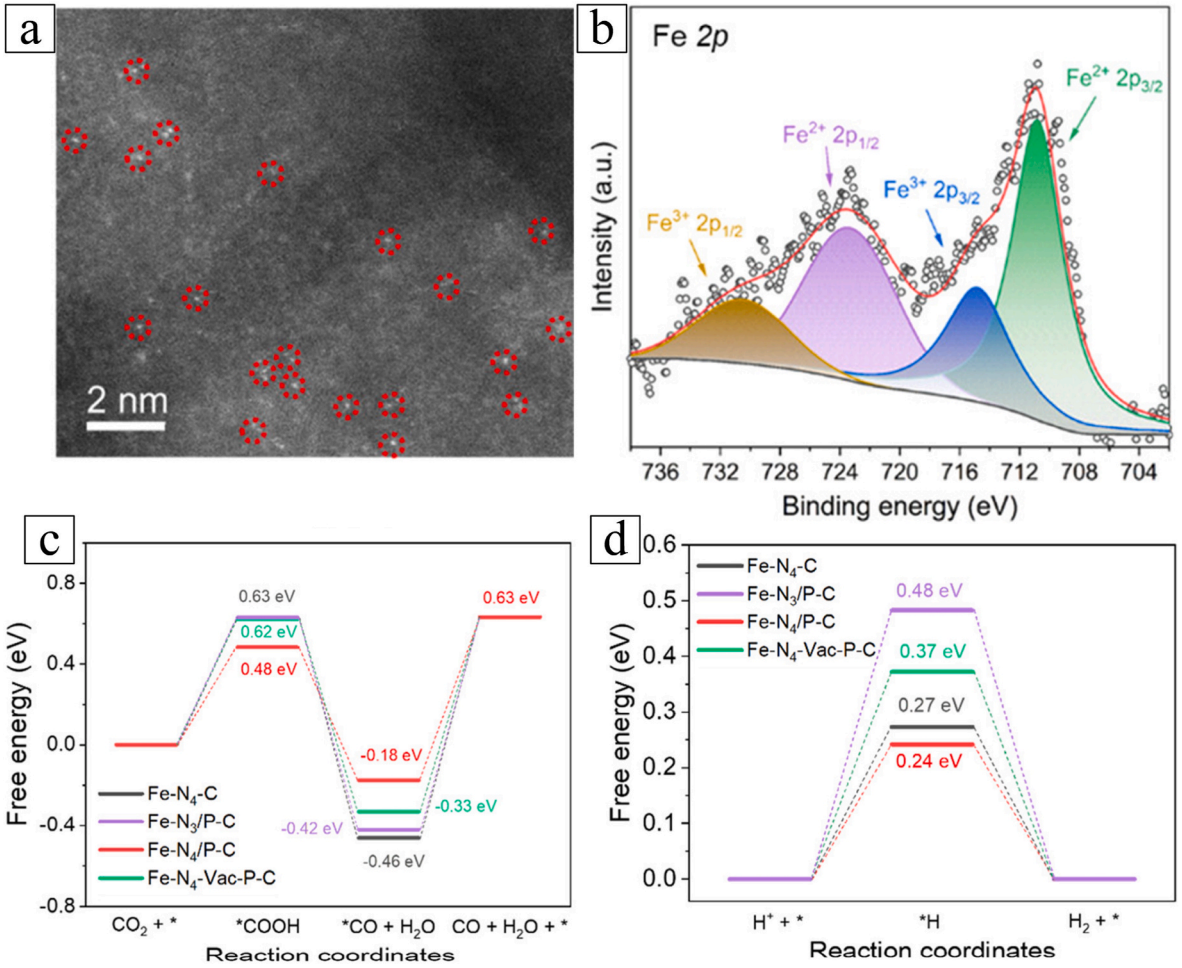

Fig. 26. (a) HAADF images showing the well-dispersed single Fe atoms in bright spots as highlighted by red circles over the entire architecture of the Fe–N/P–C catalyst; Inset: atomic structure model of the Fe–N/P–C catalyst, (b) XPS Fe 2p spectra of Fe–N/P–C, (c) Gibbs free energy profiles of the single-Fe-atom structures with different coordination environments for the electroreduction of CO_2 to CO, (d) Gibbs free energy profiles for hydrogen adsorption on the single-Fe-atom structures with different coordination environments. Inset: Atomic structure model of the Fe–N/P–C catalyst [521]. (all figures adapted with permission from American Chemical Society).

layer deposition [555] are hindered due to expensive experimental requirements and low production efficiency. To date, the largest quantity of SACs reported in the literature was ~1 kg under controlled laboratory environmental conditions [553]. To overcome the challenges of large-scale applications, the adoption of advanced manufacturing such as robotics and automation, not to forget nanotechnologies as well as the use of AI and machine learning is recommended. As such, 3D printing provides a convenient and precise ability to design and print geometrically complex functional SACs that integrate isolated atom, photoactive and catalytic functionalities.

5.2. Development of SAC support material

The performance of SACs can vary with the support material. Su et al. [556] highlighted that the limited diversity of support material for SACs has led to a narrow range of active site structures. Many works on the investigation of carbon-based support materials for SACs have been performed. The support material does not only create a strong bonding between metal atoms and the support surface, but it also affects the support for atom anchoring sites to stabilize the metal atoms [557]. Besides, the support material can improve the catalytic reaction as well. Cheng et al. [552] emphasized that a support material with a high surface area and a large number of anchoring sites can synthesize high-loading SACs. In addition, the surface material with these properties can improve the stability, selectivity, and activity of the SACs. Jing Liu et al. [479] stated that many researchers have experimentally demonstrated the application of support materials such as noble metal oxides and 2D materials to synthesize SACs. Despite the size of these metallic atoms, not all atoms are located on the surface of the catalyst and hence, are not fully accessible to the reactant. Complete accessibility can only be achieved if every single atom is well dispersed and stabilized on the support. Also, the functional groups and defects on the support surface can develop different SAC structures which can affect the stability of SAC. The selection of support material might be challenging for the mass production of SACs.

5.3. Stability of SAC under actual working environment

To produce SACs on a commercial scale, the stability performance of SACs needs to be addressed. Cheng et al. [552] emphasized the stabilization of supported highly dispersed single atoms during catalysis can be challenging due to high surface-free energy and low coordination numbers of single atoms. With the consideration of the dynamic operation conditions, the stability of SACs can be influenced by many factors such as temperature, pressure, support material, surface condition, and reactant [558]. Mostly, in harsh reaction conditions, SACs will undergo loss of active sites under particle migration and coalescence and atomic (or Ostwald) ripening deactivation [559]. In order to prolong the

lifespan and stability of the SACs, utilizing colloidal nanocrystals to independently control particle size and particle loading on the SAC is desired. However, it is very challenging to isolate a clear and precise mechanism of different species of SAC in specific reactions, due to a lack of studies in literatures. In short, further research and understanding of the stabilization of SACs under dynamic working environments is required prior to large-scale application.

5.4. Operando characterization of SAC

In the synthesis of SACs, the characterization methods are essential in determining the quality of the SAC. With the advancement in SACs, advanced characterization equipment is necessary such as STM, EXAFS, AC-STEM, and often DRIFTS [552]. These forms of characterization are in-situ methods of determining the structure of a SAC, while it undergoes its chemical reaction. Li et al. [560] highlighted that the in-situ methods can capture the reaction intermediates, identify active sites, and monitor dynamic behaviors of both geometric structure and electronic environment of catalytic sites. However, Li et al. [560] added that most of the in-situ methods are performed only for the characterization of SACs without simulating catalytic activity, simultaneously. Moreover, each characterization method has its advantage and limitation. Therefore, a detailed SAC characterization under dynamic operating conditions required the integration of in-situ characterization techniques to discover the characterization of SACs under dynamic conditions. Additionally, the cost of the characterization of SACs can be expensive before the characteristics of SACs can be fully validated for commercial use.

6. Economic and environmental aspects

As previously mentioned, the utilization of SACs in energy and chemical applications is still in its infancy (works are mainly at a lab-scale where pilot testing and prototyping are still pending), in which the Technology Readiness Level (TRL) is currently between 1 and 3 [561]. To date, there is no literature reporting on economic or environmental analyses of SACs in any applications. Thus, in order to provide an overview of the commercialization feasibility of SACs, this review article also provides preliminary economic and environmental analyses based on the available resources and information. The assessment portfolio was made based on the catalyst synthesis cost, production cost, CO_2 emission factor, and lifespan of the catalysts (they are ordered clockwise based on increasing CO_2 emissions). This representation highlights that the economic metric does not correlate with the environmental impact. Nevertheless, these findings, it is sufficient to identify the most attractive and potential catalyst, as reported in many research articles [562,563].

The first step of this investigation was the selection of possible reaction which offers suitable characteristics for integration. Based on the data available, the selected reaction was dry reforming of methane (DRM, Figure S1) and six individual case studies were chosen based on the catalyst types, noted as (A) Ni-based SAC [369]; (B) Ni/Al_2O_3 derived from Metal–Organic Framework (MIL-53) [564]; (C) Ni/Al_2O_3–CeO_2 [565]; (D) Ni/TNT [566]; (E) Ni/Al_2O_3 [565] and (F) Pure Ni [567] (note that H_2 is considered as the targeted product). The calculations step and assumptions used are included in the Supplementary information (Tables S1-S8). As presented in Fig. 29, the Ni-based SAC (Ni/HAP-Ce) was the most preferred catalyst for DRM, in terms of both being environmentally friendly and economical. According to the greater details stated in the supplementary information, the cost of preparation for Ni/HAP-Ce *via* co-precipitation was found to be the lowest among other counterparts, also, noteworthy to mention that, the cost was about 3.5 times lower than that of the Ni-MOF. In addition, the

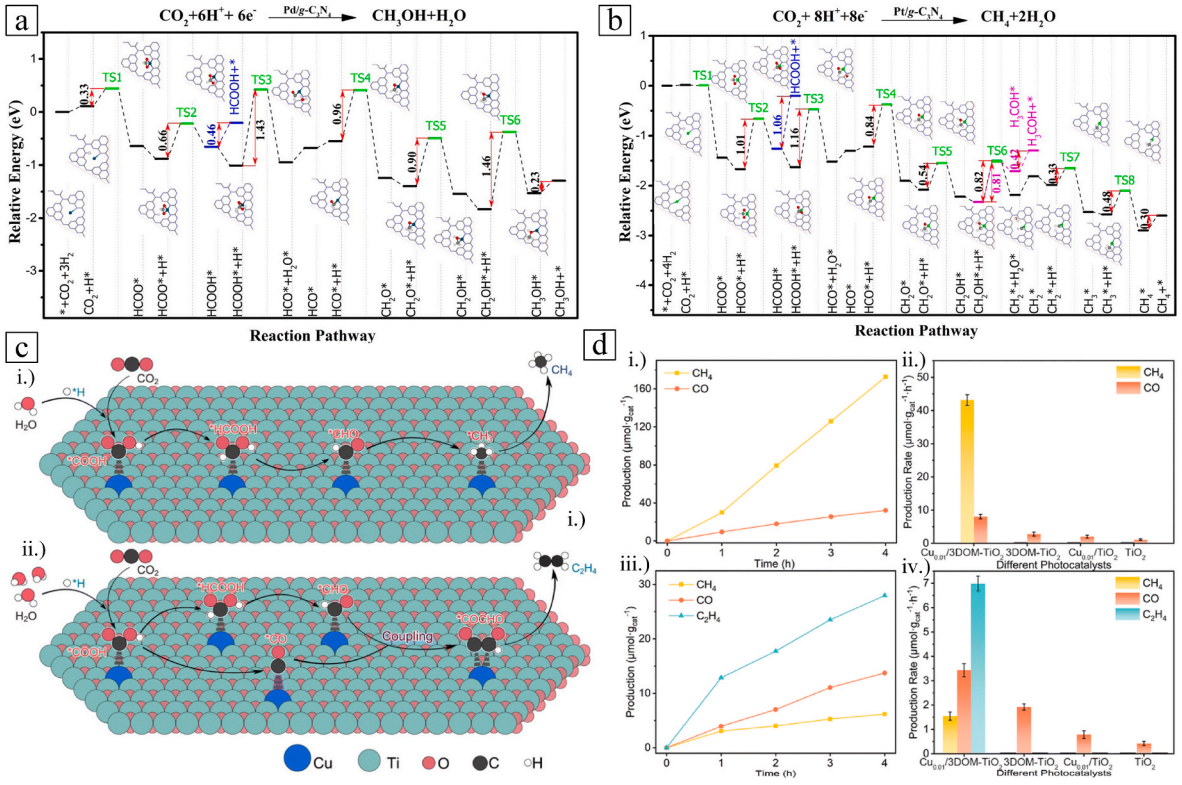

Fig. 27. Reaction pathways for CO_2 reduction to (a) COH, CH_3OH, and CH_4 on Pt/g-C_3N_4 catalyst, (adapted with permission from Elsevier b.v.) (b) CO_2 reduction to HCOOH and CH_3OH on Pd/g-C_3N_4 catalyst. The colour code for the catalyst and small molecules: Pt, green; C, grey; O, red; H, white [551], (adapted with permission from Elsevier) (c) Reaction mechanism of photocatalytic CO_2 reduction over $Cu_{0.01}$/3DOM-TiO_2 catalysts under (i) gas–solid catalytic system and (ii) liquid–solid catalytic system [419]. (adapted with permission from the Royal Society of Chemistry) (d) Photocatalytic CO_2 reduction performance (i-ii) gas–solid catalytic system (iii–iv) liquid–solid system [419]. (adapted with permission from the Royal Society of Chemistry).

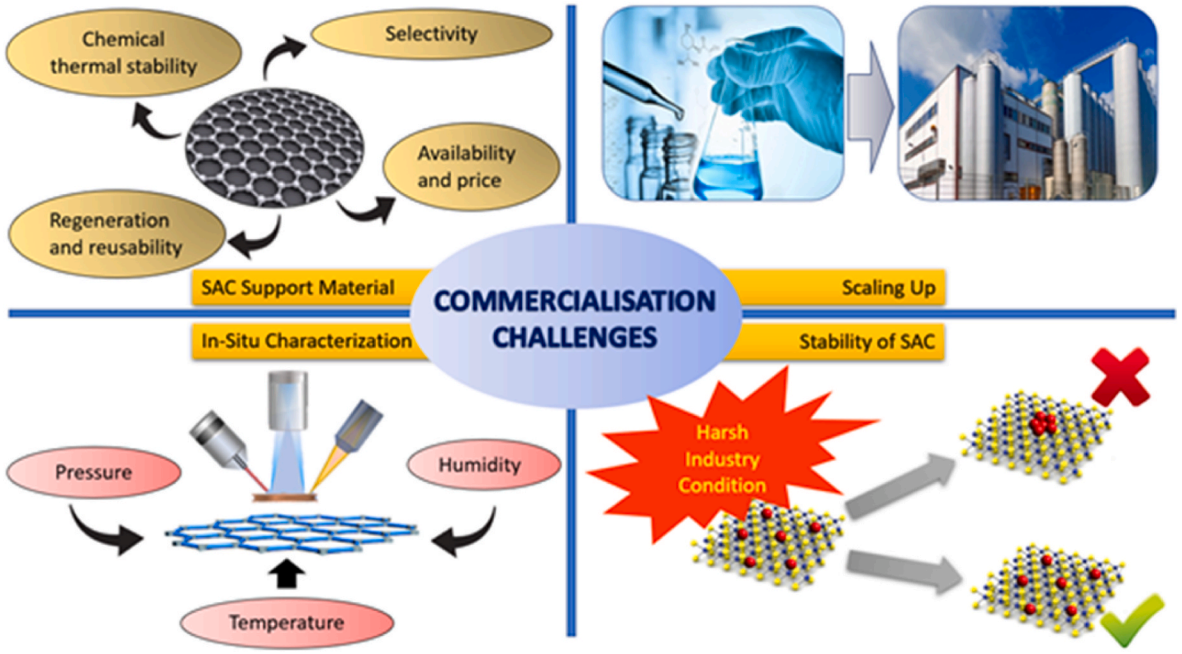

Fig. 28. Commercialization challenges of single atom catalysts (SACs).

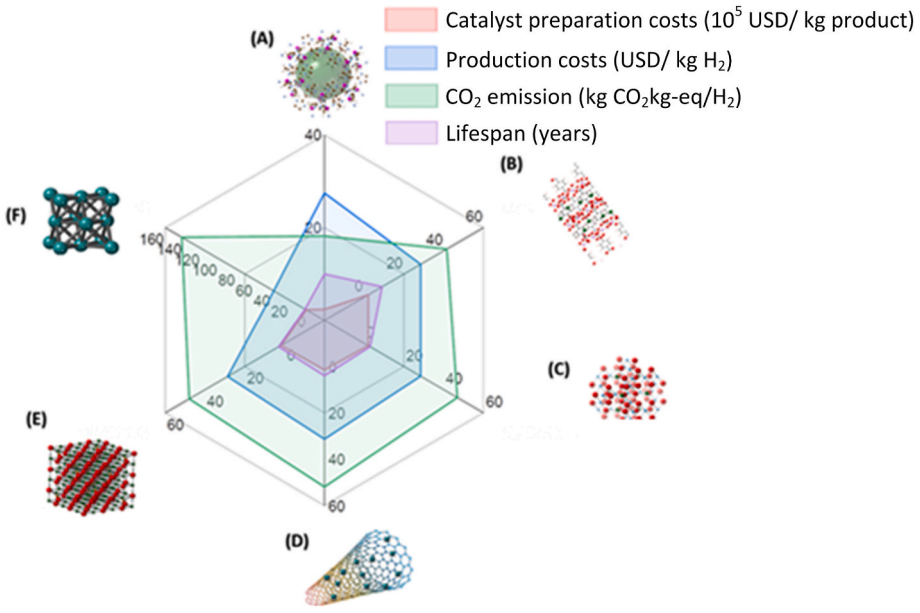

Fig. 29. Comparative Environmental and Economic analyses of different catalysis in DRM (Noting that the "Green" atom is representing the Nickel atom). (A) Ni-based SACs; (B) Ni/Al_2O_3 derived from Metal–Organic Framework (MIL-53); (C) Ni/Al_2O_3–CeO_2; (D) Ni/TNT; (E)Ni/Al_2O_3; and (F) Pure Ni.

total production cost (USD/kg H_2) of Ni-SACs was also calculated to be the lowest compared to other catalysts, which is 26.4% and 1.23% lower than pure Ni (Worst) and Ni-MOF (2nd Best), respectively. Whereas the environmental matrix is measured in terms of CO_2 emissions (kg CO_2/kg H_2 produced). Notably, the CO_2 emissions in catalytic DRM using a Ni-SAC are far lower than other catalysts, i.e., in the range of 2.3–7.5 times lower as compared to that of other catalysts. Overall, given its promising performance in the studied aspects (economic, environmental, and lifespan), SACs emerge as an attractive frontier catalyst to be exploited further too aid the commercialization purpose and strengthen other chemicals and fuel production routes. Future work on conducting rigorous "Integrated Economic, Environmental, and Energy" assessments (3Es) is required to further provide a bigger picture of the frontier of SACs, these assessments could provide decision makers in the commercialization process with feasibility data in determining the most favourable synthesis method of SACs and also suggesting the future research direction, challenges, and debottlenecking of the application of SACs in different field.

7. Concluding remarks and future Perspective

The performance of SACs has gained attention in many sectors as the new frontier in catalysis science, especially in clean energy. This paper highlights the development of SAC synthesis methods from conventional (i.e., co-precipitation or sequential incipient wetness impregnation) to new synthesis methods (i.e., coordination site, defect design,

photochemical and electrochemical). As the development of SAC synthesis is improved, advanced characterization methods such as high-resolution electron microscopes, x-ray irradiation spectroscopies, magnetic resonance spectroscopies, and other wavelength in-situ spectroscopies are used to provide an in-depth understanding of the characteristics of the SAC for clean energy application. On top of that, recent SAC experimental outcomes are reviewed with the consideration of operating conditions, catalyst loading, and types of reactor configurations. Based on the experimental and DFT method output, SACs appear to be an alternative to bridge both homogeneous and heterogenous catalysts for clean energy applications including coupling, oxidation, hydrogenation, and reforming reactions. Through the nano-engineering strategy, bulk nanoparticle catalysts can be downsized by using large surface area support materials, both the surface area and density of defect sites are favorable for the incorporation of single atoms of the active metal, providing some unique catalytic performance such as higher stability and flexible physiochemical properties. Besides that, studies demonstrated that SAC contributes to lowering the reaction activation barrier, enhancing adsorption pathways, processing uniform single active sites, and governing catalytic reactivity for selective routes. The commercialization and large-scale production of SACs require addressing various key challenges including the utilization of affordable support materials, stability of SACs under a mass production environment, and introducing of simple and effective in-situ characterization methods. From this review, it can be observed that the application of SACs is at the forefront of clean energy and chemicals production research, offering strategic alternatives to classical heterogeneous catalytic systems with a major impact on the economy and the environment.

Author contributions

The review was conceptualized by ACML, SYT, MJT, and GK. Data was acquired by ACML and SYT, the overall investigation was carried out by ACML, SYT, BSH, XZ, KWC, VB, WDL, BLFC, and CLY. The review was written by all authors and was reviewed and edited by ACML, MJT, and GK.

Declaration of competing interest

The authors declare the following financial interests/personal relationships which may be considered as potential competing interests:

Dr Martin Taylor reports financial support was provided by UK Research and Innovation. Dr Kin Wai Cheah reports financial support was provided by UK Research and Innovation.

Data availability

No data was used for the research described in the article.

Acknowledgments

MJT and KWC acknowledge funding through the THYME project (UKRI, Research England). A.C.M. Loy would also like to acknowledge the Australian Government Research Training Program for supporting this project. The research contribution from S.Y. Teng is supported by the European Union's Horizon Europe Research and Innovation Program, under Marie Skłodowska-Curie Actions grant agreement no. 101064585 (MoCEGS).

Appendix A. Supplementary data

Supplementary data to this article can be found online at https://doi.org/10.1016/j.pecs.2023.101074.

References

[1] Melhado EM. Jöns jacob Berzelius: Swedish chemist. Encycl Br 1998. https://www.britannica.com/biography/Jons-Jacob-Berzelius/Atomism-and-nomenclature. [Accessed 13 May 2020].
[2] Davis BH. Development of the science of catalysis. Handb. Heterog. Catal. 2008. https://doi.org/10.1002/9783527610044.hetcat0002.
[3] Zhou QL. Transition-metal catalysis and organocatalysis: where can progress Be expected? Angew Chem Int Ed 2016;55:5352–3. https://doi.org/10.1002/anie.201509164.
[4] Ludwig JR, Schindler CS. Catalyst: sustainable catalysis. Chem 2017;2:313–6. https://doi.org/10.1016/j.chempr.2017.02.014.
[5] Rojas Sánchez D, Khalilpour K, Hoadley AFA. How sustainable is CO_2 conversion to ethanol? – a life cycle assessment of a new electrocatalytic carbon utilisation process. Sustain Energy Fuels 2021;5:5866–80. https://doi.org/10.1039/D1SE01462E.
[6] Wei L, Kumar N, Haije W, Peltonen J, Peurla M, Grénman H, et al. Can bi-functional nickel modified 13X and 5A zeolite catalysts for CO2 methanation be improved by introducing ruthenium? Mol Catal 2020;494:111115. https://doi.org/10.1016/j.mcat.2020.111115.
[7] Hamdy MS, Alhanash AM, Eissa M, Ibrahim FA, Abboud M. Selective oxidation of cyclohexane over the bi-functional catalysts Co-MO-TUD-1 (MO = Al2O3, CeO2, NiO, or ZnO). J Porous Mater 2022;29:1287–98. https://doi.org/10.1007/s10934-022-01251-z.
[8] Wang Y, Zhang T, Xiao J, Tian X, Yuan S. Enhancing electrochemical performance of ultrasmall Fe2O3-embedded carbon nanotubes via combusting-induced high-valence dopants. J Mater Sci Technol 2023;134:142–50. https://doi.org/10.1016/j.jmst.2022.06.040.
[9] Mulik N, Bokade V. Immobilization of HPW on UiO-66-NH2 MOF as efficient catalyst for synthesis of furfuryl ether and alkyl levulinate as biofuel. Mol Catal 2022;531:112689. https://doi.org/10.1016/j.mcat.2022.112689.
[10] Hu Y, Yang H, Wang R, Duan M. Fabricating Ag@MOF-5 nanoplates by the template of MOF-5 and evaluating its antibacterial activity. Colloids Surfaces A Physicochem Eng Asp 2021;626:127093. https://doi.org/10.1016/j.colsurfa.2021.127093.
[11] Bolar S, Samanta P, Jang W, Yang C-M, Murmu NC, Kuila T. Regulating the metal concentration for selective tuning of VS 2/MoS 2 heterostructures toward hydrogen evolution reaction in acidic and alkaline media. ACS Appl Energy Mater 2022;5:10086–97. https://doi.org/10.1021/acsaem.2c01763.
[12] Wang W, Shang N, Wang J, Nie X, Du C, Zhou X, et al. A stable single-atom Zn catalyst synthesized by a ligand-stabilized pyrolysis strategy for selective oxidation of C–H bonds. Green Chem 2022;24:6008–15. https://doi.org/10.1039/D2GC01831D.
[13] Yang XF, Wang A, Qiao B, Li J, Liu J, Zhang T. Single-atom catalysts: a new frontier in heterogeneous catalysis. Acc Chem Res 2013;46:1740–8. https://doi.org/10.1021/ar300361m.
[14] Swain S, Altaee A, Saxena M, Samal AK. A comprehensive study on heterogeneous single atom catalysis: current progress, and challenges. Coord Chem Rev 2022;470:214710. https://doi.org/10.1016/j.ccr.2022.214710.
[15] Qin J, Liu H, Zou P, Zhang R, Wang C, Xin HL. Altering ligand fields in single-atom sites through second-shell anion modulation boosts the oxygen reduction reaction. J Am Chem Soc 2022;144:2197–207. https://doi.org/10.1021/jacs.1c11331.
[16] Wan X, Yu W, Niu H, Wang X, Zhang Z, Guo Y. Revealing the oxygen Reduction/Evolution reaction activity origin of Carbon-Nitride-Related Single-Atom catalysts: quantum chemistry in artificial intelligence. Chem Eng J 2022;440:135946. https://doi.org/10.1016/j.cej.2022.135946.
[17] Zhang L, Ren Y, Liu W, Wang A, Zhang T. Single-atom catalyst: a rising star for green synthesis of fine chemicals. Natl Sci Rev 2018;5:653–72. https://doi.org/10.1093/nsr/nwy077.
[18] Ren Y, Tang Y, Zhang L, Liu X, Li L, Miao S, et al. Unraveling the coordination structure-performance relationship in Pt1/Fe2O3 single-atom catalyst. Nat Commun 2019;10:1–9. https://doi.org/10.1038/s41467-019-12459-0.
[19] Qiao B, Wang A, Yang X, Allard LF, Jiang Z, Cui Y, et al. Single-atom catalysis of CO oxidation using Pt1/FeOx. Nat Chem 2011;3:634–41. https://doi.org/10.1038/nchem.1095.
[20] Haruta M, Yamada N, Kobayashi T, Iijima S. Gold catalysts prepared by coprecipitation for low-temperature oxidation of hydrogen and of carbon monoxide. J Catal 1989;115:301–9. https://doi.org/10.1016/0021-9517(89)90034-1.
[21] Haruta M, Tsubota S, Kobayashi T, Kageyama H, Genet MJ, Delmon B. Low-temperature oxidation of CO over gold supported on TiO2, α-Fe2O3, and Co3O4. J Catal 1993;144:175–92. https://doi.org/10.1006/jcat.1993.1322.
[22] Kyriakou G, Boucher MB, Jewell AD, Lewis EA, Lawton TJ, Baber AE, et al. Isolated metal atom geometries as a strategy for selective heterogeneous hydrogenations. Science 2012;335(80):1209–12. https://doi.org/10.1126/science.1215864.
[23] Knurr BJ, Weber JM. Solvent-driven reductive activation of carbon dioxide by gold anions. J Am Chem Soc 2012;134. https://doi.org/10.1021/ja308991a. 18804–8.
[24] Lin J, Wang A, Qiao B, Liu X, Yang X, Wang X, et al. Remarkable performance of Ir1/FeOx single-atom catalyst in water gas shift reaction. J Am Chem Soc 2013;135:15314–7. https://doi.org/10.1021/ja408574m.
[25] Wang L, Zhang S, Zhu Y, Patlolla A, Shan J, Yoshida H, et al. Catalysis and in situ studies of Rh1/Co3O4 nanorods in reduction of NO with H2. ACS Catal 2013;3:1011–9. https://doi.org/10.1021/cs300816u.

[26] Wang Y, Zhou Q, Yang M, Wang J. Isomorphous substituted bimetallic oxide cluster as a novel strategy for single-atom catalysis. Comput Theor Chem 2013; 1021:262–7. https://doi.org/10.1016/j.comptc.2013.07.043.

[27] Sun S, Zhang G, Gauquelin N, Chen N, Zhou J, Yang S, et al. Single-atom catalysis using Pt/graphene achieved through atomic layer deposition. Sci Rep 2013;3:1–9. https://doi.org/10.1038/srep01775.

[28] Zhang H, Kawashima K, Okumura M, Toshima N. Colloidal Au single-atom catalysts embedded on Pd nanoclusters. J Mater Chem 2014;2:13498–508. https://doi.org/10.1039/c4ta01696c.

[29] Shi Y, Zhao C, Wei H, Guo J, Liang S, Wang A, et al. Single-atom catalysis in mesoporous photovoltaics: the principle of utility maximization. Adv Mater 2014; 26:8147–53. https://doi.org/10.1002/adma.201402978.

[30] Hu P, Huang Z, Amghouz Z, Makkee M, Xu F, Kapteijn F, et al. Electronic metal-support interactions in single-atom catalysts. Angew Chem Int Ed 2014;126: 3486–9. https://doi.org/10.1002/anie.201309248.

[31] Chang Z, Zhao W, Liu M, Fan M, Wang B, Zhang R. Intrinsic activity and selectivity enhancement of single-atom Rh in syngas-to-C2 oxygenates by engineering the local coordination atom. Appl Surf Sci 2022;597:153755. https://doi.org/10.1016/j.apsusc.2022.153755.

[32] Iuliano M, Sarno M, Cirillo C, Ponticorvo E, De Pasquale S. Easy and one-step synthesis of Ir single atom doped PPy nanoparticles for highly active N-alkylation reaction. Eur J Inorg Chem 2021;2021:644–53. https://doi.org/10.1002/ejic.202000971.

[33] Zhang X, Lu G-P, Wang K, Lin Y, Wang P, Yi W. Lignin-derived Zn single atom/N-codoped porous carbon for α-alkylation of aromatic ketones with alcohols via borrowing hydrogen strategy. Nano Res 2022;15:1874–81. https://doi.org/10.1007/s12274-021-3788-y.

[34] Gao Y, Yan D, Wang C, Chen J, Chen J, Jia H. Regeneration of La 2 O 3 -supported Pt nanoparticles giving high loadings of thermally stable Pt single atoms on La 2 O 3 supports: implications for catalysis. ACS Appl Nano Mater 2022;5:2688–98. https://doi.org/10.1021/acsanm.1c04363.

[35] Wei H, Liu X, Wang A, Zhang L, Qiao B, Yang X, et al. FeO x -supported platinum single-atom and pseudo-single-atom catalysts for chemoselective hydrogenation of functionalized nitroarenes. Nat Commun 2014;5:1–8. https://doi.org/10.1038/ncomms6634.

[36] Yan H, Cheng H, Yi H, Lin Y, Yao T, Wang C, et al. Single-atom Pd1/graphene catalyst achieved by atomic layer deposition: remarkable performance in selective hydrogenation of 1,3-butadiene. J Am Chem Soc 2015;137:10484–7. https://doi.org/10.1021/jacs.5b06485.

[37] Zhang Z, Zhu Y, Asakura H, Zhang B, Zhang J, Zhou M, et al. Thermally stable single atom Pt/m-Al2O3 for selective hydrogenation and CO oxidation. Nat Commun 2017;8:1–10. https://doi.org/10.1038/ncomms16100.

[38] Lin J, Qiao B, Li N, Li L, Sun X, Liu J, et al. Little do more: a highly effective Pt1/FeOx single-atom catalyst for the reduction of NO by H2. Chem Commun 2015; 51:7911–4. https://doi.org/10.1039/c5cc00714c.

[39] Lang R, Li T, Matsumura D, Miao S, Ren Y, Cui YT, et al. Hydroformylation of olefins by a rhodium single-atom catalyst with activity comparable to RhCl(PPh3) 3. Angew Chem Int Ed 2016;55:16054–8. https://doi.org/10.1002/anie.201607885.

[40] Gu Y, Wang X, Bao A, Dong L, Zhang X, Pan H, et al. Enhancing electrical conductivity of single-atom doped Co3O4 nanosheet arrays at grain boundary by phosphor doping strategy for efficient water splitting. Nano Res 2022;15:9511–9. https://doi.org/10.1007/s12274-022-4738-z.

[41] Li F, Li Y, Zeng XC, Chen Z. Exploration of high-performance single-atom catalysts on support M1/FeOx for CO oxidation via computational study. ACS Catal 2015; 5:544–52. https://doi.org/10.1021/cs501790v.

[42] Zhang L, Wang A, Miller JT, Liu X, Yang X, Wang W, et al. Efficient and durable Au alloyed Pd single-atom catalyst for the Ullmann reaction of aryl chlorides in water. ACS Catal 2014;4:1546–53. https://doi.org/10.1021/cs500071c.

[43] Cao X, Ji Y, Luo Y. Dehydrogenation of propane to propylene by a Pd/Cu single-atom catalyst: insight from first-principles calculations. J Phys Chem C 2015;119: 1016–23. https://doi.org/10.1021/jp508625b.

[44] Pei GX, Liu XY, Wang A, Lee AF, Isaacs MA, Li L, et al. Ag alloyed Pd single-atom catalysts for efficient selective hydrogenation of acetylene to ethylene in excess ethylene. ACS Catal 2015;5:3717–25. https://doi.org/10.1021/acscatal.5b00700.

[45] Qi Y, Gao J, Zhang D, Liu C. Comparative theoretical study of formic acid decomposition on PtAg(111) and Pt(111) surfaces. RSC Adv 2015;5:21170–7. https://doi.org/10.1039/c5ra01925g.

[46] Islam MJ, Granollers Mesa M, Osatiashtiani A, Manayil JC, Isaacs MA, Taylor MJ, et al. PdCu single atom alloys supported on alumina for the selective hydrogenation of furfural. Appl Catal B Environ 2021;299:120652. https://doi.org/10.1016/j.apcatb.2021.120652.

[47] Han Y, Dai J, Xu R, Ai W, Zheng L, Wang Y, et al. Notched-polyoxometalate strategy to fabricate atomically dispersed Ru catalysts for biomass conversion. ACS Catal 2021;11:2669–75. https://doi.org/10.1021/acscatal.0c04006.

[48] Yang S, Kim J, Tak YJ, Soon A, Lee H. Single-atom catalyst of platinum supported on titanium nitride for selective electrochemical reactions. Angew Chem Int Ed 2016;55:2058–62. https://doi.org/10.1002/anie.201509241.

[49] Choi CH, Kim M, Kwon HC, Cho SJ, Yun S, Kim HT, et al. Tuning selectivity of electrochemical reactions by atomically dispersed platinum catalyst. Nat Commun 2016;7:1–9. https://doi.org/10.1038/ncomms10922.

[50] Cheng X, Wang Y, Lu Y, Zheng L, Sun S, Li H, et al. Single-atom alloy with Pt-Co dual sites as an efficient electrocatalyst for oxygen reduction reaction. Appl Catal B Environ 2022;306:121112. https://doi.org/10.1016/j.apcatb.2022.121112.

[51] Li X, Bi W, Zhang L, Tao S, Chu W, Zhang Q, et al. Single-atom Pt as Co-catalyst for enhanced photocatalytic H2 evolution. Adv Mater 2016;28:2427–31. https://doi.org/10.1002/adma.201505281.

[52] Zhang L, Han L, Liu H, Liu X, Luo J. Potential-cycling synthesis of single platinum atoms for efficient hydrogen evolution in neutral media. Angew Chem Int Ed 2017;56:13694–8. https://doi.org/10.1002/anie.201706921.

[53] Liu D, Li X, Chen S, Yan H, Wang C, Wu C, et al. Atomically dispersed platinum supported on curved carbon supports for efficient electrocatalytic hydrogen evolution. Nat Energy 2019;4:512–8. https://doi.org/10.1038/s41560-019-0402-6.

[54] Zhong B, Wen C, Peng Y, Zhang X, Qiu Z, Xu H. Hydrogen evolution reaction activity obtained using platinum single atoms on TiO2 nanosheets modified with graphene. J Mater Sci 2022;57:16448–59. https://doi.org/10.1007/s10853-022-07673-z.

[55] Kamai R, Nakanishi S, Hashimoto K, Kamiya K. Selective electrochemical reduction of nitrogen oxides by covalent triazine frameworks modified with single Pt atoms. J Electroanal Chem 2017;800:54–9. https://doi.org/10.1016/j.jelechem.2016.09.027.

[56] Ling C, Bai X, Ouyang Y, Du A, Wang J. Single molybdenum atom anchored on N-doped carbon as a promising electrocatalyst for nitrogen reduction into ammonia at ambient conditions. J Phys Chem C 2018;122:16842–7. https://doi.org/10.1021/acs.jpcc.8b05257.

[57] Tao H, Choi C, Ding LX, Jiang Z, Han Z, Jia M, et al. Nitrogen fixation by Ru single-atom electrocatalytic reduction. Chem 2019;5:204–14. https://doi.org/10.1016/j.chempr.2018.10.007.

[58] He H, Jagvaral Y. Electrochemical reduction of CO2 on graphene supported transition metals-towards single atom catalysts. Phys Chem Chem Phys 2017;19: 11436–46. https://doi.org/10.1039/c7cp00915a.

[59] Fei H, Dong J, Arellano-Jiménez MJ, Ye G, Dong Kim N, Samuel ELG, et al. Atomic cobalt on nitrogen-doped graphene for hydrogen generation. Nat Commun 2015;6:1–8. https://doi.org/10.1038/ncomms9668.

[60] Zhang L, Wang A, Wang W, Huang Y, Liu X, Miao S, et al. Co-N-C catalyst for C-C coupling reactions: on the catalytic performance and active sites. ACS Catal 2015; 5:6563–72. https://doi.org/10.1021/acscatal.5b01223.

[61] Guo X, Fang G, Li G, Ma H, Fan H, Yu L, et al. Direct, nonoxidative conversion of methane to ethylene, aromatics, and hydrogen. Science 2014;344(80):616–9. https://doi.org/10.1126/science.1253150.

[62] Liu X, Deng Y, Zheng L, Kesama MR, Tang C, Zhu Y. Engineering low-coordination single-atom cobalt on graphitic carbon nitride catalyst for hydrogen evolution. ACS Catal 2022;12:5517–26. https://doi.org/10.1021/acscatal.2c01253.

[63] Gao X, Zhou Y, Liu S, Cheng Z, Tan Y, Shen Z. Single cobalt atom anchored on N-doped graphyne for boosting the overall water splitting. Appl Surf Sci 2020;502: 144155. https://doi.org/10.1016/j.apsusc.2019.144155.

[64] Chodvadiya D, Jha PK, Chakraborty B. Theoretical inspection of Ni/α-SiX (X=N, P, As, Sb, Bi) Single-Atom catalyst: ultra-high performance for hydrogen evolution reaction. Int J Hydrogen Energy 2022;47:41733–47. https://doi.org/10.1016/j.ijhydene.2022.02.159.

[65] Xiong Y, Sun W, Han Y, Xin P, Zheng X, Yan W, et al. Cobalt single atom site catalysts with ultrahigh metal loading for enhanced aerobic oxidation of ethylbenzene. Nano Res 2021;14:2418–23. https://doi.org/10.1007/s12274-020-3244-4.

[66] Li S, Guan A, Wang H, Yan Y, Huang H, Jing C, et al. Hybrid palladium nanoparticles and nickel single atom catalysts for efficient electrocatalytic ethanol oxidation. J Mater Chem 2022;10:6129–33. https://doi.org/10.1039/D1TA08518B.

[67] Jiang W, An X, Xiao J, Yang Z, Liu J, Chen H, et al. Enhanced oxygen activation achieved by robust single chromium atom-derived catalysts in aerobic oxidative desulfurization. ACS Catal 2022;12:8623–31. https://doi.org/10.1021/acscatal.2c01329.

[68] Liang JX, Yang XF, Wang A, Zhang T, Li J. Theoretical investigations of non-noble metal single-atom catalysis: Ni1/FeO: x for CO oxidation. Catal Sci Technol 2016; 6:6886–92. https://doi.org/10.1039/c6cy00672h.

[69] Li D, Li W, Zhang J. CO oxidation on atomic nickel/phosphorene nanosheet: an efficient single-atom catalyst. Mol Catal 2021;510:111626. https://doi.org/10.1016/j.mcat.2021.111626.

[70] Ren M, Zhang L, Zhu Y, Shi J, Zhao X, Ren X, et al. Highly efficient catalytic properties of Sc and Fe single atoms stabilized on a honeycomb borophene/Al (111) heterostructure via a dual charge transfer effect. Nanoscale 2021;13: 5875–82. https://doi.org/10.1039/D0NR08065A.

[71] Cai B, Zhou J, Li D, Ao Z. New insights into the single-atom-decorated Zr2CO2 (MXene) as an efficient catalyst for CO oxidation in incomplete combustion gas. Appl Surf Sci 2022;575:151777. https://doi.org/10.1016/j.apsusc.2021.151777.

[72] Li J, Kang L. Non-noble metal single atom catalysts with S, N co-doped defective graphene support: a theoretical study of highly efficient acetylene hydration. Mater Today Commun 2021;27:102216. https://doi.org/10.1016/j.mtcomm.2021.102216.

[73] Zhao C, Dai X, Yao T, Chen W, Wang X, Wang J, et al. Ionic exchange of metal-organic frameworks to access single nickel sites for efficient electroreduction of CO2. J Am Chem Soc 2017;139:8078–81. https://doi.org/10.1021/jacs.7b02736.

[74] Jiang K, Siahrostami S, Zheng T, Hu Y, Hwang S, Stavitski E, et al. Isolated Ni single atoms in graphene nanosheets for high-performance CO2 reduction. Energy Environ Sci 2018;11:893–903. https://doi.org/10.1039/c7ee03245e.

[75] Zheng T, Jiang K, Ta N, Hu Y, Zeng J, Liu J, et al. Large-scale and highly selective CO 2 electrocatalytic reduction on nickel single-atom catalyst. Joule 2019;3: 265–78. https://doi.org/10.1016/j.joule.2018.10.015.

[76] Yang F, Song P, Liu X, Mei B, Xing W, Jiang Z, et al. Highly efficient CO2 electroreduction on ZnN4-based single-atom catalyst. Angew Chem Int Ed 2018; 57:12303–7. https://doi.org/10.1002/anie.201805871.

[77] Zhang Y, Cao X, Cao Z. Unraveling the catalytic performance of the nonprecious metal single-atom-embedded graphitic s -Triazine-Based C 3 N 4 for CO 2 hydrogenation. ACS Appl Mater Interfaces 2022;14:35844–53. https://doi.org/10.1021/acsami.2c09813.

[78] Rao P, Luo J, Wu D, Li J, Chen Q, Deng P, et al. Isolated Co atoms anchored on defective nitrogen-doped carbon graphene as efficient oxygen reduction reaction electrocatalysts. Energy Environ Mater 2022:1–6. https://doi.org/10.1002/eem2.12371.

[79] Chen Y, Ji S, Wang Y, Dong J, Chen W, Li Z, et al. Isolated single iron atoms anchored on N-doped porous carbon as an efficient electrocatalyst for the oxygen reduction reaction. Angew Chem Int Ed 2017;129:7041–5. https://doi.org/10.1002/anie.201702473.

[80] Zhang Z, Sun J, Wang F, Dai L. Efficient oxygen reduction reaction (ORR) catalysts based on single iron atoms dispersed on a hierarchically structured porous carbon framework. Angew Chem Int Ed 2018;130:9176–81. https://doi.org/10.1002/anie.201804958.

[81] Li X, Zhang Y, Zhang J, Wang C. Isolated Fe atoms dispersed on cellulose-derived nanocarbons as an efficient electrocatalyst for the oxygen reduction reaction. Nanoscale 2019;11:23110–5. https://doi.org/10.1039/c9nr07914a.

[82] Talib SH, Lu Z, Yu X, Ahmad K, Bashir B, Yang Z, et al. Theoretical inspection of M 1/PMA single-atom electrocatalyst: ultra-high performance for water splitting (HER/OER) and oxygen reduction reactions (OER). ACS Catal 2021;11:8929–41. https://doi.org/10.1021/acscatal.1c01294.

[83] Fei H, Dong J, Feng Y, Allen CS, Wan C, Volosskiy B, et al. General synthesis and definitive structural identification of MN4C4 single-atom catalysts with tunable electrocatalytic activities. Nat Catal 2018;1:63–72. https://doi.org/10.1038/s41929-017-0008-y.

[84] Zhang Z, Gao X, Dou M, Ji J, Wang F. Biomass derived N-doped porous carbon supported single Fe atoms as superior electrocatalysts for oxygen reduction. Small 2017;13:1604290. https://doi.org/10.1002/smll.201604290.

[85] Li S-L, Li Q, Chen Y, Zhao Y, Gan L-Y. Transition metal embedded graphynes as advanced bifunctional single atom catalysts for oxygen reduction and evolution reactions. Appl Surf Sci 2022;605:154828. https://doi.org/10.1016/j.apsusc.2022.154828.

[86] Ling Y, Ge H, Chen J, Zhang Y, Duan Y, Liang M, et al. General strategy toward hydrophilic single atom catalysts for efficient selective hydrogenation. Adv Sci 2022;9:2202144. https://doi.org/10.1002/advs.202202144.

[87] Liang J, Yu Q, Yang X, Zhang T, Li J. A systematic theoretical study on FeOx-supported single-atom catalysts: M1/FeOx for CO oxidation. Nano Res 2018;11:1599–611. https://doi.org/10.1007/s12274-017-1775-0.

[88] Wang D, Li H, Du N, Hou W. Single platinum atoms immobilized on monolayer tungsten trioxide nanosheets as an efficient electrocatalyst for hydrogen evolution reaction. Adv Funct Mater 2021;31:2009770. https://doi.org/10.1002/adfm.202009770.

[89] Liu J, Kong X, Zheng L, Guo X, Liu X, Shui J. Rare earth single-atom catalysts for nitrogen and carbon dioxide reduction. ACS Nano 2020;14:1093–101. https://doi.org/10.1021/acsnano.9b08835.

[90] Hu F, Liao L, Chi B, Wang H. Rare earth praseodymium-based single atom catalyst for high performance CO2 reduction reaction. Chem Eng J 2022;436:135271. https://doi.org/10.1016/j.cej.2022.135271.

[91] Ji S, Qu Y, Wang T, Chen Y, Wang G, Li X, et al. Rare-earth single erbium atoms for enhanced photocatalytic CO2 reduction. Angew Chem Int Ed 2020;59:10651–7. https://doi.org/10.1002/anie.202003623.

[92] Fu J, Dong J, Si R, Sun K, Zhang J, Li M, et al. Synergistic effects for enhanced catalysis in a dual single-atom catalyst. ACS Catal 2021;11:1952–61. https://doi.org/10.1021/acscatal.0c05599.

[93] Kaiser SK, Clark AH, Cartocci L, Krumeich F, Pérez-Ramírez J. Sustainable synthesis of bimetallic single atom gold-based catalysts with enhanced durability in acetylene hydrochlorination. Small 2021;17:2004599. https://doi.org/10.1002/smll.202004599.

[94] He X, He Q, Deng Y, Peng M, Chen H, Zhang Y, et al. A versatile route to fabricate single atom catalysts with high chemoselectivity and regioselectivity in hydrogenation. Nat Commun 2019;10:3663. https://doi.org/10.1038/s41467-019-11619-6.

[95] Giulimondi V, Ruiz–Ferrando A, Clark AH, Kaiser SK, Krumeich F, Martín AJ, et al. Catalytic synergies in bimetallic Ru-Pt single–atom catalysts via speciation control. Adv Funct Mater 2022;32:2206513. https://doi.org/10.1002/adfm.202206513.

[96] Kumar A, Bui VQ, Lee J, Wang L, Jadhav AR, Liu X, et al. Moving beyond bimetallic-alloy to single-atom dimer atomic-interface for all-pH hydrogen evolution. Nat Commun 2021;12:6766. https://doi.org/10.1038/s41467-021-27145-3.

[97] Zhao M, Yang R, Wei Y, Su J, Wang X, Zhang N, et al. Dual isolated bimetal single-atom catalysts for tumor ROS cycle and parallel catalytic therapy. Nano Today 2022;44:101493. https://doi.org/10.1016/j.nantod.2022.101493.

[98] Zhao K, Quan X, Su Y, Qin X, Chen S, Yu H. Enhanced chlorinated pollutant degradation by the synergistic effect between dechlorination and hydroxyl radical oxidation on a bimetallic single-atom catalyst. Environ Sci Technol 2021;55:14194–203. https://doi.org/10.1021/acs.est.1c04943.

[99] Deng D, Chen X, Yu L, Wu X, Liu Q, Liu Y, et al. Chemistry: a single iron site confined in a graphene matrix for the catalytic oxidation of benzene at room temperature. Sci Adv 2015;1:e1500462. https://doi.org/10.1126/sciadv.1500462.

[100] Gan T, He Q, Zhang H, Xiao H, Liu Y, Zhang Y, et al. Unveiling the kilogram-scale gold single-atom catalysts via ball milling for preferential oxidation of CO in excess hydrogen. Chem Eng J 2020;389:124490. https://doi.org/10.1016/j.cej.2020.124490.

[101] Zhao S, Cheng Y, Veder JP, Johannessen B, Saunders M, Zhang L, et al. One-pot pyrolysis method to fabricate carbon nanotube supported Ni single-atom catalysts with ultrahigh loading. ACS Appl Energy Mater 2018;1:5286–97. https://doi.org/10.1021/acsaem.8b00903.

[102] Liu P, Zhao Y, Qin R, Mo S, Chen G, Gu L, et al. Catalysis: photochemical route for synthesizing atomically dispersed palladium catalysts. Science 2016;352(80):797–800. https://doi.org/10.1126/science.aaf5251.

[103] Qu Y, Chen B, Li Z, Duan X, Wang L, Lin Y, et al. Thermal emitting strategy to synthesize atomically dispersed Pt metal sites from bulk Pt metal. J Am Chem Soc 2019;141:4505–9. https://doi.org/10.1021/jacs.8b09834.

[104] Zhao L, Zhang Y, Huang LB, Liu XZ, Zhang QH, He C, et al. Cascade anchoring strategy for general mass production of high-loading single-atomic metal-nitrogen catalysts. Nat Commun 2019;10:1–11. https://doi.org/10.1038/s41467-019-09290-y.

[105] Copéret C. Fuels and energy carriers from single-site catalysts prepared via surface organometallic chemistry. Nat Energy 2019;4:1018–24. https://doi.org/10.1038/s41560-019-0491-2.

[106] Zhang Z, Feng C, Liu C, Zuo M, Qin L, Yan X, et al. Electrochemical deposition as a universal route for fabricating single-atom catalysts. Nat Commun 2020;11:1–8. https://doi.org/10.1038/s41467-020-14917-6.

[107] Rivera-Cárcamo C, Leng F, Gerber IC, del Rosal I, Poteau R, Collière V, et al. Catalysis to discriminate single atoms from subnanometric ruthenium particles in ultra-high loading catalysts. Catal Sci Technol 2020;10:4673–83. https://doi.org/10.1039/D0CY00540A.

[108] Hai X, Xi S, Mitchell S, Harrath K, Xu H, Akl DF, et al. Scalable two-step annealing method for preparing ultra-high-density single-atom catalyst libraries. Nat Nanotechnol 2022;17:174–81. https://doi.org/10.1038/s41565-021-01022-y.

[109] Yang P, Zuo S, Zhang F, Yu B, Guo S, Yu X, et al. Carbon nitride-based single-atom Cu catalysts for highly efficient carboxylation of alkynes with atmospheric CO 2. Ind Eng Chem Res 2020;59:7327–35. https://doi.org/10.1021/acs.iecr.0c00547.

[110] Lin C, Zhang H, Song X, Kim D-H, Li X, Jiang Z, et al. 2D-organic framework confined metal single atoms with the loading reaching the theoretical limit. Mater Horiz 2020;7:2726–33. https://doi.org/10.1039/D0MH01061H.

[111] Ma M, Huang Z, Doronkin DE, Fa W, Rao Z, Zou Y, et al. Ultrahigh surface density of Co-N2C single-atom-sites for boosting photocatalytic CO2 reduction to methanol. Appl Catal B Environ 2022;300:120695. https://doi.org/10.1016/j.apcatb.2021.120695.

[112] Geonames.org. GeoNames Database. GeoNames 2020. https://www.geonames.org/4061113/excel.html.

[113] Elsevier BV. Scopus preview - Scopus - welcome to Scopus. Welcome to Scopus Preview; 2004.

[114] Google. Google. Patent. Google Pat 2020. https://patents.google.com.

[115] World Intellectual Property Organization (WIPO). PATENTSCOPE. IP databases. 2020. https://www.wipo.int/portal/en/index.html.

[116] European Patent Office. Patents. Eur Pat Search 2020. https://www.epo.org/.

[117] Liang Z, Shen J, Xu X, Li F, Liu J, Yuan B, et al. Advances in the development of single-atom catalysts for high-energy-density lithium–sulfur batteries. Adv Mater 2022;34:2200102. https://doi.org/10.1002/adma.202200102.

[118] Li W, Guo Z, Yang J, Li Y, Sun X, He H, et al. Advanced strategies for stabilizing single-atom catalysts for energy storage and conversion. Electrochem Energy Rev 2022;5:9. https://doi.org/10.1007/s41918-022-00169-z.

[119] Burda C, Chen X, Narayanan R, El-Sayed MA. Chemistry and Properties of NAnocrystals of Different Shapes. Chem Rev 2005;105(4):1025–103. https://doi.org/10.1021/cr030063a.

[120] Rashid U, Soltani S, Al-Resayes SI, Nehdi IA. Metal oxide catalysts for biodiesel production. Met. Oxides Energy Technol. 2018:303–19. https://doi.org/10.1016/B978-0-12-811167-3.00011-0. Elsevier.

[121] Mehrabadi BAT, Eskandari S, Khan U, White RD, Regalbuto JR. A review of preparation methods for supported metal catalysts. In: Adv. Catal.. 1st ed., 61. Elsevier Inc.; 2017. https://doi.org/10.1016/bs.acat.2017.10.001. 1–35.

[122] He H, Wang HH, Liu J, Liu X, Li W, Wang Y. Research progress and application of single-atom catalysts: a review. Molecules 2021. https://doi.org/10.3390/molecules26216501.

[123] Jiao L, Regalbuto JR. The synthesis of highly dispersed noble and base metals on silica via strong electrostatic adsorption: I. Amorphous silica. J Catal 2008;260:329–41. https://doi.org/10.1016/j.jcat.2008.09.022.

[124] Guo J, Liu H, Li D, Wang J, Djitcheu X, He D, et al. A minireview on the synthesis of single atom catalysts. RSC Adv 2022;12:9373–94. https://doi.org/10.1039/D2RA00657J.

[125] Liu K, Zhao X, Ren G, Yang T, Ren Y, Lee AF, et al. Strong metal-support interaction promoted scalable production of thermally stable single-atom catalysts. Nat Commun 2020;11:1263. https://doi.org/10.1038/s41467-020-14984-9.

[126] James SL, Adams CJ, Bolm C, Braga D, Collier P, Friić T, et al. Mechanochemistry: opportunities for new and cleaner synthesis. Chem Soc Rev 2012;41:413–47. https://doi.org/10.1039/c1cs15171a.

[127] Hu Y, Li H, Li Z, Li B, Wang S, Yao Y, et al. Progress in batch preparation of single-atom catalysts and application in sustainable synthesis of fine chemicals. Green Chem 2021. https://doi.org/10.1039/d1gc02331d.

[128] Chen Y, Soler L, Xie C, Vendrell X, Serafin J, Crespo D, et al. A straightforward method to prepare supported Au clusters by mechanochemistry and its

application in photocatalysis. Appl Mater Today 2020;21:100873. https://doi.org/10.1016/j.apmt.2020.100873.
[129] Imoisili PE, Ren J, Jen T-C. Single-atom catalysts for lithium sulfur batteries via atomic layer deposition process. Electrochem Commun 2022;135:107215. https://doi.org/10.1016/j.elecom.2022.107215.
[130] Lu J. Atomic lego catalysts synthesized by atomic layer deposition. Accounts Mater Res 2022;3:358–68. https://doi.org/10.1021/accountsmr.1c00250.
[131] Wang Y, Cui X, Zhang J, Qiao J, Huang H, Shi J, et al. Advances of atomically dispersed catalysts from single-atom to clusters in energy storage and conversion applications. Prog Mater Sci 2022;128:100964. https://doi.org/10.1016/j.pmatsci.2022.100964.
[132] Chen Y, Ji S, Chen C, Peng Q, Wang D, Li Y. Single-atom catalysts: synthetic strategies and electrochemical applications. Joule 2018;2:1242–64. https://doi.org/10.1016/j.joule.2018.06.019.
[133] Lang R, Xi W, Liu JC, Cui YT, Li T, Lee AF, et al. Non defect-stabilized thermally stable single-atom catalyst. Nat Commun 2019;10:1–10. https://doi.org/10.1038/s41467-018-08136-3.
[134] Wei S, Li A, Liu JC, Li Z, Chen W, Gong Y, et al. Direct observation of noble metal nanoparticles transforming to thermally stable single atoms. Nat Nanotechnol 2018;13:856–61. https://doi.org/10.1038/s41565-018-0197-9.
[135] Eggenhuisen TM, Munnik P, Talsma H, De Jongh PE, De Jong KP. Freeze-drying for controlled nanoparticle distribution in Co/SiO 2 Fischer-Tropsch catalysts. J Catal 2013;297:306–13. https://doi.org/10.1016/j.jcat.2012.10.024.
[136] Silva-Espinoza MA, Ayed C, Foster T, Camacho M del M, Martínez-Navarrete N. The impact of freeze-drying conditions on the physico-chemical properties and bioactive compounds of a freeze-dried orange puree. Foods 2019;9:32. https://doi.org/10.3390/foods9010032.
[137] Wang P, Yang X, Zhang Y, Gao Y, Zhang J. A structured catalyst with high dispersity of Au species based on hollow SiC foam with porous walls for acetylene hydrochlorination. RSC Adv 2021;11. https://doi.org/10.1039/D1RA02533C. 19819–26.
[138] Jakubczyk E, Jaskulska A. The effect of freeze-drying on the properties of polish vegetable soups. Appl Sci 2021;11:654. https://doi.org/10.3390/app11020654.
[139] Steinmiller EMP, Choi KS. Photochemical deposition of cobalt-based oxygen evolving catalyst on a semiconductor photoanode for solar oxygen production. Proc Natl Acad Sci U S A 2009;106:20633–6. https://doi.org/10.1073/pnas.0910203106.
[140] Zhou M, Dick JE, Bard AJ. Electrodeposition of isolated platinum atoms and clusters on bismuth - characterization and electrocatalysis. J Am Chem Soc 2017;139:17677–82. https://doi.org/10.1021/jacs.7b10646.
[141] Shi Y, Huang WM, Li J, Zhou Y, Li ZQ, Yin YC, et al. Site-specific electrodeposition enables self-terminating growth of atomically dispersed metal catalysts. Nat Commun 2020;11:1–9. https://doi.org/10.1038/s41467-020-18430-8.
[142] Yu Z, Xu J, Feng S, Song X, Bondarchuk O, Faria JL, et al. Rhodium single-atom catalysts with enhanced electrocatalytic hydrogen evolution performance. New J Chem 2021;45:5770–4. https://doi.org/10.1039/D1NJ00210D.
[143] Qiu HJ, Ito Y, Cong W, Tan Y, Liu P, Hirata A, et al. Nanoporous graphene with single-atom nickel dopants: an efficient and stable catalyst for electrochemical hydrogen production. Angew Chem Int Ed 2015;54:14031–5. https://doi.org/10.1002/anie.201507381.
[144] Yu X, Deng J, Liu Y, Jing L, Hou Z, Pei W, et al. Single-atom catalysts: preparation and applications in environmental catalysis. Catalysts 2022;12:1239. https://doi.org/10.3390/catal12101239.
[145] Wang L, Guan E, Zhang J, Yang J, Zhu Y, Han Y, et al. Single-site catalyst promoters accelerate metal-catalyzed nitroarene hydrogenation. Nat Commun 2018;9:1362. https://doi.org/10.1038/s41467-018-03810-y.
[146] Yan H, Su C, He J, Chen W. Single-atom catalysts and their applications in organic chemistry. J Mater Chem 2018;6:8793–814. https://doi.org/10.1039/c8ta01940a.
[147] de Lara-Castells MP. First-principles modelling of the new generation of subnanometric metal clusters: recent case studies. J Colloid Interface Sci 2022;612:737–59. https://doi.org/10.1016/j.jcis.2021.12.186.
[148] Wang Z, Xu SM, Xu Y, Tan L, Wang X, Zhao Y, et al. Single Ru atoms with precise coordination on a monolayer layered double hydroxide for efficient electrooxidation catalysis. Chem Sci 2019;10:378–84. https://doi.org/10.1039/c8sc04480e.
[149] Millet MM, Algara-Siller G, Wrabetz S, Mazheika A, Girgsdies F, Teschner D, et al. Ni single atom catalysts for CO 2 activation. J Am Chem Soc 2019;141:2451–61. https://doi.org/10.1021/jacs.8b11729.
[150] Ding G, Hao L, Xu H, Wang L, Chen J, Li T, et al. Atomically dispersed palladium catalyses Suzuki–Miyaura reactions under phosphine-free conditions. Commun Chem 2020;3:1–8. https://doi.org/10.1038/s42004-020-0289-y.
[151] Zhang L, Doyle-Davis K, Sun X. Pt-Based electrocatalysts with high atom utilization efficiency: from nanostructures to single atoms. Energy Environ Sci 2019;12:492–517. https://doi.org/10.1039/c8ee02939c.
[152] Rane AV, Kanny K, Abitha VK, Thomas S. Methods for synthesis of nanoparticles and fabrication of nanocomposites. Synth. Inorg. Nanomater. 2018:121–39. https://doi.org/10.1016/b978-0-08-101975-7.00005-1.
[153] DeRita L, Dai S, Lopez-Zepeda K, Pham N, Graham GW, Pan X, et al. Catalyst architecture for stable single atom dispersion enables site-specific spectroscopic and reactivity measurements of CO adsorbed to Pt atoms, oxidized Pt clusters, and metallic Pt clusters on TiO 2. J Am Chem Soc 2017;139:14150–65. https://doi.org/10.1021/jacs.7b07093.
[154] Fei H, Dong J, Chen D, Hu T, Duan X, Shakir I, et al. Single atom electrocatalysts supported on graphene or graphene-like carbons. Chem Soc Rev 2019. https://doi.org/10.1039/c9cs00422j.
[155] Munnik P, De Jongh PE, De Jong KP. Recent developments in the synthesis of supported catalysts. Chem Rev 2015;115:6687–718. https://doi.org/10.1021/cr500486u.
[156] Chen Y, Gao J, Huang Z, Zhou M, Chen J, Li C, et al. Sodium rivals silver as single-atom active centers for catalyzing abatement of formaldehyde. Environ Sci Technol 2017;51:7084–90. https://doi.org/10.1021/acs.est.7b00499.
[157] Kropp T, Lu Z, Li Z, Chin YHC, Mavrikakis M. Anionic single-atom catalysts for CO oxidation: support-independent activity at low temperatures. ACS Catal 2019;9:1595–604. https://doi.org/10.1021/acscatal.8b03298.
[158] Bo Z, McCullough LR, Dull S, Ardagh MA, Wang J, Notestein J. Strong electrostatic adsorption of Pt onto SiO 2 partially overcoated Al 2 O 3 —towards single atom catalysts. J Chem Phys 2019;151:214703. https://doi.org/10.1063/1.5128934.
[159] Thang HV, Pacchioni G, DeRita L, Christopher P. Nature of stable single atom Pt catalysts dispersed on anatase TiO2. J Catal 2018;367:104–14. https://doi.org/10.1016/j.jcat.2018.08.025.
[160] Pereira-Hernández XI, DeLaRiva A, Muravev V, Kunwar D, Xiong H, Sudduth B, et al. Tuning Pt-CeO2 interactions by high-temperature vapor-phase synthesis for improved reducibility of lattice oxygen. Nat Commun 2019;10:1358. https://doi.org/10.1038/s41467-019-09308-5.
[161] Resasco J, DeRita L, Dai S, Chada JP, Xu M, Yan X, et al. Uniformity is key in defining structure–function relationships for atomically dispersed metal catalysts: the case of Pt/CeO 2. J Am Chem Soc 2020;142:169–84. https://doi.org/10.1021/jacs.9b09156.
[162] Hülsey MJ, Zhang B, Ma Z, Asakura H, Do DA, Chen W, et al. In situ spectroscopy-guided engineering of rhodium single-atom catalysts for CO oxidation. Nat Commun 2019;10:1–10. https://doi.org/10.1038/s41467-019-09188-9.
[163] Ding S, Guo Y, Hülsey MJ, Zhang B, Asakura H, Liu L, et al. Electrostatic stabilization of single-atom catalysts by ionic liquids. Chem 2019;5:3207–19. https://doi.org/10.1016/j.chempr.2019.10.007.
[164] Akri M, El Kasmi A, Batiot-Dupeyrat C, Qiao B. Highly active and carbon-resistant nickel single-atom catalysts for methane dry reforming. Catalysts 2020;10:630. https://doi.org/10.3390/catal10060630.
[165] Schreyer H, Eckert R, Immohr S, de Bellis J, Felderhoff M, Schüth F. Milling down to nanometers: a general process for the direct dry synthesis of supported metal catalysts. Angew Chem Int Ed 2019;58:11262–5. https://doi.org/10.1002/anie.201903545.
[166] Cui X, Xiao J, Wu Y, Du P, Si R, Yang H, et al. A graphene composite material with single cobalt active sites: a highly efficient counter electrode for dye-sensitized solar cells. Angew Chem Int Ed 2016;55:6708–12. https://doi.org/10.1002/anie.201602097.
[167] Turner LP, Kueper BH, Jaansalu KM, Patch DJ, Battye N, El-Sharnouby O, et al. Mechanochemical remediation of perfluorooctanesulfonic acid (PFOS) and perfluorooctanoic acid (PFOA) amended sand and aqueous film-forming foam (AFFF) impacted soil by planetary ball milling. Sci Total Environ 2021;765:142722. https://doi.org/10.1016/j.scitotenv.2020.142722.
[168] Cui X, Li H, Wang Y, Hu Y, Hua L, Li H, et al. Room-temperature methane conversion by graphene-confined single iron atoms. Chem 2018;4. https://doi.org/10.1016/j.chempr.2018.05.006. 1902–10.
[169] He X, Deng Y, Zhang Y, He Q, Xiao D, Peng M, et al. Mechanochemical kilogram-scale synthesis of noble metal single-atom catalysts. Cell Reports Phys Sci 2020;1:100004. https://doi.org/10.1016/j.xcrp.2019.100004.
[170] Guo Y, Qi H, Su Y, Jiang Q, Cui Y, Li L, et al. High performance of single-atom catalyst Pd 1/MgO for semi-hydrogenation of acetylene to ethylene in excess ethylene. ChemNanoMat 2021;7:526–9. https://doi.org/10.1002/cnma.202100037.
[171] Chen Z, Vorobyeva E, Mitchell S, Fako E, López N, Collins SM, et al. Single-atom heterogeneous catalysts based on distinct carbon nitride scaffolds. Natl Sci Rev 2018;5:642–52. https://doi.org/10.1093/nsr/nwy048.
[172] Zhang X, Cui G, Feng H, Chen L, Wang H, Wang B, et al. Platinum–copper single atom alloy catalysts with high performance towards glycerol hydrogenolysis. Nat Commun 2019;10:1–12. https://doi.org/10.1038/s41467-019-13685-2.
[173] Zhou C, Liang Y, Xia W, Almatrafi E, Song B, Wang Z, et al. Single atom Mn anchored on N-doped porous carbon derived from spirulina for catalyzed peroxymonosulfate to degradation of emerging organic pollutants. J Hazard Mater 2023;441:129871. https://doi.org/10.1016/j.jhazmat.2022.129871.
[174] Mao X, Deng Z, Liu Y, Xie H, He Q, Zhang Y, et al. Iron single atoms and clusters anchored on natural N-doped nanocarbon with dual reaction sites as superior Fenton-like catalysts. Appl Surf Sci 2022;597:153625. https://doi.org/10.1016/j.apsusc.2022.153625.
[175] Jin H, Sultan S, Ha M, Tiwari JN, Kim MG, Kim KS. Simple and scalable mechanochemical synthesis of noble metal catalysts with single atoms toward highly efficient hydrogen evolution. Adv Funct Mater 2020;30:2000531. https://doi.org/10.1002/adfm.202000531.
[176] Zhang H, Sun Q, He Q, Zhang Y, He X, Gan T, et al. Single Cu atom dispersed on S, N-codoped nanocarbon derived from shrimp shells for highly-efficient oxygen reduction reaction. Nano Res 2022;15:5995–6000. https://doi.org/10.1007/s12274-022-4289-3.
[177] Liu T, Sun F, Huang M, Guan L. Atomically dispersed Co–N–C electrocatalysts synthesized by a low-speed ball milling method for proton exchange membrane fuel cells. Mater Adv 2022;3:1565–73. https://doi.org/10.1039/D1MA00809A.
[178] Kumar CV, Pattammattel A. Synthetic routes to graphene preparation from the perspectives of possible biological applications. Introd. to Graphene 2017. https://doi.org/10.1016/b978-0-12-813182-4.00002-7.

[179] Cheng N, Stambula S, Wang D, Banis MN, Liu J, Riese A, et al. Platinum single-atom and cluster catalysis of the hydrogen evolution reaction. Nat Commun 2016; 7:1–9. https://doi.org/10.1038/ncomms13638.
[180] Wang C, Gu XK, Yan H, Lin Y, Li J, Liu D, et al. Water-Mediated mars-van krevelen mechanism for CO oxidation on ceria-supported single-atom Pt1 catalyst. ACS Catal 2017;7:887–91. https://doi.org/10.1021/acscatal.6b02685.
[181] Piernavieja-Hermida M, Lu Z, White A, Low K Bin, Wu T, Elam JW, et al. Towards ALD thin film stabilized single-atom Pd1 catalysts. Nanoscale 2016;8:15348–56. https://doi.org/10.1039/c6nr04403d.
[182] Zhang L, Si R, Liu H, Chen N, Wang Q, Adair K, et al. Atomic layer deposited Pt-Ru dual-metal dimers and identifying their active sites for hydrogen evolution reaction. Nat Commun 2019;10:1–11. https://doi.org/10.1038/s41467-019-12887-y.
[183] Zhang L, Wang Q, Li L, Banis MN, Li J, Adair K, et al. Single atom surface engineering: a new strategy to boost electrochemical activities of Pt catalysts. Nano Energy 2022;93:106813. https://doi.org/10.1016/j.nanoen.2021.106813.
[184] Kong F, Liu X, Song Y, Qian Z, Li J, Zhang L, et al. Selectively coupling Ru single atoms to PtNi concavities for high-performance methanol oxidation via d -band center regulation. Angew Chem Int Ed 2022;61:e202207524. https://doi.org/10.1002/anie.202207524.
[185] Oviroh PO, Akbarzadeh R, Pan D, Coetzee RAM, Jen TC. New development of atomic layer deposition: processes, methods and applications. Sci Technol Adv Mater 2019;20:465–96. https://doi.org/10.1080/14686996.2019.1599694.
[186] Zhang L, Banis MN, Sun X. Single-atom catalysts by the atomic layer deposition technique. Natl Sci Rev 2018;5:628–30. https://doi.org/10.1093/nsr/nwy054.
[187] Feng S, Song X, Liu Y, Lin X, Yan L, Liu S, et al. In situ formation of mononuclear complexes by reaction-induced atomic dispersion of supported noble metal nanoparticles. Nat Commun 2019;10:5281. https://doi.org/10.1038/s41467-019-12965-1.
[188] Wang X, Zhang Y, Si H, Zhang Q, Wu J, Gao L, et al. Single-atom vacancy defect to trigger high-efficiency hydrogen evolution of MoS 2. J Am Chem Soc 2020;142: 4298–308. https://doi.org/10.1021/jacs.9b12113.
[189] Zhao D, Chen Z, Yang W, Liu S, Zhang X, Yu Y, et al. MXene (Ti 3 C 2) vacancy-confined single-atom catalyst for efficient functionalization of CO 2. J Am Chem Soc 2019;141:4086–93. https://doi.org/10.1021/jacs.8b13579.
[190] Fu Q, Saltsburg H, Flytzani-Stephanopoulos M. Active nonmetallic Au and Pt species on ceria-based water-gas shift catalysts. Science 2003;301(80):935–8. https://doi.org/10.1126/science.1085721.
[191] Mochizuki C, Inomata Y, Yasumura S, Lin M, Taketoshi A, Honma T, et al. Defective NiO as a stabilizer for Au single-atom catalysts. ACS Catal 2022. https://doi.org/10.1021/acscatal.2c00108. 6149–58.
[192] Yang M, Allard LF, Flytzani-Stephanopoulos M. Atomically dispersed Au-(OH)x species bound on titania catalyze the low-temperature water-gas shift reaction. J Am Chem Soc 2013;135:3768–71. https://doi.org/10.1021/ja312646d.
[193] Gong YN, Jiao L, Qian Y, Pan CY, Zheng L, Cai X, et al. Regulating the coordination environment of MOF-templated single-atom nickel electrocatalysts for boosting CO2 reduction. Angew Chem Int Ed 2020;132:2727–31. https://doi.org/10.1002/anie.201914977.
[194] Han Y, Wang YG, Chen W, Xu R, Zheng L, Zhang J, et al. Hollow N-doped carbon spheres with isolated cobalt single atomic sites: superior electrocatalysts for oxygen reduction. J Am Chem Soc 2017;139:17269–72. https://doi.org/10.1021/jacs.7b10194.
[195] Copéret C. Single-sites and nanoparticles at tailored interfaces prepared via surface organometallic chemistry from thermolytic molecular precursors. Acc Chem Res 2019;52:1697–708. https://doi.org/10.1021/acs.accounts.9b00138.
[196] Delley MF, Silaghi MC, Nuñez-Zarur F, Kovtunov KV, Salnikov OG, Estes DP, et al. X-H bond activation on Cr(III),O sites (X = R, H): key steps in dehydrogenation and hydrogenation processes. Organometallics 2017;36:234–44. https://doi.org/10.1021/acs.organomet.6b00744.
[197] Liu S, Tan JM, Gulec A, Crosby LA, Drake TL, Schweitzer NM, et al. Stabilizing single-atom and small-domain platinum via combining organometallic chemisorption and atomic layer deposition. Organometallics 2017;36:818–28. https://doi.org/10.1021/acs.organomet.6b00869.
[198] Zhang B, Asakura H, Zhang J, Zhang J, De S, Yan N. Stabilizing a Platinum1Single-atom catalyst on supported phosphomolybdic acid without compromising hydrogenation activity. Angew Chem Int Ed 2016;128:8459–63. https://doi.org/10.1002/anie.201602801.
[199] Lee BH, Park S, Kim M, Sinha AK, Lee SC, Jung E, et al. Reversible and cooperative photoactivation of single-atom Cu/TiO2 photocatalysts. Nat Mater 2019;18:620–6. https://doi.org/10.1038/s41563-019-0344-1.
[200] Matthey D, Wang JG, Wendt S, Matthiesen J, Schaub R, Lægsgaard E, et al. Enhanced bonding of gold nanoparticles on oxidized TiO2(110). Science 2007; 315(80):1692–6. https://doi.org/10.1126/science.1135752.
[201] Hansen J, Lira E, Galliker P, Wang JG, Sprunger PT, Li Z, et al. Enhanced bonding of silver nanoparticles on oxidized TiO2(110). J Phys Chem C 2010;114: 16964–72. https://doi.org/10.1021/jp101714r.
[202] Mao K, Li L, Zhang W, Pei Y, Zeng XC, Wu X, et al. A theoretical study of single-atom catalysis of CO oxidation using au embedded 2D h-BN monolayer: a CO-promoted O2 activation. Sci Rep 2014;4:1–7. https://doi.org/10.1038/srep05441.
[203] Yentekakis IV, Goula G, Hatzisymeon M, Betsi-Argyropoulou I, Botzolaki G, Kousi K, et al. Effect of support oxygen storage capacity on the catalytic performance of Rh nanoparticles for CO2 reforming of methane. Appl Catal B Environ 2019;243:490–501. https://doi.org/10.1016/j.apcatb.2018.10.048.
[204] Bliem R, McDermott E, Ferstl P, Setvin M, Gamba O, Pavelec J, et al. Subsurface cation vacancy stabilization of the magnetite (001) surface. Science 2014;346 (80):1215–8. https://doi.org/10.1126/science.1260556.
[205] Zhang J, Wu X, Cheong WC, Chen W, Lin R, Li J, et al. Cation vacancy stabilization of single-atomic-site Pt 1/Ni(OH) x catalyst for diboration of alkynes and alkenes. Nat Commun 2018;9:1–8. https://doi.org/10.1038/s41467-018-03380-z.
[206] Shen A, Zou Y, Wang Q, Dryfe RAW, Huang X, Dou S, et al. Oxygen reduction reaction in a droplet on graphite: direct evidence that the edge is more active than the basal plane. Angew Chem Int Ed 2014;126:10980–4. https://doi.org/10.1002/anie.201406695.
[207] Wang L, Zhang W, Wang S, Gao Z, Luo Z, Wang X, et al. Atomic-level insights in optimizing reaction paths for hydroformylation reaction over Rh/CoO single-atom catalyst. Nat Commun 2016;7:1–8. https://doi.org/10.1038/ncomms14036.
[208] Xie P, Pu T, Nie A, Hwang S, Purdy SC, Yu W, et al. Nanoceria-supported single-atom platinum catalysts for direct methane conversion. ACS Catal 2018;8: 4044–8. https://doi.org/10.1021/acscatal.8b00004.
[209] Giulimondi V, Kaiser SK, Agrachev M, Krumeich F, Clark AH, Mitchell S, et al. Redispersion strategy for high-loading carbon-supported metal catalysts with controlled nuclearity. J Mater Chem 2022;10:5953–61. https://doi.org/10.1039/D1TA09238C.
[210] Cheng Y, Zhao S, Johannessen B, Veder JP, Saunders M, Rowles MR, et al. Atomically dispersed transition metals on carbon nanotubes with ultrahigh loading for selective electrochemical carbon dioxide reduction. Adv Mater 2018; 30:1706287. https://doi.org/10.1002/adma.201706287.
[211] Wang Y, Chen L, Mao Z, Peng L, Xiang R, Tang X, et al. Controlled synthesis of single cobalt atom catalysts via a facile one-pot pyrolysis for efficient oxygen reduction and hydrogen evolution reactions. Sci Bull 2019;64:1095–102. https://doi.org/10.1016/j.scib.2019.06.012.
[212] Yao Y, Huang Z, Xie P, Wu L, Ma L, Li T, et al. High temperature shockwave stabilized single atoms. Nat Nanotechnol 2019;14:851–7. https://doi.org/10.1038/s41565-019-0518-7.
[213] Bi Q, Yuan X, Lu Y, Wang D, Huang J, Si R, et al. One-step high-temperature-synthesized single-atom platinum catalyst for efficient selective hydrogenation. Research 2020:9140841. https://doi.org/10.34133/2020/9140841.
[214] Qu Y, Li Z, Chen W, Lin Y, Yuan T, Yang Z, et al. Direct transformation of bulk copper into copper single sites via emitting and trapping of atoms. Nat Catal 2018;1:781–6. https://doi.org/10.1038/s41929-018-0146-x.
[215] Liu W, Ji J, Yan X, Liu W, Huang YC, Wang K, et al. A cascade surface immobilization strategy to access high-density and closely distanced atomic Pt sites for enhancing alkaline hydrogen evolution reaction. J Mater Chem 2020;8: 5255–62. https://doi.org/10.1039/d0ta00495b.
[216] Jiang K, Back S, Akey AJ, Xia C, Hu Y, Liang W, et al. Highly selective oxygen reduction to hydrogen peroxide on transition metal single atom coordination. Nat Commun 2019;10:1–11. https://doi.org/10.1038/s41467-019-11992-2.
[217] Song X, Zhang H, Bian Z, Wang H. In situ electrogeneration and activation of H2O2 by atomic Fe catalysts for the efficient removal of chloramphenicol. J Hazard Mater 2021;412:125162. https://doi.org/10.1016/j.jhazmat.2021.125162.
[218] Zhou S, Shang L, Zhao Y, Shi R, Waterhouse GIN, Huang YC, et al. Pd single-atom catalysts on nitrogen-doped graphene for the highly selective photothermal hydrogenation of acetylene to ethylene. Adv Mater 2019;31:1900509. https://doi.org/10.1002/adma.201900509.
[219] Han C, Yi W, Feng S, Li Z, Song H. Single-atom palladium anchored N-doped carbon towards oxygen electrocatalysis for rechargeable Zn–air batteries. Dalton Trans 2022;51:12314–23. https://doi.org/10.1039/D2DT01760A.
[220] Li Y, Hao J, Song H, Zhang F, Bai X, Meng X, et al. Selective light absorber-assisted single nickel atom catalysts for ambient sunlight-driven CO2 methanation. Nat Commun 2019;10:1–9. https://doi.org/10.1038/s41467-019-10304-y.
[221] Peng Y, Cao J, Sha Y, Yang W, Li L, Liu Z. Laser solid-phase synthesis of single-atom catalysts. Light Sci Appl 2021;10:168. https://doi.org/10.1038/s41377-021-00603-9.
[222] Wang Y, Shi C, Sha J, Ma L, Liu E, Zhao N. Single-atom cobalt supported on nitrogen-doped three-dimensional carbon facilitating polysulfide conversion in lithium–sulfur batteries. ACS Appl Mater Interfaces 2022;14:25337–47. https://doi.org/10.1021/acsami.2c02713.
[223] Yang R, Liu J, Wang B, Wang R, Song Y, Hua Y, et al. Synergistic effect of isolated Co and Fe dual active sites boosting the photocatalytic hydrogen evolution reaction. J Alloys Compd 2022;895:162290. https://doi.org/10.1016/j.jallcom.2021.162290.
[224] Huang J, Yan Y, Saqline S, Liu W, Liu B. High performance Ni catalysts prepared by freeze drying for efficient dry reforming of methane. Appl Catal B Environ 2020;275:119109. https://doi.org/10.1016/j.apcatb.2020.119109.
[225] Wei H, Huang K, Wang D, Zhang R, Ge B, Ma J, et al. Iced photochemical reduction to synthesize atomically dispersed metals by suppressing nanocrystal growth. Nat Commun 2017;8:1–8. https://doi.org/10.1038/s41467-017-01521-4.
[226] Liu P, Chen J, Zheng N. Photochemical route for preparing atomically dispersed Pd1/TiO2 catalysts on (001)-exposed anatase nanocrystals and P25. Cuihua Xuebao/Chinese J Catal 2017;38:1574–80. https://doi.org/10.1016/S1872-2067(17)62784-0.
[227] Zhao Y, Yang KR, Wang Z, Yan X, Cao S, Ye Y, et al. Stable iridium dinuclear heterogeneous catalysts supported on metal-oxide substrate for solar water

oxidation. Proc Natl Acad Sci U S A 2018;115:2902–7. https://doi.org/10.1073/pnas.1722137115.
[228] Li T, Liu J, Song Y, Wang F. Photochemical solid-phase synthesis of platinum single atoms on nitrogen-doped carbon with high loading as bifunctional catalysts for hydrogen evolution and oxygen reduction reactions. ACS Catal 2018;8:8450–8. https://doi.org/10.1021/acscatal.8b02288.
[229] Li H, Zhu H, Zhuang Z, Lu S, Duan F, Du M. Single-atom catalysts for electrochemical clean energy conversion: recent progress and perspectives. Sustain Energy Fuels 2020;4:996–1011. https://doi.org/10.1039/c9se01004a.
[230] Fan L, Liu PF, Yan X, Gu L, Yang ZZ, Yang HG, et al. Atomically isolated nickel species anchored on graphitized carbon for efficient hydrogen evolution electrocatalysis. Nat Commun 2016;7:1–7. https://doi.org/10.1038/ncomms10667.
[231] Tavakkoli M, Holmberg N, Kronberg R, Jiang H, Sainio J, Kauppinen EI, et al. Electrochemical activation of single-walled carbon nanotubes with pseudo-atomic-scale platinum for the hydrogen evolution reaction. ACS Catal 2017;7:3121–30. https://doi.org/10.1021/acscatal.7b00199.
[232] Zhang L, Jia Y, Liu H, Zhuang L, Yan X, Lang C, et al. Charge polarization from atomic metals on adjacent graphitic layers for enhancing the hydrogen evolution reaction. Angew Chem Int Ed 2019;131:9504–8. https://doi.org/10.1002/anie.201902107.
[233] Wu H, Zhang H, Geng L, Jia Y, Huang B, Yang M, et al. Pure metal clusters with atomic precision for nanomanufacturing. Nanomanufacturing Metrol 2022;5:230–9. https://doi.org/10.1007/s41871-022-00139-5.
[234] von Weber A, Baxter ET, Proch S, Kane MD, Rosenfelder M, White HS, et al. Size-dependent electronic structure controls activity for ethanol electro-oxidation at Pt n/indium tin oxide (n = 1 to 14). Phys Chem Chem Phys 2015;17:17601–10. https://doi.org/10.1039/C5CP01824B.
[235] Abbet S, Sanchez A, Heiz U, Schneider W-D, Ferrari AM, Pacchioni G, et al. Acetylene cyclotrimerization on supported size-selected Pd n clusters ($1 \leq n \leq 30$): one atom is enough. J Am Chem Soc 2000;122:3453–7. https://doi.org/10.1021/ja9922476.
[236] Wan W, Triana CA, Lan J, Li J, Allen CS, Zhao Y, et al. Bifunctional single atom electrocatalysts: coordination–performance correlations and reaction pathways. ACS Nano 2020;14:13279–93. https://doi.org/10.1021/acsnano.0c05088.
[237] Nesselberger M, Roefzaad M, Fayçal Hamou R, Ulrich Biedermann P, Schweinberger FF, Kunz S, et al. The effect of particle proximity on the oxygen reduction rate of size-selected platinum clusters. Nat Mater 2013;12:919–24. https://doi.org/10.1038/nmat3712.
[238] Kane MD, Roberts FS, Anderson SL. Alumina support and Pdn cluster size effects on activity of Pdn for catalytic oxidation of CO. Faraday Discuss 2013. https://doi.org/10.1039/c3fd20151a.
[239] Lee S, Fan C, Wu T, Anderson SL. Cluster size effects on CO oxidation activity, adsorbate affinity, and temporal behavior of model Aun/TiO2 catalysts. J Chem Phys 2005;123:124710. https://doi.org/10.1063/1.2035098.
[240] Gao C, Chen S, Wang Y, Wang J, Zheng X, Zhu J, et al. Heterogeneous single-atom catalyst for visible-light-driven high-turnover CO2 reduction: the role of electron transfer. Adv Mater 2018;30:1704624. https://doi.org/10.1002/adma.201704624.
[241] Wang WL, Santos EJG, Jiang B, Cubuk ED, Ophus C, Centeno A, et al. Direct observation of a long-lived single-atom catalyst chiseling atomic structures in graphene. Nano Lett 2014;14:450–5. https://doi.org/10.1021/nl403327u.
[242] Peng Y, Nellist PD, Pennycook SJ. HAADF-STEM imaging with sub-angstrom probes: a full Bloch wave analysis. J Electron Microsc 2004;53:257–66. https://doi.org/10.1093/jmicro/53.3.257.
[243] Crewe AV, Wall J, Lanomore J. Visibility of single atoms. Science 1970;168(80):1338–40. https://doi.org/10.1126/science.168.3937.1338.
[244] Lu J, Aydin C, Browning ND, Gates BC. Imaging isolated gold atom catalytic sites in zeolite NaY. Angew Chem Int Ed 2012;124:5944–8. https://doi.org/10.1002/anie.201107391.
[245] Shao X, Yang X, Xu J, Liu S, Miao S, Liu X, et al. Iridium single-atom catalyst performing a quasi-homogeneous hydrogenation transformation of CO2 to formate. Chem 2019;5:693–705. https://doi.org/10.1016/j.chempr.2018.12.014.
[246] Ma W, Mao J, Yang X, Pan C, Chen W, Wang M, et al. A single-atom Fe-N4 catalytic site mimicking bifunctional antioxidative enzymes for oxidative stress cytoprotection. Chem Commun 2019;55:159–62. https://doi.org/10.1039/c8cc08116f.
[247] Xiao M, Zhu J, Li G, Li N, Li S, Cano ZP, et al. A single-atom iridium heterogeneous catalyst in oxygen reduction reaction. Angew Chem Int Ed 2019;58:9640–5. https://doi.org/10.1002/anie.201905241.
[248] Jeong HY, Balamurugan M, Choutipalli VSK, Jeong ES, Subramanian V, Sim U, et al. Achieving highly efficient CO2 to CO electroreduction exceeding 300 mA cm-2 with single-atom nickel electrocatalysts. J Mater Chem 2019;7:10651–61. https://doi.org/10.1039/c9ta02405k.
[249] Taylor MJ, Beaumont SK, Islam MJ, Tsatsos S, Parlett CAM, Issacs MA, et al. Atom efficient PtCu bimetallic catalysts and ultra dilute alloys for the selective hydrogenation of furfural. Appl Catal B Environ 2021;284:119737. https://doi.org/10.1016/j.apcatb.2020.119737.
[250] Guo T, Tang N, Lin F, Shang Q, Chen S, Qi H, et al. High-loading single-atom copper catalyst supported on coordinatively unsaturated Al2O3 for selective synthesis of homoallylboronates. ChemSusChem 2020;13:3115–21. https://doi.org/10.1002/cssc.202000536.
[251] Terabe K, Nakayama T, Hasegawa T, Aono M. Ionic/electronic mixed conductor tip of a scanning tunneling microscope as a metal atom source for nanostructuring. Appl Phys Lett 2002;80:4009–11. https://doi.org/10.1063/1.1480887.
[252] Parkinson B. Layer-by-Layer nanometer scale etching of two-dimensional substrates using the scanning tunneling microscope. J Am Chem Soc 1990;112:7498–502. https://doi.org/10.1021/ja00177a007.
[253] Besenbacher F, Brorson M, Clausen BS, Helveg S, Hinnemann B, Kibsgaard J, et al. Recent STM, DFT and HAADF-STEM studies of sulfide-based hydrotreating catalysts: insight into mechanistic, structural and particle size effects. Catal Today 2008;130:86–96. https://doi.org/10.1016/j.cattod.2007.08.009.
[254] Zhou Y, Du L, Zou Y, Zhou J. A STM study of Ni-Rh bimetallic particles on reducible CeO2(111). Surf Sci 2019;681:47–53. https://doi.org/10.1016/j.susc.2018.10.013.
[255] Binnig G, Rohrer H. Scanning tunneling microscopy from birth to adolescence. Rev Mod Phys 1987;59:615. https://doi.org/10.1103/RevModPhys.59.615.
[256] Liu Q, Zhang Z. Platinum single-atom catalysts: a comparative review towards effective characterization. Catal Sci Technol 2019;9:4821–34. https://doi.org/10.1039/c9cy01028a.
[257] Lucci FR, Liu J, Marcinkowski MD, Yang M, Allard LF, Flytzani-Stephanopoulos M, et al. Selective hydrogenation of 1,3-butadiene on platinum-copper alloys at the single-atom limit. Nat Commun 2015;6:1–8. https://doi.org/10.1038/ncomms9550.
[258] Van Spronsen MA, Van Baarle GJC, Herbschleb CT, Frenken JWM, Groot IMN. High-pressure operando STM studies giving insight in CO oxidation and NO reduction over Pt(1 1 0). Catal Today 2015;244:85–95. https://doi.org/10.1016/j.cattod.2014.07.008.
[259] Nartova AV, Gharachorlou A, Bukhtiyarov AV, Kvon RI, Bukhtiyarov VI. New Pt/Alumina model catalysts for STM and in situ XPS studies. Appl Surf Sci 2017;401:341–7. https://doi.org/10.1016/j.apsusc.2016.12.179.
[260] Patera LL, Bianchini F, Africh C, Dri C, Soldano G, Mariscal MM, et al. Real-time imaging of adatom-promoted graphene growth on nickel. Science 2018;359(80):1243–6. https://doi.org/10.1126/science.aan8782.
[261] Besenbacher F, Chorkendorff I, Clausen BS, Hammer B, Molenbroek AM, Nørskov JK, et al. Design of a surface alloy catalyst for steam reforming. Science 1998;279(80):1913–5. https://doi.org/10.1126/science.279.5358.1913.
[262] Wang J, Jia L, Zhong J, Xiao Q, Wang C, Zang K, et al. Single-atom catalyst boosts electrochemical conversion reactions in batteries. Energy Storage Mater 2019;18:246–52. https://doi.org/10.1016/j.ensm.2018.09.006.
[263] Quartieri S. X-ray absorption spectroscopy (XAS, EXAFS, XANES). Encycl. Archaeol. Sci. 2018:1–6. https://doi.org/10.1002/9781119188230.saseas0613.
[264] Kwon Y, Kim TY, Kwon G, Yi J, Lee H. Selective activation of methane on single-atom catalyst of rhodium dispersed on zirconia for direct conversion. J Am Chem Soc 2017;139:17694–9. https://doi.org/10.1021/jacs.7b11010.
[265] Venezia AM. X-ray photoelectron spectroscopy (XPS) for catalysts characterization. Catal Today 2003;77:359–70. https://doi.org/10.1016/S0920-5861(02)00380-2.
[266] Zeng X, Shui J, Liu X, Liu Q, Li Y, Shang J, et al. Single-atom to single-atom grafting of Pt 1 onto Fe-N 4 center: Pt 1 @Fe-N-C multifunctional electrocatalyst with significantly enhanced properties. Adv Energy Mater 2018;8:1701345. https://doi.org/10.1002/aenm.201701345.
[267] Nie L, Mei D, Xiong H, Peng B, Ren Z, Hernandez XIP, et al. Activation of surface lattice oxygen in single-atom Pt/CeO2 for low-temperature CO oxidation. Science 2017;358(80):1419–23. https://doi.org/10.1126/science.aao2109.
[268] Song P, Luo M, Liu X, Xing W, Xu W, Jiang Z, et al. Zn single atom catalyst for highly efficient oxygen reduction reaction. Adv Funct Mater 2017;27:1700802. https://doi.org/10.1002/adfm.201700802.
[269] Chen Y, Ji S, Sun W, Chen W, Dong J, Wen J, et al. Discovering partially charged single-atom Pt for enhanced anti-markovnikov alkene hydrosilylation. J Am Chem Soc 2018;140:7407–10. https://doi.org/10.1021/jacs.8b03121.
[270] Zhong L, Chen D, Zafeiratos S. A mini review of in situ near-ambient pressure XPS studies on non-noble, late transition metal catalysts. Catal Sci Technol 2019;9:3851–67. https://doi.org/10.1039/c9cy00632j.
[271] Song D, Li J, Cai Q. In situ diffuse reflectance FTIR study of CO adsorbed on a cobalt catalyst supported by silica with different pore sizes. J Phys Chem C 2007;111:18970. https://doi.org/10.1021/jp0751357. –9.
[272] Kumar VV, Naresh G, Deepa S, Bhavani PG, Nagaraju M, Sudhakar M, et al. Influence of W on the reduction behaviour and Brønsted acidity of Ni/TiO2catalyst in the hydrogenation of levulinic acid to valeric acid: pyridine adsorbed DRIFTS study. Appl Catal Gen 2017;531:169–76. https://doi.org/10.1016/j.apcata.2016.10.032.
[273] Wang D, Zhang L, Kamasamudram K, Epling WS. In situ-DRIFTS study of selective catalytic reduction of NOx by NH3 over Cu-exchanged SAPO-34. ACS Catal 2013;3:871–81. https://doi.org/10.1021/cs300843k.
[274] Zhang Q, Mo S, Li J, Sun Y, Zhang M, Chen P, et al. In situ DRIFT spectroscopy insights into the reaction mechanism of CO and toluene co-oxidation over Pt-based catalysts. Catal Sci Technol 2019;9:4538–51. https://doi.org/10.1039/c9cy00751b.
[275] Lang R, Du X, Huang Y, Jiang X, Zhang Q, Guo Y, et al. Single-atom catalysts based on the metal-oxide interaction. Chem Rev 2020. https://doi.org/10.1021/acs.chemrev.0c00797.
[276] Pasquini C, D'Amario L, Zaharieva I, Dau H. Operando Raman spectroscopy tracks oxidation-state changes in an amorphous Co oxide material for electrocatalysis of the oxygen evolution reaction. J Chem Phys 2020;152:194202. https://doi.org/10.1063/5.0006306.
[277] Maghsoumi A, Ravanelli A, Consonni F, Nanni F, Lucotti A, Tommasini M, et al. Design and testing of an operando-Raman annular reactor for kinetic studies in heterogeneous catalysis. React Chem Eng 2017;2:908–18. https://doi.org/10.1039/c7re00092h.

[278] Zhang B, Asakura H, Yan N. Atomically dispersed rhodium on self-assembled phosphotungstic acid: structural features and catalytic CO oxidation properties. Ind Eng Chem Res 2017;56:3578–87. https://doi.org/10.1021/acs.iecr.7b00376.
[279] Deng Y, Ting LRL, Neo PHL, Zhang YJ, Peterson AA, Yeo BS. Operando Raman spectroscopy of amorphous molybdenum sulfide (MoSx) during the electrochemical hydrogen evolution reaction: identification of sulfur atoms as catalytically active sites for H+ reduction. ACS Catal 2016;6:7790–8. https://doi.org/10.1021/acscatal.6b01848.
[280] Ball P. Single-atom catalysis: a new field that learns from tradition. Natl Sci Rev 2018;5:690–3. https://doi.org/10.1093/nsr/nwy043.
[281] Copéret C, Liao WC, Gordon CP, Ong TC. Active sites in supported single-site catalysts: an NMR perspective. J Am Chem Soc 2017;139:10588–96. https://doi.org/10.1021/jacs.6b12981.
[282] Bakandritsos A, Kadam RG, Kumar P, Zoppellaro G, Medved' M, Tuček J, et al. Mixed-valence single-atom catalyst derived from functionalized graphene. Adv Mater 2019;31:1900323. https://doi.org/10.1002/adma.201900323.
[283] Jin X, Wang R, Zhang L, Si R, Shen M, Wang M, et al. Electron configuration modulation of nickel single atoms for elevated photocatalytic hydrogen evolution. Angew Chem Int Ed 2020;132:6894–8. https://doi.org/10.1002/anie.201914565.
[284] Zhang X, Sun Z, Wang B, Tang Y, Nguyen L, Li Y, et al. C-C coupling on single-atom-based heterogeneous catalyst. J Am Chem Soc 2018;140:954–62. https://doi.org/10.1021/jacs.7b09314.
[285] Tang Y, Fung V, Zhang X, Li Y, Nguyen L, Sakata T, et al. Single-atom high-temperature catalysis on a Rh 1 O 5 cluster for production of syngas from methane. J Am Chem Soc 2021;143:16566–79. https://doi.org/10.1021/jacs.1c06432.
[286] Jiménez-Lamana J, Wojcieszek J, Jakubiak M, Asztemborska M, Szpunar J. Single particle ICP-MS characterization of platinum nanoparticles uptake and bioaccumulation by Lepidium sativum and Sinapis alba plants. J Anal At Spectrom 2016;31:2321–9. https://doi.org/10.1039/C6JA00201C.
[287] Abbar A H. Electrochemical preparation of ultrafine zinc powder. Int J Electrochem Sci 2017. https://doi.org/10.20964/2017.08.35. 7075–88.
[288] Li J, Chen S, Yang N, Deng M, Ibraheem S, Deng J, et al. Ultrahigh-loading zinc single-atom catalyst for highly efficient oxygen reduction in both acidic and alkaline media. Angew Chem Int Ed 2019;58:7035–9. https://doi.org/10.1002/anie.201902109.
[289] Dong C, Lian C, Hu S, Deng Z, Gong J, Li M, et al. Size-dependent activity and selectivity of carbon dioxide photocatalytic reduction over platinum nanoparticles. Nat Commun 2018;9:1–11. https://doi.org/10.1038/s41467-018-03666-2.
[290] Yodsin N, Rungnim C, Tungkamani S, Promarak V, Namuangruk S, Jungsuttiwong S. DFT study of catalytic CO2 hydrogenation over Pt-decorated carbon nanocones: H2 dissociation combined with the spillover mechanism. J Phys Chem C 2020;124. https://doi.org/10.1021/acs.jpcc.9b08776. 1941–9.
[291] Moses-DeBusk M, Yoon M, Allard LF, Mullins DR, Wu Z, Yang X, et al. CO oxidation on supported single Pt atoms: experimental and ab initio density functional studies of CO interaction with Pt atom on θ-Al 2 O 3 (010) surface. J Am Chem Soc 2013;135:12634–45. https://doi.org/10.1021/ja401847c.
[292] Jørgensen M, Grönbeck H. Scaling relations and kinetic Monte Carlo simulations to bridge the materials gap in heterogeneous catalysis. ACS Catal 2017;7:5054–61. https://doi.org/10.1021/acscatal.7b01194.
[293] Ding S, Chen H-A, Mekasuwandumrong O, Hülsey MJ, Fu X, He Q, et al. High-temperature flame spray pyrolysis induced stabilization of Pt single-atom catalysts. Appl Catal B Environ 2021;281:119471. https://doi.org/10.1016/j.apcatb.2020.119471.
[294] Zhao S, Lin J, Wu P, Ye C, Li Y, Li A, et al. A hydrothermally stable single-atom catalyst of Pt supported on high-entropy oxide/Al 2 O 3 : structural optimization and enhanced catalytic activity. ACS Appl Mater Interfaces 2021;13:48764–73. https://doi.org/10.1021/acsami.1c14456.
[295] Kaiser SK, Fako E, Surin I, Krumeich F, Kondratenko VA, Kondratenko EV, et al. Performance descriptors of nanostructured metal catalysts for acetylene hydrochlorination. Nat Nanotechnol 2022;17:606–12. https://doi.org/10.1038/s41565-022-01105-4.
[296] Kaiser SK, Fako E, Manzocchi G, Krumeich F, Hauert R, Clark AH, et al. Nanostructuring unlocks high performance of platinum single-atom catalysts for stable vinyl chloride production. Nat Catal 2020;3:376–85. https://doi.org/10.1038/s41929-020-0431-3.
[297] Tao Q, Song J, Sun N, Ren Y, Xiang L, Liu S, et al. Boosting the activity of single-atom Pt 1/CeO 2 via Co doping for low-temperature catalytic oxidation of CO. Inorg Chem 2022;61:11932–8. https://doi.org/10.1021/acs.inorgchem.2c01666.
[298] Yang C, Miao Z, Zhang F, Li L, Liu Y, Wang A, et al. Hydrogenolysis of methyl glycolate to ethanol over a Pt–Cu/SiO 2 single-atom alloy catalyst: a further step from cellulose to ethanol. Green Chem 2018;20:2142–50. https://doi.org/10.1039/C8GC00309B.
[299] Dong S, Liu W, Liu S, Li F, Hou J, Hao R, et al. Single atomic Pt on amorphous ZrO2 nanowires for advanced photocatalytic CO2 reduction. Mater Today Nano 2022;17:100157. https://doi.org/10.1016/j.mtnano.2021.100157.
[300] Fang S, Zhu X, Liu X, Gu J, Liu W, Wang D, et al. Uncovering near-free platinum single-atom dynamics during electrochemical hydrogen evolution reaction. Nat Commun 2020;11:1–8. https://doi.org/10.1038/s41467-020-14848-2.
[301] Sun X, Lin J, Chen Y, Wang Y, Li L, Miao S, et al. Unravelling platinum nanoclusters as active sites to lower the catalyst loading for formaldehyde oxidation. Commun Chem 2019;2:27. https://doi.org/10.1038/s42004-019-0129-0.
[302] Xie S, Zhang X, Xu P, Hatcher B, Liu Y, Ma L, et al. Effect of surface acidity modulation on Pt/Al2O3 single atom catalyst for carbon monoxide oxidation and methanol decomposition. Catal Today 2022;402:149–60. https://doi.org/10.1016/j.cattod.2022.03.028.
[303] Wang H, Dong J, Allard LF, Lee S, Oh S, Wang J, et al. Single-site Pt/La-Al2O3 stabilized by barium as an active and stable catalyst in purifying CO and C3H6 emissions. Appl Catal B Environ 2019;244:327–39. https://doi.org/10.1016/j.apcatb.2018.11.034.
[304] Zhang W, Wang H, Jiang J, Sui Z, Zhu Y, Chen D, et al. Size dependence of Pt catalysts for propane dehydrogenation: from atomically dispersed to nanoparticles. ACS Catal 2020;10:12932–42. https://doi.org/10.1021/acscatal.0c03286.
[305] Yang S, Tak YJ, Kim J, Soon A, Lee H. Support effects in single-atom platinum catalysts for electrochemical oxygen reduction. ACS Catal 2017;7:1301–7. https://doi.org/10.1021/acscatal.6b02899.
[306] Kuai L, Liu L, Tao Q, Yu N, Kan E, Sun N, et al. High-areal density single-atoms/metal oxide nanosheets: a micro-gas blasting synthesis and superior catalytic properties. Angew Chem Int Ed 2022;61:e202212338. https://doi.org/10.1002/anie.202212338.
[307] Deng L, Han S, Li Y, Shen W. Subnanometric Pt-Sn monolayers over a rod-shaped Al 2 O 3 for propane dehydrogenation. ChemCatChem 2022;14:e202200400. https://doi.org/10.1002/cctc.202200400.
[308] Yang T, Fukuda R, Hosokawa S, Tanaka T, Sakaki S, Ehara M. A theoretical investigation on CO oxidation by single-atom catalysts M1/γ-Al2O3 (M=Pd, Fe, Co, and Ni). ChemCatChem 2017;9:1222–9. https://doi.org/10.1002/cctc.201601713.
[309] Xing F, Jeon J, Toyao T, Shimizu KI, Furukawa S. A Cu-Pd single-atom alloy catalyst for highly efficient NO reduction. Chem Sci 2019;10:8292–8. https://doi.org/10.1039/c9sc03172c.
[310] Jiang D, Wan G, García-Vargas CE, Li L, Pereira-Hernández XI, Wang C, et al. Elucidation of the active sites in single-atom Pd 1/CeO 2 catalysts for low-temperature CO oxidation. ACS Catal 2020;10:11356–64. https://doi.org/10.1021/acscatal.0c02480.
[311] Li J, Li M, Li J, Wang S, Li G, Liu X. Hydrodechlorination and deep hydrogenation on single-palladium-atom-based heterogeneous catalysts. Appl Catal B Environ 2021;282:119518. https://doi.org/10.1016/j.apcatb.2020.119518.
[312] Qiao B, Lin J, Li L, Wang A, Liu J, Zhang T. Highly active small palladium clusters supported on ferric hydroxide for carbon monoxide-tolerant hydrogen oxidation. ChemCatChem 2014;6:547–54. https://doi.org/10.1002/cctc.201300947.
[313] Sun X, Lin J, Zhou Y, Li L, Su Y, Wang X, et al. FeO x supported single-atom Pd bifunctional catalyst for water gas shift reaction. AIChE J 2017;63:4022–31. https://doi.org/10.1002/aic.15759.
[314] Zhang N, Zhang X, Kang Y, Ye C, Jin R, Yan H, et al. A supported Pd 2 dual-atom site catalyst for efficient electrochemical CO 2 reduction. Angew Chem Int Ed 2021;60:13388–93. https://doi.org/10.1002/anie.202101559.
[315] Xiang W, Zhao Y, Jiang Z, Li X, Zhang H, Sun Y, et al. Palladium single atoms supported by interwoven carbon nanotube and manganese oxide nanowire networks for enhanced electrocatalysis. J Mater Chem 2018;6:23366–77. https://doi.org/10.1039/C8TA09034C.
[316] Ren X, Li C, Liu J, Li H, Bing L, Bai S, et al. The fabrication of Pd single atoms/clusters on COF layers as Co-catalysts for photocatalytic H 2 evolution. ACS Appl Mater Interfaces 2022;14:6885–93. https://doi.org/10.1021/acsami.1c23465.
[317] Kuai L, Chen Z, Liu S, Kan E, Yu N, Ren Y, et al. Titania supported synergistic palladium single atoms and nanoparticles for room temperature ketone and aldehydes hydrogenation. Nat Commun 2020;11:1–9. https://doi.org/10.1038/s41467-019-13941-5.
[318] Zhao Y, Zhou H, Chen W, Tong Y, Zhao C, Lin Y, et al. Two-step carbothermal welding to access atomically dispersed Pd 1 on three-dimensional zirconia nanonet for direct indole synthesis. J Am Chem Soc 2019;141:10590–4. https://doi.org/10.1021/jacs.9b03182.
[319] He X, Deng Y, Zhang Y, He Q, Xiao D, Peng M, et al. Mechanochemical kilogram-scale synthesis of noble metal single-atom catalysts. Cell Reports Phys Sci 2020;1:100004. https://doi.org/10.1016/j.xcrp.2019.100004.
[320] Xin P, Li J, Xiong Y, Wu X, Dong J, Chen W, et al. Revealing the active species for aerobic alcohol oxidation by using uniform supported palladium catalysts. Angew Chem Int Ed 2018;57:4642–6. https://doi.org/10.1002/anie.201801103.
[321] Hou Z, Dai L, Liu Y, Deng J, Jing L, Pei W, et al. Highly efficient and enhanced sulfur resistance supported bimetallic single-atom palladium–cobalt catalysts for benzene oxidation. Appl Catal B Environ 2021;285:119844. https://doi.org/10.1016/j.apcatb.2020.119844.
[322] Zhou Y, Gao G, Kang J, Chu W, Wang LW. Transition metal-embedded two-dimensional C3N as a highly active electrocatalyst for oxygen evolution and reduction reactions. J Mater Chem 2019;7. https://doi.org/10.1039/c9ta01389j. 12050–9.
[323] Deng Q, Zhao J, Wu T, Chen G, Hansen HA, Vegge T. 2D transition metal–TCNQ sheets as bifunctional single-atom catalysts for oxygen reduction and evolution reaction (ORR/OER). J Catal 2019;370:378–84. https://doi.org/10.1016/j.jcat.2018.12.012.
[324] Liang J, Lin J, Liu J, Wang X, Zhang T, Li J. Dual metal active sites in an Ir 1/FeO x single-atom catalyst: a redox mechanism for the water-gas shift reaction. Angew Chem Int Ed 2020;59:12868–75. https://doi.org/10.1002/anie.201914867.
[325] Jakub Z, Hulva J, Meier M, Bliem R, Kraushofer F, Setvin M, et al. Local structure and coordination define adsorption in a model Ir1/Fe3O4 single-atom catalyst. Angew Chem Int Ed 2019;131:14099–106. https://doi.org/10.1002/anie.201907536.

[326] Yang J, Zhang J, Jiang Q, Su Y, Cui Y, Li X, et al. Highly active and stable Ir nanoclusters derived from Ir 1/MgAl 2 O 4 single-atom catalysts. J Chem Phys 2021;154:131105. https://doi.org/10.1063/5.0048565.
[327] Jiang K, Luo M, Peng M, Yu Y, Lu YR, Chan TS, et al. Dynamic active-site generation of atomic iridium stabilized on nanoporous metal phosphides for water oxidation. Nat Commun 2020;11:1–9. https://doi.org/10.1038/s41467-020-16558-1.
[328] Wen N, Xia Y, Wang H, Zhang D, Wang H, Wang X, et al. Large-scale synthesis of spinel Ni x Mn 3-x O 4 solid solution immobilized with iridium single atoms for efficient alkaline seawater electrolysis. Adv Sci 2022;9:2200529. https://doi.org/10.1002/advs.202200529.
[329] Zhao Y, Yan X, Yang KR, Cao S, Dong Q, Thorne JE, et al. End-on bound iridium dinuclear heterogeneous catalysts on WO3 for solar water oxidation. ACS Cent Sci 2018;4:1166–72. https://doi.org/10.1021/acscentsci.8b00335.
[330] Liu Q, Li Y, Zheng L, Shang J, Liu X, Yu R, et al. Sequential synthesis and active-site coordination principle of precious metal single-atom catalysts for oxygen reduction reaction and PEM fuel cells. Adv Energy Mater 2020;10:2000689. https://doi.org/10.1002/aenm.202000689.
[331] Shen Q, Jin H, Li P, Yu X, Zheng L, Song W, et al. Breaking the activity limitation of iridium single-atom catalyst in hydrogenation of quinoline with synergistic nanoparticles catalysis. Nano Res 2022;15:5024–31. https://doi.org/10.1007/s12274-022-4235-4.
[332] Yang Y, Li F, Chen J, Fan J, Xiang Q. Single Au atoms anchored on amino-group-enriched graphitic carbon nitride for photocatalytic CO2 reduction. ChemSusChem 2020;13. https://doi.org/10.1002/cssc.202000375. 1979–85.
[333] Liu L, Su H, Tang F, Zhao X, Liu Q. Confined organometallic Au1N single-site as an efficient bifunctional oxygen electrocatalyst. Nano Energy 2018;46:110–6. https://doi.org/10.1016/j.nanoen.2018.01.044.
[334] Xiang Y, He J, Sun N, Fan Y, Yang L, Fang C, et al. Hollow mesoporous CeO2 microspheres for efficient loading of Au single-atoms to catalyze the water-gas shift reaction. Microporous Mesoporous Mater 2020;603:117746. https://doi.org/10.1016/j.micromeso.2020.110507.
[335] Qiao B, Liu J, Wang Y-G, Lin Q, Liu X, Wang A, et al. Highly efficient catalysis of preferential oxidation of CO in H 2 -rich stream by gold single-atom catalysts. ACS Catal 2015;5:6249–54. https://doi.org/10.1021/acscatal.5b01114.
[336] Xing Y, Wang C, Li D, Wang R, Liang S, Li Y, et al. Solution Plasma processing single-atom Au 1 on CeO 2 nanosheet for low temperature photo-enhanced Mars–van Krevelen CO oxidation. Adv Funct Mater 2022;32:2207694. https://doi.org/10.1002/adfm.202207694.
[337] Lou Y, Cai Y, Hu W, Wang L, Dai Q, Zhan W, et al. Identification of active area as active center for CO oxidation over single Au atom catalyst. ACS Catal 2020;10:6094–101. https://doi.org/10.1021/acscatal.0c01303.
[338] Qiao B, Liang J-X, Wang A, Xu C-Q, Li J, Zhang T, et al. Ultrastable single-atom gold catalysts with strong covalent metal-support interaction (CMSI). Nano Res 2015;8:2913–24. https://doi.org/10.1007/s12274-015-0796-9.
[339] Dong F, Guo Y, Zhang D, Zhu B, Huang W, Zhang S. Gold nanoparticles supported on urchin-like CuO: synthesis, characterization, and their catalytic performance for CO oxidation. Nanomaterials 2019;10:67. https://doi.org/10.3390/nano10010067.
[340] Cai C, Han S, Wang Q, Gu M. Direct observation of yolk-shell transforming to gold single atoms and clusters with superior oxygen evolution reaction efficiency. ACS Nano 2019;13:8865–71. https://doi.org/10.1021/acsnano.9b02135.
[341] Shi JL, Zhao XJ, Zhang LY, Xue XL, Guo ZX, Gao YF, et al. An oxidized magnetic Au single atom on doped TiO2(110) becomes a high performance CO oxidation catalyst due to the charge effect. J Mater Chem 2017;5:19316–22. https://doi.org/10.1039/c7ta05483a.
[342] Cao S, Yang M, Elnabawy AO, Trimpalis A, Li S, Wang C, et al. Single-atom gold oxo-clusters prepared in alkaline solutions catalyse the heterogeneous methanol self-coupling reactions. Nat Chem 2019;11:1098–105. https://doi.org/10.1038/s41557-019-0345-3.
[343] Zeng Y, Tang Z, Wu X, Huang A, Luo X, Xu GQ, et al. Photocatalytic oxidation of methane to methanol by tungsten trioxide-supported atomic gold at room temperature. Appl Catal B Environ 2022;306:120919. https://doi.org/10.1016/j.apcatb.2021.120919.
[344] Back S, Lim J, Kim NY, Kim YH, Jung Y. Single-atom catalysts for CO2 electroreduction with significant activity and selectivity improvements. Chem Sci 2017;8:1090–6. https://doi.org/10.1039/c6sc03911a.
[345] Wang F, Chen H, Sun X, Wang C, Ma Y, Song X, et al. Single atom Fe in favor of carbon disulfide (CS2) adsorption and thus the removal efficiency. Separ Purif Technol 2021;258:118086. https://doi.org/10.1016/j.seppur.2020.118086.
[346] Cheong WC, Yang W, Zhang J, Li Y, Zhao D, Liu S, et al. Isolated iron single-atomic site-catalyzed chemoselective transfer hydrogenation of nitroarenes to arylamines. ACS Appl Mater Interfaces 2019;11:33819–24. https://doi.org/10.1021/acsami.9b09125.
[347] Zhang R, Jiao L, Yang W, Wan G, Jiang HL. Single-Atom catalysts templated by metal-organic frameworks for electrochemical nitrogen reduction. J Mater Chem 2019;7:26371–7. https://doi.org/10.1039/c9ta10206j.
[348] Zhao YM, Zhang PC, Xu C, Zhou XY, Liao LM, Wei PJ, et al. Design and preparation of Fe-N5 catalytic sites in single-atom catalysts for enhancing the oxygen reduction reaction in fuel cells. ACS Appl Mater Interfaces 2020;12:17334–42. https://doi.org/10.1021/acsami.9b20711.
[349] Hou T, Peng H, Xin Y, Wang S, Zhu W, Chen L, et al. Fe single-atom catalyst for visible-light-driven photofixation of nitrogen sensitized by triphenylphosphine and sodium iodide. ACS Catal 2020;10:5502–10. https://doi.org/10.1021/acscatal.0c00920.
[350] Wang L, Liu X, Cao L, Zhang W, Chen T, Lin Y, et al. Active sites of single-atom iron catalyst for electrochemical hydrogen evolution. J Phys Chem Lett 2020;11:6691–6. https://doi.org/10.1021/acs.jpclett.0c01943.
[351] Jiao L, Yang W, Wan G, Zhang R, Zheng X, Zhou H, et al. Single-atom electrocatalysts from multivariate metal–organic frameworks for highly selective reduction of CO2 at low pressures. Angew Chem Int Ed 2020;59:20589–95. https://doi.org/10.1002/anie.202008787.
[352] Duan J, Zhou Y, Ren Y, Feng D, Shang J, Ge H, et al. Insights into the effect of substrate adsorption behavior over heme-like Fe1/AC single-atom catalyst. Nano Res 2022;15:5970–6. https://doi.org/10.1007/s12274-022-4274-x.
[353] Huang Y, An C, Zhang Q, Zang L, Shao H, Liu Y, et al. Cost-effective mechanochemical synthesis of highly dispersed supported transition metal catalysts for hydrogen storage. Nano Energy 2021;80:105535. https://doi.org/10.1016/j.nanoen.2020.105535.
[354] Cheng X, Wang J, Zhao K, Bi Y. Spatially confined iron single-atom and potassium ion in carbon nitride toward efficient CO2 reduction. Appl Catal B Environ 2022;316:121643. https://doi.org/10.1016/j.apcatb.2022.121643.
[355] Chen Z, Zhang J, Zheng S, Ding J, Sun J, Dong M, et al. The texture evolution of g-C 3 N 4 nanosheets supported Fe catalyst during Fischer-Tropsch synthesis. Mol Catal 2018;444:90–9. https://doi.org/10.1016/j.molcata.2016.12.011.
[356] An S, Zhang G, Wang T, Zhang W, Li K, Song C, et al. High-density ultra-small clusters and single-atom Fe sites embedded in graphitic carbon nitride (g-C 3 N 4) for highly efficient catalytic advanced oxidation processes. ACS Nano 2018;12:9441–50. https://doi.org/10.1021/acsnano.8b04693.
[357] Wang X, Jin B, Jin Y, Wu T, Ma L, Liang X. Supported single Fe atoms prepared via atomic layer deposition for catalytic reactions. ACS Appl Nano Mater 2020;3:2867–74. https://doi.org/10.1021/acsanm.0c00146.
[358] Qin F, Zhang J, Zhou Z, Xu H, Cui L, Lv Z, et al. TiO 2 nanoflowers decorated with FeO x nanocluster and single atoms by atomic layer deposition for peroxidase-mimicking nanozymes. ACS Appl Nano Mater 2022;5:13090–9. https://doi.org/10.1021/acsanm.2c02875.
[359] Zhu Z-H, Yu B, Sun W, Chen S, Wang Y, Li X, et al. Triazine organic framework derived Fe single-atom bifunctional electrocatalyst for high performance zinc air batteries. J Power Sources 2022;542:231583. https://doi.org/10.1016/j.jpowsour.2022.231583.
[360] Qu W, Liu X, Chen J, Dong Y, Tang X, Chen Y. Single-atom catalysts reveal the dinuclear characteristic of active sites in NO selective reduction with NH3. Nat Commun 2020;11:1–7. https://doi.org/10.1038/s41467-020-15261-5.
[361] Meng J, Li J, Liu J, Zhang X, Jiang G, Ma L, et al. Universal approach to fabricating graphene-supported single-atom catalysts from doped ZnO solid solutions. ACS Cent Sci 2020;6:1431–40. https://doi.org/10.1021/acscentsci.0c00458.
[362] Su L, Wang P, Ma X, Wang J, Zhan S. Regulating local electron density of iron single sites by introducing nitrogen vacancies for efficient photo-fenton process. Angew Chem Int Ed 2021;60:21261–6. https://doi.org/10.1002/anie.202108937.
[363] Zhu C, Nie Y, Cun F, Wang Y, Tian Z, Liu F. Two-step pyrolysis to anchor ultrahigh-density single-atom FeN5 sites on carbon nitride for efficient Fenton-like catalysis near 0 °C. Appl Catal B Environ 2022;319:121900. https://doi.org/10.1016/j.apcatb.2022.121900.
[364] Harrath K, Yu X, Xiao H, Li J. The key role of support surface hydrogenation in the CH4 to CH3OH selective oxidation by a ZrO2-supported single-atom catalyst. ACS Catal 2019;9:8903–9. https://doi.org/10.1021/acscatal.9b02093.
[365] Hu L, Huang J, Wang J, Jiang S, Sun C, Song S. Efficiently photocatalytic H2O overall splitting within the strengthened polarized field by reassembling surface single atoms. Appl Catal B Environ 2023;320:121945. https://doi.org/10.1016/j.apcatb.2022.121945.
[366] Kwak M, Bok J, Lee BH, Kim J, Seo Y, Kim S, et al. Ni single atoms on carbon nitride for visible-light-promoted full heterogeneous dual catalysis. Chem Sci 2022;13:8536–42. https://doi.org/10.1039/d2sc02174a.
[367] Ma J, Zhang F, Tan Y, Wang S, Chen H, Zheng L, et al. Promoted electron transfer and surface absorption by single nickel atoms for photocatalytic cross-coupling of aromatic alcohols and aliphatic amines under visible light. ACS Appl Mater Interfaces 2022;14:18383–92. https://doi.org/10.1021/acsami.2c00311.
[368] Tang Y, Wei Y, Wang Z, Zhang S, Li Y, Nguyen L, et al. Synergy of single-atom Ni1 and Ru1 sites on CeO2 for dry reforming of CH4. J Am Chem Soc 2019;141:7283–93. https://doi.org/10.1021/jacs.8b10910.
[369] Akri M, Zhao S, Li X, Zang K, Lee AF, Isaacs MA, et al. Atomically dispersed nickel as coke-resistant active sites for methane dry reforming. Nat Commun 2019;10:1–10. https://doi.org/10.1038/s41467-019-12843-w.
[370] Lv S, Pei M, Liu Y, Si Z, Wu X, Ran R, et al. An isolation strategy to anchor atomic Ni or Co cocatalysts on TiO2(A) for photocatalytic hydrogen production. Nano Res 2022;15:5848–56. https://doi.org/10.1007/s12274-022-4217-6.
[371] Wu J, Gao J, Lian S, Li J, Sun K, Zhao S, et al. Engineering the oxygen vacancies enables Ni single-atom catalyst for stable and efficient C-H activation. Appl Catal B Environ 2022;314:121516. https://doi.org/10.1016/j.apcatb.2022.121516.
[372] Ling C, Shi L, Ouyang Y, Zeng XC, Wang J. Nanosheet supported single-metal atom bifunctional catalyst for overall water splitting. Nano Lett 2017;17:5133–9. https://doi.org/10.1021/acs.nanolett.7b02518.
[373] Zhang Q, Guo L, Hao Z. CO hydrogenation on M1/W6S8 (M = Co and Ni) single-atom catalysts: competition between C2 hydrocarbons and methanol synthesis pathways. Mol Catal 2019;464:10. https://doi.org/10.1016/j.mcat.2018.12.001.
[374] Wu Y, Li C, Liu W, Li H, Gong Y, Niu L, et al. Unexpected monoatomic catalytic-host synergetic OER/ORR by graphitic carbon nitride: density functional theory. Nanoscale 2019;11:5064–71. https://doi.org/10.1039/c8nr09300h.

[375] Pei J, Peng B, Lin H, Chen W, Wang Y, Dong J, et al. Single-atom Ru on Al 2 O 3 for highly active and selective 1,2-dichloroethane catalytic degradation. ACS Appl Mater Interfaces 2021;13:53683–90. https://doi.org/10.1021/acsami.1c08471.
[376] Ge L, Qiu M, Zhu Y, Yang S, Li W, Li W, et al. Synergistic catalysis of Ru single-atoms and zeolite boosts high-efficiency hydrogen storage. Appl Catal B Environ 2022;319:121958. https://doi.org/10.1016/j.apcatb.2022.121958.
[377] Cao L, Luo Q, Chen J, Wang L, Lin Y, Wang H, et al. Dynamic oxygen adsorption on single-atomic Ruthenium catalyst with high performance for acidic oxygen evolution reaction. Nat Commun 2019;10:1–9. https://doi.org/10.1038/s41467-019-12886-z.
[378] Lin J, Ding J, Wang H, Yang X, Zheng X, Huang Z, et al. Boosting energy efficiency and stability of Li–CO 2 batteries via synergy between Ru atom clusters and single-atom Ru–N 4 sites in the electrocatalyst cathode. Adv Mater 2022;34:2200559. https://doi.org/10.1002/adma.202200559.
[379] Li C, Dong X, Zhang Y, Hu J, Yuan J, Li G, et al. Micro-tailored g-C3N4 enables Ru single-atom loading for efficient photocatalytic H2 evolution. Appl Surf Sci 2022;596:153471. https://doi.org/10.1016/j.apsusc.2022.153471.
[380] Li L, Yu Y, Lin S, Chu W, Sun D, Su Q, et al. Single ruthenium atom supported on g-C3N4 as an efficient photocatalyst for nitrogen fixation in ultra-pure water. Catal Commun 2021;153:106294. https://doi.org/10.1016/j.catcom.2021.106294.
[381] Sarma BB, Kim J, Amsler J, Agostini G, Weidenthaler C, Pfänder N, et al. One-pot cooperation of single-atom Rh and Ru solid catalysts for a selective tandem olefin isomerization-hydrosilylation process. Angew Chem Int Ed 2020;59:5806–15. https://doi.org/10.1002/anie.201915255.
[382] Sivan SE, Kang KH, Han SJ, Francis Ngome Okello O, Choi S-Y, Sudheeshkumar V, et al. Facile MOF-derived one-pot synthetic approach toward Ru single atoms, nanoclusters, and nanoparticles dispersed on CeO2 supports for enhanced ammonia synthesis. J Catal 2022;408:316–28. https://doi.org/10.1016/j.jcat.2022.03.019.
[383] Zeng K, Tian M, Chen X, Zhang J, Rummeli MH, Strasser P, et al. Strong electronic coupling between single Ru atoms and cobalt-vanadium layered double hydroxide harness efficient water splitting. Chem Eng J 2023;452:139151. https://doi.org/10.1016/j.cej.2022.139151.
[384] Sun L, Cao L, Su Y, Wang C, Lin J, Wang X. Ru1/FeOx single-atom catalyst with dual active sites for water gas shift reaction without methanation. Appl Catal B Environ 2022;318:121841. https://doi.org/10.1016/j.apcatb.2022.121841.
[385] Yang Y, Yang F, Wang H, Zhou B, Hao S. Amine-promoted Ru1/Fe3O4 encapsulated in hollow periodic mesoporousorganosilica sphere as a highly selective and stable catalyst for aqueous levulinic acid hydrogenation. J Colloid Interface Sci 2021;581:167–76. https://doi.org/10.1016/j.jcis.2020.07.114.
[386] Tiwari JN, Dang NK, Sultan S, Thangavel P, Jeong HY, Kim KS. Multi-heteroatom-doped carbon from waste-yeast biomass for sustained water splitting. Nat Sustain 2020;3:556–63. https://doi.org/10.1038/s41893-020-0509-6.
[387] Li J, Yi D, Zhan F, Zhou B, Gao D, Guo D, et al. Monolayered Ru1/TiO2 nanosheet enables efficient visible-light-driven hydrogen evolution. Appl Catal B Environ 2020;271:118925. https://doi.org/10.1016/j.apcatb.2020.118925.
[388] Liu S, Wang Y, Wang S, You M, Hong S, Wu T-S, et al. Photocatalytic fixation of nitrogen to ammonia by single Ru atom decorated TiO 2 nanosheets. ACS Sustainable Chem Eng 2019;7:6813–20. https://doi.org/10.1021/acssuschemeng.8b06134.
[389] Liu Z, Li H, Gao X, Guo X, Wang S, Fang Y, et al. Rational highly dispersed ruthenium for reductive catalytic fractionation of lignocellulose. Nat Commun 2022;13:4716. https://doi.org/10.1038/s41467-022-32451-5.
[390] Li M, Zhao S, Li J, Chen X, Ji Y, Yu H, et al. Partially charged single-atom Ru supported on ZrO2 nanocrystals for highly efficient ethylene hydrosilylation with triethoxysilane. Nano Res 2022;15:5857–64. https://doi.org/10.1007/s12274-022-4227-4.
[391] Bai L, Sun H, Wu Q, Yao W. Supported Ru single atoms and clusters on P-doped carbon nitride as an efficient photocatalyst for H 2 O 2 production. ChemCatChem 2022;14:e202101954. https://doi.org/10.1002/cctc.202101954.
[392] Hoffman AJ, Asokan C, Gadinas N, Kravchenko P, Bean Getsoian A, Christopher P, et al. Theoretical and experimental characterization of adsorbed CO and NO on γ-Al 2 O 3 -supported Rh nanoparticles. J Phys Chem C 2021;125. https://doi.org/10.1021/acs.jpcc.1c05160. 19733–55.
[393] Hoffman AJ, Asokan C, Gadinas N, Schroeder E, Zakem G, Nystrom SV, et al. Experimental and theoretical characterization of Rh single atoms supported on γ-Al2O3with varying hydroxyl contents during NO reduction by CO. ACS Catal 2022;12:11697–715. https://doi.org/10.1021/acscatal.2c02813.
[394] Zhang J, Asokan C, Zakem G, Christopher P, Medlin JW. Enhancing sintering resistance of atomically dispersed catalysts in reducing environments with organic monolayers. Green Energy Environ 2022;7:1263–9. https://doi.org/10.1016/j.gee.2021.01.022.
[395] Ponticorvo E, Iuliano M, Cirillo C, Sarno M. Selective C2 electrochemical synthesis from methane on modified alumina supporting single atom catalysts. Chem Eng J 2023;451:139074. https://doi.org/10.1016/j.cej.2022.139074.
[396] Ding W, Li W. First-principles study of NO reduction by CO on transition metal atoms-doped CeO2(111). Chin J Catal 2014;35:1937–43. https://doi.org/10.1016/S1872-2067(14)60169-8.
[397] Wu B, Yu X, Huang M, Zhong L, Sun Y. Rh single atoms embedded in CeO2 nanostructure boost CO2 hydrogenation to HCOOH. Chin J Chem Eng 2022;43:62–9. https://doi.org/10.1016/j.cjche.2021.11.018.
[398] Wu D, Liu S, Zhong M, Zhao J, Du C, Yang Y, et al. Nature and dynamic evolution of Rh single atoms trapped by CeO 2 in CO hydrogenation. ACS Catal 2022;12:12253–67. https://doi.org/10.1021/acscatal.2c02103.
[399] Li X, Li L, Qin T, Gun G, Lin T, Zhong L. Atomically dispersed Rh on hydroxyapatite as an effective catalyst for tandem hydroaminomethylation of olefins. Mol Catal 2021;509:111671. https://doi.org/10.1016/j.mcat.2021.111671.
[400] Shen P, Li X, Luo Y, Zhang N, Zhao X, Chu K. Ultra-efficient N2 electroreduction achieved over a rhodium single-atom catalyst (Rh1/MnO2) in water-in-salt electrolyte. Appl Catal B Environ 2022;316:121651. https://doi.org/10.1016/j.apcatb.2022.121651.
[401] Lou Y, Zheng Y, Li X, Ta N, Xu J, Nie Y, et al. Pocketlike active site of Rh1/MoS2 single-atom catalyst for selective crotonaldehyde hydrogenation. J Am Chem Soc 2019;141:19289. https://doi.org/10.1021/jacs.9b06628. –95.
[402] Zhang S, Tang Y, Nguyen L, Zhao YF, Wu Z, Goh TW, et al. Catalysis on singly dispersed Rh atoms anchored on an inert support. ACS Catal 2018;8:110–21. https://doi.org/10.1021/acscatal.7b01788.
[403] Guan H, Lin J, Qiao B, Miao S, Wang AQ, Wang X, et al. Enhanced performance of Rh1/TiO2 catalyst without methanation in water-gas shift reaction. AIChE J 2017;63:2081–8. https://doi.org/10.1002/aic.15585.
[404] Sun Q, Wang N, Zhang T, Bai R, Mayoral A, Zhang P, et al. Zeolite-encaged single-atom rhodium catalysts: highly-efficient hydrogen generation and shape-selective tandem hydrogenation of nitroarenes. Angew Chem Int Ed 2019;58:18570–6. https://doi.org/10.1002/anie.201912367.
[405] Han B, Lang R, Tang H, Xu J, Gu XK, Qiao B, et al. Superior activity of Rh1/ZnO single-atom catalyst for CO oxidation. Chin J Catal 2019;40:1847–53. https://doi.org/10.1016/S1872-2067(19)63411-X.
[406] Chen S, Wang B, Zhu J, Wang L, Ou H, Zhang Z, et al. Lewis acid site-promoted single-atomic Cu catalyzes electrochemical CO 2 methanation. Nano Lett 2021;21:7325–31. https://doi.org/10.1021/acs.nanolett.1c02502.
[407] Islam MJ, Granollers Mesa M, Osatiashtiani A, Taylor MJ, Manayil JC, Parlett CMA, et al. The effect of metal precursor on copper phase dispersion and nanoparticle formation for the catalytic transformations of furfural. Appl Catal B Environ 2020;273:119062. https://doi.org/10.1016/j.apcatb.2020.119062.
[408] Yang Z, Chen B, Chen W, Qu Y, Zhou F, Zhao C, et al. Directly transforming copper (I) oxide bulk into isolated single-atom copper sites catalyst through gas-transport approach. Nat Commun 2019;10:1–7. https://doi.org/10.1038/s41467-019-11796-4.
[409] Ren P, Ren P, Li Q, Li Q, Song T, Yang Y. Facile fabrication of the Cu-N-C catalyst with atomically dispersed unsaturated Cu-N2 active sites for highly efficient and selective glaser-hay coupling. ACS Appl Mater Interfaces 2020;12:27210–8. https://doi.org/10.1021/acsami.0c05100.
[410] Sun T, Li Y, Cui T, Xu L, Wang YG, Chen W, et al. Engineering of coordination environment and multiscale structure in single-site copper catalyst for superior electrocatalytic oxygen reduction. Nano Lett 2020;20:6206–14. https://doi.org/10.1021/acs.nanolett.0c02677.
[411] Lee BH, Gong E, Kim M, Park S, Kim HR, Lee J, et al. Electronic interaction between transition metal single-atoms and anatase TiO2boosts CO2photoreduction with H2O. Energy Environ Sci 2022;15:601–9. https://doi.org/10.1039/d1ee01574e.
[412] Ž Kovačič, Likozar B, Huš M. Photocatalytic CO2Reduction: a review of ab initio mechanism, kinetics, and multiscale modeling simulations. ACS Catal 2020. https://doi.org/10.1021/acscatal.0c02557.
[413] Wang G, Zhang T, Yu W, Si R, Liu Y, Zhao Z. Modulating location of single copper atoms in polymeric carbon nitride for enhanced photoredox catalysis. ACS Catal 2020;10:5715–22. https://doi.org/10.1021/acscatal.0c01099.
[414] Liu J, He H, Shen Z, Wang HH, Li W. Photoassisted highly efficient activation of persulfate over a single-atom Cu catalyst for tetracycline degradation: process and mechanism. J Hazard Mater 2022;429:128398. https://doi.org/10.1016/j.jhazmat.2022.128398.
[415] Wu B, Yang R, Shi L, Lin T, Yu X, Huang M, et al. Cu single-atoms embedded in porous carbon nitride for selective oxidation of methane to oxygenates. Chem Commun 2020;56:14677–80. https://doi.org/10.1039/D0CC06492K.
[416] Song J, Chen Z, Cai X, Zhou X, Zhan G, Li R, et al. Promoting dinuclear-type catalysis in Cu 1 –C 3 N 4 single-atom catalysts. Adv Mater 2022;34:2204638. https://doi.org/10.1002/adma.202204638.
[417] Gao X, Ma W, Mao J, He C-T, Ji W, Chen Z, et al. A single-atom Cu–N 2 catalyst eliminates oxygen interference for electrochemical sensing of hydrogen peroxide in a living animal brain. Chem Sci 2021;12:15045–53. https://doi.org/10.1039/D1SC04755H.
[418] Jiang M, Chen J, Gao Y, Lv X, Yan D, Jia H. Using the interaction between copper and manganese to stabilize copper single-atom for CO oxidation. Chem Eur J 2021;27:9060–70. https://doi.org/10.1002/chem.202100442.
[419] Chen C, Wang T, Yan K, Liu S, Zhao Y, Li B. Photocatalytic CO 2 reduction on Cu single atoms incorporated in ordered macroporous TiO 2 toward tunable products. Inorg Chem Front 2022;9:4753–67. https://doi.org/10.1039/D2QI01155G.
[420] Zhao H, Yu R, Ma S, Xu K, Chen Y, Jiang K, et al. The role of Cu1–O3 species in single-atom Cu/ZrO2 catalyst for CO2 hydrogenation. Nat Catal 2022;5:818–31. https://doi.org/10.1038/s41929-022-00840-0.
[421] Zong L, Fan K, Wu W, Cui L, Zhang L, Johannessen B, et al. Anchoring single copper atoms to microporous carbon spheres as high-performance electrocatalyst for oxygen reduction reaction. Adv Funct Mater 2021;31:2104864. https://doi.org/10.1002/adfm.202104864.
[422] Mou X, Wang D, Liu X, Liu W, Cao L, Yao T. XAFS study on single-atomic-site Cu1/N-graphene catalyst for oxygen reduction reaction. Radiat Phys Chem 2020;175:108230. https://doi.org/10.1016/j.radphyschem.2019.03.034.
[423] Yan H, Zhao X, Guo N, Lyu Z, Du Y, Xi S, et al. Atomic engineering of high-density isolated Co atoms on graphene with proximal-atom controlled reaction

selectivity. Nat Commun 2018;9:1–9. https://doi.org/10.1038/s41467-018-05754-9.
[424] Liu X, Huang D, Lai C, Qin L, Liu S, Zhang M, et al. Single cobalt atom anchored on carbon nitride with cobalt nitrogen/oxygen active sites for efficient Fenton-like catalysis. J Colloid Interface Sci 2023;629:417–27. https://doi.org/10.1016/j.jcis.2022.08.108.
[425] Yan B, He Y, Yang G. Electronic structure regulation of cobalt oxide clusters for promoting photocatalytic hydrogen evolution. J Mater Chem 2022;10. https://doi.org/10.1039/D1TA08279E. 1899–908.
[426] Wang H, Li X, Jiang Y, Li M, Xiao Q, Zhao T, et al. A universal single-atom coating strategy based on tannic acid chemistry for multifunctional heterogeneous catalysis. Angew Chem Int Ed 2022;61:e202200465. https://doi.org/10.1002/anie.202200465.
[427] Jin H, Li P, Cui P, Shi J, Zhou W, Yu X, et al. Unprecedentedly high activity and selectivity for hydrogenation of nitroarenes with single atomic Co1-N3P1 sites. Nat Commun 2022;13:723. https://doi.org/10.1038/s41467-022-28367-9.
[428] Ohyama J, Abe D, Hirayama A, Iwai H, Tsuchimura Y, Sakamoto K, et al. Selective oxidation of methane to formaldehyde over a silica-supported cobalt single-atom catalyst. J Phys Chem C 2022;126:1785–92. https://doi.org/10.1021/acs.jpcc.1c08739.
[429] Geng Z, Cao Y, Chen W, Kong X, Liu Y, Yao T, et al. Regulating the coordination environment of Co single atoms for achieving efficient electrocatalytic activity in CO2 reduction. Appl Catal B Environ 2019;240:234–40. https://doi.org/10.1016/j.apcatb.2018.08.075.
[430] Hai X, Zhao X, Guo N, Yao C, Chen C, Liu W, et al. Engineering local and global structures of single Co atoms for a superior oxygen reduction reaction. ACS Catal 2020;10:5862–70. https://doi.org/10.1021/acscatal.0c00936.
[431] Jiang M, Yan D, Lv X, Gao Y, Jia H. Recognition of water-dissociation effect toward lattice oxygen activation on single-atom Co catalyst in toluene oxidation. Appl Catal B Environ 2022;319:121962. https://doi.org/10.1016/j.apcatb.2022.121962.
[432] Kyriakou G, Beaumont SK, Humphrey SM, Antonetti C, Lambert RM. Sonogashira coupling catalyzed by gold nanoparticles: does homogeneous or heterogeneous catalysis dominate? ChemCatChem 2010;2:1444–9. https://doi.org/10.1002/cctc.201000154.
[433] Beaumont SK, Kyriakou G, Lambert RM. Identity of the active site in gold nanoparticle-catalyzed sonogashira coupling of phenylacetylene and iodobenzene. J Am Chem Soc 2010;132:12246–8. https://doi.org/10.1021/ja1063179.
[434] Cao S, Tao FF, Tang Y, Li Y, Yu J. Size- and shape-dependent catalytic performances of oxidation and reduction reactions on nanocatalysts. Chem Soc Rev 2016;45:4747–65. https://doi.org/10.1039/c6cs00094k.
[435] Joo SH, Park JY, Renzas JR, Butcher DR, Huang W, Somorjai GA. Size effect of ruthenium nanoparticles in catalytic carbon monoxide oxidation. Nano Lett 2010;10:2709–13. https://doi.org/10.1021/nl101700j.
[436] Zhang H, Watanabe T, Okumura M, Haruta M, Toshima N. Catalytically highly active top gold atom on palladium nanocluster. Nat Mater 2012;11:49–52. https://doi.org/10.1038/nmat3143.
[437] Pei GX, Liu XY, Yang X, Zhang L, Wang A, Li L, et al. Performance of Cu-alloyed Pd single-atom catalyst for semihydrogenation of acetylene under simulated front-end conditions. ACS Catal 2017;7:1491–500. https://doi.org/10.1021/acscatal.6b03293.
[438] Yang M, Li S, Wang Y, Herron JA, Xu Y, Allard LF, et al. Catalytically active Au-O(OH)x- species stabilized by alkali ions on zeolites and mesoporous oxides. Science 2014;346(80):1498–501. https://doi.org/10.1126/science.1260526.
[439] Lee E-K, Park S-A, Woo H, Hyun Park K, Kang DW, Lim H, et al. Platinum single atoms dispersed on carbon nanotubes as reusable catalyst for Suzuki coupling reaction. J Catal 2017;352:388–93. https://doi.org/10.1016/j.jcat.2017.05.005.
[440] Kim SK, Kim HW, Han SJ, Lee SW, Shin J, Kim YT. Mechanistic and microkinetic study of non-oxidative methane coupling on a single-atom iron catalyst. Commun Chem 2020;3:58. https://doi.org/10.1038/s42004-020-0306-1.
[441] Chen Z, Vorobyeva E, Mitchell S, Fako E, Ortuño MA, López N, et al. A heterogeneous single-atom palladium catalyst surpassing homogeneous systems for suzuki coupling. Nat Nanotechnol 2018. https://doi.org/10.1038/s41565-018-0167-2.
[442] Liu S, Yang H Bin, Hung S, Ding J, Cai W, Liu L, et al. Elucidating the electrocatalytic CO 2 reduction reaction over a model single-atom nickel catalyst. Angew Chem Int Ed 2020;59:798–803. https://doi.org/10.1002/anie.201911995.
[443] Boucher MB, Zugic B, Cladaras G, Kammert J, Marcinkowski MD, Lawton TJ, et al. Single atom alloy surface analogs in Pd0.18Cu15 nanoparticles for selective hydrogenation reactions. Phys Chem Chem Phys 2013;15:12187–96. https://doi.org/10.1039/c3cp51538a.
[444] Zhou G, Zhao S, Wang T, Yang S-Z, Johannessen B, Chen H, et al. Theoretical calculation guided design of single-atom catalysts toward fast kinetic and long-life Li–S batteries. Nano Lett 2020;20:1252–61. https://doi.org/10.1021/acs.nanolett.9b04719.
[445] Crespo-Quesada M, Cárdenas-Lizana F, Dessimoz A-L, Kiwi-Minsker L. Modern trends in catalyst and process design for alkyne hydrogenations. ACS Catal 2012;2:1773–86. https://doi.org/10.1021/cs300284r.
[446] Meemken F, Baiker A. Recent progress in heterogeneous asymmetric hydrogenation of C=O and C=C bonds on supported noble metal catalysts. Chem Rev 2017;117:11522–69. https://doi.org/10.1021/acs.chemrev.7b00272.
[447] Zhang L, Zhou M, Wang A, Zhang T. Selective hydrogenation over supported metal catalysts: from nanoparticles to single atoms. Chem Rev 2020;120:683–733. https://doi.org/10.1021/acs.chemrev.9b00230.
[448] Siddqui N, Sarkar B, Pendem C, Khatun R, Sivakumar Konthala LN, Sasaki T, et al. Highly selective transfer hydrogenation of α,β-unsaturated carbonyl compounds using Cu-based nanocatalysts. Catal Sci Technol 2017;7:2828–37. https://doi.org/10.1039/C7CY00989E.
[449] Matsubu JC, Yang VN, Christopher P. Isolated metal active site concentration and stability control catalytic CO2 reduction selectivity. J Am Chem Soc 2015;137:3076–84. https://doi.org/10.1021/ja5128133.
[450] Li Z, Wang D, Wu Y, Li Y. Recent advances in the precise control of isolated single-site catalysts by chemical methods. Natl Sci Rev 2018;5:673–89. https://doi.org/10.1093/nsr/nwy056.
[451] Ren X, Li J, Wang S, Zhang D, Wang Y. Preparation and hydrogenation performance of single atom Pt catalytic active sites anchored on the surface of metallic supports. Catal Commun 2019;128:105709. https://doi.org/10.1016/j.catcom.2019.105709.
[452] Liu W, Chen Y, Qi H, Zhang L, Yan W, Liu X, et al. A durable nickel single-atom catalyst for hydrogenation reactions and cellulose valorization under harsh conditions. Angew Chem Int Ed 2018;130:7189–93. https://doi.org/10.1002/anie.201802231.
[453] Yan X, Duan P, Zhang F, Li H, Zhang H, Zhao M, et al. Stable single-atom platinum catalyst trapped in carbon onion graphitic shells for improved chemoselective hydrogenation of nitroarenes. Carbon N Y 2019;143:378–84. https://doi.org/10.1016/j.carbon.2018.11.021.
[454] Jiang L, Liu K, Hung S-F, Zhou L, Qin R, Zhang Q, et al. Facet engineering accelerates spillover hydrogenation on highly diluted metal nanocatalysts. Nat Nanotechnol 2020;15:848–53. https://doi.org/10.1038/s41565-020-0746-x.
[455] Song X, Shao F, Zhao Z, Li X, Wei Z, Wang J. Single-atom Ni-modified Al 2 O 3 -supported Pd for mild-temperature semi-hydrogenation of alkynes. ACS Catal 2022. https://doi.org/10.1021/acscatal.2c04883. 14846–55.
[456] Cao W, Lin L, Qi H, He Q, Wu Z, Wang A, et al. In-situ synthesis of single-atom Ir by utilizing metal-organic frameworks: an acid-resistant catalyst for hydrogenation of levulinic acid to γ-valerolactone. J Catal 2019;373:161–72. https://doi.org/10.1016/j.jcat.2019.03.035.
[457] Morin C, Simon D, Sautet P. Intermediates in the hydrogenation of benzene to cyclohexene on Pt(111) and Pd(111): a comparison from DFT calculations. Surf Sci 2006;600:1339–50. https://doi.org/10.1016/j.susc.2006.01.033.
[458] Chen C-S, Chen H-W, Cheng W-H. Study of selective hydrogenation of acetophenone on Pt/SiO2. Appl Catal Gen 2003;248:117–28. https://doi.org/10.1016/S0926-860X(03)00156-X.
[459] Chen M, Maeda N, Baiker A, Huang J. Molecular insight into Pt-catalyzed chemoselective hydrogenation of an aromatic ketone by in situ modulation–excitation IR spectroscopy. ACS Catal 2012;2. https://doi.org/10.1021/cs300408x. 2007–13.
[460] Wang J, Zhao X, Lei N, Li L, Zhang L, Xu S, et al. Hydrogenolysis of glycerol to 1,3-propanediol under low hydrogen pressure over WO x -supported single/pseudo-single atom Pt catalyst. ChemSusChem 2016;9:784–90. https://doi.org/10.1002/cssc.201501506.
[461] Thirumalai H, Kitchin JR. Investigating the reactivity of single atom alloys using density functional theory. Top Catal 2018;61:462–74. https://doi.org/10.1007/s11244-018-0899-0.
[462] Jørgensen M, Grönbeck H. Selective acetylene hydrogenation over single-atom alloy nanoparticles by kinetic Monte Carlo. J Am Chem Soc 2019;141:8541–9. https://doi.org/10.1021/jacs.9b02132.
[463] Fu Q, Luo Y. Catalytic activity of single transition-metal atom doped in Cu(111) surface for heterogeneous hydrogenation. J Phys Chem C 2013;117:14618–24. https://doi.org/10.1021/jp403902g.
[464] Ma J, Gong H, Zhang T, Yu H, Zhang R, Liu Z, et al. Hydrogenation of CO2 to formic acid on the single atom catalysis Cu/C2N: a first principles study. Appl Surf Sci 2019;488:1–9. https://doi.org/10.1016/j.apsusc.2019.03.187.
[465] Frauenheim T, Blaudeck P, Stephan U, Jungnickel G. Atomic structure and physical properties of amorphous carbon and its hydrogenated analogs. Phys Rev B 1993;48:4823–34. https://doi.org/10.1103/PhysRevB.48.4823.
[466] Mudiyanselage K, Yang Y, Hoffmann FM, Furlong OJ, Hrbek J, White MG, et al. Adsorption of hydrogen on the surface and sub-surface of Cu(111). J Chem Phys 2013;139:044712. https://doi.org/10.1063/1.4816515.
[467] Omodara L, Turpeinen EM, Pitkäaho S, Keiski RL. Substitution potential of rare earth catalysts in ethanol steam reforming. Sustain Mater Technol 2020;26:e00237. https://doi.org/10.1016/j.susmat.2020.e00237.
[468] Guo X, Traitangwong A, Hu M, Zuo C, Meeyoo V, Peng Z, et al. Carbon dioxide methanation over nickel-based catalysts supported on various mesoporous. Material. Energy Fuels 2018;32:3681–9. https://doi.org/10.1021/acs.energyfuels.7b03826.
[469] Loy ACM, Yusup S, Lam MK, Chin BLF, Shahbaz M, Yamamoto A, et al. The effect of industrial waste coal bottom ash as catalyst in catalytic pyrolysis of rice husk for syngas production. Energy Convers Manag 2018;165:541–54. https://doi.org/10.1016/j.enconman.2018.03.063.
[470] Yan X, Sun W, Fan L, Duchesne PN, Wang W, Kübel C, et al. Nickel@Siloxene catalytic nanosheets for high-performance CO2 methanation. Nat Commun 2019;10:2608. https://doi.org/10.1038/s41467-019-10464-x.
[471] Sánchez-Bastardo N, Schlögl R, Ruland H. Methane pyrolysis for zero-emission hydrogen production: a potential bridge technology from fossil fuels to a renewable and sustainable hydrogen economy. Ind Eng Chem Res 2021;60:11855–81. https://doi.org/10.1021/acs.iecr.1c01679.
[472] Duarte RB, Krumeich F, van Bokhoven JA. Structure, activity, and stability of atomically dispersed Rh in methane steam reforming. ACS Catal 2014;4:1279–86. https://doi.org/10.1021/cs400979q.

[473] Gu X-K, Qiao B, Huang C-Q, Ding W-C, Sun K, Zhan E, et al. Supported single Pt 1/Au 1 atoms for methanol steam reforming. ACS Catal 2014;4:3886–90. https://doi.org/10.1021/cs500740u.
[474] Zuo Z, Liu S, Wang Z, Liu C, Huang W, Huang J, et al. Dry reforming of methane on single-site Ni/MgO catalysts: importance of site confinement. ACS Catal 2018;8:9821–35. https://doi.org/10.1021/acscatal.8b02277.
[475] Ding K, Gulec A, Johnson AM, Schweitzer NM, Stucky GD, Marks LD, et al. Identification of active sites in CO oxidation and water-gas shift over supported Pt catalysts. Science 2015;350(80):189–92. https://doi.org/10.1126/science.aac6368.
[476] Yang M, Liu J, Lee S, Zugic B, Huang J, Allard LF, et al. A common single-site Pt (II)–O(OH) x – species stabilized by sodium on "active" and "inert" supports catalyzes the water-gas shift reaction. J Am Chem Soc 2015;137:3470–3. https://doi.org/10.1021/ja513292k.
[477] Ammal SC, Heyden A. Water-gas shift activity of atomically dispersed cationic platinum versus metallic platinum clusters on titania supports. ACS Catal 2017;7:301–9. https://doi.org/10.1021/acscatal.6b02764.
[478] Aranifard S, Ammal SC, Heyden A. On the importance of metal–oxide interface sites for the water–gas shift reaction over Pt/CeO2 catalysts. J Catal 2014;309:314–24. https://doi.org/10.1016/j.jcat.2013.10.012.
[479] Liu J, Bunes BR, Zang L, Wang C. Supported single-atom catalysts: synthesis, characterization, properties, and applications. Environ Chem Lett 2018;16:477–505. https://doi.org/10.1007/s10311-017-0679-2.
[480] Li X. Selective oxidation of C–H bonds with Fe-N-C single-atom catalyst. Chin J Catal 2018;39:1–3. https://doi.org/10.1016/S1872-2067(17)63002-X.
[481] Lei Y, Mehmood F, Lee S, Greeley J, Lee B, Seifert S, et al. Increased silver activity for direct propylene epoxidation via subnanometer size effects. Science 2010;328(80):224–8. https://doi.org/10.1126/science.1185200.
[482] Qiao B, Wang A, Li L, Lin Q, Wei H, Liu J, et al. Ferric oxide-supported Pt subnano clusters for preferential oxidation of CO in H 2 -rich gas at room temperature. ACS Catal 2014;4:2113–7. https://doi.org/10.1021/cs500501u.
[483] Poh CK, Lim SH, Lin J, Feng YP. Tungsten carbide supports for single-atom platinum-based fuel-cell catalysts: first-principles study on the metal–support interactions and O 2 dissociation on W x C low-index surfaces. J Phys Chem C 2014;118:13525–38. https://doi.org/10.1021/jp4070328.
[484] Tang L, Wang Y, Li Y, Feng H, Lu J, Li J. Preparation, structure, and electrochemical properties of reduced graphene sheet films. Adv Funct Mater 2009;19:2782–9. https://doi.org/10.1002/adfm.200900377.
[485] Védrine JC. Importance, features and uses of metal oxide catalysts in heterogeneous catalysis. Chin J Catal 2019;40:1627–36. https://doi.org/10.1016/S1872-2067(18)63162-6.
[486] Duprez D, Cavani F. Handbook of advanced methods and processes in oxidation catalysis. IMPERIAL COLLEGE PRESS; 2014. https://doi.org/10.1142/p791.
[487] Mars P, van Krevelen DW. Oxidations carried out by means of vanadium oxide catalysts. Chem Eng Sci 1954;3:41–59. https://doi.org/10.1016/S0009-2509(54)80005-4.
[488] Xie J, Yin K, Serov A, Artyushkova K, Pham HN, Sang X, et al. Selective aerobic oxidation of alcohols over atomically-dispersed non-precious metal catalysts. ChemSusChem 2017;10:359–62. https://doi.org/10.1002/cssc.201601364.
[489] Li M, Wu S, Yang X, Hu J, Peng L, Bai L, et al. Highly efficient single atom cobalt catalyst for selective oxidation of alcohols. Appl Catal Gen 2017;543:61–6. https://doi.org/10.1016/j.apcata.2017.06.018.
[490] Zhu Y, Sun W, Luo J, Chen W, Cao T, Zheng L, et al. A cocoon silk chemistry strategy to ultrathin N-doped carbon nanosheet with metal single-site catalysts. Nat Commun 2018;9:3861. https://doi.org/10.1038/s41467-018-06296-w.
[491] Wang P, Ren Y, Wang R, Zhang P, Ding M, Li C, et al. Atomically dispersed cobalt catalyst anchored on nitrogen-doped carbon nanosheets for lithium-oxygen batteries. Nat Commun 2020;11:1576. https://doi.org/10.1038/s41467-020-15416-4.
[492] Schultz MJ, Sigman MS. Recent advances in homogeneous transition metal-catalyzed aerobic alcohol oxidations. Tetrahedron 2006;62:8227–41. https://doi.org/10.1016/j.tet.2006.06.065.
[493] Zhang H, Lu L, Kawashima K, Okumura M, Haruta M, Toshima N. Synthesis and catalytic activity of Crown jewel-structured (IrPd)/Au trimetallic nanoclusters. Adv Mater 2015;27:1383–8. https://doi.org/10.1002/adma.201404870.
[494] Zhang P, Lu H, Zhou Y, Zhang L, Wu Z, Yang S, et al. Mesoporous MnCeOx solid solutions for low temperature and selective oxidation of hydrocarbons. Nat Commun 2015;6:8446. https://doi.org/10.1038/ncomms9446.
[495] Zhang X, Yang Y, Que W, Du Y. Synthesis of high quality CuO nanoflakes and CuO–Au nanohybrids for superior visible light photocatalytic behavior. RSC Adv 2016;6:81607–13. https://doi.org/10.1039/C6RA12281G.
[496] Padhi SK, Gottapu SN, Krishna MG. Electron-beam irradiation induced transformation of Cu 2 (OH) 3 NO 3 nanoflakes into nanocrystalline CuO. Nanoscale 2016;8:11194–201. https://doi.org/10.1039/C6NR02572B.
[497] Trimpalis A, Giannakakis G, Cao S, Flytzani-Stephanopoulos M. NiAu single atom alloys for the selective oxidation of methacrolein with methanol to methyl methacrylate. Catal Today 2020;355:804–14. https://doi.org/10.1016/j.cattod.2019.04.021.
[498] Long B, Tang Y, Li J. New mechanistic pathways for CO oxidation catalyzed by single-atom catalysts: supported and doped Au1/ThO2. Nano Res 2016;9:3868–80. https://doi.org/10.1007/s12274-016-1256-x.
[499] Esrafili MD, Asadollahi S. Exploring different reaction mechanisms for oxidation of CO over a single Pd atom incorporated nitrogen-doped graphene: a DFT study. Appl Surf Sci 2019;463:526–34. https://doi.org/10.1016/j.apsusc.2018.08.249.
[500] Han B, Ling L, Fan M, Liu P, Wang B, Zhang R. A DFT study and microkinetic analysis of CO oxidation to dimethyl oxalate over Pd stripe and Pd single atom-doped Cu(111) surfaces. Appl Surf Sci 2019;479:1057–67. https://doi.org/10.1016/j.apsusc.2019.02.112.
[501] Wang Q, Lei Y, Wang D, Li Y. Defect engineering in earth-abundant electrocatalysts for CO 2 and N 2 reduction. Energy Environ Sci 2019;12:1730–50. https://doi.org/10.1039/C8EE037.
[502] Chu S, Majumdar A. Opportunities and challenges for a sustainable energy future. Nature 2012. https://doi.org/10.1038/nature11475.
[503] Cao Y, Chen S, Luo Q, Yan H, Lin Y, Liu W, et al. Atomic-level insight into optimizing the hydrogen evolution pathway over a Co 1 -N 4 single-site photocatalyst. Angew Chem Int Ed 2017;56:12191–6. https://doi.org/10.1002/anie.201706467.
[504] Xue ZH, Luan D, Zhang H, David (, Lou XW. Single-atom catalysts for photocatalytic energy conversion. Joule 2022. https://doi.org/10.1016/j.joule.2021.12.011.
[505] Teng Z, Cai W, Sim W, Zhang Q, Wang C, Su C, et al. Photoexcited single metal atom catalysts for heterogeneous photocatalytic H2O2 production: pragmatic guidelines for predicting charge separation. Appl Catal B Environ 2021;282:119589. https://doi.org/10.1016/j.apcatb.2020.119589.
[506] Zhang Q, Guan J. Single-atom catalysts for electrocatalytic applications. Adv Funct Mater 2020. https://doi.org/10.1002/adfm.202000768.
[507] Ameta R, Solanki MS, Benjamin S, Ameta SC. Photocatalysis. Adv. Oxid. Process. Waste water treat.. Elsevier; 2018. p. 135–75. https://doi.org/10.1016/B978-0-12-810499-6.00006-1.
[508] Khan MM, Adil SF, Al-Mayouf A. Metal oxides as photocatalysts. J Saudi Chem Soc 2015. https://doi.org/10.1016/j.jscs.2015.04.003.
[509] Shen J, Zhu Y, Yang X, Zong J, Zhang J, Li C. One-pot hydrothermal synthesis of graphenequantum dots surface-passivated by polyethylene glycol and their photoelectric conversion under near-infrared light. New J Chem 2012;36:97–101. https://doi.org/10.1039/C1NJ20658C.
[510] Chen Y, Wang D, Deng X, Li Z. Metal–organic frameworks (MOFs) for photocatalytic CO 2 reduction. Catal Sci Technol 2017;7:4893–904. https://doi.org/10.1039/C7CY01653K.
[511] Hu R, Liao G, Huang Z, Qiao H, Liu H, Shu Y, et al. Recent advances of monoelemental 2D materials for photocatalytic applications. J Hazard Mater 2021;405:124179. https://doi.org/10.1016/j.jhazmat.2020.124179.
[512] Sayed M, Yu J, Liu G, Jaroniec M. Non-noble plasmonic metal-based photocatalysts. Chem Rev 2022;122:10484–537. https://doi.org/10.1021/acs.chemrev.1c00473.
[513] Li X, Chen Y, Tao Y, Shen L, Xu Z, Bian Z, et al. Challenges of photocatalysis and their coping strategies. Chem Catal 2022;2:1315–45. https://doi.org/10.1016/j.checat.2022.04.007.
[514] Debe MK. Electrocatalyst approaches and challenges for automotive fuel cells. Nature 2012;486:43–51. https://doi.org/10.1038/nature11115.
[515] Zhang Y, Luo M, Yang Y, Li Y, Guo S. Advanced multifunctional electrocatalysts for energy conversion. ACS Energy Lett 2019;4:1672–80. https://doi.org/10.1021/acsenergylett.9b01045.
[516] Khan MA, Zhao H, Zou W, Chen Z, Cao W, Fang J, et al. Recent progresses in electrocatalysts for water electrolysis. Electrochem Energy Rev 2018;1:483–530. https://doi.org/10.1007/s41918-018-0014-z.
[517] Stamenkovic VR, Fowler B, Mun BS, Wang G, Ross PN, Lucas CA, et al. Improved oxygen reduction activity on Pt 3 Ni(111) via increased surface site availability. Science 2007;315(80):493–7. https://doi.org/10.1126/science.1135941.
[518] Zhang J, Sasaki K, Sutter E, Adzic RR. Stabilization of platinum oxygen-reduction electrocatalysts using gold clusters. Science 2007;315(80):220–2. https://doi.org/10.1126/science.1134569.
[519] Wu G, More KL, Johnston CM, Zelenay P. High-performance electrocatalysts for oxygen reduction derived from polyaniline, iron, and cobalt. Science 2011;332(80):443–7. https://doi.org/10.1126/science.1200832.
[520] Furukawa H, Cordova KE, O'Keeffe M, Yaghi OM. The chemistry and applications of metal-organic frameworks. Science 2013;(80). https://doi.org/10.1126/science.1230444.
[521] Li K, Zhang S, Zhang X, Liu S, Jiang H, Jiang T, et al. Atomic tuning of single-atom Fe–N–C catalysts with phosphorus for robust electrochemical CO 2 reduction. Nano Lett 2022;22:1557–65. https://doi.org/10.1021/acs.nanolett.1c04382.
[522] Yang H, Wu Y, Li G, Lin Q, Hu Q, Zhang Q, et al. Scalable production of efficient single-atom copper decorated carbon membranes for CO 2 electroreduction to methanol. J Am Chem Soc 2019;141:12717–23. https://doi.org/10.1021/jacs.9b04907.
[523] Cai Y, Fu J, Zhou Y, Chang Y-C, Min Q, Zhu J-J, et al. Insights on forming N,O-coordinated Cu single-atom catalysts for electrochemical reduction CO2 to methane. Nat Commun 2021;12:586. https://doi.org/10.1038/s41467-020-20769-x.
[524] Han G, Zhang X, Liu W, Zhang Q, Wang Z, Cheng J, et al. Substrate strain tunes operando geometric distortion and oxygen reduction activity of CuN2C2 single-atom sites. Nat Commun 2021;12:6335. https://doi.org/10.1038/s41467-021-26747-1.
[525] Di J, Chen C, Yang S-Z, Chen S, Duan M, Xiong J, et al. Isolated single atom cobalt in Bi3O4Br atomic layers to trigger efficient CO2 photoreduction. Nat Commun 2019;10:2840. https://doi.org/10.1038/s41467-019-10392-w.
[526] Zhang P, Zhan X, Xu L, Fu X, Zheng T, Yang X, et al. Mass production of a single-atom cobalt photocatalyst for high-performance visible-light photocatalytic CO 2 reduction. J Mater Chem 2021;9:26286–97. https://doi.org/10.1039/D1TA07169F.
[527] Zhang W, Peng Q, Shi L, Yao Q, Wang X, Yu A, et al. Merging single-atom-dispersed iron and graphitic carbon nitride to a joint electronic system for high-

efficiency photocatalytic hydrogen evolution. Small 2019;15:1905166. https://doi.org/10.1002/smll.201905166.
[528] Artz J, Müller TE, Thenert K, Kleinekorte J, Meys R, Sternberg A, et al. Sustainable conversion of carbon dioxide: an integrated review of catalysis and life cycle assessment. Chem Rev 2018. https://doi.org/10.1021/acs.chemrev.7b00435.
[529] Tackett BM, Gomez E, Chen JG. Net reduction of CO2 via its thermocatalytic and electrocatalytic transformation reactions in standard and hybrid processes. Nat Catal 2019;2:381–6. https://doi.org/10.1038/s41929-019-0266-y.
[530] Wei X, Yin Z, Lyu K, Li Z, Gong J, Wang G, et al. Highly selective reduction of CO 2 to C 2+ hydrocarbons at copper/polyaniline interfaces. ACS Catal 2020;10:4103–11. https://doi.org/10.1021/acscatal.0c00049.
[531] Wang Z, Zhao Z, Li Y, Zhong Y, Zhang Q, Liu Q, et al. Ruthenium-catalyzed hydrogenation of CO 2 as a route to methyl esters for use as biofuels or fine chemicals. Chem Sci 2020;11:6766–74. https://doi.org/10.1039/D0SC02942D.
[532] Butera V, Detz H. DFT study of GaN clusters decorated with Rh and Pt nanoparticles for the photochemical reduction of CO 2. ACS Appl Energy Mater 2022;5:4684–90. https://doi.org/10.1021/acsaem.2c00110.
[533] Meshitsuka S, Ichikawa M, Tamaru K. Electrocatalysis by metal phthalocyanines in the reduction of carbon dioxide. J Chem Soc, Chem Commun 1974;158. https://doi.org/10.1039/c39740000158.
[534] Li S, Lu X, Zhao S, Ceccato M, Hu X-M, Roldan A, et al. p-Block indium single-atom catalyst with low-coordinated in–N motif for enhanced electrochemical CO 2 reduction. ACS Catal 2022;12:7386–95. https://doi.org/10.1021/acscatal.2c01805.
[535] Kim J, Kim HE, Lee H. Single-atom catalysts of precious metals for electrochemical reactions. ChemSusChem 2018. https://doi.org/10.1002/cssc.201701306.
[536] Sreekanth N, Nazrulla MA, Vineesh TV, Sailaja K, Phani KL. Metal-free boron-doped graphene for selective electroreduction of carbon dioxide to formic acid/formate. Chem Commun 2015;51:16061–4. https://doi.org/10.1039/C5CC06051F.
[537] Liu Y, Zhang Y, Cheng K, Quan X, Fan X, Su Y, et al. Selective electrochemical reduction of carbon dioxide to ethanol on a boron- and nitrogen-Co-doped nanodiamond. Angew Chem Int Ed 2017;56:15607–11. https://doi.org/10.1002/anie.201706311.
[538] Huo S, Lu J, Wang X. Recent progress in electrochemical reduction of carbon dioxide on metal single-atom catalysts. Energy Sci Eng 2022. https://doi.org/10.1002/ese3.1036.
[539] Liu L, Corma A. Metal catalysts for heterogeneous catalysis: from single atoms to nanoclusters and nanoparticles. Chem Rev 2018. https://doi.org/10.1021/acs.chemrev.7b00776.
[540] Hori Y, Kikuchi K, Suzuki S. Production of CO and CH4 in electrochemical reduction of CO2 at metal electrodes in aqueous hydrogencarbonate solution. Chem Lett 1985;14:1695–8. https://doi.org/10.1246/cl.1985.1695.
[541] Ju W, Bagger A, Hao G-P, Varela AS, Sinev I, Bon V, et al. Understanding activity and selectivity of metal-nitrogen-doped carbon catalysts for electrochemical reduction of CO2. Nat Commun 2017;8:944. https://doi.org/10.1038/s41467-017-01035-z.
[542] Butera V, Detz H. Photochemical CO 2 conversion on pristine and Mg-doped gallium nitride (GaN): a comprehensive DFT study based on a cluster model approach. Mater Chem Front 2021;5:8206–17. https://doi.org/10.1039/D1QM01118A.
[543] Kibria MG, Edwards JP, Gabardo CM, Dinh CT, Seifitokaldani A, Sinton D, et al. Electrochemical CO2 reduction into chemical feedstocks: from mechanistic electrocatalysis models to system design. Adv Mater 2019. https://doi.org/10.1002/adma.201807166.
[544] Zhang H, Li J, Xi S, Du Y, Hai X, Wang J, et al. A graphene-supported single-atom FeN 5 catalytic site for efficient electrochemical CO 2 reduction. Angew Chem Int Ed 2019;58:14871–6. https://doi.org/10.1002/anie.201906079.
[545] Miyake J, Ogawa Y, Tanaka T, Ahn J, Oka K, Oyaizu K, et al. Rechargeable proton exchange membrane fuel cell containing an intrinsic hydrogen storage polymer. Commun Chem 2020;3:138. https://doi.org/10.1038/s42004-020-00384-z.
[546] Mangiatordi GF, Butera V, Russo N, Laage D, Adamo C. Charge transport in poly-imidazole membranes: a fresh appraisal of the Grotthuss mechanism. Phys Chem Chem Phys 2012;14:10910. https://doi.org/10.1039/c2cp23727j.
[547] Ioroi T, Siroma Z, Yamazaki S ichi, Yasuda K. Electrocatalysts for PEM fuel cells. Adv Energy Mater 2019. https://doi.org/10.1002/aenm.201801284.
[548] Jasinski R. A new fuel cell cathode catalyst [13]. Nature 1964. https://doi.org/10.1038/2011212a0.
[549] Calle-Vallejo F, Martínez JI, Rossmeisl J. Density functional studies of functionalized graphitic materials with late transition metals for oxygen reduction reactions. Phys Chem Chem Phys 2011;13:15639. https://doi.org/10.1039/c1cp21228a.
[550] Cui L, Cui L, Li Z, Zhang J, Wang H, Lu S, et al. A copper single-atom catalyst towards efficient and durable oxygen reduction for fuel cells. J Mater Chem 2019;7:16690–5. https://doi.org/10.1039/C9TA03518D.
[551] Gao G, Jiao Y, Waclawik ER, Du A. Single atom (Pd/Pt) supported on graphitic carbon nitride as an efficient photocatalyst for visible-light reduction of carbon dioxide. J Am Chem Soc 2016;138:6292–7. https://doi.org/10.1021/jacs.6b02692.
[552] Cheng N, Zhang L, Doyle-Davis K, Sun X. Single-atom catalysts: from design to application. Electrochem Energy Rev 2019;2:539–73. https://doi.org/10.1007/s41918-019-00050-6.
[553] Yang H, Shang L, Zhang Q, Shi R, Waterhouse GIN, Gu L, et al. A universal ligand mediated method for large scale synthesis of transition metal single atom catalysts. Nat Commun 2019;10:4585. https://doi.org/10.1038/s41467-019-12510-0.
[554] Vajda S, White MG. Catalysis applications of size-selected cluster deposition. ACS Catal 2015;5:7152–76. https://doi.org/10.1021/acscatal.5b01816.
[555] Li J, Guan Q, Wu H, Liu W, Lin Y, Sun Z, et al. Highly active and stable metal single-atom catalysts achieved by strong electronic metal–support interactions. J Am Chem Soc 2019;141:14515–9. https://doi.org/10.1021/jacs.9b06482.
[556] Su J, Ge R, Dong Y, Hao F, Chen L. Recent progress in single-atom electrocatalysts: concept, synthesis, and applications in clean energy conversion. J Mater Chem 2018;6:14025–42. https://doi.org/10.1039/C8TA04064H.
[557] Liu J, Zhu D, Zheng Y, Vasileff A, Qiao S-Z. Self-supported earth-abundant nanoarrays as efficient and robust electrocatalysts for energy-related reactions. ACS Catal 2018;8:6707–32. https://doi.org/10.1021/acscatal.8b01715.
[558] Liu J-C, Tang Y, Wang Y-G, Zhang T, Li J. Theoretical understanding of the stability of single-atom catalysts. Natl Sci Rev 2018;5:638–41. https://doi.org/10.1093/nsr/nwy094.
[559] Goodman ED, Johnston-Peck AC, Dietze EM, Wrasman CJ, Hoffman AS, Abild-Pedersen F, et al. Catalyst deactivation via decomposition into single atoms and the role of metal loading. Nat Catal 2019;2:748–55. https://doi.org/10.1038/s41929-019-0328-1.
[560] Li X, Yang X, Zhang J, Huang Y, Liu B. In situ/operando techniques for characterization of single-atom catalysts. ACS Catal 2019;9:2521–31. https://doi.org/10.1021/acscatal.8b04937.
[561] US Government Accountability Office. Technology readiness assessment guide: best practices for evaluating the readiness of technology for use in acquisition programs and projects. 2020.
[562] Olcay H, Malina R, Upadhye AA, Hileman JI, Huber GW, Barrett SRH. Techno-economic and environmental evaluation of producing chemicals and drop-in aviation biofuels via aqueous phase processing. Energy Environ Sci 2018;11:2085–101. https://doi.org/10.1039/C7EE03557H.
[563] Lari GM, Pastore G, Haus M, Ding Y, Papadokonstantakis S, Mondelli C, et al. Environmental and economical perspectives of a glycerol biorefinery. Energy Environ Sci 2018;11:1012–29. https://doi.org/10.1039/C7EE03116E.
[564] Karam L, Reboul J, Casale S, Massiani P, El Hassan N. Porous nickel-alumina derived from metal-organic framework (MIL-53): a new approach to achieve active and stable catalysts in methane dry reforming. ChemCatChem 2020;12:373–85. https://doi.org/10.1002/cctc.201901278.
[565] Chein R-Y, Fung W-Y. Syngas production via dry reforming of methane over CeO2 modified Ni/Al_2O_3 catalysts. Int J Hydrogen Energy 2019;44:14303–15. https://doi.org/10.1016/j.ijhydene.2019.01.113.
[566] Gac W, Zawadzki W, Słowik G, Sienkiewicz A, Kierys A. Nickel catalysts supported on silica microspheres for CO_2 methanation. Microporous Mesoporous Mater 2018;272:79–91. https://doi.org/10.1016/j.micromeso.2018.06.022.
[567] Wang S. CO_2 reforming of methane on Ni catalysts: effects of the support phase and preparation technique. Appl Catal B Environ 1998;16:269–77. https://doi.org/10.1016/S0926-3373(97)00083-0.